Unveiling Protostellar Disk Formation

around Low-Mass Stars

Unveiling Protostellar Disk Formation

around Low-Mass Stars

Proefschrift

ter verkrijging van
de graad van Doctor aan de Universiteit Leiden,
op gezag van de Rector Magnificus prof. mr. C. J. J. M. Stolker,
volgens besluit van het College voor Promoties
te verdedigen op woensdag 24 september 2014
klokke 10.00 uur

door

Daniel Santoso Harsono

geboren te Sumenep, Indonesië
in 1985

Promotiecommissie

Promotor: Prof. dr. E. F. van Dishoeck

Co-promotor: Dr. S. Bruderer   Max-Planck-Institut Für Extraterrestrische Physik

Overige leden: Dr. M. R. Hogerheijde
                      Prof. dr. H. Röttgering
                      Prof. dr. F. F. S. van der Tak   Space Research Organization Netherlands,
                                                        and RUG
                      Prof. dr. L. Hartmann   University of Michigan
                      Prof. dr. Z.-Y. Li   University of Virginia
                      Dr. J. K. Jørgensen   University of Copenhagen

To those who travel far and wide

Table of contents

Chapter 6.   Volatile snowlines in embedded disks around low-mass protostars   109

Chapter 1

Introduction

A̲ᴛ least one planet is orbiting every star (Batalha et al. 2013). Planets are formed within the accretion disk that is an important part of star formation. Most of the stellar mass is transported and processed by the disk while the left-over gas and dust become the building blocks of the planetary system. The processing within the disk alters the chemical structure of the gas and dust during the formation and evolution of disks up to their dissipation. While these two stages (formation and dissipation) are crucial, they are not well understood. One of the big questions in astronomy is how these changes in the physical and chemical structure during the early stages of star formation affect the planet formation process and the emergence of life.

The majority of chemical elements essential for life (SPONCH) as we know it are produced inside the stars. In the early universe, only chemical elements up to Lithium are synthesized (Galli & Palla 2013). The life-cycle of stars enriches the interstellar medium (ISM) by fusing elements to produce heavier elements up to iron (Fe) in the core through nuclear burning. The mass of the element that is synthesized in the stellar core is related to the mass of the star: only the more massive stars can produce Fe in their cores. Over time, more of these heavier elements are produced and incorporated into the next generation(s) of star and planet formation. These elements are then integrated into molecules, both simple and complex, during the star and planet formation process.

Star and planet formation are intimately linked through the disk. Disks have been proposed by Kant and Laplace in the 18th century. Yet, it took another 2 centuries for the direct observational evidence of disks. The formation and evolution of disks dictate the amount of material delivered onto the star and of that what remains to form planets. This thesis focuses on the physical and chemical processes in the early stages of disk formation and evolution.

1.1 Star and planet formation

Stars form out of cold ($\sim 10 - 20$ K) dense molecular clouds (Bergin & Tafalla 2007) composed mostly of H_2 gas with 1% by mass in dust (Tielens 2005). With recent high sensitivity observations using the *Herschel Space Observatory*, it is known that these molecular clouds and star formation are located along filaments (André et al. 2010; Kennicutt & Evans 2012). Within these filaments, there are a variety of sizes and masses of molecular clouds. The more massive of these, especially at the point where filaments merge, will form star clusters (Schneider et al. 2012). There are small dense cores (≤ 0.1 pc, $n \sim 10^4$–10^5 cm^{-3}) along the filament which will form low-mass stars such as our Sun. Significant progress has been made recently in understanding the formation of these filaments and molecular clouds within them (Hennebelle & Falgarone 2012; André et al. 2014). Supersonic turbulence in the ISM causes the gas to compress into sheets and filaments. As a molecular cloud accumulates mass, gravity starts to become the dominant force and the cloud collapses to form cores that will form each individual star. In

addition, magnetic fields also control the flow of material on different physical scales.

The central protostar is a hot luminous ball of gas powered by the energy released by accretion in the protostellar phase and by nuclear reactions in its center at later stages. The stages of low-mass star formation ($M \leq 2\ M_\odot$) are relatively well understood compared to their higher mass counterparts but still several aspects remain unclear. While massive stars are luminous and easier to observe, low mass stars are more common. The study of the physical processes that take place during their formation provides insight into how our planetary system formed and on the emergence of life on Earth.

As the collapse proceeds, some material forms a disk as a consequence of energy and momentum conservation. Theoretical studies of disk properties did not start until the 1970s (Shakura & Sunyaev 1973). Early indirect evidence of disks has been found through optical polarization and spectra (Hartmann & Kenyon 1985, 1987) and mm-wave velocity fields (Sargent & Beckwith 1987). However, it is not until Strom et al. (1989) that the first statistical studies of disks emerged through the characterization of their spectral energy distributions (SEDs), thanks to the *Infrared Astronomical Satellite (IRAS)*. A follow-up survey of millimeter continuum emission by Beckwith et al. (1990) provided early mass estimates of disks around young stars. The key evidence was the first direct image of disks in 1994 using the *Hubble Space Telescope* (O'Dell & Wen 1994). Now, it is known that an accretion disk is present around every young star and it is a crucial part of star and planet formation (see Dullemond & Monnier 2010, Williams & Cieza 2011 and Luhman 2012 for recent reviews). This disk is usually called a circumstellar or protoplanetary disk (see Evans et al. 2009a for nomenclature). During the early stages of its evolution, the disk contains substantial amounts of gas, which is essential for the formation of gas-rich giants such as Jupiter.

Within these disks, planets eventually will form. Currently, there are over 1000 confirmed planets around other stars and more than 3000 candidates[1]. The current favorite scenario is that these planets are formed through coagulation of small dust particles to form larger bodies (Safronov 1969; Hayashi 1981; Pollack et al. 1996). It is expected that larger grains (>cm radius) move at larger velocities with respect to the gas. The drift velocity is maximal for 1 meter size bodies. At such velocities, the dust can either collide and fragment or drift inward onto the star before they grow to planetesimal size. This theoretical problem in planet formation is called the meter-size barrier. One possible solution is that these grains are covered by ices as proposed by Eddington (1937) and, finally, detected by Gillett & Forrest (1973). Over recent years following many surveys using ground-based telescopes and space observatories, it is clear that water is the main constituent of these ices as molecules freeze out and form on cold dust grains (e.g., Gibb et al. 2004; Öberg et al. 2011a). The growth of particles may well be enhanced in regions of the circumstellar disk where these ices remain on the dust grains (Stevenson & Lunine 1988; Ros & Johansen 2013). The main difference between the mechanisms proposed by Safronov (1969) and the Kyoto model (Hayashi 1981) is that the latter focuses on the importance of gas dynamics.

To illustrate the stages of star formation leading toward planet formation, it is simplest to present the general sequence of the formation of an isolated low-mass star (see Figure 1.1). Isolated here means that it is formed out of a gravitationally collapsing spherical ball of gas and dust without the presence of any stars near enough such that they provide disturbances. The general sequence of star formation can be split into four 'Stages' that describe the transfer of mass from the large-scale envelope (M_{env}) to the star ($M_\star$) (Robitaille et al. 2006; Dunham et al. 2014).

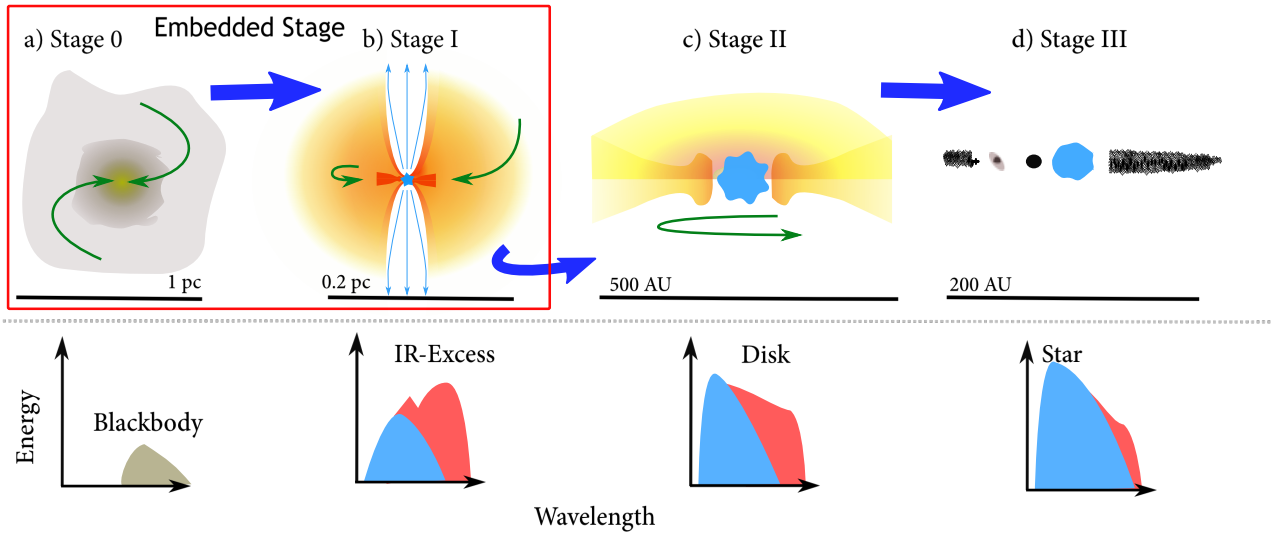[1] see exoplanets.org for updated values

Figure 1.1 — *Top:* A sketch of low-mass star and planet formation. *a*: The embedded stage is indicated by the red box. Gravitational contraction occurs during Stage 0 on scales of 1 pc. *b*: A rotationally supported disk is present by Stage I embedded inside an envelope up to 0.1 pc. Jets and winds (thin blue arrows) launched from the inner regions create bipolar outflows and carve out a cavity. *c*: The envelope has dissipated away by Stage II and a ~ 200 AU radius disk surrounds the pre-main sequence star (blue object). *d*: A planetary system has formed by Stage III. *Bottom:* Spectral energy distribution (SED) at each stage of evolution (energy as a function of wavelength increasing to the right). The different colors highlight the different components: the cold envelope is indicated by the brown color (*far left*), the warm disk/envelope emission is the red color, and the star is depicted by the blue color.

- **Stage 0** – Envelope mass is much greater than the central or protostellar mass ($M_{\mathrm{env}} \gg M_\star$). The dust thermal emission during this stage indicates a cold outer envelope. Highly collimated bipolar outflows are typically observed toward such objects (e.g., Bachiller & Tafalla 1999; Arce et al. 2007). This phase proceeds for $\sim 10^5$ years.
- **Stage I** – The central protostellar mass is greater than the envelope mass ($M_\star > M_{\mathrm{env}}$). The star and a possible disk contribution to the thermal emission is visible indicating a warm dust component. A weaker outflow component is typically associated with sources in this stage. The phase lasts $\sim 10^{5-6}$ years.
- **Stage II** – The envelope is largely dispersed and the central star is surrounded by a circumstellar disk. The sources in this stage are called classical T-Tauri stars. The emission at short wavelengths is dominated by the central protostar while the disk dominates the emission at longer wavelengths. The phase lasts $\sim 10^{6-7}$ years.
- **Stage III** – At this stage, the protostar is surrounded by a gas poor circumstellar disk (debris disk, see Wyatt 2008 and Matthews et al. 2014 for recent reviews). Planet(s) and asteroid belts must already be formed by this stage.

Stages 0 and I represent the embedded phase of star formation where a substantial mass still resides within the large-scale envelope as depicted in Fig. 1.1. This thesis focuses on the physical processes that act during this particular time, $\sim 10^5$ years after the gravitational collapse of a pre-stellar core. It is well accepted that planets form inside disks and that disks are important in the formation and evolution of stars. Planet formation is generally considered within disks in Stage II, but could start as early as Stage 0 and I if the conditions are favorable. Disk formation and its early evolution are not at all yet understood (e.g., Bodenheimer 1995; Williams & Cieza 2011; Li et al. 2014a). The main questions of this thesis are as follows:

- Do disks like those observed around pre-main sequence stars exist in the embedded phase of star formation?
- Are they observable and how can they be differentiated from the infalling rotating envelope?
- Are their physical and chemical structure consistent with the current models of disk formation?
- How stable are embedded disks and can they sustain a high infall rate from their envelope?
- How much does the embedded disk contribute to the observed molecular lines?

1.1.1   Radiation: dust and gas

Inferring the properties of young stellar objects (YSOs) is typically done through the dust continuum radiation in images and spectral energy distribution (SED, see Fig. 1.1). The peak of the SED determines the dominant dust temperature of the system. Dust warms up by reprocessing the stellar radiation from high-energy (short wavelengths) to lower-energy photons (long wavelengths). The dust temperature structure is determined by the protostellar luminosity ($L_\star$) and the dust properties, through absorption and re-emission of photons. The widely adopted dust opacities for YSOs are given by Ossenkopf & Henning (1994). Furthermore, the bulk dominant dust sizes and mineralogy of dust grains are found to be similar in disks across different star-forming regions (e.g., Oliveira et al. 2010, 2011). The warm dust in the inner disk emits in the infrared. However, during the embedded phase of star formation, the cold massive envelope surrounds the disk and re-radiates the disk emission. For a given physical structure, a complete SED and image(s) at different wavelengths can be simulated using radiative transfer tools to interpret observations in continuum (Dullemond et al. 2007) and in lines (van der Tak 2011).

While the dust thermal emission indicates the bulk energetics that are present in the system, atomic and molecular lines are used to probe the bulk mass of the protostellar system. The universe is filled with a wide variety of molecules residing in clouds with different physical conditions (see Tielens 2013 for a review on the 'molecular universe'). The observable molecular emission can be split into three types of different transitions: electronic transitions, vibrational transitions, and rotational transitions. In this thesis, vibrational and rotational transitions of CO are discussed (see Fig. 1.2). Vibrational transitions are due to the release of energy from one rotational level within a vibrational state to a rotational level within a lower vibrational state by photon emission. The rotational transition is caused by the change of angular momentum of the molecule, which for a diatomic molecule is given by $E_J = \frac{\hbar^2}{2\mu R_0^2} J(J+1)$ where μ is the reduced mass, R_0 is the equilibrium distance, and J is the quantum rotational number. The rotational levels can be populated through collisions with another molecule, which is H_2 in most cases while it is also possible to have H and electrons as collision partners. Thus, this gives a concept of critical density ($n_{\rm crit} = \frac{A_{\rm ij}}{\sum C_{\rm ij}}$, where $A_{\rm ij}$ is the Einstein coefficient and $C_{\rm ij}$ is the collisional rate coefficient), which describes a density regime where the density of the collisional partner is sufficient for the excitation to balance the spontaneous de-excitation. For densities larger than the critical density, the level populations are expected to be thermalized such that they follow the Boltzmann distribution with a given gas kinetic temperature (local thermal equilibrium or LTE). Most importantly, these transitions are quantized such that they are emitted at a certain frequency (i.e., CO $J = 1 - 0$ is at 115.271 GHz) and any gas motions are imprinted by introducing Doppler shifts. Hence, by observing frequency resolved lines, one can study the gas kinematics (e.g., Sargent & Beckwith 1987; Yen et al. 2013).
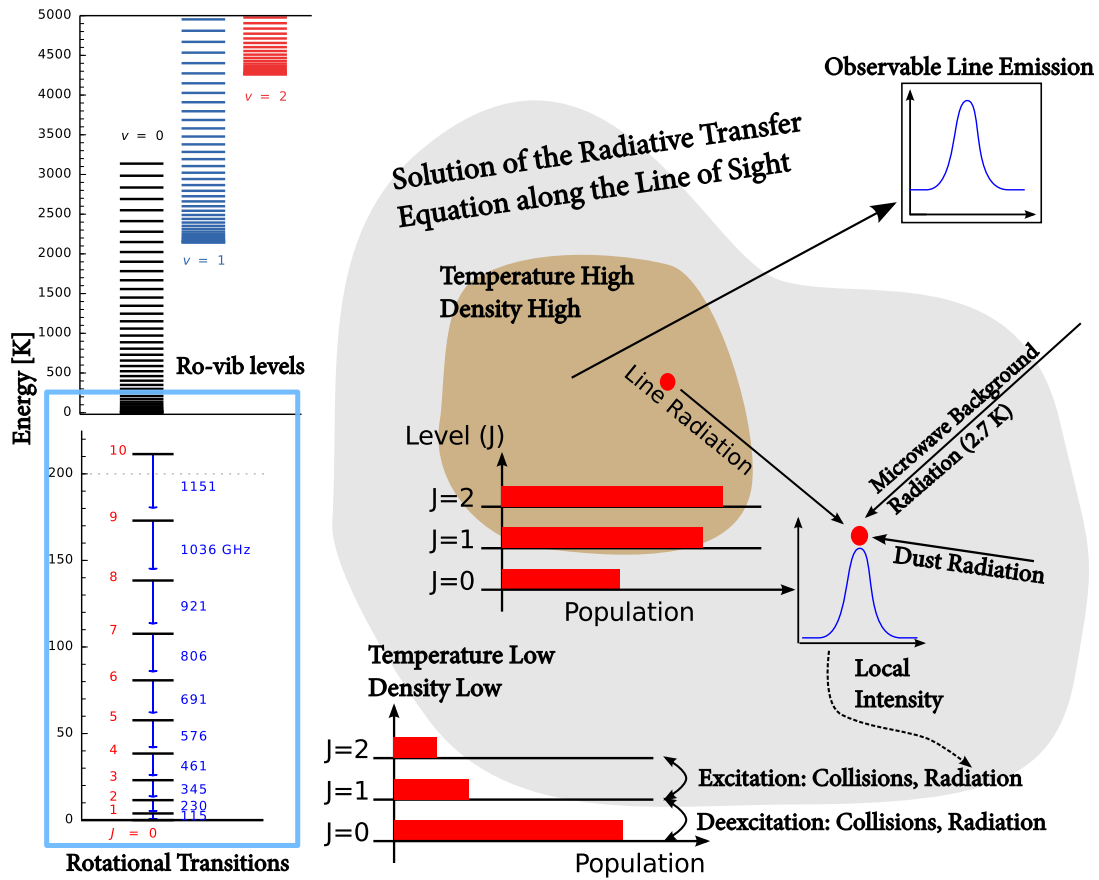
Figure 1.2 — *Top left:* The vibrational and rotational levels of ^{12}CO up to $v = 2$ and $J = 40$. *Bottom left:* A zoom in of the rotational transitions up to $J_\mathrm{u} = 10$. A cartoon depicting the molecular line excitation and radiation propagation from an envelope to the observed line profile. The low J levels are populated in the low density and low temperature regimes while higher rotational levels are populated in dense warm gas. The excitation of molecular levels include collisions with H_2 (sometimes with H, He, and electrons) and radiation from dust, other CO molecules if sufficiently optically thick, and the cosmic microwave background at 2.7 K. Adapted from Bruderer 2010.

1.1.2 Observational tools

Disks in Stage II of star formation are directly observable through the SED. However, in the early stages of star formation, the SED is a combination of the dust thermal emission of both envelope and disk. In order to study the embedded disk, interferometric observations at longer millimeter wavelengths are needed to observe the thermal dust emission from the inner envelope where the disk resides. Interferometry is a technique in which signals from multiple telescopes are correlated in order to gain enough spatial resolution (see Fig. 1.3). Millimeter and submillimeter interferometric observations of dust and gas have been crucial in revealing the inner workings of star-forming regions. These telescopes are separated by certain baselines to cover different angular resolutions (0.5″–20″). A pair of telescopes with a short baseline is sensitive to large-scale structure while a pair that has a very long baseline can resolve the small-scale structures. By combining different configurations, one can simultaneously resolve all scales. These different scales correspond to (u, v)-distances in Fourier space that relate the spacing of a pair of telescopes to the source position. An image is obtained by the Fourier
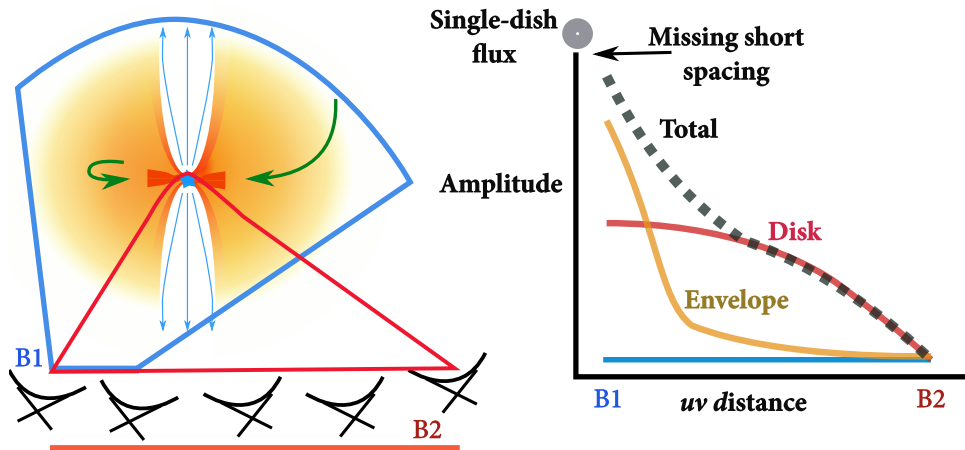
Figure 1.3 — *Left:* Sketch of how interferometry probes the physical structure of an embedded disk. A short baseline (*blue*) and a long baseline (*red*) are indicated. *Right:* The correlated flux as function of baseline length in terms of u, v distance is shown by the black dashed line. The expected contribution of the envelope and the disk are shown in orange and red, respectively. The single dish flux is indicated by the circle on top which could be larger than the correlated flux at short baselines.

transform of a collection of (u, v) points. By utilizing the Earth's rotation, a more complete (u, v) coverage can be obtained which greatly increases the image quality. On the other hand, the largest physical scale that one probes is defined by the shortest baseline. Consequently, emission from the large scale is always filtered out due to the missing short spacings since the telescopes cannot be placed infinitely close together. Beckwith et al. (1984) demonstrated the power of such observations when they revealed the compact structure of gas and dust around HL Tau. With the availability of the Plateau de Bure Interferometer (PdBI, 7 telescopes) and Atacama Large Millimeter Array (ALMA, 66 telescopes), such observations can be routinely done with much better sensitivity than before to reveal faint structures. Furthermore, the jump from 6 to 66 telescopes will provide unprecedented imaging capabilities at submillimeter wavelengths. The full ALMA will provide an angular resolution $< 0.1''$ or < 14 AU spatial resolution at typical distances of 140 pc, which is sufficient to study the disk formation process.

1.2   Disk formation: energy and momentum conservation

Significant theoretical work has gone into studying the disk formation process. Current observations provide the spatial resolution and sensitivity to test these theoretical models. The star formation process is very complex with dynamical processes occurring at physical scales ranging from a few stellar radii of ~0.1 AU to envelope scales of 10^4 AU and densities of 10^4 cm^{-3} to 10^{15} cm^{-3}. The disk forms out of conservation of energy and momentum as the core collapses from the large-scale molecular cloud. This section introduces the basic idea of how this proceeds and the problems with current theories.

1.2.1   Large scale: envelope

The physical processes that control the collapse of a large scale protostellar core include turbulence, gravity, thermal pressure, rotation, and magnetic field. Turbulence is an important aspect of galactic dynamics as a whole. It is defined by chaotic, non-linear changes to density, velocity, temperature and magnetic field during energy transfer from large scale to smaller scales.

Recent major advances in theoretical models of star formation have focused on the role of turbulence in star and disk formation simulations (Mac Low & Klessen 2004; McKee & Ostriker 2007). Gravity takes over once there is substantial mass within a sufficiently small volume. In the presence of gravity alone, the gas and dust simply stream toward the center. The presence of rotation changes the trajectory of the gas and dust as they spiral toward the growing protostar. In general, the dynamics at large scale are unchanged by rotation, however the densities and velocities are changed at small scales. Finally, magnetic fields permeate the galaxy and regulate the star-formation process (see e.g., McKee et al. 1993; Crutcher 2012). Its origin and how it is regulated is still debated. In reality, all of these forces act together during the dynamical evolution of the forming star and disk system. Fast and reliable computer programs are required to investigate the combined effects of all these forces.

Envelope rotation has been observed by Goodman et al. (1993) by mapping N_2H^+ emission on scales of $\sim$0.1 pc. The typical rotational rates of 10^{-13}–10^{-15} Hz seem to be consistent with that expected from turbulent cloud simulations by Burkert & Bodenheimer (2000). However, recent three-dimensional simulations by Dib et al. (2010) suggest that the inferred rotation rates from observations could be up to one order of magnitude higher than the true specific angular momentum of the core.

The strength of the magnetic fields toward molecular cloud cores has been inferred through statistical analysis of observations of the Zeeman effect (see e.g., Crutcher 2012). Sufficient magnetic pressure can prevent gravitational collapse when its mass is subcritical such that $M < M_{\phi_B} = \frac{\pi R^2 B}{2\pi\sqrt{G}}$ for a slab of gas and a uniform magnetic field B (Nakano & Nakamura 1978; McKee et al. 1993). In the supercritical case ($M > M_{\phi_B}$), the core simply collapses to form a star. The interesting case for a subcritical cloud is that the magnetic field prevents the ionized gas and dust from collapsing, but the neutral material can proceed to form a star (ambipolar diffusion, Zweibel 1988). More important for the disk formation and the trajectory of material is the fact that the presence of a magnetic field can remove angular momentum due to the twisted magnetic field lines. This strongly affects the formation of disks at scales $R < 1000$ AU as rotation dominates the motion on smaller scales than the magnetic fields.

1.2.2 Small scale: star and disk

The flow of material from the large-scale structure (> 1000 AU) to small scales (< 1000 AU) is determined by the angular momentum conservation and evolution. The sun's specific angular momentum is $\sim 10^{15}$ cm^2 s^{-1} (Pinto et al. 2011). For comparison, the typical specific angular momentum of molecular cloud cores is $\sim 10^{21-22}$ cm^2 s^{-1} (Goodman et al. 1993), so > 6 orders of magnitude need to be removed. This problem was first recognized by Mestel & Spitzer (1956). Perhaps, some of the angular momentum has already been lost either before or during the gravitational collapse such as described above through magnetic fields. Since angular momentum is strictly conserved in equations of motion, it needs to be transferred to other bodies or removed by other mechanism(s).

The infalling matter with excess angular momentum will form a flattened structure or a rotationally supported disk. Disks are found to have a typical specific angular momentum of $\sim 10^{19-21}$ cm^2 s^{-1}, which are lower than their envelope but still higher than the growing star (Williams & Cieza 2011; Belloche 2013). Consequently, the disk must further remove the angular momentum excess. It does so either by launching a wind/jet or by viscous transport. For the purpose of this thesis, viscous transport will be discussed. Viscosity can arise either from the collisions between gas molecules or the mixing of fluid elements through turbulence. The latter is the most commonly used viscosity parameter to describe the viscous evolution

of disks while molecular collisions are unimportant. The most commonly used viscous disk evolution model is that of the alpha-disk (α prescription) as described by Shakura & Sunyaev (1973). It is assumed that the energy loss and momentum transfer occurs locally within a length scale that corresponds to the disk's scale height (H_{disk}). From such models, a constant $\alpha \sim 10^{-2}$ is found to be a good description of the observed disk evolution and physical structure (Hartmann et al. 1998; Hughes et al. 2011).

1.2.3 Infall and accretion

The embedded phase of star formation is the period in which both of the physics at large scale and at small scales are intertwined and affect each other. The trajectory of the infalling matter from the large scale dictates the distribution of matter that forms the disk. The physical structure of the disk is crucial in determining its accretion properties. Infall describes the general trajectory of gas and dust from the envelope to the disk or star. Accretion is the transport of material inward through the disk onto the star. In the embedded phase of low-mass star formation, the dominant heating comes from the combination of infall and accretion since the protostar is still growing. Hence, the dust temperature structure that affects the physical and chemical structure of the disk and the inner envelope (< 1000 AU) relies on the understanding of the rate at which the material is being transported onto the star. This process does not have to be continuous, but it is likely episodic to avoid the luminosity problem (e.g., Evans et al. 2009b; Dunham et al. 2014). The 'luminosity problem' describes the discrepancy between the observed luminosities of embedded protostellar systems and the luminosity produced by the accretion process at a steady rate needed to build up a solar mass star (see Kenyon & Hartmann 1990).

1.3 Simplified models of star formation

As described in previous sections, star formation involves a wide range of physical processes at both large scale (~ 0.1 pc) and small scale (< 100 AU). However, simplified models of star formation that only look at one or two physical processes, in general, capture the physical structure of the large-scale envelope and the disk. These physical structures are used to interpret the observational data. There are two types of simplified models of star formation: analytical models and hydrodynamic simulations.

1.3.1 Analytical models

A subset of these simplified models can be solved analytically to describe the general sequence of star formation (Shu 1977). A significant fraction of our understanding of star formation is obtained through investigation of how different, separated physical processes independently affect the collapse and disk formation. A few of the simplifications are presented here with an increasing level of complexity. The following sections introduce analytical models of disk and envelope around protostars.

1.3.1.1 *Large-scale envelope*

The simplest model of the large-scale envelope is a spherically symmetric power law model: $\rho \propto r^{-p}$ where ρ is the total (gas+dust) density, r is the spherical radius, and p is the power-law slope. Such a power-law model stems from earlier studies such as the collapse of a singular isothermal sphere (Larson 1969). The exact density profile may change depending on the polytropic equation of the gas ($P \propto \rho^{\gamma}$, see Ogino et al. 1999 for detailed discussion). Furthermore, the presence of magnetic fields slows down the contraction process that will eventually lead
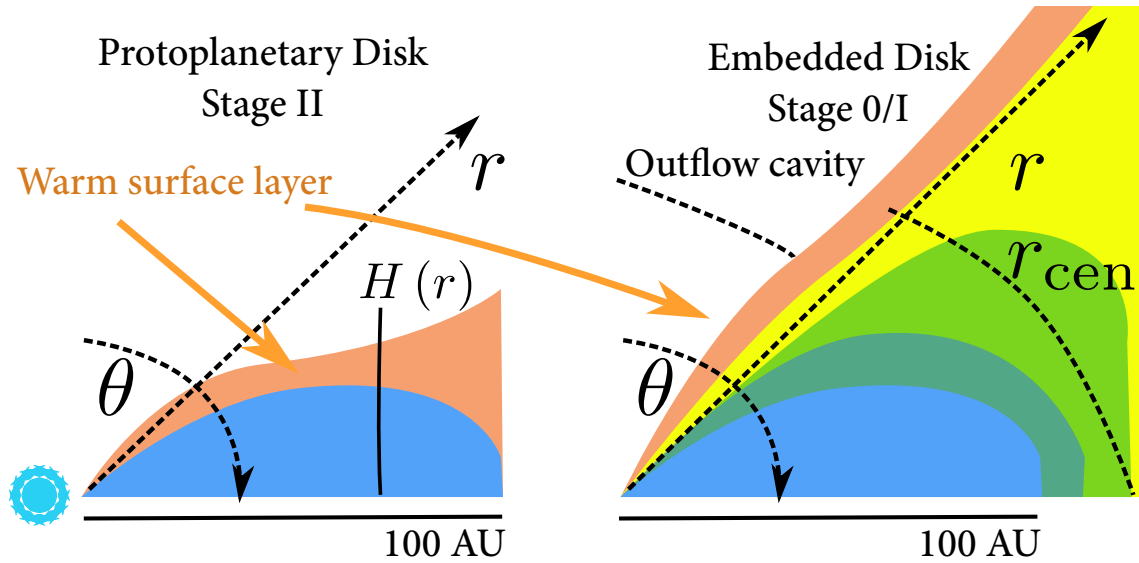
Figure 1.4 — Schematic of the 2D protoplanetary disk (*left*) and an embedded disk (*right*) physical structure in spherical coordinates (r, θ). The scale height of the disk $H(r)$ is indicated along with the warm surface layer that emits most of the IR irradiation. The outflow cavity and centrifugal radius r_{cen} are indicated in the embedded disk model.

to the isothermal solution as shown by Shu (1977). The temperature structure of such a model can be determined by assuming a central protostar with a temperature of ~ 5000 K. Such a model has been shown to reproduce the observed properties (SED and continuum images) of protostellar envelopes (e.g., Kenyon et al. 1993; Jørgensen et al. 2002).

The effects of rotation on the collapse process of the envelope were investigated in the early 70s using two- and three-dimensions with imposed axisymmetry (Larson 1972; Woodward 1978). Ulrich (1976) calculated the density structure of the envelope by imposing angular momentum conservation as the parcels of gas and dust fall toward the center. From these assumptions, the 2D density structure is described by the following equation:

$$\rho(r, \mu) = \rho_0 \left(\frac{r}{r_{cen}} \right)^{-3/2} \left(1 + \frac{\mu}{\mu_0} \right)^{-1/2} \left(\frac{\mu}{\mu_0} + \frac{2r_{cen}}{r} \mu_0^2 \right)^{-1}, \qquad (1.1)$$

where $\mu \equiv \cos\theta$, r_{cen} is the centrifugal radius where the infalling material is stopped by centrifugal force, and finally μ_0, θ_0 is the solution to the streamline at r and θ from θ_0 (see Fig. 1.4, Cassen & Moosman 1981, Whitney & Hartmann 1993). The scaling factor ρ_0 could be a free parameter or connected to the infall rate from the envelope. Compared with the spherically symmetric power-law models, this particular model in 2D is similar at large scale (> 1000 AU) while the inner regions are flattened (disk-like). The flattened region is determined by the r_{cen} parameter which describes the regime in which the material starts to enter the disk, and, consequently, can be larger than the extent of the rotationally supported disk where the azimuthal velocities are Keplerian. Such a simple two-dimensional model has been used to model the observed properties of both dust and gas toward YSOs (e.g., Whitney & Hartmann 1993; Eisner 2012; Yen et al. 2013).

1.3.1.2   Flaring disk

At small scales (< 100 AU), an accretion disk forms. The density and velocity structures described above tend to break down when comparing to observations that probe the inner regions. In 1D, the disk's axisymmetric physical structure is generally described by (e.g., Beckwith et al. 1990; Fedele et al. 2013):

$$\Sigma = \Sigma_0 \left(\frac{r}{r_0} \right)^{-p}, \; T = T_0 \left(\frac{r}{r_0} \right)^{-q}, \tag{1.2}$$

where Σ is the dust surface density, and T_0, Σ_0, and r_0 are the scaling factors where T can refer to either the dust or gas temperature. Such parametric models are found to reproduce most of the observed gas and dust emission from disks at both short and long wavelengths. Disk flaring is required to account for some missing flux emitted from the surface layer at mid-infrared wavelengths which is warmer than the disk's midplane (see Fig. 1.4, Kenyon & Hartmann 1987; Dullemond et al. 2007). A full detailed vertical structure calculation of disks is typically needed to reproduce both continuum and molecular line data (see Chiang et al. 2001; Dullemond et al. 2007). The general 2D accretion disk model is described by

$$\rho\left(r,\theta\right) = \frac{\Sigma}{\sqrt{2\pi}H} \exp\left(-\frac{r^2 \cos\theta^2}{2H^2} \right), \tag{1.3}$$

where $H = H_0 \left(\frac{r}{r_0} \right)^h$ is the scale height of the disk with a power-law exponent $h \sim 9/7$ (see Fig. 1.4, Chiang & Goldreich 1997). With the increased of computing power, 2D disk models are routinely used to model the observed dust and gas emission from disks including vertical hydrostatic equilibrium or a parametrized flaring index (Williams & Cieza 2011 and references therein).

1.3.1.3   Disk formation and evolution: time-dependence

Terebey et al. (1984) calculated the collapse of a rotating singular isothermal sphere. Cassen & Moosman (1981) focused on the early build up and evolution of disks using the streamline of particles from the large-scale envelope in the embedded phase of star formation. The merging of these two solutions describes the time-dependent analytical solution of disk formation in the absence of magnetic fields and turbulence. Such models have been coupled to protostellar evolution models to include the heating from a growing protostar. These types of models have been used to predict the observed evolutionary properties of YSOs (e.g., Young & Evans 2005). Visser et al. (2009) coupled such time-dependent models with simple chemistry to look at the chemical changes that take place as the disk forms and their connection to the chemical inventory of comets.

A semi-analytical description of the collapse including magnetic fields was given by Galli & Shu (1993). They showed that a 'pseudodisk' forms when the collapse proceeds in the presence of magnetic fields. A 'pseudodisk' is an infalling flattened density structure that can extend up to ~ 1000 AU due to preferential mass settling along field lines toward the equatorial plane. This differs from a 'true' disk whose angular velocity is Keplerian and radial velocity is defined by the viscous transport. Efficient magnetic breaking poses a problem for disk formation in the case of ideal magnetic forces as the disk is not rotationally supported (Galli et al. 2006; Li et al. 2014a). Similar results are obtained from 3D magneto-hydrodynamic (MHD) simulations.

The path that the material takes as it spirals down to the central protostar strongly affects the chemical structure of the disk. It is also found that complex molecules tend to be enhanced

if a rotationally supported disk is present instead of a pseudodisk. This occurs due to the lack of photodissociating photons coupled with a sufficiently warm disk for complex molecules to form. Therefore, continuum and molecular line observables that can differentiate between the two modes of disk formation are required to connect the physical and chemical changes during the early stages of star formation to our Solar System.

1.3.2 Numerical hydrodynamic simulations

Recent progress in numerical simulations of star formation has been made due to advances in computing. While analytical solutions can describe the general features of star formation, hydrodynamic simulations can investigate the non-linear effects of the different physical processes at once. However, one should be cautious of the numerical artefacts that are inherent in these simulations. In general, there are three types of numerical simulations that one can adopt: smoothed particle hydrodynamics (SPH), grid-based, and moving mesh. The two most tested and benchmarked of these are SPH and grid-based. There are indeed fundamental differences in the two methods as described in Agertz et al. (2007) and Tasker et al. (2008). In this thesis, SPH and grid-based codes are used.

1.3.2.1 Smoothed Particle Hydrodynamics (SPH)

This method solves the equations of fluid dynamics by interpolation (smoothed) between many dynamic particles. The implementation was started roughly 40 years ago by Lucy (1977) and Gingold & Monaghan (1977). In recent years, the treatment of different physical processes including magnetic fields has been added which are reviewed in Springel (2010) (see also Monaghan 1992 for an introduction to SPH). Any physical properties such as density (ρ), temperature described by sound speed c_s, and velocities are calculated through kernel W smoothing such that

$$\rho\left(\bar{r}\right) = \int \rho\left(\bar{r}\right) W\left(\bar{\delta r}, h_\mathrm{SPH}\right) d\bar{r}' = \sum_\mathrm{i} \rho_\mathrm{i} W\left(\bar{\delta r}_\mathrm{i}, h_\mathrm{SPH}\right) \tag{1.4}$$

with $\bar{r}$ the position of the particle i and h_SPH the smoothing length. Most current codes adopt a cubic smoothing kernel based on the distance normalized by the smoothing h_SPH. This method follows the particles as they move through space and time (Lagrangian method), which ensures the conservation of energy and momentum. SPH has been used to simulate star formation, stellar encounters, planet formation, and disk evolution.

1.3.2.2 Grid methods and AMR

Grid-based codes fix the number of resolution elements in which the fluid equations are solved. Thus, the equations of motions are solved within a set of boundary conditions and information (transfer of mass, energy, and momentum) must be propagated to adjacent grids (Eulerian) through numerical schemes. Adaptive-mesh refinement (AMR) splits up or refines certain grid(s) that satisfy a few pre-defined conditions in order to resolve the physics within that region. Different methods have been used to propagate information from one cell to nearby cells such as those (and variations of them) in van Leer (1979), Woodward & Colella (1984), and Stone & Norman (1992). In particular, Fleming et al. (2000) introduced methods to solve non-ideal magneto-hydrodynamics (MHD) equations. In the ideal MHD limit, the magnetic field is always frozen to the fluid element, while in the non-ideal case, the field is allowed numerically to diffuse and reconnect. Non-ideal MHD treatment is found to allow for rotationally supported disk formation, although not conclusively.
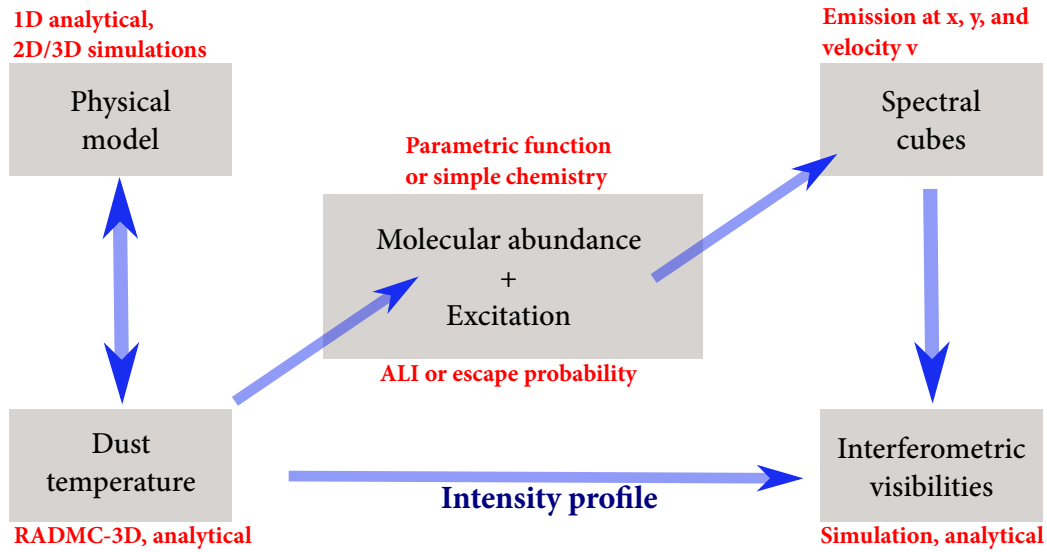
Figure 1.5 — Flowchart indicating the steps taken to generate observables in both continuum and molecular gas lines. The methods are indicated in red. The analytical physical models are listed in § 1.3. Simulations of interferometric visibilities are performed with *Common Astronomy Software Applications* (CASA) and GILDAS. Analytical calculations of visibilities are described in Chapter 5.

1.3.3   Parallelization

Recent advances in computing allow for large dynamic range (few pc down to few AU) star formation simulations to be performed. Most of these calculations can be done more efficiently by performing them in parallel using multiple central processing units (CPUs). There are two types of parallelization that have been used in this thesis: multicore computing and cluster computing. Multicore computing describes a method in which a computational task is distributed over multiple cores in one desktop computer. Cluster computing is made out of several desktops that are connected within a local area network. Even when the hardware is available, a parallel programming language is required to instruct tasks and memory distribution.

Most of the parallelization done during this thesis was performed using the built-in *multiprocessing* in Python. This is done by distributing a number of tasks such as the simulation of ≥30 rotational or ro-vibrational molecular transitions over many CPUs. The hydrodynamical codes mostly have the Message Passing Interface (MPI) language built in them. For example, using MPI, the particles in SPH simulations are distributed over different CPUs. Each of the CPUs then calculates the forces acting on the particles, then the updated properties are communicated to other CPUs to inform other tasks for the next iteration. Finally, another parallelization software is Open Multi-Processing (OpenMP). OpenMP is typically used within a repeated task (e.g., photon propagation or solving radiative transfer equations at one pixel/velocity). The software then distributes a task or a loop over the specified number of threads and CPUs. Most of the molecular line radiative transfer calculations were parallelized using multicore computing while the hydrodynamic simulations were performed on a cluster of computers.

1.4   Bridging theory and observations

A suite of radiative transfer tools is required to bridge the theoretical models described in previous sections to observations. One radiative transfer tool is needed to calculate the dust

temperature structure by simulating the photon propagation through dusty media. Another set of radiative transfer tools is required to simulate the molecular line emission. In most cases, these two tools are completely independent of each other. The typical flow of modelling the observables is illustrated in Fig. 1.5.

1.4.1 Radiative transfer: dust and masses

Dust makes up about 1% of the total mass. For a given central heating and mass distribution as in § 1.3, dust continuum radiative transfer simulates the propagation of photons as they are absorbed or scattered and re-emitted by dust. The most common method is the Monte Carlo (MC) approach (Bjorkman & Wood 2001) where photon packages with energy $L_\star/N_{\mathrm{photons}}$ are launched from the central source. Through the absorption and re-emission of these photon packages, the dust temperature structure can be obtained. The amount of energy that the dust absorbs depends on the dust optical properties.

The photon propagation is easy computationally for optically thin radiation. In this thesis, a few tricks are used to efficiently compute the dust temperature structure of optically thick ($\tau \geq 10^6$) embedded disks. Computationally, regions are taken as optically thick, when the opacity towards the star is larger than a few 1000 at the peak wavelength of the star. In general, a higher number of photons ($\sim 10^7$) are required to obtain a smooth dust temperature structure. The exact number of photons depends on the number of grids. The propagation of a photon through an optically thick region is modified such that it is not trapped within one computational cell (see Min et al. 2009). An additional source of heating such as accretion heating can be added. There are two ways to add such a term, either by depositing the energy that each cell has or by launching another set of photons from the disk. Furthermore, the diffusion approximation ($\nabla \frac{\nabla T^4}{3\rho\kappa_{\mathrm{P}}} = 0$, where κ_{P} is the Planck opacity) is used to smooth the midplane's temperature structure. The diffusion approximation is valid in the highly optically thick region ($\tau_{0.1\,\mu\mathrm{m}} >> 1$) since the radiation field is in thermal equilibrium such that the source function is the Planck function. A smooth dust temperature structure is crucial in the determination of molecular abundances in embedded disks.

The dust thermal emission can be simulated by solving the radiative transfer equation along a line of sight similar to that depicted in Fig. 1.2. One generally finds that the emission at long wavelengths is optically thin and, consequently, it is a direct measure of the dust mass. Disk and envelope masses have been obtained through such assumptions. The simplest envelope model is by assuming spherical symmetry ($\rho \propto r^{-p}$). Through dust continuum radiative transfer programs such as *DUSTY* (Ivezic & Elitzur 1997), the thermal structure can be obtained and its SED compared to observation. Jørgensen et al. (2002) and Kristensen et al. (2012) used such a method to constrain the large-scale envelope structure. In order to determine the disk mass, Jørgensen et al. (2009) explored the contribution of such a model to interferometric dust thermal emission. Thus, by accounting for the large-scale contribution, the disk emission can be extracted and, in turn, their masses (see also Looney et al. 2003; Enoch et al. 2011). More sophisticated tools such as RADMC (Dullemond & Dominik 2004), RADMC-3D, and Hyperion (Robitaille 2011) are required to build 2D and 3D physical models. Recent developments in 3D radiative transfer tools are reviewed by Steinacker et al. (2013).

1.4.2 Chemical abundances

To simulate the observed molecular lines, the gas phase molecular abundances are needed. A simple gas phase abundance can be obtained by considering the adsorption and thermal desorption of molecules on the dust grains. In addition, a lower abundance is expected along

the warm surface layers close to the star (see Fig. 1.4) where molecules can be photodissociated by absorption of energetic ultraviolet (UV) photons (see van Dishoeck et al. 2006). Ices could also be photodesorbed from the grain if they are not well shielded from energetic UV photons (e.g., Öberg et al. 2009; Fayolle et al. 2011). This thesis limits the chemistry to adsorption and thermal desorption of molecules on the dust grains. The adsorption rate is the rate at which ices of species X accumulate on the dust grain given the gas temperature and size of the dust ($\sim 0.1~\mu$m). A molecular species X also has a binding energy that describes how strongly it is bound on the grain surface. The binding energies of well known ice species such as H_2O and CO have been inferred through controlled laboratory experiments (e.g., Bisschop et al. 2006; Burke & Brown 2010). At steady state, the adsorption rate k_{ads} is balanced by the thermal desorption rate k_{thdes}. Using such a balance, one finds that CO is in the gas phase for $T_{dust} > 20$ K while it is 100 K for H_2O. The temperature of this transition is pressure dependent such that it can be up to 160 K for H_2O at high densities ($n_H \sim 10^{16}~cm^{-3}$). This is not necessarily valid at low densities such as those found in the large-scale envelope since the adsorption timescale is longer than the lifetime of the residing material. The physical processes such as infall tend to occur on timescales much shorter than the chemical timescales for the embedded phase of star formation. However, for most of the purposes of this thesis, steady state chemistry is appropriate to simulate the observables from theoretical models.

1.4.3   Molecular emission as a probe of physical structure

The dust physical structure is the first step in the determination of molecular abundances toward YSOs (e.g., Hogerheijde et al. 1998; Yıldız et al. 2013). While the low-J transitions of CO can be treated in local thermal equilibrium (LTE or thermalized) due to their low critical densities, higher-J lines tend not to be in LTE. Non-LTE population levels are calculated by considering different excitation and de-excitation mechanisms (van der Tak et al. 2007):

$$n_i \sum_i^N P_{ij} = \sum_{j\neq i}^N n_j P_{ji},$$ (1.5)

where $n_{i,j}$ are the populations of levels i and j, respectively, N is the total number of levels, and P_{ij} indicate the rate of transition between level i and j. The rates take into account the probability of spontaneous emission given by Einstein A_{ij} coefficient, probability of stimulated emission $B_{ij}\langle J_{ij}\rangle$, and collisional rates.

Thanks to many years of primarily theoretical studies in determination of potential energy surfaces and the subsequent collision dynamics on these surfaces, these properties are known and tabulated in the *Leiden Atomic and Molecular Database* (LAMDA Schöier et al. 2005) for well-known molecules. Theoretical calculations of collisional rate coefficients typically employ the close coupling (CC), coupled-states (CS) and infinite order sudden (IOS) approximations. While CC is exact, the CS approximation assumes that the angular momentum is conserved and the IOS approximation assumes that the molecules do not rotate during collision (see Schöier et al. 2005; Roueff & Lique 2013). Most recent calculations employ the CC method, which solves the nuclear Schrödinger equation exactly given the detailed potential energy surfaces (Roueff & Lique 2013). Most of the molecular databases only contain collisional rate coefficients for the rotational levels within the vibrational ground state. For example, Yang et al. (2010) calculated the CO collisional rate coefficients up to $J = 40$. To reproduce recent observations of high-J CO molecular lines ($J > 40$), extrapolations are needed as used in Chapter 4 to calculate the population levels of $J > 40$ (see also Neufeld 2012). For a simple rigid rotor such as CO, the extrapolation considers the cross section of a linear molecule with an atom as described by a

scattering matrix in the IOS approximation $S_l(\theta|E) = \sum_L S_L^l P_L(\cos\theta)$ where P_L is the Legendre polynomial of L degree at energy E. The generalized CS cross section for a linear rigid rotor colliding with a spherical rigid body is given by

$$
\sigma_n\left(j_a'j_b'|j_aj_b|E\right) = \frac{\pi}{k^2} \sum_{lmm'} (2l+1) \begin{pmatrix} j_a & j_b & n \\ m & -m' & m'-m \end{pmatrix} \begin{pmatrix} j_a' & j_b' & n \\ m & -m' & m'-m \end{pmatrix}
$$

$$
\times (-1)^{j_b+j_b'} \sqrt{\frac{2j_a'+1}{2j_a+1}} \left| \delta_{j_aj_a',j_bj_b'} - S_{jm}^l \right|^2,
\tag{1.6}
$$

where $j_{a,b}$ are the rotational quantum numbers, m is the magnetic quantum number, l describes the orbital angular momentum, () is Wigner's 3-j symbol, δ is the Kronecker delta symbol, and n describes the tensor rank for the relaxation mechanism at a given energy E (see Goldflam et al. 1977). S_{jm}^l is the scattering matrix represented by the basis vectors $|jm\rangle$ such that $S_{jm}^l = \langle j'm'|S|jm\rangle$. The inelastic collisional relaxation is dominated by $n = 0$ since there is no change in rotation as consequence of the IOS approximation, which in turn simplifies most of these terms. This simplification leads to the following relation

$$
C(T|J_u \to J_l, \Delta v = 0) = (2J_l+1) \sum_{J=|J_u-J_l|}^{J_u+J_l} \begin{pmatrix} J_u & J_l & J \\ 0 & 0 & 0 \end{pmatrix}^2 \times C(T|J_u \to 0, \Delta v = 0),
\tag{1.7}
$$

where $C(T|J_u \to 0)$ is the collisional rate coefficient from J_u to the ground rotational state at kinetic temperature T without a change of the vibration level. Such extrapolations can be extended to include vibrational levels and to approximate the collisional rate coefficients for tri-atomic linear molecules (e.g., Chandra & Sharma 2001).

Once the abundances are known, the non-LTE population levels can be treated in two ways. The Monte Carlo Accelerated Lambda Iteration technique (ALI) employed by Hogerheijde & van der Tak (2000) and Brinch & Hogerheijde (2010) can be used to iteratively find the radiation field ($\langle J_{ij} \rangle$). The rate of stimulated absorption and decay depends on it (see Fig. 1.2), thus the problem of finding the radiation field and the level population is coupled. A faster method is by adopting the escape probability approach that considers whether the photon has escaped or is absorbed at another location which depends on the optical depth of the transition (Bruderer et al. 2012, and references therein).

With recent observations obtained with *Herschel Space Observatory*, it is possible to observe CO transitions up to rotational levels of ≥ 40. A recent survey of molecular emission toward young embedded objects has been conducted as part of the Water in Star-forming Regions with Herschel (WISH van Dishoeck et al. 2011) and Dust, Ice, and Gas in Time (DIGIT, PI: Evans) key programs. Through the modelling of ^{13}CO and C^{18}O emission up to the $J = 9$–8 transition toward one particular region, Yıldız et al. (2013) constrained the CO abundance structure in the large-scale envelope. Visser et al. (2012) included the UV heating of the gas such that $T_{gas} > T_{dust}$ in order to explain the observed high-J ($J_u > 16$) fluxes. The high-J emission arises from the thin warm layer along the outflow cavity wall (see Fig. 1.4). Thus, the excitation and the simulated emission are sensitive to the setup of the computational cells along the cavity wall. With the access to such highly excited rotational transitions, it is then possible to probe different excitation conditions and, thus, the range of gas temperature within the envelope.

1.5   This thesis and outlook

This thesis explores both the theoretical and observational aspects of disk formation during the embedded stage of star formation. Semi-analytical and numerical hydrodynamic models have been coupled to dust continuum and line radiative transfer tool(s) as depicted in Fig. 1.5. The predicted spectrally resolved rotational transitions of CO isotopologs are simulated for comparison with observations. These simulations and predictions are accompanied by spatially and spectrally resolved observations of optically thin CO emission toward less embedded (more evolved Stage I) young stellar objects. The observations were carried out with the Plateau de Bure Interferometer (PdBI) located in France. The following list outlines the results of this thesis.

- The continuum and molecular line observables obtained from 3D MHD disk formation simulations are compared with 2D axisymmetric models in **Chapter 2**. The two MHD simulations differ in their initial magnetic field orientation: the magnetic field vector is aligned with the rotation axis in one case while it is strongly misaligned in the other ($90°$). These two represent the extreme outcomes of 3D MHD simulation of disk formation in which the simulation with the aligned magnetic field vector inhibits the formation of a Keplerian disk (see § 1.3.1.3). The 2D semi-analytical models are the same as described in § 1.3.1.3. The comparison shows that spatially resolved continuum observations at ~ 15 AU scale are required to determine the presence of Keplerian disks solely by continuum. This problem is alleviated if it is accompanied with spatially and spectrally resolved molecular line emission. The kinematical signatures of a pseudodisk are different from that of a rotationally supported disk if observed with sufficient spatial resolution (15 AU). Furthermore, these kinematics tend to give a good estimate (within a factor of 2) of their respective stellar masses.
- During the earliest stages of the embedded phase, the disk can be cold and massive, and thus prone to gravitationally instability. In addition, such gravitationally unstable disks are embedded inside an infalling envelope. To study the effect of infalling material onto the disk, the SPH (§ 1.3.2.1) code GADGET2 (Springel 2005) has been used to simulate such a scenario in **Chapter 3**. The angular momentum transport within the disk is enhanced by the infalling material without any fragmentation under the adopted cooling prescription. The simulation suggests that under such a scenario, a relatively low mass disk ($M_{\rm d}/M_\star \sim 0.1$) can undergo a high accretion rate driven by gravitational instability.
- As shown in Chapter 2, spectrally and spatially resolved molecular lines are the key in detecting embedded Keplerian disks. The new observational data from *Herschel*, APEX, and ALMA allow for access to highly excited rotational transitions of CO lines for the first time that probe the inner warm and dense gas (see Fig. 1.2). Thus, it is timely to provide predictions from theoretical models. **Chapter 4** focuses on the predicted evolution of molecular line observables from 2D axi-symmetric disk formation models with three different initial conditions that change the final disk properties. Similar to the result of Chapter 2, the ^{13}CO and C^{18}O $J_{\rm u} \geq 6$ lines can be broadened by the infall process. The excitation temperatures of CO within typical single-dish beams ($\geq 9''$), however, do not change with time, in contrast with the dust temperature as observed and predicted through the spectral energy distribution. The molecular line simulations are extended to include the near-IR ro-vibrational fundamental ($\Delta v = 1$) CO absorption lines at $\sim 4.5\ \mu$m as observed by VLT CRIRES. The ro-vibrational excitation is found to evolve with time following the dust temperatures.

- Chapters 2 and 4 suggest that the deeply embedded disk is easily revealed by spatially and spectrally resolved molecular line observations. Furthermore, the disk's contribution to the integrated optically thin CO line is predicted to be high during the later phase of the embedded stages of star formation. **Chapter 5** presents the spatially and spectrally resolved ^{13}CO and $C^{18}O$ 2–1 lines toward four well-known Stage I embedded objects in the nearby Taurus molecular cloud (d=140 pc). At a spatial resolution of $\leq 0.8''$ (~ 110 AU diameter), three out of the four targeted sources have ~ 100 AU radius Keplerian disks as traced by the $C^{18}O$ 2–1 line. The properties of the claimed embedded disks in the literature combined with the sources studied in this chapter are compared with the 2D disk formation models of Chapter 4. This comparison suggests that the models with initial rotation of $\Omega = 10^{-14}$ Hz and slow sound speeds match well with the observed disks.

- As a consequence of an actively accreting disk, the energy dissipated away during the angular momentum transfer heats up the disk's midplane (viscous heating). This affects the regions where ices can survive on the dust grains (snowlines). **Chapter 6** presents a theoretical study of the snowlines of the major volatile ice species (H_2O, CO, CO_2) within an actively accreting embedded disk (see Fig. 1.4). Water is particularly relevant because the location of the water snowline is important for grain growth and planet formation. Water vapor emission has been recently detected toward embedded YSOs arising from the inner 50 AU diameter. This chapter explores whether such an embedded accreting disk model (§ 1.3.1) can explain the observed emission. The water snowline is located at >20 AU radius for a highly accreting disk ($\dot{M} \geq 10^{-5} \, M_\odot \, yr^{-1}$). CO_2 can be in the gas phase up to ~ 40 AU at low accretion rates while CO is generally expected to be in the gas phase throughout the disk. The observed strength of optically thin water emission can be reproduced by the models. However, the models can only attribute the water emission to the disk for emission extending up to 30 AU.

The main conclusions of this thesis drawn from all of the chapters are as follows:

- Subarcsec spatially resolved line observations can distinguish rotationally supported disks from pseudodisks found in MHD simulations (*Chapter 2*).
- Excitation temperatures as derived from single-dish rotational transitions of CO do not evolve with time contrary to the dust continuum emission (*Chapter 4*).
- Rotationally supported disks up to 100 AU are likely present in the majority of embedded young stellar objects by the end of the collapse process. Semi-analytical models of disk formation can reproduce the disk radii found in these and even younger systems for modest initial rotation rates and sound speeds (*Chapters 4* and *5*).
- Embedded disks can undergo a high accretion rate due to the interaction with the infalling rotating envelope. Such interaction creates a non-axisymmetric disk that affects the chemical structure and evolution during the early stages of disk formation and evolution (*Chapters 2* and *3*)
- The inner 30 AU of an actively accreting embedded disk is characterized by warm dust temperatures ($T_{dust} > 100$ K). Such high temperatures allow for major volatile ice species to be in the gas phase, which can recondense when the disk cools. Consequently, the chemical content inherited from the collapsing envelope could be reset. The hot young solar nebula scenario can only occur during Stage 0 phase of star formation, not during the Stage II phase (*Chapter 6*).

Future outlook   Current observations have revealed the presence of rotationally supported disks in the inner few 100 AU toward a couple of embedded protostars (Tobin et al. 2012; Murillo et al. 2013), which are compared with disk formation models. However, to further study the details of the disk formation and evolution process in the earliest stages of star formation, the spatial resolution and sensitivity of ALMA down to scales of 10 AU is required. The higher spatial and spectral resolution observations of molecular lines can differentiate the Keplerian disk from the infalling envelope. The temperature structure of the disk, which is crucial to investigate the heating processes, requires two different molecular transitions of a molecule to investigate their excitation conditions. Furthermore, high sensitivity observations are necessary to study the velocity structure of the disk since the molecular emission at high velocities is much weaker than at line center. This will be easier done in the future to reveal the kinematics at small scales and allow disk tomography in radial and vertical direction. In addition, the combination of short and long baselines that ALMA can deliver will reveal the kinematics of the gas as it falls onto the disk.

   This thesis employs steady-state accretion models of disk formation to investigate the molecular excitation. It is known that the accretion process is episodic during the early stages of star formation (Vorobyov et al. 2013; Dunham et al. 2014). The processes within the disk and the movement of the gas and dust during this phase has direct consequences for the physical and chemical structure of an evolving embedded disk (Visser & Bergin 2012; Jørgensen et al. 2013). The main challenge is to couple these simulations that include the disk's vertical structure with radiative transfer tools and chemical models to compare with observations.

   Time dependence is needed to investigate the true gas and ice abundances that are present within the Keplerian disk. Time dependent radiative transfer and chemical models such as that applied to the 2D models need to be coupled with MHD simulations of disk formation. Furthermore, the comparison between the disk formation scenarios with and without turbulence is still an unexplored territory. The different scenarios also predict different protostellar formation histories that dictate the heating events during the early stages of star formation and, thus, the temperature structure of the newly formed disk. The predicted observables from the hot gas in the inner envelope and disk can be compared with observations that will be taken by the *James Webb Space Telescope* (JWST). The synergy between ALMA, VLT CRIRES, JWST, and ultimately E-ELT METIS will reveal the physical and chemical structure of the young disk at all scales, including the planet forming zones.

Chapter 2

Discriminating protostellar disk formation models with continuum and spectral line observations

Abstract. *Context*. Recent simulations have explored different ways to form accretion disks around low-mass stars. However, it has been difficult to differentiate between the proposed mechanisms because of a lack of observable predictions from these numerical studies.

Aims. We aim to present observables that can differentiate a rotationally supported disk from an infalling rotating envelope toward deeply embedded young stellar objects ($M_{\mathrm{env}} > M_{\mathrm{disk}}$) and infer their masses and sizes.

Methods. Two 3D MHD disk formation simulations of Li and collaborators are studied, with a rotationally supported disk (RSD) forming in one but not the other (where a pseudo-disk is formed instead), together with the 2D semi-analytical model. The dust temperature structure is determined through continuum radiative transfer RADMC3D modelling. A simple temperature dependent CO abundance structure is adopted and synthetic spectrally resolved submm rotational molecular lines up to $J_{\mathrm{u}} = 10$ are compared with existing data to provide predictions for future ALMA observations.

Results. 3D MHD simulations and 2D semi-analytical model predict similar compact components in continuum if observed at the spatial resolutions of 0.5–1″ typical of the observations to date. A spatial resolution of ∼14 AU and high dynamic range (> 1000) are required in order to differentiate between RSD and pseudo-disk formation scenarios in the continuum. The moment one maps of the molecular lines show a blue- to red-shifted velocity gradient along the major axis of the flattened structure in the case of RSD formation, as expected, whereas it is along the minor axis in the case of pseudo-disk. The peak-position velocity diagrams indicate that the pseudo-disk shows a flatter velocity profile with radius than an RSD. On larger-scales, the CO isotopolog line profiles within large ($> 9″$) beams are similar and are narrower than the observed line widths of low-J (2–1 and 3–2) lines, indicating significant turbulence in the large-scale envelopes. However a forming RSD can provide the observed line widths of high-J (6–5, 9–8, and 10–9) lines. Thus, either RSDs are common or a higher level of turbulence ($b \sim 0.8$ km s^{-1}) is required in the inner envelope compared with the outer part (0.4 km s^{-1}).

Conclusions. Spatially and spectrally resolved molecular line observations can differentiate between the pseudo-disk and the RSD much better than continuum data. The continuum data give a better estimate on disk masses whereas the disk sizes can be estimated from the spatially resolved molecular lines observations. The general observable trends are similar between the 2D semi-analytical models and 3D MHD RSD simulations.

D. Harsono, E. F. van Dishoeck, S. Bruderer, Z. Y. Li, J. K. Jørgensen
submitted

2.1 Introduction

THE formation of stars and their planetary systems is linked through the formation and evolution of accretion disks. In the standard star formation picture, the infalling material forms

an accretion disk simply from angular momentum conservation (e.g., Lin & Pringle 1990; Bodenheimer 1995; Belloche 2013). However, magnetic field strengths observed toward molecular cores (see Crutcher 2012,for a recent review) are expected theoretically to be sufficient in affecting the formation and evolution of disks around low-mass stars (e.g., Galli et al. 2006; Joos et al. 2012; Krumholz et al. 2013; Li et al. 2013, 2014a). Recent advances in both observational and theoretical studies give an opportunity to test the star formation process at small-scales (< 1000 AU).

It has been known for a long time that the presence of magnetic fields can drastically change the flow dynamics around low-mass stars (e.g., Galli & Shu 1993) and potentially suppresses disk formation (e.g., Galli et al. 2006). The latter is due to catastrophic magnetic braking where essentially all of the angular momentum of the accreting material is removed by twisted field lines. Recently, Li et al. (2011) investigate the collapse and disk formation from a uniform cloud while Joos et al. (2012) and Machida & Matsumoto (2011) performed simulations starting with a steep density profile and a Bonnor-Ebert sphere, respectively. They found that rotationally supported disks (RSDs) do not form out of uniform and non-uniform cores under strong magnetic fields unless the field is misaligned with respect to the rotation axis (Hennebelle & Ciardi 2009). Turbulence has also been shown to help with disk formation (Santos-Lima et al. 2012; Seifried et al. 2012; Myers et al. 2013; Joos et al. 2013; Li et al. 2014b).

In spite of a number of disk formation and evolution simulations, only a few observables have been presented so far. The expected observables in the continuum (spectral energy distribution or SED) from 1D and 2D disk formation models have been presented in Young & Evans (2005) and Dunham et al. (2010). Continuum observables out of 2D hydrodynamics simulations with a thin disk approximation have been shown by Dunham & Vorobyov (2012) and Vorobyov et al. (2013). However, only a handful of synthetic observables from 3D magnetohydrodynamics (MHD) simulations have been presented in the literature (e.g., Commerçon et al. 2012a,b).

Continuum observations probe the dust thermal emission and the dust structure around the protostar. However, high spatial and spectral resolution molecular line observations are needed to probe the kinematical structure as the disk forms. The aim of this paper is to present high-spatial (down to $0.1''$, 14 AU at a typical distance of 140 pc) synthetic observations of continuum and molecular lines from two of the 3D MHD collapse simulations presented in Li et al. (2013). The two simulations differ in the initial magnetic field direction with respect to the rotation axis: aligned and strongly misaligned where the magnetic field vector is perpendicular to the rotation axis. The two cases represent the two extremes of the field orientation. The synthetic observations will be compared with those from a 2D semi-analytical disk formation model presented in Visser et al. (2009) to investigate whether the predicted observables differ. The 2D models allow us to break down the different input parameters of the MHD simulations into two parameters: sound speed (c_s) and rotation rate. Rotational transitions of CO are simulated to trace the observable kinematical signatures.

Another motivation in simulating CO molecular lines is the availability of high-quality spectrally and spatially resolved observational data toward embedded young stellar objects (YSOs) on larger scales (> 1000 AU). Spectrally resolved lines have been obtained for low-excitation transitions $J_u \leq 7$ ($E_u = 155$ K) using ground-based facilities (e.g., Jørgensen et al. 2002; van Kempen et al. 2009a,c) and higher excited lines up to $J_u = 16$ ($E_u = 660$ K) using *Herschel*-HIFI (de Graauw et al. 2010) in beams of 9–20$''$ (Yıldız et al. 2010, 2013; Kristensen et al. 2013). Interestingly, San Jose-Garcia et al. (2013) found that the $C^{18}O$ 9–8 lines are broader than the 3–2 lines for low-mass YSOs. The observed line widths are larger than that expected from the thermal broadening, which indicates a significant contribution of microscopic turbu-

Table 2.1 — Stellar ($M_\star$), envelope (M_{env}), and disk (M_d) masses for the three simulations. R_d is the extent of the rotationally supported disk for each simulation.

Model	$M_\star$ [$M_\odot$]	M_{env} [$M_\odot$]	M_d [$M_\odot$]	R_d [AU]
3D MHD RSD	0.38	0.29	0.06	250–300
3D MHD No RSD	0.24	0.35	0.13*	...
2D RSD	0.35	0.32	0.04	65

* Mass of pseudo-disk is the sum of the regions with number densities $n_{H_2} > 10^{7.5}$ cm^{-3}; no radius is tabulated for this case.

lence or some other forms of motion, such as rotation and infall. Through the characterization of spectrally resolved molecular lines on such physical scales, we aim to test the kinematics predicted in various star and disk formation models.

Another key test of star formation models is to compare the predicted mass evolution from the envelope to the star with observations (e.g., Jørgensen et al. 2009; Li et al. 2014a). Inferring these properties toward embedded YSOs are not straightforward due to confusion between disk and envelope. The mass evolution of the disk and envelope can be deduced from millimeter surveys combining both aperture synthesis and single dish observations (Keene & Masson 1990; Terebey et al. 1993; Looney et al. 2003; Jørgensen et al. 2009; Enoch et al. 2011). However, precise determination of stellar masses requires spatially and spectrally resolved molecular line observations of the velocity gradient in the inner regions of embedded YSOs (Sargent & Beckwith 1987; Ohashi et al. 1997a; Brinch et al. 2007a; Lommen et al. 2008; Jørgensen et al. 2009; Takakuwa et al. 2012; Yen et al. 2013). Here we apply a similar analysis on the synthetic continuum and molecular line data as performed on the observations to test the reliability of the inferred masses.

This paper is structured as follows. Section 6.2 describes the simulations and the radiative transfer method that are used. The synthetic continuum images are presented in Section 2.3. Section 2.4 presents the synthetic CO moment maps and line profiles for the different simulations. The results are then discussed in Section 6.4 and summarized in Section 6.5.

2.2 Numerical simulations and radiative transfer

2.2.1 Magneto-hydrodynamical simulations

We utilize the 3D MHD simulations of the collapse of a 1 $M_\odot$ uniform, spherical envelope as described in Li et al. (2013). The envelope initially has a density of $\rho_0 = 4.77 \times 10^{-19}$ g cm^{-3}, a solid-body rotation of $\Omega_0 = 10^{-13}$ Hz, and a relatively weak, uniform magnetic field of $B_0 = 11 \mu$G. The details of the simulations can be found in Li et al. (2013).

A snapshot of two simulations at $t = 3.9 \times 10^{12}$ s $= 1.24 \times 10^5$ years is used. This corresponds to near the end of the Stage 0 phase of star formation where almost one half of the initial core mass has collapsed onto the star (Robitaille et al. 2006; Dunham et al. 2014). The difference between the two simulations is the tilt angle between the rotation axis and the direction of initial magnetic field vector, θ_0. One simulation starts with an initial tilt angle $\theta_0 = 0°$ in which a pseudo-disk forms but not an RSD. The other simulation starts with an initial tilt angle of $\theta_0 = 90°$ in which an RSD forms (see Fig. 2.1 and Figure 1 in Li et al. 2013).

The RSD simulation (*left*) forms a flattened structure with number gas densities $n_{H_2} > 10^{7.5}$ cm^{-3} in the inner 300 AU radius. In the region $r > 100$ AU, the magnitude of the radial and angular velocities are within a factor of 2 of each other. The radial velocities nearly vanish in
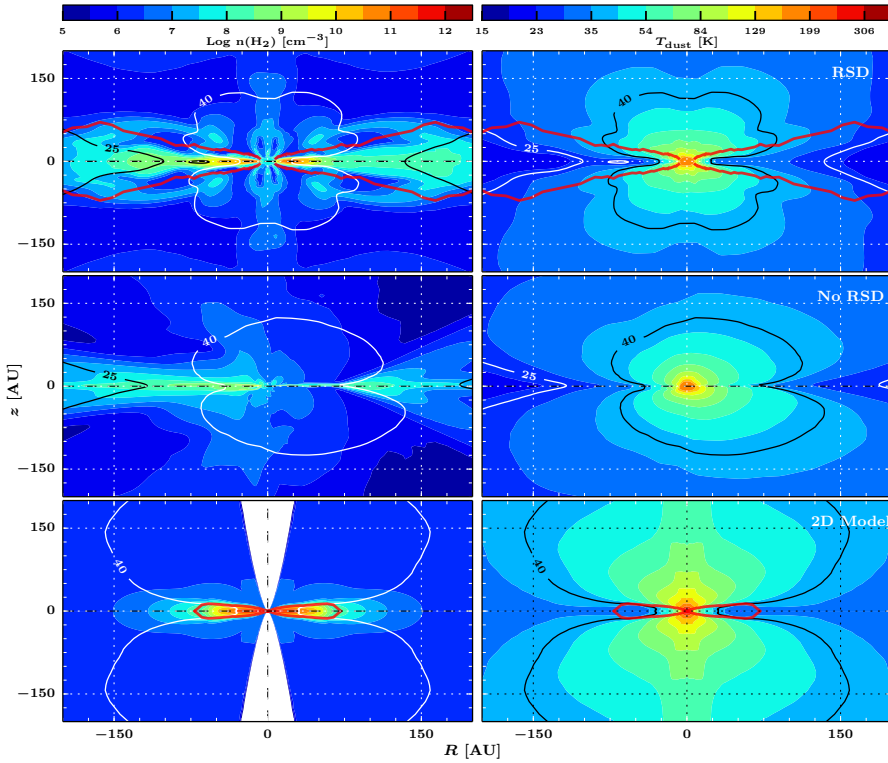
Figure 2.1 — Density and dust temperature structures in the inner 200 AU radius for all three simulations at $t \sim 1.2 \times 10^5$ years. Temperature contours at 25 K and 40 K are indicated in the right panels. *Top:* A vertical slice ($R - z$ slice at $\phi = 0$ where R denotes the cylindrical radial coordinate) of the 3D MHD simulation of RSD formation. *Middle:* A vertical slice of the 3D MHD simulation of a pseudo-disk (No RSD). *Bottom:* 2D semi-analytical disk formation model. The red lines highlight the region of the stable RSD.

the inner 70 AU radius (see Fig. 4.2). The streamlines in the RSD simulation show a coherent flattened rotating component (see Fig. 2.2). In the case of the pseudo-disk simulation, number
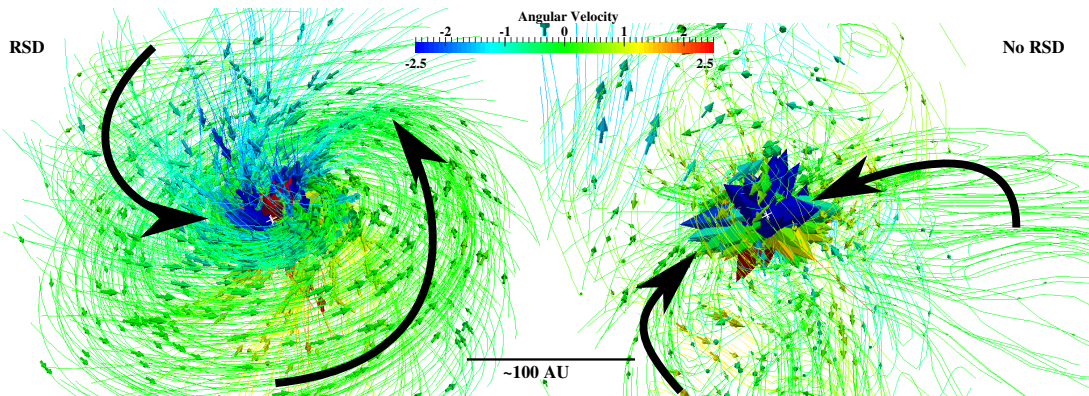

Figure 2.2 — Velocity streamlines for the two MHD simulations in Li et al. (2013). The simulations are rendered with *paraview* (http://www.paraview.org). *Left*: 3D MHD simulation of a collapsing uniform sphere with the magnetic field vector perpendicular to the rotation axis. *Right*: The simulation with magnetic field vector aligned with the rotation axis. The color of the arrows indicate the angular velocity vector, v_ϕ, in km s^{-1}. The solid black arrows indicate the general stream lines in the two simulations.
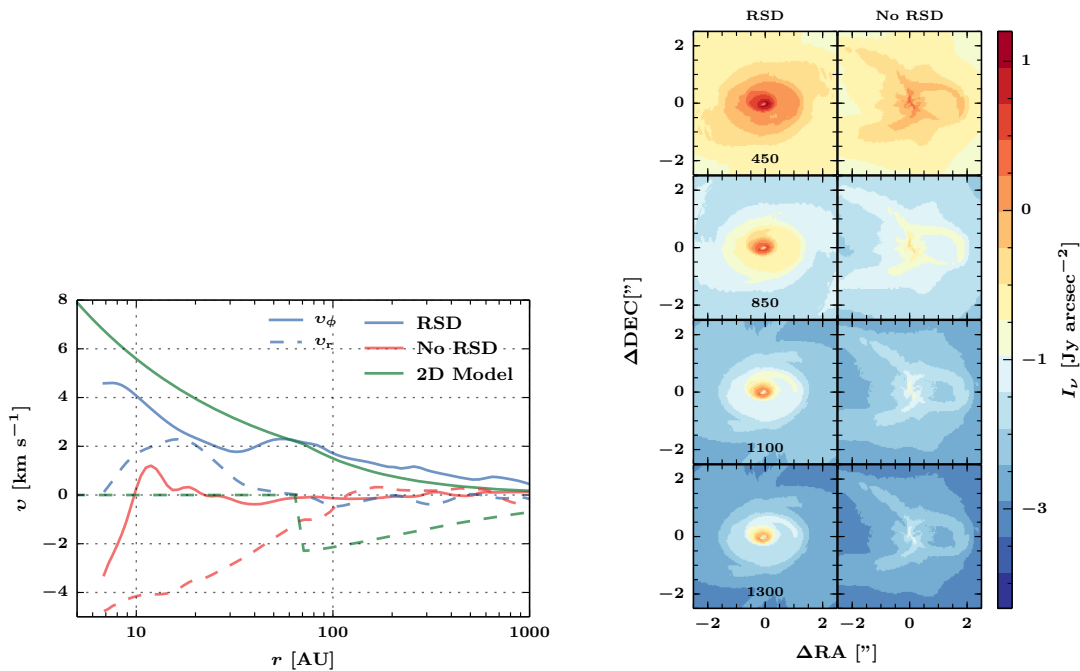
Figure 2.3 — *Left*: Radial (*solid*) and angular velocities (*dashed*) at the midplane ($\theta = \pi/2$, $\phi = 0$) for the three different models: 3D RSD MHD simulation (*blue*), 3D No RSD (*red*), and 2D model (*green*). *Right*: Continuum intensity maps of 450, 850, 1100, and 1300 μm for the MHD disk formation simulation (left panels) and pseudo-disk (No RSD, right panels) at $i = 45°$ at 5 AU pixels. Note the large dynamic range needed to see all of the structures.

densities of $n_{H_2} > 10^{7.5}$ cm^{-3} encompass $r < 700$ AU regions, which is a factor of 2 larger than the RSD simulation. An outflow cavity is present in this simulation with an expanding velocity field as shown in Fig. 1 (*Left*) of Li et al. (2013). The magnitude of the radial velocities are much larger than the angular velocities in the inner $r < 300$ AU along most ϕ directions. In this simulation, the streamlines show infalling material straight from the large-scale envelope onto the forming star. Using these two simulations with very different outcomes, we can investigate the similarities and differences in both continuum and molecular line profiles for pseudo-disk and RSD formation in 3D.

2.2.2   Semi-analytical model

For comparison, synthetic images from 2D semi-analytical axisymmetric models of collapsing rotating envelope and disk formation as described in Visser et al. (2009) with modifications introduced in Visser & Dullemond (2010) and Harsono et al. (2013) are also simulated. These models are based on the collapse and disk formation solutions of Terebey et al. (1984), and Cassen & Moosman (1981) including a prescription of an outflow cavity. The disk evolution follows the α-disk formalism as described in Shakura & Sunyaev (1973) and Lynden-Bell & Pringle (1974). The disk surface is defined by hydrostatic equilibrium as described in Visser & Dullemond (2010) and is assumed to be in Keplerian rotation. In order to compare with the MHD simulations, we consider the collapse of 1 $M_\odot$, $c_s = 0.26$ km s^{-1}, and $\Omega_0 = 10^{-13}$ Hz core. The synthetic observables are produced at $t = 3.9 \times 10^{12}$ s. The bottom of Fig. 2.1 shows the physical structure of the 2D semi-analytical model at the time when a ~ 65 AU radius RSD is present.

A major difference between the 2D semi-analytical axisymmetric model and the 3D simula-

tions is the outflow cavity. The photon propagation is still treated in 3D. Although outflowing gas is present in the pseudo-disk simulation (No RSD), the cavity remains filled with high number density (10^5 cm^{-3}) gas while lower density (10^{2-3} cm^{-3}) gas occupies the cavity in the 2D model. The outflowing gas in the pseudo-disk model has relatively low velocities such that it does not clear out the cavity. As a result, the dust temperature structure along the cavity wall is higher in the 2D model due to the direct illumination of the central star. This is readily seen in the 40 K contour in Fig. 2.1 where it is elongated in the z direction in the 2D case.

2.2.3 Rotationally supported disk sizes and masses

The extent of the RSD in the 2D semi-analytical model is defined by hydrostatic equilibrium. Using these properties, the RSD is a region with densities $> 10^{7.5}$ cm^{-3} and angular velocities $v_\phi > 1.2$ km s^{-1}. The disk evolution in 2D follows the alpha-disk formalism with $\alpha = 10^{-2}$, which in turns define the radial velocities as $v_r/v_\phi \sim \alpha(H/R)^2 \sim 10^{-3}$ where H is the disk's scale height. Similar criteria are used to extract the extent of the RSD in the 3D simulation with the additional constraint of $v_\phi > v_r$. Note that we apply the criteria from the 2D models to define the RSD from the 3D simulations, thus the RSD is not necessarily in hydrostatic equilibrium. Using these criteria, an RSD up to 260 AU is found in the mis-aligned simulation.

The extent of the 3D RSD is 300 AU if $v_\phi > 1$ km s^{-1} is used. With the former criterion, the disk masses contained within such a region are 0.06 $M_\odot$ for the 3D RSD and 0.04 $M_\odot$ for the 2D RSD surrounding 0.38 $M_\odot$ and 0.35 $M_\odot$ stars, respectively (see Table 6.1). As Fig. 4.2 shows, the radial velocity component of the pseudodisk is a significant fraction of the Keplerian velocity. Due to such high radial velocities, the surface density of the pseudodisk remains low. However, the total mass of the high density regions ($n_{H_2} > 10^{7.5}$ cm^{-3}) is a factor of 2 higher than the RSD mass.

2.2.4 Observables and radiative transfer

The first step before producing observables is the calculation of the dust temperature structure, which is critical for the molecular abundances since it controls the freeze-out from the gas onto the dust. The dust temperature is computed using the 3D continuum radiative transfer code RADMC3D[1] with a central temperature of 5000 K, which is the typical central temperature in the 2D semi-analytical models at around the end of Stage 0 phase. The central luminosity is fixed at 3.5 $L_\odot$ for all models. The dust opacities used are those corresponding to a mix of silicates and graphite grains covered by ice mantles (Crapsi et al. 2008). The luminosity is fixed at 3.5 $L_\odot$. The same opacities and central temperature are adopted for all simulations in order to focus on the general features of the observables. The gas temperatures are assumed to be equal to the dust temperatures, which is valid for the optically thin lines simulated here that trace the bulk mass where $T_{gas} \sim T_{dust}$ (Doty et al. 2002; Doty et al. 2004).

CO abundance. In this paper, we concentrate on simulating CO molecular lines of $J =$ 2–1, 3–2, 6–5, and 9–8. For simplicity, the ^{12}CO abundance is set to a constant value of 10^{-4} with respect to H$_2$ except in regions with $T_{dust} < 25$ K, where it is reduced by a factor of 20 to mimic freeze-out (Jørgensen et al. 2005b; Yıldız et al. 2013). We adopt constant isotopic ratios of ^{12}C/^{13}C= 70, ^{16}O/^{18}O= 540, and ^{18}O/^{17}O= 3.6 (Wilson & Rood 1994) to compute the abundance structures of the isotopologs.

---

[1]http://www.ita.uni-heidelberg.de/ dullemond/software/radmc-3d

Synthetic images. This paper presents synthetic continuum maps at 450, 850, 1100, and 1300 μm. The images are rendered using RADMC3D with an image size of 8000 AU at scales of 5 AU pixels.

They are placed at a distance of 140 pc. Synthetic images at inclinations of $0°$ (face-on; down the z-axis), $45°$, and $90°$ are produced. The latter option is included because one of the claimed embedded disk sources is close to edge-on ($i \sim 90°$, L1527 in Tobin et al. 2012). For the synthetic molecular lines, the LTE population levels are computed using the partition functions adopted from the HITRAN database (Rothman et al. 2009). LTE is a good assumption because the densities in the simulations are greater than the critical densities of the lines we simulate. Non-LTE effects may play a minor role for synthetic $J_u \geq 6$ lines from the pseudo-disk simulation due to its lower densities relative to the other two simulations. The line optical depth (τ_L) is also not expected to play a role since the focus of this paper is on the minor isotopologs and on the kinematics dominated by the line wings where opacities are lower than at the line center. The properties of the molecules (E_{up} and A_{ul}) are taken from the LAMDA database (Schöier et al. 2005). Only thermal broadening is included in simulating the molecular lines without any additional microturbulence. The image cubes are rendered at a spectral resolution of 0.1 km s^{-1} covering velocities from -7.5 to 7.5 km s^{-1}. In order to simulate observations, the synthetic images are then convolved with Gaussian beams between 0.1$''$ to 20$''$. The convolution is performed in the Fourier space with normalized Gaussian images.

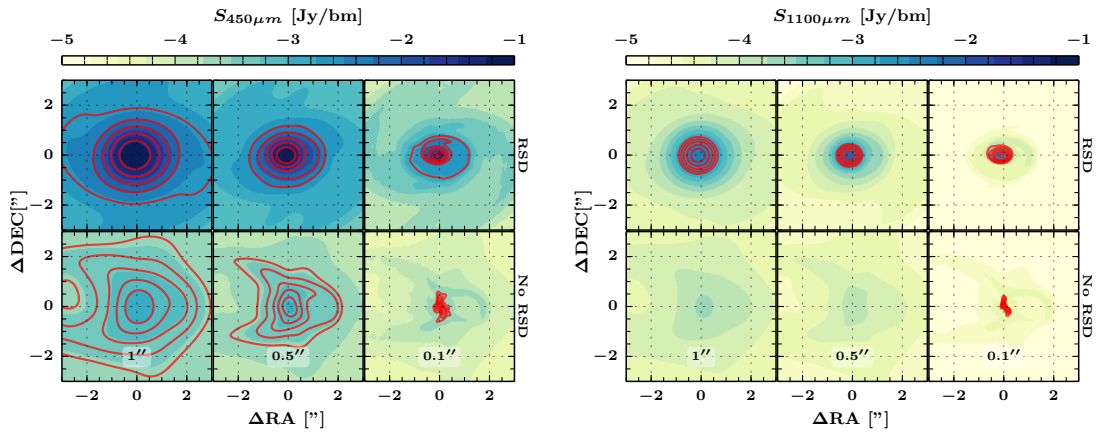## 2.3 Continuum

2.3.1 Images and prospects for ALMA

Figure 2.4 — Convolved continuum maps in the inner 5$''$ of 450 (*left*) and 1100 (*right*) μm at $i = 45°$. The images are convolved with 1$''$, 0.5$''$, and 0.1$''$ beams as indicated in each panel. For each panel, the top row shows synthetic image of RSD simulation and the pseudo-disk simulation is shown in the bottom row. The color scale presents the full range of the emission above 10^{-2} mJy/bm, not all of which may be detectable. Solid red contours are drawn from 3σ up to maximum at 6 logarithmic steps where 1σ is 0.01 $\times$ the maximum (dynamical range of 100) with a minimum at 0.5 mJy/bm for the 1$''$ and 0.5$''$ images. For the images convolved with a 0.1$''$ beam, the red contours are drawn with a minimum noise level of 0.5 mJy/bm for 450 μm and 0.05 mJy/bm at longer wavelengths with a dynamic range of 1000, as appropriate for the full ALMA.

Continuum images are rendered at four wavelengths and viewed at three different inclinations. Figure 4.2 presents the synthetic 450, 850, 1100 and 1300 μm continuum images at an inclination of 45° for the two 3D MHD simulations. The left panels present the images from 3D RSD simulation while the right panels show images from the pseudo-disk simulation (labeled

as No RSD). The features produced during the collapse are clearly visible in the 450 μm map; most of them are two orders of magnitude fainter at 1300 μm. The spiral structure in the 450 μm image is due to magnetically channelled, supersonically collapsing material on its way to the RSD, rather than a feature of the RSD itself.

One of the aims of this paper is to investigate whether these features are observable with current observational limits and what is possible with future Atacama Large Millimeter/sub-millimeter Array (ALMA) data. With the full ALMA, a sensitivity of σ=0.5 mJy bm^{-1} (bm = beam) at ~ 450 μm and 0.05 mJy bm^{-1} at 1100 μm can be achieved at spatial resolutions $\leq 0.1''$ for 30 minutes of integration (1.8 GHz bandwidth). In addition, a high dynamic range of > 1000 ($\sigma = 0.001 \times S_{\mathrm{peak}}$) can also be achieved. Figure 2.4 presents the images convolved with a $0.1''$ beam for the two 3D MHD simulations (right-most panels). The color scale indicates the full range of emission, while the red solid lines show the region above 3σ where σ is either dynamically limited to 1000 or to the σ values listed above. This simply means that the solid red lines indicate the detectable features. With a combination of high dynamic range and sensitivity, the features of the collapse are observable and distinguishable in both 450 μm and 1100 μm continuum maps. At a spatial resolution of $0.1''$, most of the emission at 1100 μm is due to the rotationally supported disk with little contribution from the surrounding envelope.

As Figs. 4.2 and 2.4 show, both the strength of the features and their extent change with wavelength, as indicated by the red line contours. With a resolution of $0.1''$, the extent of the detectable emission decreases from $1.5''$ at 450 μm to $< 1''$ at 1100 μm for the RSD case. At long wavelengths, the dust emission is given by $I_\nu \sim T_{\mathrm{dust}}\nu^2 \times (1 - e^{-\tau_{\mathrm{dust}}})$. Since the dust emission is optically thin at long wavelengths, the intensity is $\propto T_{\mathrm{dust}}\nu^2\tau_{\mathrm{dust}}$. The variables that depend on position are T_{dust} and $\tau_{\mathrm{dust}} \propto \rho_{\mathrm{dust}}\kappa_\nu$. The frequency dependence of the opacity is $\kappa_\nu \propto \nu^{1.5}$ for the adopted opacity table. The extent of the detectable emission depends on these quantities. At one particular position, the ratio of the emission at the two wavelengths is simply $I_{450\mu\mathrm{m}}/I_{1100\mu\mathrm{m}} \propto \nu^{3.5}$. Thus, the predicted difference in size at the two wavelengths is due to the frequency dependence of the emission.

For ALMA early science observations (cycles 0 and I), the capabilities provided a dynamic range only up to 100 at a spatial resolution of $\sim 0.5''$. Figure 2.4 presents the synthetic 50 and 1100 μm images convolved with $1''$ and $0.5''$ beams, compared with the $0.1''$ beam images. The color scale again indicates the full range of emission, while the red solid lines now show the region above 3σ where the noise level, σ, is dynamically limited to 100 with a minimum of 0.5 mJy/beam at both wavelengths. The red lines again present the emission that is observable. The 450 μm images convolved with a $1''$ beam show an elongated flattened structure for both RSD and pseudo-disk simulations and are therefore indistinguishable. Most of the emission at 1100 μm and longer wavelengths is not detectable at the assumed noise level of 0.5 mJy bm^{-1}. A similar result is found after convolution with a $0.5''$ beam. Although the synthetic observations from the pseudodisk indicate a 'cometary' structure, this may be affected by the presence of outflow cavity which is absent in the case of RSD. Thus, the full ALMA capabilities are needed to distinguish models based on continuum data only.

2.3.2 Inclination effects

The images for a face-on system ($i = 0°$) are similar to those of the moderately inclined system ($i = 45°$) presented in Fig. 2.4. For low inclinations between 0 to 45°, the continuum images only change slightly in terms of absolute flux density and show a small elongation due to orientation.

In contrast, the two simulations rendered at edge-on ($i \sim 90°$) geometry exhibit similar compact components even at the highest angular resolution (Fig. 2.5). They both show an
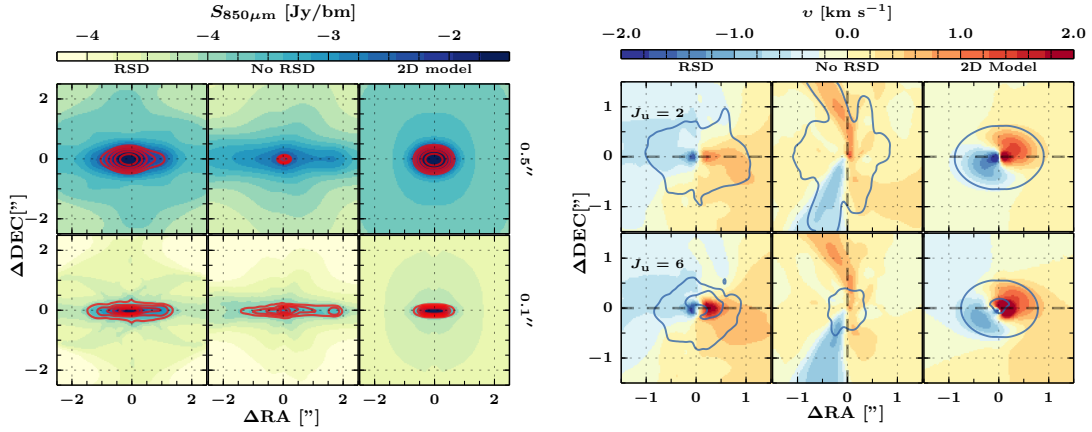
Figure 2.5 — *Left*: Synthetic 850 μm continuum images convolved with $0.5''$ (*top*) and $0.1''$ (*bottom*) beams for the three simulations viewed at $90°$ (edge-on): RSD formation (*left*), pseudo-disk (*center*), and 2D semi-analytical model (*right*). The red solid lines are drawn at the same contours as in Fig. 2.4. *Right*: Moment one maps of $C^{18}O$ 2–1 (*top*) and 6–5 (*bottom*) for the three simulations viewed $i = 45°$ convolved with a $0.1''$ beam. The solid line shows the 20% intensity contour of the moment zero ($\int S_v dv$) peak map to indicate the flattened structure. The black dashed lines indicate direction at which the PV slices are constructed and the direction of the elongation in the moment zero maps.
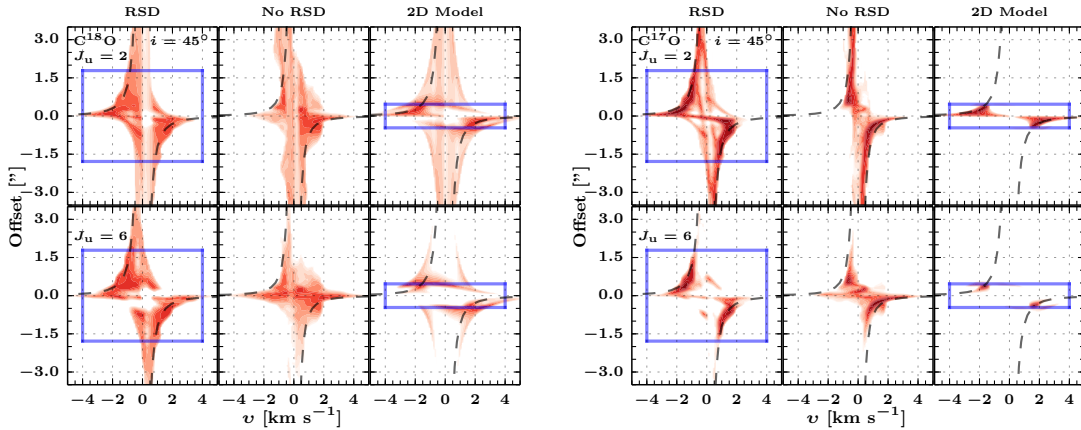

Figure 2.6 — PV maps of $C^{18}O$ (*left*) and $C^{17}O$ (*right*) along the velocity gradients as seen in Fig. 2.5 for an inclination of $45°$ and $0.1''$ beam. The top panels show the $J = 2-1$ line and the bottom panels show the 6–5 transition. The blue rectangle indicates the radii of RSDs. The dashed lines indicate the inclination corrected Keplerian curves associated to the stellar mass. The red color scales show emission from 10% to the peak intensity.

elongated flattened disk-like emission similar to the 2D semi-analytical model. This signature suggests an RSD, but it is due to the pseudo-disk in the 3D MHD simulation with the aligned magnetic field. The peak continuum emission of the pseudo-disk is a factor of 10 lower than that of the other two models while it is similar between the 3D RSD and the 2D semi-analytical models (difference of $< 10\%$). The main difference is the extent of the elongated emission where the 2D model predicts a very compact ($\sim 1''$ radius) structure while the pseudo-disk component shows an extended flattened structure ($\leq 2''$). This illustrates the difficulties in testing disk formation models for highly inclined systems, such as L1527, based on continuum data only.

2.4 Molecular lines

The continuum emission arises from thermal dust emission and does not contain kinematical information. As shown in the previous section, a compact flattened structure is expected in the continuum maps in the inner regions of all three models. Kinematical information as contained in spectrally resolved molecular lines is essential to distinguish the models and to derive stellar masses. The rotational lines of CO isotopologs are used to investigate this.

The rotational lines of ^{13}CO, C^{18}O, and C^{17}O are simulated. CO is chosen since its abundance is less affected by the chemistry. We do not investigate ^{12}CO lines since they are dominated by the entrained outflow material and are optically thick. The isotopolog lines are more optically thin and are expected to probe the higher density region where the disk is forming. These predicted spatially resolved molecular line maps can be compared with ALMA data. Moreover, high quality spectrally resolved CO isotopolog lines probing the larger-scale envelope toward low-mass embedded YSOs have been obtained with single-dish telescopes (see §1). The characterization of these C^{18}O and C^{17}O line profiles provide a test for the kinematical and density structures of the collapsing protostellar envelope on larger scales (e.g., Hogerheijde et al. 1998; Jørgensen et al. 2002).

2.4.1 Moment maps: RSDs or not?

Observationally, the kinematical information of the infalling envelope and RSD is inferred through moment maps. Elongated moment zero (velocity integrated intensity) maps give an indication of the presence of a flattened structure that is associated with a disk. Meanwhile, coherent velocity gradients in the moment one (velocity weighted intensity) map may point to a rotating component. Analysis of synthetic moment maps of the simulations are presented and compared in this section. We focus on presenting the synthetic 'interferometric' maps of optically thin C^{18}O and C^{17}O lines by convolving the image cubes with a $0.1''$ beam. The construction of moment maps only takes into account emission $> 1\%$ of the peak emission. This translates to a noise level of 0.3% of the peak emission. Although ALMA can achieve a dynamic range of > 500, it is more likely that the molecular lines of minor isotopologs from low-mass YSOs will be noise limited at the line wings since they are weaker than the emission near the line center for typical observations with 1–2 hours integration time.

Figure 2.5 presents synthetic first moment (flux-weighted velocity) maps. The moment zero contours at 20% of peak intensity indicate the elongation direction. The flattened density structure is oriented in the east-west direction (horizontal) for all three models as seen in Fig. 2.1. Coherent velocity gradients from blue- to red-shifted velocity are seen in all three models but not necessarily in the same direction. The presence of an embedded RSD is revealed in the 3D RSD and 2D model by the coherent blue- to red-shifted velocity gradient in the east-west direction similar to the flattened disk structure. On the other hand, in the pseudo-disk simulation, the velocity gradient is in the north-south direction similar to the continuum image as shown in Fig. 2.4 (right-most panels). Such velocity gradients can be mistaken to be along the major axis of the disk without higher spatial resolution and sensitivity data.

A number of effects conspire to generate a velocity gradient along the minor axis of the flattened structure in the pseudo-disk simulation. First, since the magnetic braking is efficient in this case, the dominant motion of the material is in the radial direction (see Figs. 2.2 and 4.2). Second, the flattened structure in this particular simulation has lower-density gas than the RSD simulation (see Section 2.2.1). The $n_{\text{H}_2} > 6.5$ cm^{-3} region extends up to 700 AU in size and at an angle with respect to the rotation axis (see Fig. 2.1). Thus, the north-south direction in the pseudo-disk model shows the infalling material along the streamlines connecting the

large-scale envelope and the central star.

At moderate inclinations, the pseudo-disk simulation therefore shows a coherent velocity gradient in a more-or-less straight north-south line. The velocity gradient changes to an east-west direction at high inclinations. At high inclinations, the observer has a direct line of sight on the high density region shown in Fig. 2.1 and therefore the line emissions pick up the rotational motions of the flattened structure similar to the RSD simulations. Furthermore, the skewness that is present in the moment one maps of RSD simulations largely disappears at high inclinations for the same reason. Thus, it is difficult to separate the envelope from the disk for high inclinations from moment one map alone.

2.4.2 Velocity profiles

2.4.2.1 PV cuts

Observationally, the presence of embedded Keplerian disks is often established by constructing position velocity (PV) diagrams along the major axis of the system as seen in moment zero maps. In theory, the PV analysis is straight-forward. It is symmetric in both position and velocity space (4 quadrants are occupied) if the system is infall dominated (e.g., Ohashi et al. 1997a; Brinch et al. 2008). The symmetry is broken if rotation is present and the emission peaks are shifted to larger offsets corresponding to the strength of the rotational velocities (2 quadrants are occupied).

Figure 2.6 presents synthetic PV diagrams along the major axis of the disk where it corresponds to the direction of the blue- to red-shifted velocity gradient. For the images in Fig. 2.5, an east-west slice (horizontal) is taken for the RSD simulations, while a north-south (vertical) slice is adopted for the case of the simulation without an RSD. These slices are not exactly the major axis of the moment zero map, however these directions pick up most of the velocity gradient present in the inner $1''$. Both $C^{18}O$ and $C^{17}O$ lines are simulated. Interestingly, the PV slices suggest that rotational motions are present regardless of whether an RSD is present or not. This is most readily seen in the $C^{17}O$ PV maps (right of Fig. 2.6) in which only 2 of the 4 quadrants are occupied by molecular emissions for all three models at $i = 45°$. This shows that $C^{17}O$ emission readily picks up the rotational motion at small-scales but also that infalling motion can be confused with rotation if the wrong direction for the PV cut is chosen (No RSD model).

The $C^{18}O$ PV maps indicate contributions from the infalling envelope since the maps are more symmetric than those in $C^{17}O$. The $C^{18}O$ PV slices of the pseudo-disk simulations indicate an infall-dominated structure in which the 4 quadrants are occupied. On the other hand, there is a clear indication of a rotating component for the two RSD simulations in which only 2 of the 4 quadrants are filled at small radii. This suggests that spatially and spectrally resolved $C^{18}O$ lines can distinguish between a pseudo-disk and an RSD.

Figures 2.6 compares the PV maps of the 2–1 and 6–5 transitions. Most of the emission in the 6–5 transition occupies only 2 of the 4 quadrants indicating signatures of rotational motions, whereas the 2–1 lines also show some emission in the other 2 quadrants from larger scales. This is a clear indication that the 6–5 line is a better probe of the rotational motions in the inner 100 AU than the 2–1 line.

2.4.2.2 Peak position-velocity diagrams

While it is clear that there is indeed a rotating component for some models, the question is whether the extent of the Keplerian structure can be extracted from such an analysis. A Keplerian rotating flattened structure exhibits a velocity profile $v \propto r^{-0.5}$, where r is the distance
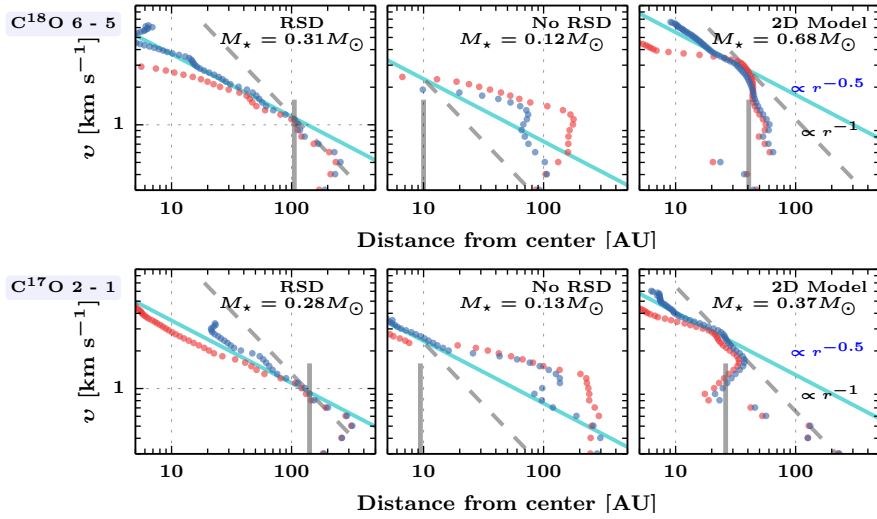
Figure 2.7 — Peak position-velocity diagrams of $C^{18}O$ 6–5 (*top*) and $C^{17}O$ 2–1 (*bottom*) at $i = 45°$ after convolution with a $0.1''$ beam. The red and blue symbols correspond to the red- and blue-shifted velocity components, respectively. The different panels present the PPV for the different simulations. Vertical solid lines show the disk radii extracted for the three models and dashed lines show the steep velocity profile ($v \propto r^{-1}$) while the solid cyan lines indicate the Keplerian curves. The stellar masses are indicated in the top right of each panel. The offset between blue- and red-shifted points are due to the limited spatial and spectral resolution at the high velocities.

from the central source. These positions are either determined from fitting interferometric visibilities of each velocity channel (Lommen et al. 2008; Jørgensen et al. 2009) or determination of the peak positions in the image space (Tobin et al. 2012; Yen et al. 2013). We here determine the peak positions directly in the image space to assess whether a velocity profile is visible in the synthetic molecular lines.

Peak positions are determined for each of the velocity channel maps for each molecular line for the red and blue-shifted components separately taking into account channels whose peak flux density (S_ν in Jy bm^{-1}) are $> 1\%$ of $S_{\max}$. They are subsequently rotated according to the direction of the velocity gradient. If an RSD is present, the peak positions of both red- and blue-shifted velocities are expected to follow the Keplerian velocity profile ($v \propto r^{-0.5}$). The combination of infalling rotating envelope and RSD, which exhibits a skewness in the moment one map, is expected to show a steeper velocity profile ($v \propto r^{-1}$) (Lin et al. 1994). However, at high velocities, the peak positions of the red- and blue-shifted velocities can be misaligned at scales of 5 AU due to the limited spatial resolution. The disk radius is determined by minimizing the difference ($\sim 10\%$) between the best-fit stellar mass inside and at the disk radius.

The peak position-velocity diagrams (PPVs) for $C^{18}O$ 6–5 and $C^{17}O$ 2–1 are shown in Fig. 2.7. These lines are chosen because they represent two observational extremes in terms of excitation and optical depth. There is a clear distinction between the RSD simulations and a pseudo-disk. The velocity profile of the pseudo-disk is much flatter than that expected from an RSD. Thus, spatially and spectrally resolved molecular lines observations can clearly differentiate between an RSD and a pseudo-disk.

All three PPVs indicate a velocity profile close to $v \propto r^{-0.5}$ (for the pseudo-disk see $C^{17}O$ 2–1 PPV in the inner 20 AU). This reflects the fact that the inner 300 AU of the models is dominated by velocity structure that is proportional to $r^{-0.5}$, which is both the radial veloc-

ity $\left(v_{\mathrm{infall}} \propto \sqrt{\frac{2GM_\star}{r}} \right)$ and angular velocity $\left(v_{\mathrm{rot}} \propto \sqrt{\frac{GM_\star}{r}} \right)$ (Brinch et al. 2008). From such characterization, the stellar masses can be calculated and indicated in the top right corner of Fig. 2.7. In general, the best-fit stellar masses in the case of RSD are within 30% of the true stellar masses tabulated in Table 6.1. This is not so for the 2D model in the $C^{18}O$ 6–5 and also $C^{17}O$ 6–5 (not shown) due to the fact that the inner flattened envelope is warm (> 40 K) and dense.

Another parameter that one would like to extract is the disk radius, R_{d}, as indicated by the vertical solid line in Fig. 2.7. The break at R_{d} is readily seen in the 2D model at ~ 40 AU for both $C^{18}O$ 6–5 and $C^{17}O$ 2–1. For the case of the 3D MHD simulation (RSD), the best-fit radius varies between 100 and 300 AU. It also exhibits a steep velocity profile ($v \propto r^{\sim -1}$) at radii > 100 AU. The large range of disk radii is due to the envelope emission overwhelms the molecular emission because CO is frozen out in the cold part of the disk at those large radii. The issue of disk versus envelope emission becomes apparent in the case of large embedded disk ($R_{\mathrm{d}} > 100$ AU).

The comparison shows that there is a clear distinct PPV profile associated with RSD formation from $r^{-0.5}$ to r^{-1}. A steep velocity profile ($v \propto r^{-1}$) is not visible in the pseudo-disk simulation. This seems to indicate that such a steep velocity profile describes on-going RSD formation based on the given simulations. A pseudo-disk is characterized by a flat velocity profile in the inner regions. Furthermore, the PPV method can simultaneously derive the stellar mass and the extent of the RSD while separating the infalling rotating envelope from it. With respect to differentiating between RSD and non-RSD, PPV is a better tool than PV-diagrams.
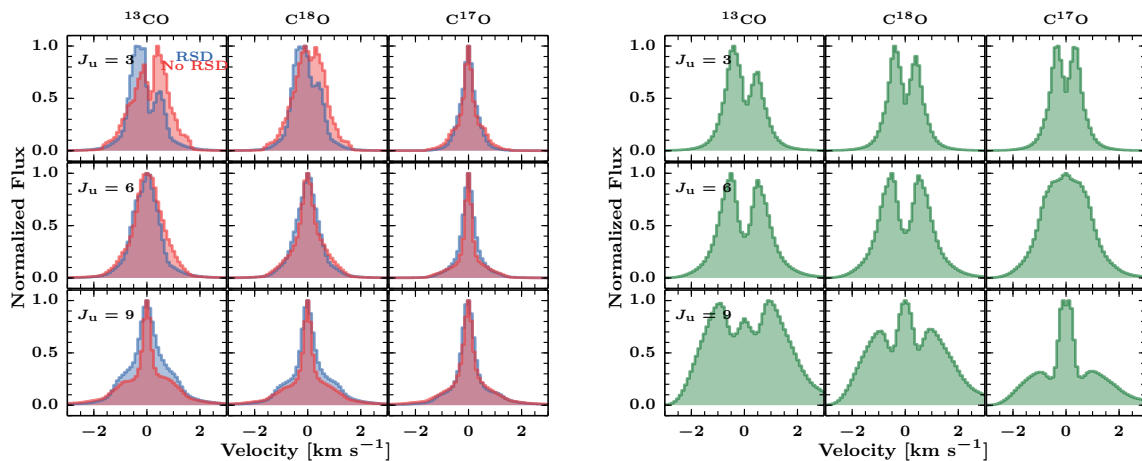
2.4.3 Single-dish line profiles

Figure 2.8 — *Left:* ^{13}CO, $C^{18}O$, and $C^{17}O$ 3–2 (*top*), 6–5 (*middle*), and 9–8 (*bottom*) spectra at $i \sim 0°$ within a $9''$ beam. The blue line shows the synthetic line from simulation with an RSD while the red line is the simulation without an RSD. *Right:* Spectral lines convolved with a $9''$ beam simulated from 2D semi-analytical model viewed at face-on orientation.

The previous sections focus on features at small-scales as expected from interferometric observations. The next assessment is to compare the synthetic molecular lines with single-dish observations which probe the physical structure of the large-scale envelope on scales up to a few thousand AU. The image cubes are convolved with 3 different beams: $9''$, $15''$, and $20''$. These different beams are typical for single-dish CO observations using the JCMT ($15''$), Ata-

cama Pathfinder EXperiment (APEX, $9''$), and *Herschel* ($20''$). Figure 2.8 presents the synthetic CO lines (J_u = 3, 6, and 9) for the two MHD simulations viewed face-on ($i \sim 0°$) convolved with a $9''$ beam. The face-on orientation is considered first to compare with the line profiles in Harsono et al. (2013) for the 2D simulation. The low-lying transitions (J_u = 3) probe the kinematics in the large-scale envelope.

Double peaked line profiles are present in the ^{13}CO and C^{18}O 3–2 regardless whether an RSD is present or not. For the ^{13}CO line, an inverse P-Cygni line profile is seen due to the coherent infalling material onto the disk while a P-Cygni profile is associated to the pseudo-disk, which is tracing the expanding material due to outflowing material present in the pseudo-disk simulation. Self-absorption causes the double peak in the ^{13}CO 3–2 line due to optical depth (typically, $\tau_L > 5$) at line center whereas it is weakly affecting the C^{18}O 3–2 line.

It is interesting to note that there is no significant difference in the 6–5 lines between a simulation that forms an RSD versus a pseudo-disk. This transition ($E_u \sim$110 K) traces the dense warm gas where a large fraction of the emission comes from $\geq$ 40 K gas (Yıldız et al. 2010). The P-Cygni line profile is still visible in the ^{13}CO line, however it is not significant in the C^{18}O line. The lines are also not Gaussian with significant wing emission extending up to ± 2 km s^{-1}.

The line profiles for the semi-analytical models within a $9''$ beam are shown in the bottom of Fig. 2.8. They are significantly different from the 3D MHD models, which arises from the prescribed velocity structure. In Harsono et al. (2013), an additional microturbulent broadening of 0.8 km s^{-1} was added, which results in Gaussian line profiles consistent with the observed single-dish CO line profiles. However, in this paper, we have not included the additional broadening term in order to investigate the emission arising from the true kinematical information. The peaks are more prominent than those in the 3D MHD simulations due to a jump between the velocity structures of the RSD component and the infalling envelope. In general, the 2D semi-analytical models produce significantly broader lines and significant variations between the CO isotopologs and transitions compared with 3D simulations because of a warmer disk and outflow cavity wall (see Section 2.2.2) which allow for stronger wing emissions.

2.4.3.1   Inclination effects

The simulated lines viewed face-on may not pick up all of the dynamics of the system. Figure 2.9 shows how the line profiles change with inclination for the three different simulations within a $15''$ beam. The lines become broader with increasing inclination as they readily pick up the different velocity components. The J_u = 3 lines exhibit inverse P-Cygni line profiles that are associated with infalling gas. Meanwhile, the higher J transitions show more structured line profiles compared with the systems viewed face-on. The C^{18}O 6–5 lines are double-peaked in both cases of RSD formation while it is single-peaked for the pseudo-disk model. On the other hand, the 9–8 line is significantly broader than the low-J lines reflecting the complexity of the dynamics of the warm dense gas.

2.4.3.2   Origin of the line broadening

To investigate the source of the line broadening, the molecular lines are simulated with zero radial velocity ($v_r = 0$ km s^{-1}) and also with zero azimuthal velocity ($v_\phi = 0$ km s^{-1}). For the MHD simulation with RSD, the $FWHM$ value of the C^{18}O 9–8 line decreases to < 0.5 km s^{-1} at all inclinations without any angular velocity component. Such a decrease is not dramatic for face-on orientation, however it is more than a factor of 3 for intermediate ($i \sim 45°$) and high inclination ($i > 75°$) cases. On the other hand, in the case of pseudo-disk formation, both radial
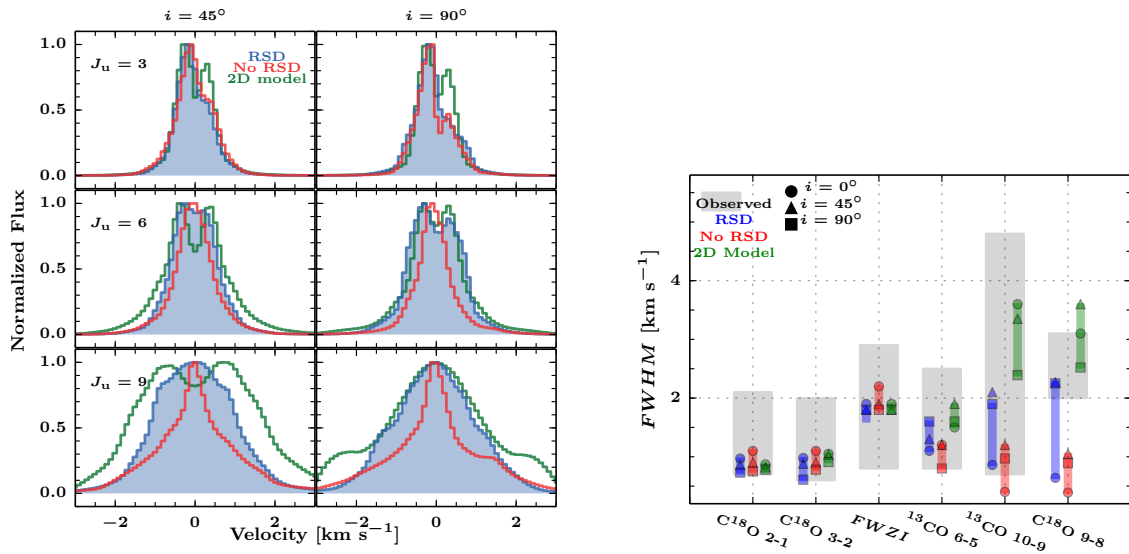
Figure 2.9 — *Left*: C^{18}O line profiles for the different simulations viewed at $i = 45°$ and $i = 90°$ in $15''$ beam. *Right*: $FWHM$ values of the observed (gray shaded region) and simulated (symbols) rotational lines of ^{13}CO and C^{18}O as indicated in a $20''$ beam. The observed values are taken from Jørgensen et al. (2002), van Kempen et al. (2009a), and San Jose-Garcia et al. (2013). The $FWHM$ of synthetic lines are indicated at specific inclinations as indicated by the symbols: circles for $0°$, triangles for $45°$, and squares for $90°$. The comparison of the $FWZI$ values are specifically for the C^{18}O 3–2 line. The different colors represent the different type of simulations: 3D RSD (RSD), 3D pseudo-disk (No RSD), and 2D semi-analytical model (2D Model).

Table 2.2 — $FWHM$ ($FWZI$ as defined at 10% of the peak emission) in km s^{-1} of the ^{13}CO and C^{18}O lines within a $20''$ beam for the MHD simulations viewed at $i = 45°$.

	^{13}CO		C^{18}O	
J	RSD	No RSD	RSD	No RSD
3–2	0.8 (1.8)	1.1 (2.2)	0.9 (1.8)	0.9 (1.9)
6–5	1.1 (2.3)	1.0 (2.2)	1.3 (2.3)	0.9 (2.2)
9–8	2.1 (3.7)	1.2 (3.9)	2.3 (4.0)	1.0 (3.9)

and angular velocities are of equal importance. The origin of the line broadening therefore depends on whether or not an RSD is forming. If an RSD is indeed forming, the C^{18}O 9–8 is broadened by rotational motions at moderate and high inclinations; at low inclinations, infall dominates the broadening.

2.4.3.3 Line widths and comparison with observation

Molecular line observations are typically characterized by their peak flux densities (or intensities), $FWHM$, and integrated line flux densities. While the peak flux densities and integrated line fluxes depend on the adopted physical and chemical structure, their $FWHM$ should reflect the general kinematics that are present in the system. In this paper, we focus on the comparison of $FWHM$ and full-width at zero intensity ($FWZI$) as calculated at 10% of the peak with observations. A 10% cut-off is chosen since most single-dish observations do not reach higher signal-to-noise, especially for the higher-J lines.

These values are calculated for ^{13}CO and C^{18}O lines of the different models from the convolved image cubes. The $FWHM$ and $FWZI$ within a $20''$ beam are listed in Table 2.2 at

moderate inclination ($i = 45°$) comparing the two 3D MHD simulations. Within such a large beam, their values for ^{13}CO and $C^{18}O$ are similar. The $FWHM$ values do not necessarily increase between $J_u = 3$ and 6, in contrast with the $FWZI$ values (see Fig. 2.9). This is expected since the wing emissions are much lower than the peak because the emitting region is much smaller than the beam (beam dilution).

Considering all inclinations ($0°$, $45°$, and $90°$), the $FWHM$ values of the low-J CO lines are similar between the 3D simulations and 2D semi-analytical models. On the other hand, the line widths of the high-J lines differ significantly. This is expected since most of the 2–1 and 3–2 emission originates from the large-scale envelope, which is similar in terms of kinematics in the three simulations. However, the high-J lines originate from the warm inner regions in which the three simulations show different velocity structures.

Figure 2.9 presents the comparison between the simulated and observed lines. The observed line widths toward low-mass YSOs are taken from Jørgensen et al. (2002), van Kempen et al. (2009a), and San Jose-Garcia et al. (2013, $FWHM_N$ for the narrow component). Sources with known confusion in their line profiles from other nearby sources have been excluded. It is clear that the observed line widths of the low-J lines ($J_u = 2$ and 3) are significantly greater than the model simulations, by a factor of 2. Since these lines probe the large-scale quiescent envelope, the discrepancy between the predicted and observed line widths suggests that the large-scale envelope is turbulent with $FWHM \approx 1 \, \mathrm{km \, s^{-1}}$ or a Doppler b of $\sim 0.4 \, \mathrm{km \, s^{-1}}$, i.e., more than what is included in the current simulations that could be due to an interaction with fast outflow, at least in part. The comparison of the $FWZI$ values also supports this conclusion.

For the dense and warm gas probed by the higher $J_u \geq 6$ lines, the predicted line widths are consistent with observations. Moreover, the pseudo-disk (No RSD) simulations predict much smaller line widths than those observed. This line originates from the inner warm parts that are rotationally supported. Thus, this comparison may suggest that the large observed line widths of $C^{18}O$ 9–8 line indicate that most of the low-mass embedded YSOs have or are forming an RSD. Alternatively, a turbulence with $FWHM = 2 \, \mathrm{km \, s^{-1}}$ would be required in the inner parts if RSDs are absent.

2.5 Discussion

2.5.1 Variations with viewing angles

This paper presents synthetic continuum maps and CO isotopolog lines from 3D MHD simulations and 2D semi-analytical disk formation models out of collapsing rotating envelopes. The aim is to present signatures that can differentiate between embedded rotationally supported disks (RSDs) and a pseudo-disk. Thus far, we have analyzed the continuum and synthetic molecular lines with respect to one viewing angle in the azimuthal direction with $\phi = 0°$. As shown previously by Smith et al. (2012), the line profiles may change with different viewing angles since the collapse process is not spherically symmetric.

In order to look at the general trend with viewing angles, synthetic images at 4 different inclinations (i) from $15°$ to $150°$ and 8 azimuthal angles from $8°$ to $315°$ are generated. We concentrate the analysis on 850 μm, 1100 μm, $C^{18}O$, and $C^{17}O$ images. Figure 2.10 presents the continuum and molecular lines at a few viewing angles for the two 3D MHD simulations. The 3D RSD formation predicts an observable spiral feature at near face-on ($i \approx 0°$) with high dynamic range (1000). As mentioned earlier, this is due to the infalling material on its way to the disk.

In terms of kinematical signatures, the moment one maps of the $C^{18}O$ 2–1 line are compared for the two cases. Both the RSD and pseudo-disk simulations predict a coherent velocity
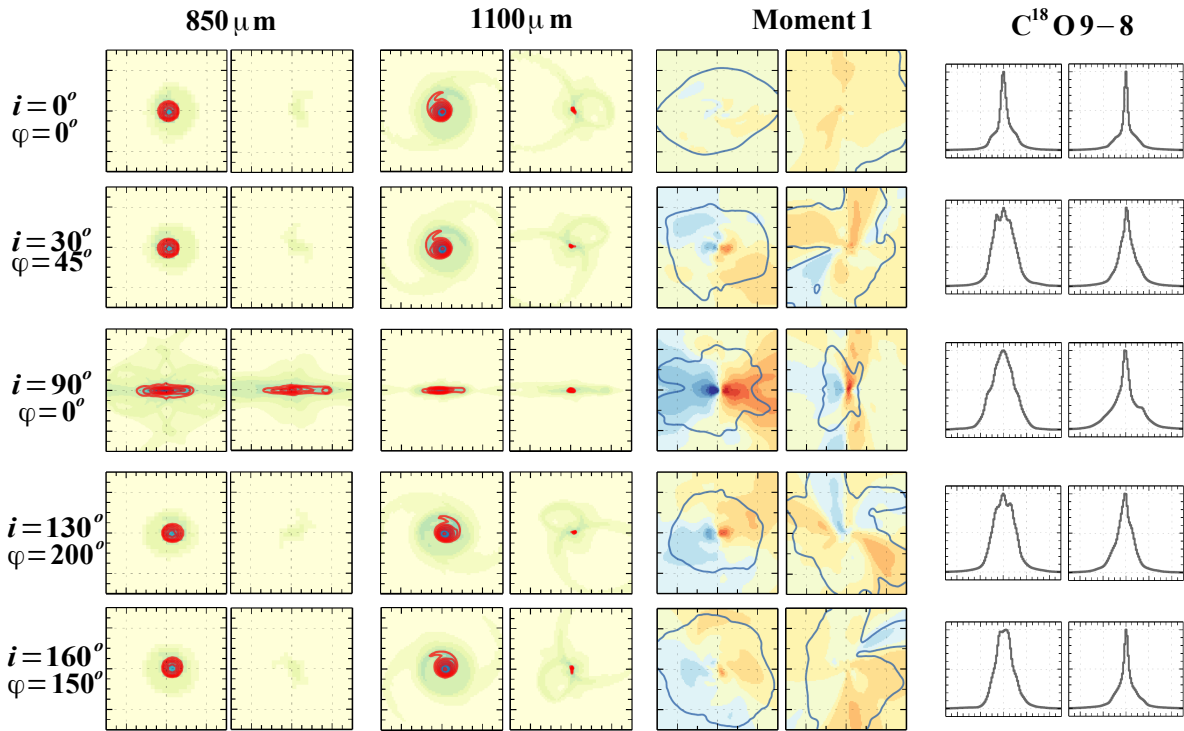
Figure 2.10 — Comparison of synthetic 850 μm, 1100 μm, C^{18}O 2–1 moment one maps and normalized C^{18}O 9–8 spectra for the 3D RSD (*left*) and pseudo-disk (*right*) MHD simulations viewed at a few orientations. The images and image cubes are convolved with a $0.1''$ beam. The maps sizes are $5''$ across similar to Fig. 2.4. The color scales and line contours are defined in Figs. 2.4 and 2.5. The normalized C^{18}O 9–8 spectra refer to a $15''$ beam on the same scale as Fig. 2.9. The inclination and rotation values are representative only and not exact.

gradient in the inner 300 AU. However, the velocity gradient is more robust if an RSD is forming. The pseudo-disk simulation shows a velocity gradient that is not necessarily along the disk major axis (see Fig. 2.1 and Section 2.4.1). Such a direction corresponds to the streamlines of the infalling material from the large-scale envelope to the central star. At high inclinations ($i > 75°$), this direction of the velocity gradient shifts to east-west direction similar to the RSD simulation, because the moment one map is dominated by the rotational motions which are in the east-west direction.

To assess the general predictions for the large-scale envelope, C^{18}O 9–8 spectra within a $15''$ beam are compared. The low-J lines ($J_{\mathrm{u}} = 2$ and 3) exhibit inverse P-Cygni profiles indicating infalling material in both RSD and pseudo-disk simulations. For the high-J lines, the 3D RSD simulation predicts a broader line than the pseudo-disk simulation in most orientations consistent with Fig. 2.9.

In summary, the results that are presented in previous sections are robust and do not depend on the viewing angles. A pseudo-disk shows more distinct features in the kinematics in the moment one maps that are different from an RSD. A coherent blue- to red-shifted velocity gradient in the inner 1 arcseconds aligned with the major axis is most likely a signature of an RSD or on-going RSD formation. Although these lines are simulated assuming LTE conditions, non-LTE effects generally decrease the strength of the emission but do not alter the results of the kinematics derived from the molecular limes.
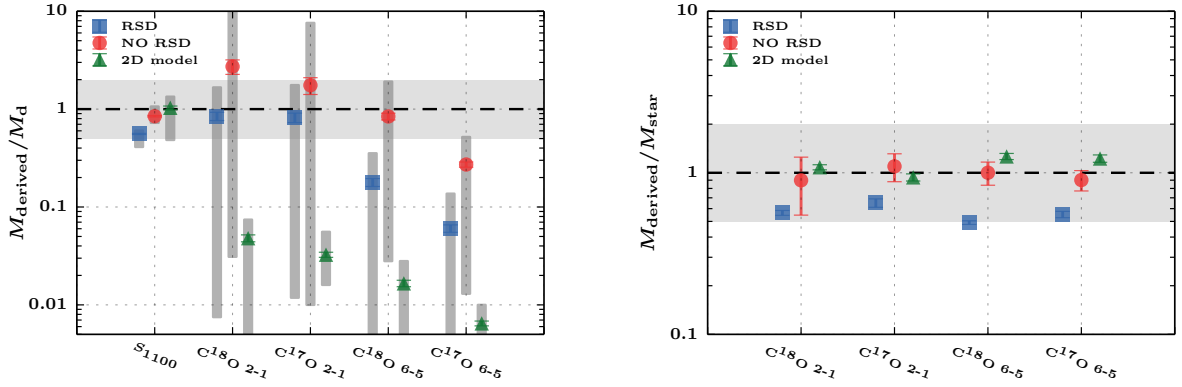
Figure 2.11 — *Left:* Mean deviation of disk masses (gas + dust) derived from 1100 μm continuum and molecular lines fluxes from the true disk mass extracted from the simulations. The gray bars indicate the full range of values for the different orientations. *Right:* Mean deviation of stellar masses measured from molecular lines from the true stellar mass. The colors indicate the different simulations: 3D MHD simulations in blue, 3D MHD pseudo-disk simulation in red, and 2D semi-analytical model in green. The error bars indicate the standard error of the mean. The shaded region shows the area within a factor of 2.

2.5.2   Masses and sizes

2.5.2.1   Analysis with continuum

To test models of star and disk formation (e.g., Hueso & Guillot 2005), the flow of mass from envelope to disk to star with time needs to be known. In practice, this means that the masses of the central (proto-)star and of its envelope-disk system need to be extracted from observations and models at different evolutionary stages. A pragmatic way to 'extract' the envelope and disk masses is to compare the continuum fluxes within a large beam with those found at 'small' scales. Here, $5''$ area is taken as the 'small' scale corresponding to 50kλ at a distance of 140 pc as probed previously with the SMA. Specifically, Jørgensen et al. (2009) gives the following formulae:

$$S_{5''} = S_{\text{disk}} + f_{\text{env}} \times S_{\text{env}} \tag{2.1}$$
$$S_{15''} = S_{\text{disk}} + S_{\text{env}}, \tag{2.2}$$

where f_{env} is the envelope contribution at 'small' scales, $S_{5''}$ is the flux within a $5''$ area, $S_{15''}$ is the flux within a $15''$ beam, S_{env} is the total envelope flux, and S_{disk} is the total disk flux. The set of equations above roughly separates the envelope from the disk in terms of continuum flux contribution. There are two issues that need to be addressed in utilizing the equations above: the envelope fraction (f_{env}) and the 'small' scale flux.

The first issue is presented in §4.1 of Jørgensen et al. (2009). They calculated the envelope contribution as determined from $\rho_{\text{dust}} \propto r^{-1.5}$ spherical envelopes. This yields a maximum contribution of 8% at 850 μm within a scale of $5''$ compared with that at $15''$. The contribution increases with increasing power-law exponent (16% for $\rho \propto r^{-1.8}$). Note that Jørgensen et al. (2009) computed the relative contribution between $S_{50\,\text{k}\lambda}$ at 1.1 mm and $15''$ in 850 μm. In order to compute the contributions within the same wavelengths, these values are scaled assuming $F_\nu \propto \nu^{2.5}$. In addition, for a given 2D embedded disk model, the projected spherical envelope model is one with an increasing exponent with inclination (i.e., $\rho \propto r^{-1.8}$ as $i \to 90°$). In other words, for an embedded YSO viewed at face-on, the best representative spherical model is one with a rather flat density profile. As a result, the envelope contribution from an embedded YSO on small scales changes with inclination.

Another issue is the 'small' scale flux at which to determine the envelope contribution. If the size is too small (i.e., 1″), the envelope contribution is naturally negligible and it is easy to extract the disk flux. However, the disk flux can be underestimated within such a small scale. Furthermore, the flux that is measured at each pixel is always a combination of the envelope and the disk. Thus, it is more intuitive to calculate the envelope's contribution at scales larger than the disk ($\sim 5″$, 700 AU at 140 pc) in order to obtain all of the disk's flux.

For this purpose, following the method in the literature, the envelope and disk masses are determined from comparing the fluxes within a 15″ beam and a 5″ area. This procedure is performed on the images rendered at the 32 different viewing angles as described in the previous paragraphs. A typical constant envelope fraction of 8% at 850 μm (2% at 1100 μm) is adopted to see how well such a simple estimation based on spherically symmetric envelope model can extract the disk properties of the 2D and 3D simulations.

Once the disk and envelope fluxes at 850 μm have been obtained, the conversion to dust mass follows Jørgensen et al. (2009), Eq. (1), which takes into account the fact that there is a distribution of temperatures in the envelope set by the luminosity of the protostar. The envelope mass therefore scales both with distance and bolometric luminosity ($L_{\rm bol}$). For the disk, a dust temperature of 30 K is adopted to calculate its mass as it is done in observations. These values are compared to the masses of different components in the simulations (Table 6.1). The disk mass in the simulation is defined by the velocity structure as described in Section 2.2.3. The left-over material within the computational box is the envelope mass.

Figure 2.11 presents the ratio of disk masses derived from synthetic continuum observations to the true masses tabulated in Table 6.1. In the case of the pseudo-disk, the disk mass is taken to be the mass of the region with number densities $n_{\rm H_2} > 10^{7.5}$ cm^{-3}. The masses inferred from the continuum fluxes are within a factor of 2 of the true disk mass. There is a little difference in the disk mass between 1100 μm and 850 μm for both 3D RSD and 2D semi-analytical model. Envelope masses agree if scaled to the same 15″ beam.

The spread in the inferred disk masses is greater in the 2D model than in the 3D simulation. The lower end of the spread is occupied by simulations at high inclinations ($i > 75°$). In such an orientation, the continuum optical depth even at 1100 μm is high since the disk is viewed edge-on and, consequently, a large part of the disk does not contribute to the observable emission. The high end of the spread is when the system is viewed almost face-on where the inner flattened inner envelope deviates from the spherically symmetric assumption. Finally, the equations above underestimate the disk mass from the 3D simulations because a $T_{\rm dust} = 30$ K was assumed to obtain the disk mass whereas the temperature within the disk is < 30 K at large radii. A lower temperature ~ 10 K would be best for the 3D RSD simulation while it is inclination dependent for the 2D model case.

The results suggest that disk masses can be well estimated from the continuum flux even for the pseudodisk. However, there is a clear difference in how the disk is defined in all three different cases. In the 3D and 2D RSD, the disk mass is defined by its velocity structure such that it is indeed rotationally supported while the pseudodisk is defined by density. Hence, in the latter case, the difference between the disk and the infalling envelope is not well defined.

In summary, we find that the disk masses as inferred from continuum emission in the 3D simulations and 2D semi-analytical model are within a factor of 2 of the true value. This factor-of-2 is due to the viewing angle and the dust temperature within the disk is lower than the assumed 30 K. However, we find that the pseudo-disk also indicate similar emission at such scales (see also, Chiang et al. 2008). In this case, the disk does not corresponds to a Keplerian disk.

2.5.2.2   Disk radii and stellar masses

Analysis of the continuum toward a large sample of sources yields disk and envelope masses. In order to fully test the evolutionary models, the stellar masses need to be derived from the kinematics of molecular lines. In addition, the disk radii can be determined from the velocity profiles (see Section 2.4.2) and can also serve as tests for the evolutionary models since disk radius is expected to increase with evolutionary state but to also depend on the initial angular momentum of the core (see Fig. 13 in Harsono et al. 2014). The extent of the RSD is determined from the break in the peak-position velocity diagrams (see Fig. 2.7) for the simulated $C^{18}O$ 2–1, $C^{18}O$ 6–5, $C^{17}O$ 2–1 and $C^{17}O$ 6–5 lines. For the 2D semi-analytical models, the average radius from the 4 lines is 64 ± 8 AU as derived from the break. For the 3D MHD RSD simulation, the average radius is 230 ± 100 AU. Thus, the inferred drop-off gives a good estimate of the extent of small disks, while a larger disk has a larger error bar associated to it.

Disk masses can also be calculated from the integrated flux densities ($\int S_\nu d\upsilon$ in Jy km s^{-1}) of molecular lines. In this method, the integrated flux densities are extracted within the region defined by the radius in the previous paragraph. The mass calculation is given by (Scoville et al. 1986; Momose et al. 1998; Hogerheijde et al. 1998):

$$
\begin{aligned}
M_{\mathrm{gas}} \quad = \quad & 5.9 \times 10^6 \frac{Q(T_{\mathrm{ex}})}{g_{\mathrm{u}} A_{\mathrm{ul}} \exp\left(-E_{\mathrm{u}}/k_{\mathrm{B}} T_{\mathrm{ex}}\right)} \frac{\mu_{\mathrm{H_2}} m_{\mathrm{H_2}}}{[X/\mathrm{H_2}]} \\
& \frac{\tau_{\mathrm{L}}}{1 - \exp^{-\tau_{\mathrm{L}}}} \left(\frac{d}{140\mathrm{pc}}\right)^2 \int S_\upsilon d\upsilon \; M_\odot,
\end{aligned}
\tag{2.3}
$$

where A_{ul} is the Einstein A coefficient of the transition, g_{u} is the degeneracy of the upper level, E_{u} is the upper level energy, $Q(T_{\mathrm{ex}})$ is the partition function at an excitation temperature $T_{\mathrm{ex}} = 40$ K, $\mu_{\mathrm{H_2}}$ is the mean weight of the gas, $[X/\mathrm{H_2}]$ is the abundance of molecule X with respect to $\mathrm{H_2}$, τ_{L} is the line optical depth, and k_{B} is the Boltzmann constant. A constant line optical depth of 0.5 for the $C^{18}O$ and 0.3 for the $C^{17}O$ lines is used, which characterizes the average optical depth over all velocities. The crucial assumption here is the CO abundance, $[X/\mathrm{H_2}]$, which is taken to be 10^{-4}. Since the CO abundance will be affected by freeze-out in the cooler parts of the disk, this assumption provides a lower limit to the disk mass.

Figure 2.11 presents the masses obtained from the integrated line flux densities. They show a much larger scatter than the masses obtained from the dust continuum flux. The symbols indicate the values appropriate for masses derived at moderate inclinations. For the case of RSD formation, the low-end of the spread is due to near face-on orientation ($30° > i > 150°$) in which the obtained disk sizes are half of the true RSD and, consequently, the disk mass is lower than average. In the 2D semi-analytical model case, the physical structure of the inner envelope plays a role. The conversion between integrated flux to mass also assumes that the emission at all velocities is dominated by the disk, which is only true for emission at the wings (high velocities). However, in the 2D semi-analytical model, the inner envelope is highly flattened compared to that of the 3D MHD simulation such that high density gas ($n_{\mathrm{H_2}} > 10^6$ cm^{-3}) surrounds the RSD (see Fig. 2.1). So, the disk does not dominate the integrated flux density at this particular time (see Fig. 8 of Harsono et al. 2013) and, consequently, the integrated flux density is not correlated with its mass. Therefore, a good estimate of the disk's molecular mass can only be obtained if the system is oriented at moderate inclinations and the RSD is assumed to dominate the molecular emission at all velocities.

The disk masses derived from the 2–1 line are generally higher than that from the 6–5 line. Since the RSD size obtained from the 6–5 emission is smaller than that from the 2–1 line (e.g., 200 vs 100 AU), the integrated line flux density is extracted from a smaller region, which results

in a much lower mass. The size of the RSD is smaller in the 6–5 emission because the emission arises from the dense warm regions in the vicinity of the protostar and, thus, its mass. The masses obtained from the integrated 2–1 line are better estimates for the true disk mass.

The 3D MHD and 2D semi-analytical RSD formation predict the same behaviour in terms of disk masses in both $C^{17}O$ and $C^{18}O$ lines. The difference of the masses obtained in the 2–1 and the 6–5 lines are also similar for the two isotopologs. The 2D semi-analytical model predicts a smaller spread than the 3D RSD model in the disk masses obtained from the $C^{17}O$ 2–1 line since the high density region is more compact in the 2D case and, therefore, the $C^{17}O$ 2–1 integrated flux density obtained in the 2D model does not vary as much as in the 3D simulation. The comparison between the 2D semi-analytical model and 3D MHD shows that the reliability of the observables to trace the true masses depends on the physical structure of the inner envelope.

The stellar masses obtained from the PPV method are shown in Fig. 2.11. They are typically within a factor of 2 of the true stellar masses. The best-fit values for synthetic molecular lines viewed at $i < 15°$ tend to be more than twice the true stellar mass. This is due to the difficulties in obtaining the peak positions at high velocities since they are most likely to be below the noise level. The 2D semi-analytical model indicates better agreement with true stellar masses than those of the 3D model because their velocity structures are different. The kinematics of the envelope is the same at all viewing angles in 2D. However, there are lines of sights that pick up significant sub-Keplerian gas ($v_\phi > v_r$) infalling onto the disk in 3D as shown in Fig. 4.2. Therefore, stellar masses as obtained from spatially and spectrally resolved molecular observations are good estimates of the true stellar mass within a factor of 2, which is smaller than the uncertainty in the inclination.

From the analysis of the synthetic observations, spatially ($\lesssim 0.1''$ at 140 pc) and spectrally (≤ 0.1 km s^{-1}) resolved optically thin molecular lines at two energy levels (e.g., 2–1 and 6–5) are required to understand the physical structure of the inner envelope. The disk masses obtained from the two lines are similar in the pseudodisk case while they can differ by an order of magnitude in RSD case. The simple PPV analysis directly from the data can already differentiate between the RSD and a pseudodisk. However, sophisticated modelling tools are needed to infer the physical structure of the disk.

2.6 Summary and conclusions

We have presented the observables in continuum and molecular lines for two 3D MHD simulations of Li et al. (2013) and 2D semi-analytical models of collapse and disk formation. Snapshots of two different MHD simulations of a relatively weakly magnetized core ($B_0 = 11$ μG) at the same time after the onset of collapse are used. One simulation has an initial magnetic field axis aligned with the rotation axis in which a rotational supported disk (RSD) does not form, however a pseudo-disk and outflowing gas are present. The other MHD simulation starts with the magnetic field axis oriented perpendicular to the rotation axis, which results in the formation of an RSD (see Figs. 2.1 and 4.2). These simulations explore the two extremes of the magnetic field orientation. The synthetic observables are then compared to a 2D semi-analytical model without magnetic field (Visser et al. 2009) with similar initial conditions (1 $M_\odot$ and $\Omega_0 = 10^{-13}$ Hz). Accurate dust temperatures are calculated using the 3D continuum radiative transfer tool RADMC3D with the same dust opacities and central temperature for all three models. Continuum images and thermalized CO molecular lines are produced using the same radiative transfer code and method. Freeze-out of CO onto grains is included. This paper focuses on presenting similarities and differences in the predicted observables. The main results and conclusions are as follows.

- Synthetic continuum images of the two MHD simulations and 2D semi-analytical model indicate that a spatial resolution of 14 AU and high dynamic range (1000) are required to differentiate between disk formation scenarios. Furthermore, the features that are present during the collapse are more easily observed in the 450 μm continuum images than at longer wavelengths. It is difficult to test disk formation models toward highly inclined systems using continuum data since both RSD and pseudo-disk formation show similar elongated features.

- The kinematical structures as revealed by the moment one maps of the synthetic molecular lines show a coherent blue- to
  red-shifted velocity gradient for both RSD models and for the pseudo-disk in the inner ~ 300 AU. However, the pseudo-disk shows a velocity gradient in north-south direction while the RSD shows an east-west gradient similar to the orientation of the flattened structure in the model. Moreover, the RSD formation in both 3D and 2D exhibits skewness in their moment one maps caused by the infalling rotating envelope component on larger scales which is absent in the case of pseudo-disk. The velocity gradient in the case of the pseudo-disk is a nearly straight line from the star to the large-scale structure since it is tracing the streams of material directly from the envelope onto the star. Thus, one can readily mistake a pseudo-disk with an RSD unless one performs additional analysis such as the peak position diagrams.

- Position-velocity (PV) diagrams constructed from C^{18}O and C^{17}O image cubes predict rotational signatures in both pseudo-disk and RSD formation, seen most prominently in C^{17}O data. This is due to the strength of rotation in the inner regions for both simulations. A combination of C^{18}O and C^{17}O lines is required to disentangle the RSD from a pseudo-disk. The signatures of infalling material in the pseudo-disk simulation are stronger in the C^{18}O lines. The velocity structure constructed from the peak positions (*peak-PV diagrams*) are used to differentiate between the pseudo-disk and the RSD. Velocity structures described by $v \propto r^{-0.5}$ and $v \propto r^{-1}$ are present in both cases of RSD formation whereas a flatter velocity profile is seen in the pseudo-disk case. We find that this conclusion is robust for different inclinations and rotations.

- The image cubes are convolved with large beams ($\geq 9''$) to simulate single-dish observations probing the large-scale envelope. The C^{18}O 2–1 and 3–2 line widths are similar between the three simulations with $FWHM \sim 1\,\mathrm{km\,s^{-1}}$ or Doppler b of $0.4\,\mathrm{km\,s^{-1}}$. This is due to the fact that the emitting regions in the large-scale envelopes are similar. The observed $FWHM$ values are larger than in those predicted from the simulations by a factor of 2. This suggests that the large-scale envelopes of low-mass embedded YSOs are significantly more turbulent than these models, which may be due to an interaction with a fast outflow (San Jose-Garcia et al. 2013).

- The comparison of the high-J lines (^{13}CO 6–5, ^{13}CO 10–9, and C^{18}O 9–8) indicates that the current simulations with RSD formation can reproduce the observed line widths solely due to the rotation + infall motions. On the other hand, the predicted line widths from the pseudo-disk are significantly smaller than the observed values. Thus, the mechanism(s) that are responsible for broadening the 6–5 and 9–8 lines depend on the whether or not an RSD is present. If no RSD is present, the observations would imply an increasing level of turbulence with decreasing radii; if an RSD is present, turbulence would not be needed, although it can still be present in the disk at some level.

- Masses derived from continuum and molecular lines from simulations and analyzed in the same way as observations depend on the physical structure at small-scales. The disk masses obtained from the continuum flux in small beams (a few $''$) are generally in agree-

ment with the true disk mass. Disk masses obtained from the integrated molecular line flux depend strongly on the physical structure. If the disk is small and cold with respect to the flattened inner envelope, inferred masses can be smaller by an order of magnitude from the true disk mass since the disk does not contribute to the integrated line flux density. However, if the disk is large and warm enough to prevent significant freeze-out, the mass obtained from the low-*J* lines can give a good estimate of the true RSD mass provided that the system is inclined toward us. Both the stellar masses and disk-to-envelope mass ratios are within a factor of 2 of the true masses. The presence of the RSD cannot be determined solely from continuum data alone, however the continuum flux provides a good estimate on the mass at small scales.

Acknowledgements

Chapter 3

Global Gravitational Instabilities in Discs with Infall

Abstract. Gravitational instability plays an important role in driving gas accretion in massive protostellar discs. Particularly strong is the global gravitational instability, which arises when the disc mass is of order 0.1 of the mass of the central star and has a characteristic spatial scale much greater than the disc's vertical scale-height. In this paper we use three-dimensional numerical hydrodynamics to study the development of gravitational instabilities in a disc which is embedded in a dense, gaseous envelope. We find that global gravitational instabilities are the dominant mode of angular momentum transport in the disc with infall, in contrast to otherwise identical isolated discs. The accretion torques created by low-order, global modes of the gravitational instability in a disc subject to infall are larger by a factor of several than an isolated disc of the same mass. We show that this global gravitational instability is driven by the strong vertical shear at the interface between the disc and the envelope, and suggest that this process may be an important means of driving accretion on to young stars.

3.1 Introduction

ACCRETION discs play a fundamental role in many aspects of astrophysics. Objects as diverse as planets, stars and super-massive black holes are all thought to acquire significant fractions of their mass through disc accretion, and consequently understanding accretion disc physics is important in understanding the formation of all of these objects. Critical to our understanding of accretion discs is the process of angular momentum transport, but despite many years of research on this subject we still do not fully understand the mechanism(s) by which angular momentum is transported in gaseous discs. In many cases we believe that magneto-hydrodynamic instabilities, such as the magnetorotational instability (MRI, Balbus & Hawley 1991; Balbus & Hawley 1998) is the dominant transport mechanism. However, some systems, notably protostellar discs, are insufficiently ionized for the MRI to operate everywhere (e.g., Gammie 1996), and it is also not clear whether or not the MRI can drive accretion rates as high as those which are observed (King, Pringle, & Livio 2007). Consequently, it is still desirable to investigate other mechanisms for angular momentum transport in discs.

One such mechanism which has received considerable interest in recent years is angular momentum transport by gravitational instabilities (GIs; see, e.g., Durisen et al. 2007; Lodato 2008, and references therein). Gaseous discs in Keplerian rotation become unstable to self-gravity when the Toomre (1964) Q parameter is less than some critical value of order unity. The Toomre parameter is defined as

$$Q = \frac{c_{\mathrm{s}}\Omega}{\pi G \Sigma},$$

(3.1)

where c_{s} is the sound speed of the gas, Ω is the angular frequency and Σ is the surface density. Shearing discs generally become unstable to non-axisymmetric perturbations before axisymmetric ones, so GIs in discs initially manifest themselves as spiral density waves. It was recognised long ago that such spiral density waves can transport angular momentum (Lynden-Bell & Kalnajs 1972) but detailed study of the non-linear development of GIs in gaseous discs has only recently become possible. This process has been studied in great detail using numerical hydrodynamics, and we now have a well-established picture whereby angular momentum transport by GIs is primarily governed by disc thermodynamics. GIs in isolated thin gas discs tend to evolve to a self-regulating state, where the energy liberated by accretion is balanced by local (radiative) cooling (e.g., Gammie 2001; Lodato & Rice 2004; Mejía, Durisen, Pickett, & Cai 2005; Cossins, Lodato, & Clarke 2009), and although gravity is a long-range force, "global" effects generally do not dominate unless the disc mass is an appreciable fraction ($\gtrsim 25\%$) of the mass of the central object (Laughlin, Korchagin, & Adams 1998; Lodato & Rice 2005). In this picture the efficiency of angular momentum transport can be parametrized in terms of a classical Shakura & Sunyaev (1973) α-prescription (Gammie 2001; Lodato & Rice 2004), where

$$\alpha_{\mathrm{GI}} = \frac{4}{9}\frac{1}{\gamma(\gamma-1)t_{\mathrm{cool}}\Omega} . \tag{3.2}$$

Here t_{cool} is the local cooling time-scale and γ is the adiabatic index of the gas. Faster cooling leads to deeper spiral density waves (i.e., with higher density contrasts), and thus to more efficient transport of angular momentum. However, if the cooling becomes too rapid the disc is unable to maintain its self-regulating state, and the GIs instead lead to fragmentation of the disc (Gammie 2001; Rice et al. 2003). This in turn imposes a maximum efficiency at which angular momentum can be transported by GIs without leading to disc fragmenting, and numerical simulations place typically this "fragmentation boundary" at $\alpha_{\mathrm{GI}} \lesssim 0.1$ (corresponding to $\beta = t_{\mathrm{cool}}\Omega \gtrsim 3$–$5$, e.g., Gammie 2001; Rice, Armitage, Bate, & Bonnell 2003; Rice, Lodato, & Armitage 2005). When extended to consider discs with realistic opacities, these results imply a maximum accretion rate that can be sustained by GIs in a self-regulating state (e.g., Levin 2003; Matzner & Levin 2005; Levin 2007; Clarke 2009; Rafikov 2009, see also Fig. 3.1). Except at very small radii this rate is low, $\sim 10^{-6}\ M_{\odot}\ \mathrm{yr}^{-1}$, and this raises questions as to how many astrophysical objects are able to accrete their mass in a plausible time-scale. The star may continue accreting bound clumps of gas even after the disc fragments (eg., Vorobyov & Basu 2010), but the details of this process remain uncertain.

To date most numerical studies of GIs have looked at isolated self-gravitating discs, but in reality it seems likely that most gravitationally unstable discs will still be subject to some level of infall on to the disc. Indeed, in many cases it is likely that the instantaneous infall rate on to the disc exceeds the accretion rate through the disc. For example, observed accretion rates on to protostellar discs are typically an order of magnitude larger than the accretion rates on to the protostars themselves (e.g., Kenyon & Hartmann 1990; Calvet, Hartmann, & Strom 2000). Similar discrepancies between infall and disc accretion rates have been found in models of low-mass star formation (e.g., Vorobyov & Basu 2009), and in models of star formation in black hole accretion discs (e.g., Milosavljević & Loeb 2004). In this paper we present an initial investigation of this problem, by using three-dimensional numerical hydrodynamics to follow the evolution of a self-gravitating accretion disc subject to quasi-spherical infall. In Section 6.2 we present our numerical method, and in Section 6.3 we discuss the results of our simulations. We find that infall on to the disc can substantially enhance the efficiency of angular momentum transport, through the excitation of low-order, global, spiral density waves. We discuss the consequences of this result for real astrophysical systems, along with the limitations of our
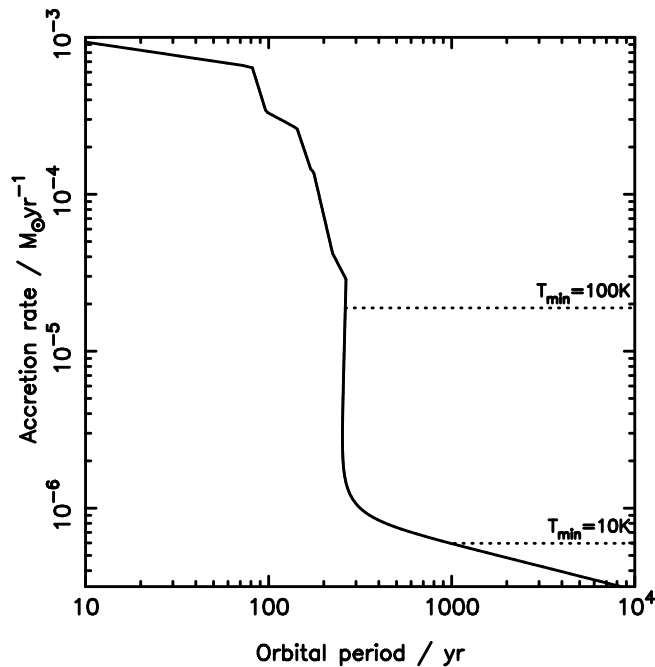
Figure 3.1 — Maximum sustainable accretion rate in a critically self-gravitating disc with $\alpha = 0.1$, computed following the procedure described in Levin (2007) and using the opacities $\kappa(\rho, T)$ of Bell & Lin (1994) and Bell et al. (1997). The sharp jump in the critical accretion rate at an orbital period of $\simeq 300$yr is caused by the transition between the optically thick inner disc and optically thin outer disc (Matzner & Levin 2005). This corresponds to a radius of $\simeq 40$ AU for a 1 $M_\odot$ central star, or $\simeq 100$ AU for a 10 $M_\odot$ star. The maximum sustainable accretion rate at larger radii is small, $\sim 10^{-6}$ $M_\odot$ yr^{-1}; in the "local limit", larger accretion rates lead to fragmentation. In some cases external irradiation can be the dominant source of heating, imposing a temperature "floor" (denoted by $T_{\min}$) and enhancing the maximum accretion rate. Similar figures can be found in Clarke (2009) and Rafikov (2009).

analysis, in Section 6.4, and summarize our conclusions in Section 3.5.

3.2 Numerical Method

Our simulations are conducted using the publicly-available smoothed-particle hydrodynamic (SPH) code GADGET-2 (Springel 2005). We have modified the code to include a simple scale-free cooling prescription, as used in previous simulations (Gammie 2001; Lodato & Rice 2004; Cossins et al. 2009), which has the following form:

$$\frac{du_\mathrm{i}}{dt} = -\frac{u_\mathrm{i}}{t_{cool}}, \tag{3.3}$$

Here u_i is the internal energy of particle i, and the cooling time-scale t_{cool} is proportional to the local dynamical time-scale thus

$$t_{\mathrm{cool}} = \frac{\beta}{\Omega}. \tag{3.4}$$

Operationally, the cooling time-scale is computed as

$$t_{\mathrm{cool}} = \beta \sqrt{\frac{R_\mathrm{i}^3}{GM_\star}}, \tag{3.5}$$

where R_i is the cylindrical radius of the ith particle. The cooling time thus depends only on radius, and does not vary with z or with the instantaneous orbital speed (which can be perturbed significantly in unstable discs). As mentioned in Section 6.1, previous simulations of self-gravitating discs have found that values of $\beta \lesssim 3$–5 result in fragmentation of the disc, while larger values lead to transport of angular momentum (e.g., Gammie 2001; Rice et al. 2003, 2005). We do not wish to see disc fragmentation due to rapid cooling alone, and therefore set $\beta = 7.5$ throughout. We adopt an adiabatic equation of state, with adiabatic index $\gamma = 5/3$.

We make use of a single sink particle as the central gravitating mass, which accretes all gas particles within its sink radius (as described in Cuadra et al. 2006). This is primarily a numerical convenience, used in order to prevent the time-step being limited by a small number of SPH particles at very small radii, and has no physical effect on the simulations. We use the standard Barnes-Hut formalism to calculate the gravitational force tree, and use $N_{ngb} = 64 \pm 2$ as the number of SPH neighbours. We allow a variable gravitational softening length, which is equal to the SPH smoothing length throughout (as demanded by Nelson 2006). The simulations are scale-free: we use a system of units where the central gravitating mass has an initial mass $M_\star = 1$, the inner edge of the disc is at $R = 1$[1], and the time unit is the orbital period at $R = 1$. (Thus $G = 4\pi^2$ in code units.)

3.2.1 Artificial viscosity

We adopt the standard Monaghan-Gingold-Balsara form for the artificial viscosity (Monaghan & Gingold 1983; Balsara 1995), as described in Equations 11–12 of Springel (2005). This prescription contains both linear and quadratic terms (characterised by the parameters α_{sph} and β_{sph} respectively, with $\beta_{sph} = 2\alpha_{sph}$), and the "Balsara switch" which acts to limit the artificial viscosity in pure shear flows. We adopt $\alpha_{sph} = 0.3$ throughout.

As we are primarily interested in how angular momentum is transported in our simulations, great care must be taken to ensure that this transport is not dominated by numerical effects. It is well-known that SPH artificial viscosity can drive significant angular momentum transport in disc simulations (e.g., Murray 1996; Lodato & Rice 2004), so we have conducted tests to ensure that this is not the dominant source of transport in our models. From our standard disc initial conditions (see next Section) we ran simulations with the self-gravity of the gas turned off; with this set-up, Reynolds stresses due to numerical effects (primarily the artificial viscosity) are the only source of angular momentum transport. By expressing this stress in units of the local pressure (see, e.g., Lodato & Rice 2004) we can parametrize the efficiency of the numerical transport as a familiar α-parameter thus:

$$\alpha_{art} = \frac{2}{3} \frac{\delta v_r \delta v_\phi}{c_s^2}, \tag{3.6}$$

where $\delta\mathbf{v} = \mathbf{v} - \langle\mathbf{v}\rangle$ (i.e., the perturbation from the mean fluid velocity). Except in the regions near the inner boundary ($R \lesssim 10$), where the flow is in any case dominated by boundary effects, we find that the efficiency of artificial transport is typically $\alpha_{art} \simeq 0.001$–0.005, and never exceeds 0.01. Numerical transport of angular momentum is therefore at least an order of magnitude less efficient than the transport we expect from GIs, and we are confident that angular momentum transport by artificial viscosity does not have a strong influence on our results.

---

[1]Note that we use upper-case R to denote cylindrical radius, and lower-case r for spherical radius.

3.2.2 Initial Conditions

3.2.2.1 Disc

Our discs are set up to use the same initial conditions as Rice et al. (2005). The central gravitating mass is surrounded by a gaseous disc with mass M_d, which is represented by 250,000 SPH particles. The initial velocity profile is Keplerian, with a first-order (spherical) correction to account for the effect of the disc mass. The disc extends from $R = 1$ to $R = 100$, with initial surface density and temperature profiles

$$\Sigma(R) \propto R^{-1}, \tag{3.7}$$

and

$$T(R) \propto R^{-1/2}. \tag{3.8}$$

Thus $Q \propto R^{-3/4}$ (approximately), and we normalise the disc temperature so that $Q = 2$ at the outer disc edge ($R = 100$). The disc is thus initially stable, and is allowed to cool into instability. The vertical density distribution is Gaussian, with scale-height $H = c_\mathrm{s}/\Omega$. Because the disc's self-gravity is not negligible this configuration is not strictly in vertical hydrostatic equilibrium, but the discs adjust to equilibrium on a dynamical time-scale. We performed two such simulations with different disc masses: $q = M_\mathrm{d}/M_\star = 0.1$ and $q = 0.2$.

3.2.2.2 Spherical envelope

In order to study the effects of infall on the development of gravitational instabilities in the disc, we took the simplest possible approach and surrounded the $q = 0.1$ disc with a uniform density spherical envelope. The envelope has the same mass as the disc ($0.1 \ M_\star$), and thus uses a further 250,000 SPH particles, and extends from $r = 1$ to $r = 500$. The envelope is initially isothermal, with a temperature equal to that at the disc outer edge. In order to prevent gas particles spiralling tightly around the vertical axis resulting in unreasonably short time-steps, the spherical envelope has a cylindrical hole around the z-axis which extends to $R = 10$. The envelope was initially given solid body rotation, with the angular frequency fixed to be 0.08 of the Keplerian value at the outer disc radius. This value was chosen so that the bulk of the envelope mass falls on to the disc away from the inner boundary, where the disc is numerically well-behaved. With this set-up, most of the initial infall occurs at radii from $R \simeq 20$–100. The measured infall rate is around an order of magnitude greater than the maximum quasi-steady accretion rate through the disc, as shown in Fig. 3.2. This discrepancy between the infall rate and the disc accretion rate can be understood as follows. The infall is roughly spherical, and the cooling time-scale is long compared to the infall (dynamical) time-scale, so the infall rate is approximately

$$\dot{M}_\mathrm{infall} \sim \frac{c_\mathrm{s}^3}{G}. \tag{3.9}$$

By contrast, the maximum sustainable accretion rate through the disc (in the local limit) is

$$\dot{M}_\mathrm{acc,max} \sim \alpha_\mathrm{max} \frac{c_\mathrm{s}^3}{G}. \tag{3.10}$$

The sound speeds in these two equations are not necessarily the same: the first is in the envelope, while the second is in the disc midplane. However, in our simulations the radial variation of c_s in the disc is weak ($\propto R^{-1/4}$) and the cooling is slow, so in practice the two sound speeds
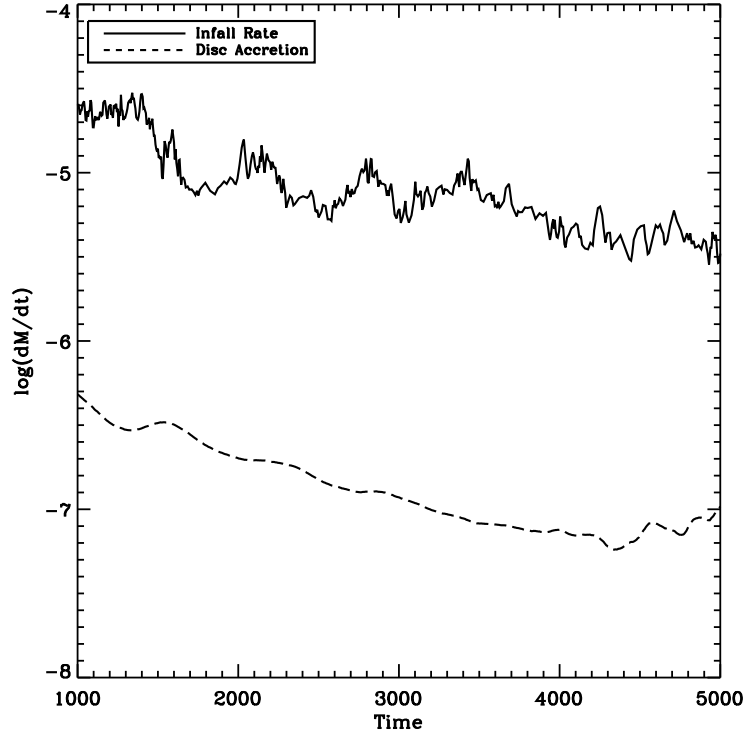
Figure 3.2 — Measured accretion rate on to the disc in the infall model, and the quasi-steady accretion rate through the $q = 0.1$ disc. The quasi-steady rate is evaluated as $\dot{M} = 3\pi\alpha_{GI}c_s^2\Sigma/\Omega$, with $\alpha_{GI} = 0.1$ (see text) and the sound speed evaluated at the disc midplane, averaged over the radial region $R = 20\text{–}80$. The infall rate is determined from the time derivative of the disc mass.

are very similar. The fragmentation boundary in isolated discs is $\alpha_{max} \simeq 0.1$ (Rice et al. 2005), and thus it is physically reasonable for $\dot{M}_{infall}$ to exceed $\dot{M}_{acc,max}$ by approximately a factor of 10. This situation, however, naturally leads to an unsustainable bottleneck, as the infalling mass cannot be accreted in the "normal" manner. We therefore expect this simulation to have dramatic results: presumably, the disc must either fragment (despite slow cooling), or undergo some sort of violent relaxation process (with rapid transport of angular momentum).

3.3 Results

We performed three simulations: two isolated disc simulations with $q = 0.1$ and $q = 0.2$, and the "infall" (disc + spherical envelope) simulation. The isolated disc simulations act as reference models: the $q = 0.1$ disc is identical to that in the infall model (but with no infall), and the $q = 0.2$ disc serves as a reference where all of the envelope mass instead initially resides in the disc. The two isolated disc models essentially "bracket" the infall model (which has an initial mass of 0.1 $M_\star$ and a maximum final mass of 0.2 $M_\star$), and allow us to discriminate between mass and infall effects. We followed each simulation to $t = 5000$ (code units). This corresponds to 5 outer disc orbital periods (i.e., slightly less than one outer cooling time-scale), after which time most of the material in the envelope has already fallen onto the disc[2]. In the region where the disc is numerically well-behaved (approximately $R = 20\text{–}80$; away from the

---

[2]Note, however, that a significant fraction of the envelope mass falls to the midplane at $R > 100$, beyond the outer edge of the initial disc.

disc boundaries) we are thus able to follow the dynamics for tens of dynamical time-scales, allowing the instabilities to develop in a physical manner.

3.3.1 Isolated Discs

Many previous studies have studied the transport properties of GI in low-mass ($q \lesssim 0.25$) discs (e.g., Lodato & Rice 2004; Boley et al. 2006; Cossins et al. 2009). Our low-mass ($q = 0.1$) isolated disc is essentially identical to that used in previous simulations (Rice et al. 2005; Cossins et al. 2009), and its expected behaviour is well understood. The transport of angular momentum is dominated by high-order ($m \sim 10$) spiral density waves, and the dynamics are consistent with the local approximation. The characteristic length-scale of such spiral density waves is in the order of disc scale height H. This simulation therefore serves two purposes here: it acts as a code test, as our calculation should reproduce previous results, and it also provides us with a reference model with which to compare our "disc with infall" calculation[3]. Previous studies have also shown that increasing the disc mass results in the GI generating more power in the lower-m, global spiral modes (Lodato & Rice 2005). We therefore ran a second reference simulation, with $q = 0.2$, so that we are able to distinguish the effects of infall from those that are simply due to the increasing disc mass.

Our isolated disc simulations essentially repeat these previous studies, and we observe the same general behaviour described in (for example) Lodato & Rice (2004) and Cossins et al. (2009). The time evolution of the simulations is shown in Fig. 3.3, which shows the midplane density evolution from $t = 2000$ to $t = 4000$. The isolated discs initially cool and become gravitationally unstable, and then develop long-lived spiral density waves which transport angular momentum in a quasi-steady manner. Both discs quickly settle into a self-regulating state, with $Q \simeq 1$ at all radii (see Fig. 3.4). The maximum density contrast in the spiral arms reaches approximately 1.5 orders of magnitude. The drop in surface density at small radii is due to the artificial pressure gradient introduced by the inner boundary, and is not physical; for this reason, we neglect the inner region of the discs ($R \leq 20$) in our subsequent analysis. Some additional power in low-order spiral modes is seen in the more massive ($q = 0.2$) disc, but for the most part the transport is well-characterised by a local model, where energy released by accretion is locally balanced by the imposed cooling.

The induced global spiral density waves can be examined by decomposing the disc's structure into Fourier modes. In order to compute the Fourier amplitudes, we divided the disc into concentric annuli and computed the amplitudes of the azimuthal modes for each annulus. We then integrated these amplitudes radially to give global Fourier amplitudes A_{m}, where m is the Fourier mode:

$$A_{\mathrm{m}} = \frac{1}{N_{\mathrm{disc}}} \left| \sum_{R=20}^{80} \sum_{j=1}^{N_{\mathrm{ann}}} \exp^{-im\phi_{\mathrm{j}}} \right| . \tag{3.11}$$

Here N_{ann} is the number of SPH particles in each annulus, and N_{disc} is the total number of particles in all the annuli (i.e., the disc mass). m is the azimuthal mode number, and ϕ_{j} is

---

[3]For numerical reasons $q = 0.1$ is also approximately the lowest mass disc that can be well-resolved in these simulations. The resolution requirements in such simulations essentially amount to always ensuring that the disc scale-height is resolved into several SPH smoothing lengths (Nelson 2006). In a self-gravitating disc the scale-height is proportional to the disc mass, so for three-dimensional simulations a factor of two decrease in the disc mass typically costs more than an order of magnitude in computation time (an increase of $\sim 2^3$ in particle number, plus a shortening of the time-step). Consequently, long-duration simulations of discs with $q \ll 0.1$ remain prohibitively expensive.
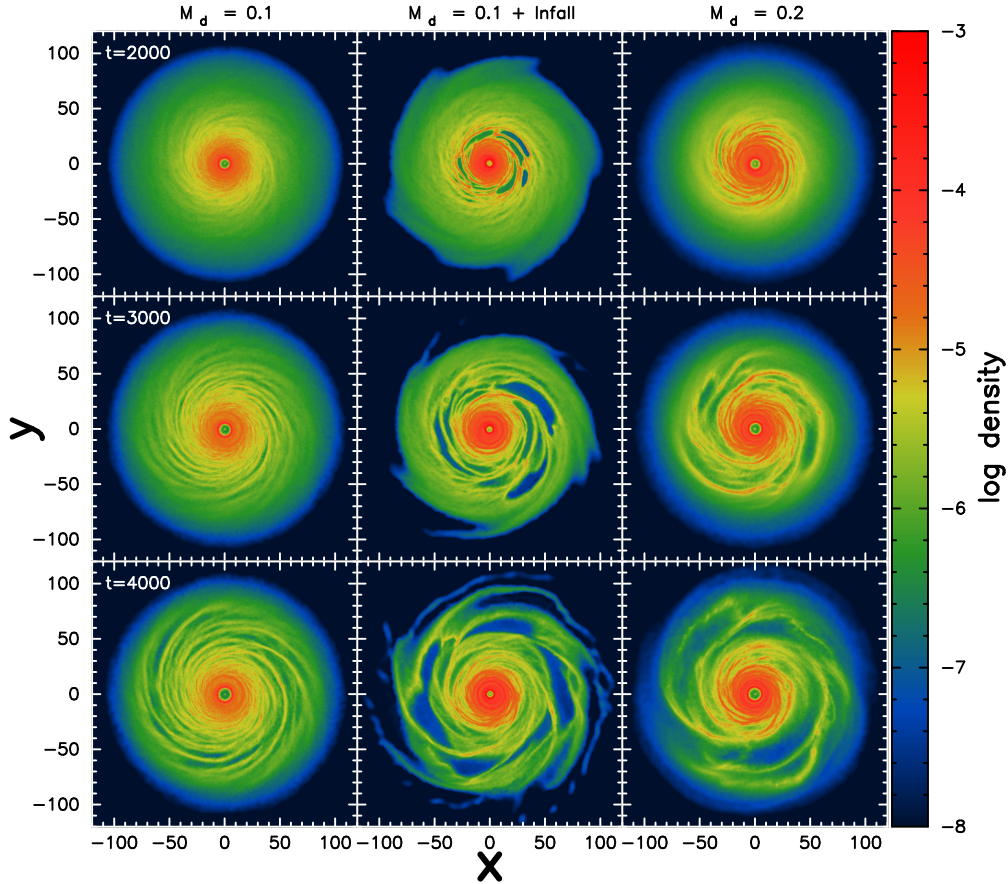
Figure 3.3 — Time evolution of midplane density in the different simulations. From left-to-right, the three columns show the time evolution of the $q = 0.1$, infall and $q = 0.2$ discs respectively. The isolated disc models evolve into a self-regulating state, with quasi-stable transport of angular momentum. In the presence of infall, however, the disc shows dramatic departures from self-regulation, with high-amplitude spiral density waves, low-order spiral modes, and increased rates of angular momentum transport.

the azimuthal angle (phase) of the jth particle. We use annuli of width $\Delta R = 1.0$, which gives $N_{\mathrm{ann}} \sim 2000$ particles in each annulus. Because of the strong influence the outer and (especially) inner boundaries, we limit ourselves to the radial range $20 \leq R \leq 80$; numerical effects are likely to be significant outside this range.

Figure 3.5 shows the time evolution of the Fourier amplitudes in our simulations. In the $q = 0.1$ disc modes with $m \geq 5$ dominate the spiral structure, as expected for a relatively thin disc where the transport is primarily local (Lodato & Rice 2004; Cossins et al. 2009). The $q = 0.2$ disc shows more power in the lower-m ($m = 2$–4) modes, similar to the behaviour seen in previous simulations (e.g., Lodato & Rice 2005). We are thus satisfied that our isolated disc models are consistent with previous results, and that our numerical method is satisfactory.

3.3.2 Disc with infall

The central column in Fig. 3.3 shows the evolution of the disc with infall. The behaviour is very different from that of either of the isolated discs. The first notable difference is the formation of high-amplitude spiral density waves at $t \simeq 2000$, and the onset and growth of the GI occurs much faster than in the isolated discs. In the presence of infall the disc shows much higher density contrasts (factors of $\simeq 2$–5) than the isolated discs, and well-ordered low-m spi-
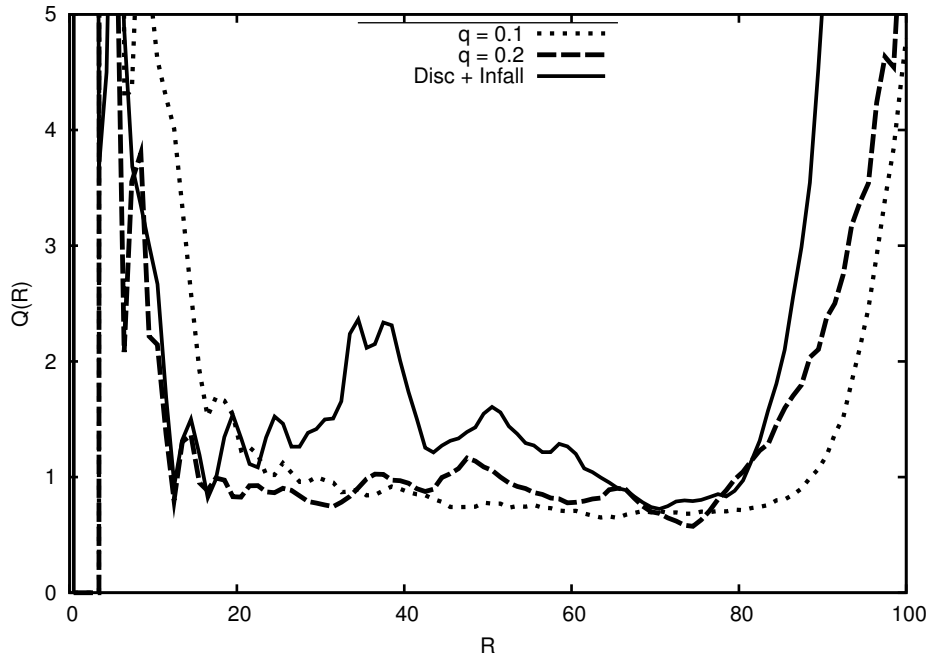
Figure 3.4 — Azimuthally-averaged Toome Q parameter for the three different simulations, plotted at $t = 3500$. Note the strong divergence from $Q \simeq 1$ in the infall simulation.
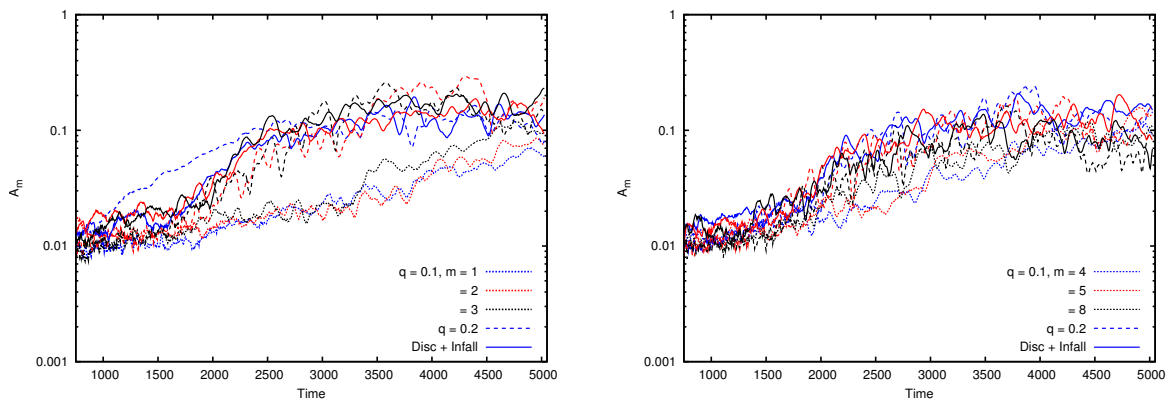

Figure 3.5 — *Left*: Time evolution of the lowest-order Fourier modes, A_m, in the three simulations: $q = 0.1$ (dotted), $q = 0.2$ (dashed) and disc + infall (solid). Blue, red and black lines denote $m = 1, 2$ & 3 respectively. The $q = 0.1$ disc shows significantly less power in these low-order modes than the other models. *Right*: Time evolution of higher-order Fourier modes, A_m, in the three simulations: $q = 0.1$ (dotted), $q = 0.2$ (dashed) and disc + infall (solid). Here blue, red and black denote $m = 4, 5$ & 8 respectively. For these higher-order modes, the differences between the different models are much less pronounced than in figure on the left.

ral structures. It is also worth noting that the disc does not fragment, despite being subject to high rates of infall; instead it is able to transport angular momentum fast enough to prevent any "pile-up" of the infalling material.

In order to make a detailed comparison between the infall model and the isolated discs, it is first necessary to define the disc in the infall model (excluding envelope gas). We define the disc as all gas within 3 scale-heights of the midplane, with the scale-height computed as
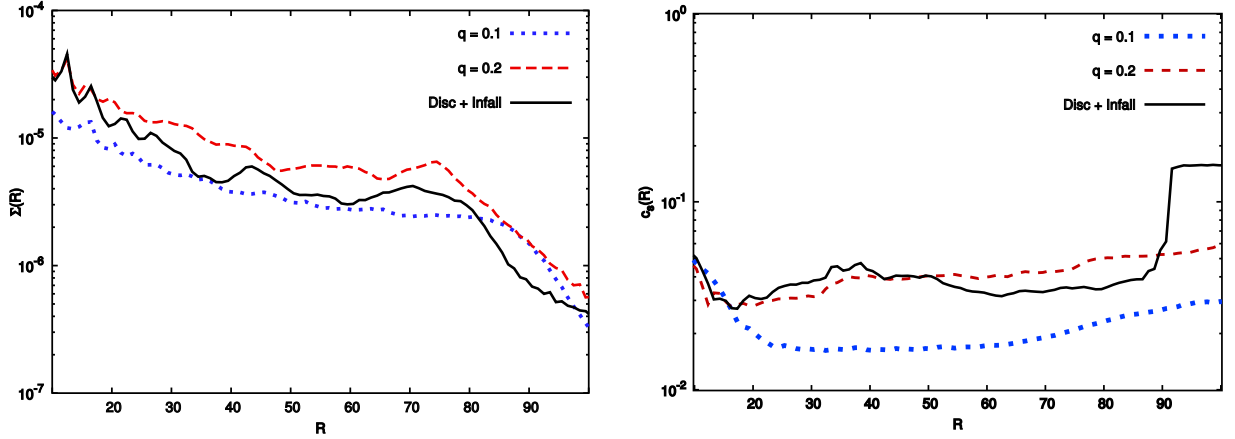
Figure 3.6 — Azimuthally-averaged radial profiles of surface density Σ (top) and sound speed c_s (bottom), plotted for all three simulations at $t = 3500$. In both cases the disc with infall lies between the $q = 0.1$ and $q = 0.2$ disc (except near the outer disc edge at $R = 100$), suggesting that disc mass and temperature are not the primary differences between these simulations.
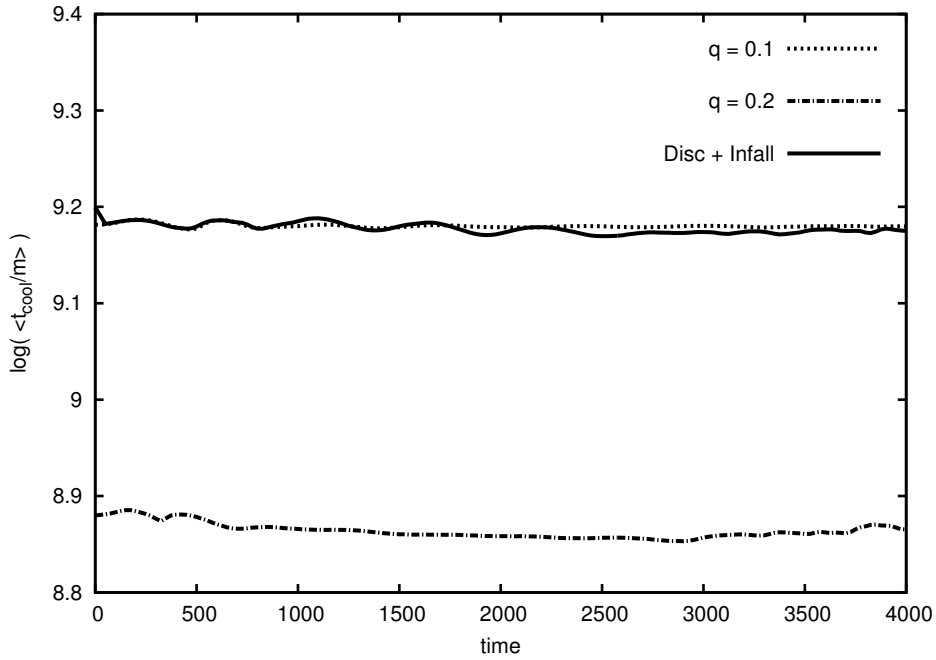

Figure 3.7 — Time evolution of the mass-weighted cooling time for the three different models, averaged over the radial range $R = 60$–80, plotted in arbitrary units (on a logarithmic scale). The infall model shows no significant differences with respect to the $q = 0.2$ disc, and differs only by a factor of $\simeq 2$ from the $q = 0.1$ disc, allowing us to rule out variations in the cooling time-scale as a factor in the enhanced GIs seen.

$H = c_s/\Omega$ at the midplane. Again we restrict our analysis to the region $20 \leq R \leq 80$, to prevent boundary effects from becoming dominant. The total mass in the disc at $R \leq 100$ at the end of the simulation is ($t = 5000$) is $0.14\ M_\star$, an increase of $0.04\ M_\star$ from the initial disc mass. The disc is also more radially extended than the isolated discs, with significant mass at $R > 100$ (and consequently higher temperatures at $R \gtrsim 90$). Fig.3.6 shows the azimuthally-averaged surface density and temperature (sound speed) profiles for all three models. Within the region
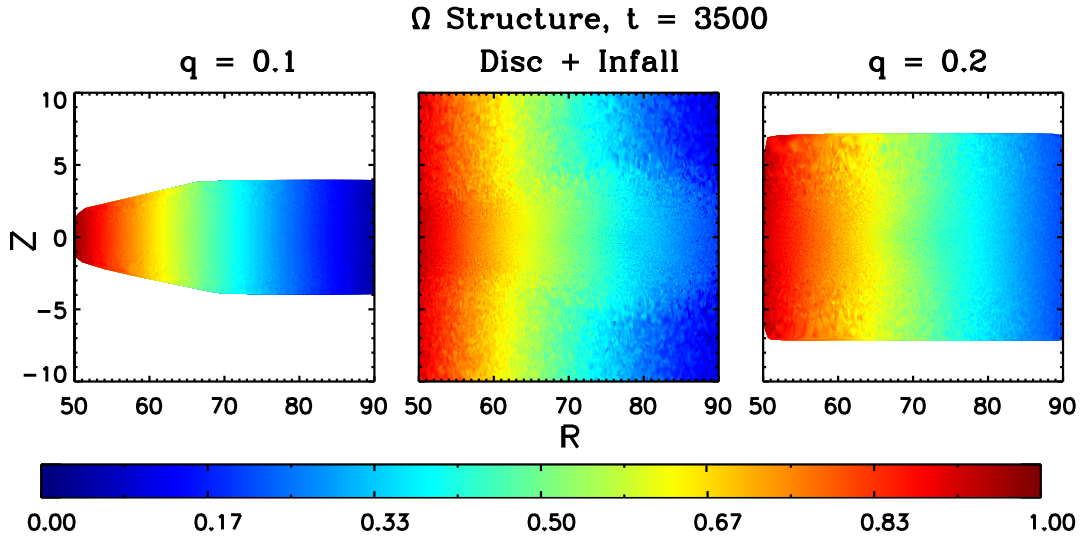
Figure 3.8 — Azimuthally-averaged $R - z$ projections of the orbital frequency $\Omega = v_\phi/R$ for the three different simulations, plotted at $t = 3500$. For clarity we have limited the plots to the radial range $R = 50$–90, and for the disc-only models plotted only the region within within $\pm 3H$ of the midplane. In each case the values of Ω are normalised to the maximum value (that at $R = 50$). The vertical shear caused by the sub-Keplerian infall is clearly visible in the middle panel.
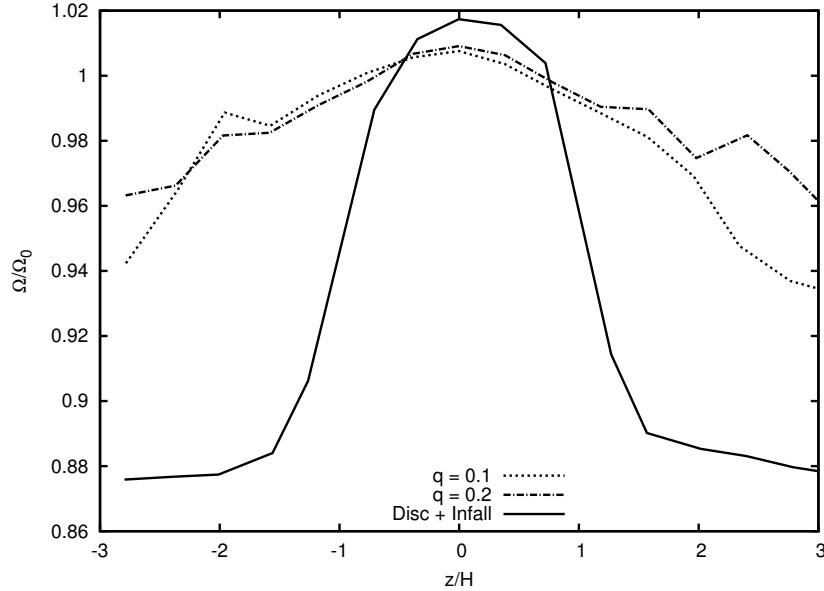

Figure 3.9 — Vertical profile of the orbital frequency $\Omega(z)$, azimuthally-averaged and normalised to the Keplerian orbital frequency Ω_0. The dotted and dashed lines denote the isolated discs ($q = 0.1$ and 0.2, respectively) while the solid line denotes the disc + infall. The upper layers of the disc in the infall model are strongly sub-Keplerian, due to the interaction with the (sub-Keplerian) infall.

$20 \leq R \leq 80$ the surface density of the infall model lies between those of the two isolated discs. At smaller radii the temperature of the infall model is similar to that of the $q = 0.2$ disc, while at larger radii it lies between those of the $q = 0.1$ and $q = 0.2$ discs. The fact that the surface

density in the infall model is lower than in the $q = 0.2$ disc rules out the $\simeq 40\%$ increase in disc mass as being responsible for the changes seen in the infall model. In addition, the mass-weighted cooling time-scales in the three models are very similar (see Fig.3.7), so we can rule out variations in the cooling time-scale as being responsible for difference between the disc-only simulations and the case with infall. Instead, we find that the presence of an infalling envelope qualitatively changes the behaviour of the disc, and excites deep low-order spiral density waves.

As seen in Fig.3.4, the infall model never reaches the self-regulated, $Q \simeq 1$ state seen in sim-ulations of isolated discs. Instead, we see strong departures from $Q \simeq 1$, which are primarily due to the substantial variations in the disc's surface density seen in Fig.3.6. The Fourier analy-sis shows that the low-m ($m = 1$–4) modes dominate the spiral structures, and despite the lower surface density the power spectrum of the disc with infall shows no clear differences from the $q = 0.2$ disc. This suggests that infall can drive global transport of angular momentum even in relatively thin discs.

We can gain some insight into the behaviour of the disc subject to infall by looking at the vertical rotation profile. Fig.3.8 shows a 2-D, azimuthally-averaged projection of the orbital frequency in the discs (at $t = 3500$), and Fig. 3.9 shows the orbital frequency as a function of vertical position in the discs $\Omega(z)$, at $R = 75$ (effectively a vertical cross section of Fig.3.8). In all three cases the midplane rotation is very close to Keplerian. As expected the isolated discs show nearly constant $\Omega(z)$; the slight fall-off at high z is primarily due to numerical effects, as the isolated disc models are not well-resolved for $|z| \gtrsim 2.5H$ (where there is little mass, and therefore few SPH particles). However, the model with infall shows strongly sub-Keplerian rotation away from the disc midplane: more than one scale-height away from the midplane, the rotation is sub-Keplerian by 5–10%. This occurs because infalling gas from the envelope is sub-Keplerian where it lands on the disc. This vertical velocity shear has the potential to excite deeper spiral density waves than occur in the isolated discs, and drives the low-order spiral waves (which have a sub-Keplerian pattern speed).

At this point it is instructive to consider the time-scales involved in both the GI and the vertical shearing. The unstable modes of a gravitationally unstable disc grow on the dynam-ical time-scale, so if the vertical velocity shear is to play a significant role in modifying the behaviour of the GI it must occur on a similar (or shorter) time-scale. We see from Fig.3.9 that in the presence of infall the disc surface layer is sub-Keplerian by approximately 10%. The velocity difference across this shear is therefore $\simeq 0.1\Omega R$, and the shearing time-scale $t_{\rm sh} \sim H/(0.1\Omega R) \sim (H/0.1R)t_{\rm dyn}$. In our disc $H/R \sim 0.1$, so the shearing time-scale is approx-imately equal to the dynamical time-scale. This argument suggests that shearing does occur on a sufficiently short time-scale to influence the growth of GIs significantly, and supports our argument that the vertical velocity shear is responsible for the strong global modes seen in our disc in the presence of infall. We note, however, that we cannot rule out the presence of other destabilising mechanisms also being present.

As mentioned above, we did not see any evidence for fragmentation with $\beta = 7.5$ even when the infall rate substantially exceeds the fragmentation threshold set by the local limit. It appears, therefore, that when subject to infall the disc instead undergoes global transport of angular momentum, with consequent enhancement of accretion. Unfortunately, although our simulations run for many dynamical periods their total duration is still relatively short compared to the ("viscous") time-scale for angular momentum transport. This makes deter-mining the rate of angular momentum transport somewhat difficult, as at any given time in the simulations transients can be dominant. Moreover, any transport by low-m spiral modes is intrinsically non-local (Balbus & Papaloizou 1999), so looking purely at the local stresses
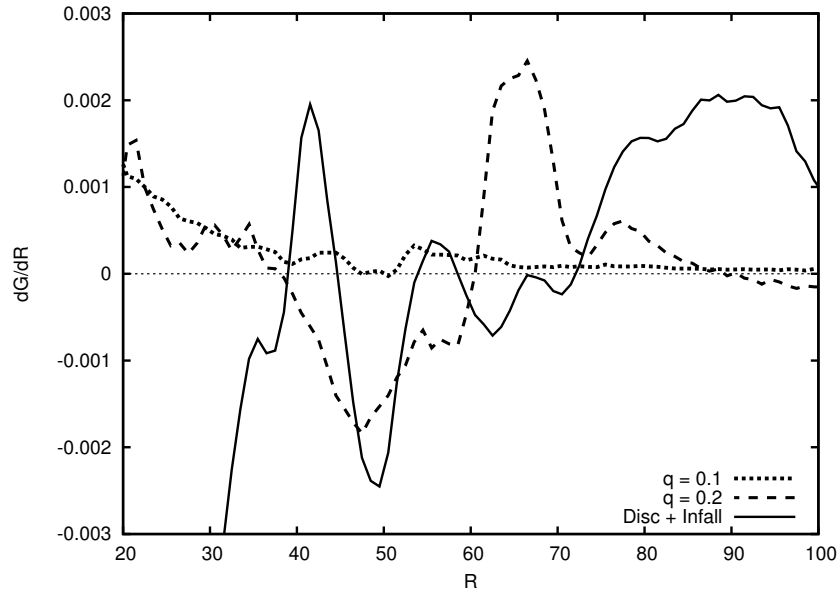
Figure 3.10 — Azimuthally-averaged profile of the gravitational torque in the discs, plotted at $t = 3500$, with line-styles as in Fig.3.9. The horizontal dotted line denotes $dG/dR = 0$; negative torques correspond to the removal of angular momentum (accretion). Unlike in the isolated discs, long-range gravitational torques dominate the angular momentum transport in the disc with infall.

(as in Lodato & Rice 2004) is not appropriate. Instead, we computed the differential gravitational torque dG/dR as a function of radius, as this should highlight any non-local angular momentum transport. The torque profiles from the three models are shown in Fig. 3.10. In the $q = 0.1$ disc the gravitational torques are small everywhere, with transport dominated by local stresses. Substantially larger gravitational torques are seen in the $q = 0.2$ disc, but the peaks in dG/dR correspond to individual spiral density waves and "cancel" over relatively small radial scales, and when averaged over many orbits. Moreover, the torques are negligible at large radii ($R \gtrsim 70$) in both isolated discs. By contrast we see strong torques throughout the disc subject to infall, primarily negative at small radii ($R \lesssim 60$) and positive at larger radii, which persist over several orbital periods. These torques are therefore transporting angular momentum outward through the disc on length-scales comparable to the disc radius. If the torques on the disc were solely due to the interaction with the envelope we would expect to see $dG/dR < 0$ at all radii, as the infall is sub-Keplerian. Instead we see both negative and positive torques at the midplane in different regions of the disc, which strongly suggests that global gravitational torques are the primary mechanism driving its evolution.

3.4 Discussion

3.4.1 Limitations

We have presented calculations on the effect of infall on to a gravitationally unstable accretion disc, but our approach is highly idealised. This approach allows us to study the key physical processes in detail, but imposes some limitations when we apply our results to real astrophysical situations.

Our first major simplification is in the initial conditions of our infall model. In order to ensure that we understand the various numerical effects in our calculations, we chose to let a rotating cloud fall on to an already-present disc, rather than letting the disc form self-consistently.

The advantages of our set-up are two-fold. First, we can control the accretion rate on to the disc, and ensure that the ratio between infall rate and theoretical accretion rate is approximately constant over the duration of our simulation (as seen in Fig.3.2). Second, we can compare our results directly to our isolated disc models, where the physics is well-understood, and thus isolate the effects of infall from the myriad of other potential effects. However, the trade-off is that the simulations are highly idealised, and not always realistic. In particular, we note that quasi-spherical infall is only expected in the early stages of protostellar collapse, when the disc and envelope masses are likely to be much larger than those considered here (e.g., Boley 2009; Vorobyov & Basu 2009). Our results have relevance to almost any case of infall on to a gravitationally unstable disc (as any infall is, by definition, sub-Keplerian), but we note that care be taken when applying our results to real systems.

Our second major simplification lies in our treatment of the disc thermodynamics. Our scale-free cooling law has previously been studied in great detail (Gammie 2001; Rice et al. 2003; Lodato & Rice 2004; Cossins et al. 2009), but it is recognised to be a poor approximation to real systems. The effect of our scale-free cooling law can be seen in Fig. 3.6: the disc temperature increases slightly with radius. Real discs almost invariably have cooling time-scales that are shorter (relative to the local dynamical time-scale) at large radii than at small radii, and are thus not scale-free (e.g., Rafikov 2007; Clarke 2009). A more realistic treatment would require an opacity-based cooling prescription (e.g., Boley et al. 2006; Stamatellos et al. 2007), but this would introduce several new free parameters to the problem. Again, our simplifications are not entirely physical in this regard, but do allow us to study the important processes in detail. Essentially we have chosen to perform a well-controlled numerical experiment instead of a physically realistic simulation, and our results should be interpreted with this in mind.

3.4.2   Comparison to Previous Work

The majority of previous work in this area has studied the transport properties of isolated gravitationally unstable discs (Laughlin & Bodenheimer 1994; Lodato & Rice 2004; Rice et al. 2005; Boley et al. 2006; Cossins et al. 2009). Our reference simulations exhibit the same behaviour as in these previous studies, as discussed in Section 3.3.1. However, the influence of infall on the evolution of GIs has not yet been explored in great detail. Krumholz et al. (2007) studied angular momentum transport in a self-consistently-formed disc subject to a very high rate of infall. They found very high accretion rates, equivalent to $\sim$30% of the total disc mass per dynamical time-scale, with effective α-values that exceeded unity. Most of the power was found in the $m = 1$ mode, and Krumholz et al. (2007) attributed this very rapid accretion to the SLING instability (Adams et al. 1989; Shu et al. 1990). We note, however, that the discs formed in these simulations were much more massive than those considered here, with $q \sim 0.5$–1. It has long been known that low-order spiral modes can drive rapid accretion in massive discs (e.g., Laughlin et al. 1998), and in this regards the results of Krumholz et al. (2007) are not directly comparable to those of our simulations.

In addition, a number of recent studies have used one- and two-dimensional simulations to study the formation and evolution of protostellar discs (e.g., Hueso & Guillot 2005; Vorobyov & Basu 2007, 2009; Vorobyov 2009; Visser & Dullemond 2010; Zhu et al. 2009, 2010). These simulations are less computationally intensive than 3-D simulations, and are therefore able to follow the evolution of the system for much longer time-scales. They also make use of more physically realistic prescriptions for both infall and thermodynamics, forming discs self-consistently from collapsing clouds and incorporating realistic models for radiative heating and cooling. These simulations generally predict that most of the GIs' power is found in low-order spiral modes, due to both infall and the relatively high masses of the discs which form.

In addition, many of these simulations have been seen to exhibit transient accretion outbursts, triggered in some cases by the accretion of bound clumps of gas (e.g., Vorobyov & Basu 2006, 2007) and in others by interaction between gravitational instability in the outer disc and layered accretion in the inner disc (e.g., Zhu et al. 2010). Unfortunately it is not straightforward to draw direct comparisons between these results and ours, due to the complex effects of both the cooling and infall prescriptions used. We note, however, that the vertical shear effect observed in our simulations is intrinsically a three-dimensional phenomenon, and consequently cannot be observed in 2-D, vertically-integrated simulations. Our results point towards an additional mechanism for driving transient transport of angular momentum, and lend further weight to the well-established idea that low-order spiral modes drive accretion in protostellar discs.

By contrast, to date only a handful of similar studies have been conducted in three dimensions. Most relevant here is the work of Boley (2009) and Kratter et al. (2010), who used three-dimensional hydrodynamics to study the formation and evolution of protostellar discs. Boley (2009) used grid-based hydrodynamics with a similar set-up to that considered here: prescribed infall on to an already-present disc. In some cases the discs fragmented, while in others angular momentum transport was dominated by low-order spiral density waves. We note, however, that the discs in the simulations of Boley (2009) are significantly more massive than ours ($q \sim 0.3$–0.5), increasing the importance of global modes. Given the additional differences between the simulations (most notably in the adopted cooling models) it is difficult to make direct comparisons, but in general our result – that infall on to the disc enhances the importance of global modes – seems consistent with those of Boley (2009).

By contrast, in the models of Kratter et al. (2010) discs form and evolve in a self-consistent manner, and they were able to explore a larger range in parameter space than we have achieved here. They found, as we do, that low-order spiral modes dominate the transport of angular momentum, although this again may in part be driven by the fact that their discs are somewhat more massive than ours. However, Kratter et al. (2010) found that infall rates of $\gtrsim 3$ times the disc accretion rate typically led to fragmentation, while we find that no fragmentation despite an infall rate nearly an order of magnitude higher than the "local limit" for disc accretion. Unfortunately it is not straightforward to compare these apparently contradictory results directly, due to the different prescriptions used for disc thermodynamics. Kratter et al. (2010) adopted an isothermal equation of state, and defined their models with two parameters (representing the accretion rate and angular momentum of the infalling gas). By contrast, we adopt an adiabatic equation of state with a parametrized cooling function, with the spherical envelope given a uniform initial temperature. The prescribed cooling time-scale is much longer than the dynamical time-scale (by a factor $\beta = 7.5$), so the infalling gas is effectively adiabatic. This results in slight heating of the infalling gas, and a corresponding increase in temperature in the disc. The increase in the disc temperature is not dramatic (see Fig.3.6), but given that the rate of spherical accretion scales as c_s^3 even this small difference could account for the factor of ~ 3 discrepancy between our results and those of Kratter et al. (2010). Additional simulations, using different initial cloud temperatures and cooling laws, are required to investigate this issue in more detail, but such simulations are beyond the scope of this paper. It is not clear whether the isothermal or adiabatic approximation is more relevant to real discs; most probably both have some validity in different regions of the disc. We thus regard our results as complementary to those of Kratter et al. (2010), and encourage further work in this area.

3.4.3 Applications to Observed Systems

Our results have obvious applications to the physics of star formation, in particular the formation of low-mass ($\sim 1\ M_\odot$) stars. Observations suggest that essentially all low-mass stars form

with discs (e.g., Haisch et al. 2001), and disc accretion is thought to play a major role in the build-up of stellar mass. Moreover, in the earliest, embedded phases gravitational instability is likely to be the dominant mechanism for angular momentum transport: such discs are insufficiently ionized to sustain transport via magnetohydrodyamic turbulence (Matsumoto & Tajima 1995; Gammie 1996), but both observations and theory suggest that they are indeed massive enough to be gravitationally unstable (e.g., Greaves et al. 2008; Andrews et al. 2009; Hueso & Guillot 2005; Vorobyov & Basu 2009). Our results argue that accretion in such discs is likely to be highly transient, and in general terms are consistent with a picture where the bulk of the stellar mass is accreted during a small number of intense outbursts (e.g., Armitage et al. 2001; Lodato & Rice 2005; Vorobyov & Basu 2006, 2010; Zhu et al. 2010).

The consequences of our results for massive star formation are less clear. Although discs are expected to form around massive, forming stars, observational evidence of their existence is somewhat thin (e.g., Cesaroni et al. 2006, 2007). It is clear, however, that if such discs do indeed exist they are likely to be gravitationally unstable, but in this scenario the maximum stable disc accretion rate ($\lesssim 10^{-5}$ $M_\odot$ yr^{-1}; Levin 2003; Cesaroni et al. 2006; Rafikov 2007) is much too low for these massive stars to accumulate their mass in a plausible time-scale. It has previously been suggested that the formation of massive stars is likely to be dominated by transient episodes and highly variable accretion (Cesaroni et al. 2007). Our results suggest that the global gravitational torques driven by infall on to the disc result in exactly this type of behaviour, and may be an important accretion mechanism in massive star formation.

In addition, we suggest that our results may have important consequences for the formation of massive stars close to super-massive black holes. A large population of massive O- and Wolf-Rayet-type stars is now known to exist within ~ 0.1 pc of the super-massive black hole (SMBH) at the centre of the Galaxy (Genzel et al. 2003; Ghez et al. 2005), and a popular scenario for the formation of these stars is "in situ" formation via the fragmentation of an accretion disc around the SMBH (Levin & Beloborodov 2003; Nayakshin 2006). This picture has a number of attractive features, but an open question has always been how the stars attain their final masses. Both analytic theory and numerical simulations suggest that the initial fragment masses are small, ~ 1 $M_\odot$, and that the bulk of the stellar mass is subsequently accreted from the SMBH disc (e.g., Alexander et al. 2008; Bonnell & Rice 2008). However, the estimated infall rates through the Hill sphere on to these protostellar discs are extremely high, $\sim 10^{-4}$ $M_\odot$yr^{-1} (Milosavljević & Loeb 2004), and in the local limit these discs are expected to fragment, preventing rapid growth of the protostars and limiting the resulting stellar masses (see also Matzner & Levin 2005; Kratter & Matzner 2006). Our results suggest that discs subject to high infall rates may instead be able to transport angular momentum much more rapidly, through global modes of the GI, and this mechanism provides a potential solution to the "accretion problem" of massive star formation at the centre of the Galaxy.

3.5   Summary

We have presented numerical simulations of gravitationally unstable accretion discs subject to infall from a surrounding envelope. Our numerical set-up is highly idealised, but this allows us to study the angular momentum transport properties of the system in detail. Our disc has a relatively slow cooling rate ($t_{\mathrm{cool}}\Omega = 7.5$), and we find that the disc does not fragment even though the infall rate on to the disc is an order of magnitude greater than the "quasi-steady" accretion rate in the self-regulating self-gravitating disc. Instead, despite relatively low disc masses ($M_{\mathrm{d}}/M_\star \simeq 0.14$), we see evidence that angular momentum is transported rapidly by torques from low-order, global, spiral density waves, which are excited by the interaction be-

tween the disc and the infalling envelope. This drives accretion at a rate significantly higher than is possible in a local model, and we suggest that this mechanism may play an important role in a number of different astrophysical systems.

Acknowledgements

Chapter 4

Evolution of CO lines in time-dependent models of protostellar disk formation

Abstract. *Context*. Star and planet formation theories predict an evolution in the density, temperature, and velocity structure as the envelope collapses and forms an accretion disk. While continuum emission can trace the dust evolution, spectrally resolved molecular lines are needed to determine the physical structure and collapse dynamics.

Aims. The aim of this work is to model the evolution of the molecular excitation, line profiles, and related observables during low-mass star formation. Specifically, the signatures of disks during the deeply embedded stage ($M_{env} > M_\star$) are investigated.

Methods. The semi-analytic 2D axisymmetric model of Visser and collaborators has been used to describe the evolution of the density, stellar mass, and luminosity from the pre-stellar to the T-Tauri phase. A full radiative transfer calculation is carried out to accurately determine the time-dependent dust temperatures. The time-dependent CO abundance is obtained from the adsorption and thermal desorption chemistry. Non-LTE near-IR, FIR, and submm lines of CO have been simulated at a number of time steps.

Results. In single dish (10–20″ beams), the dynamics during the collapse are best probed through highly excited ^{13}CO and C^{18}O lines, which are significantly broadened by the infall process. In contrast to the dust temperature, the CO excitation temperature derived from submm/FIR data does not vary during the protostellar evolution, consistent with C^{18}O observations obtained with *Herschel* and from ground-based telescopes. The near-IR spectra provide complementary information to the submm lines by probing not only the cold outer envelope but also the warm inner region. The near-IR high-J (≥ 8) absorption lines are particularly sensitive to the physical structure of the inner few AU, which does show evolution. The models indicate that observations of ^{13}CO and C^{18}O low-J submm lines within a $\leq 1''$ (at 140 pc) beam are well suited to probe embedded disks in Stage I ($M_{env} < M_\star$) sources, consistent with recent interferometric observations. High signal-to-noise ratio subarcsec resolution data with ALMA are needed to detect the presence of small rotationally supported disks during the Stage 0 phase and various diagnostics are discussed. The combination of spatially and spectrally resolved lines with ALMA and at near-IR is a powerful method to probe the inner envelope and disk formation process during the embedded phase.

D. Harsono, R. Visser, S. Bruderer, E. F. van Dishoeck, L. E. Kristensen

4.1 Introduction

THE semi-analytical model of the collapse of protostellar envelopes (Shu 1977; Cassen & Moosman 1981; Terebey et al. 1984) has been used extensively to study the evolution of gas and dust from core to disk and star (Young & Evans 2005; Dunham et al. 2010; Visser et al. 2009). Others have explored the effects of envelope and disk parameters representative of specific evolutionary stages on the spectral energy distribution (SED) and other diagnostics (Whitney et al. 2003a; Robitaille et al. 2006; Robitaille et al. 2007; Crapsi et al. 2008; Tobin

et al. 2011). These studies have focused primarily on the dust emission and its relation to the physical structure. On the other hand, spectroscopic observations toward young stellar objects (YSOs) performed by many ground-based (sub)millimeter and infrared telescopes also contain information on the gas structure (Evans 1999). The molecular lines are important in revealing the kinematical information of the collapsing envelope as well as the physical parameters of the gas based on the molecular excitation. The *Herschel* Space Observatory and the Atacama Large Millimeter/submillimeter Array (ALMA) provide new probes of the excitation and kinematics of the gas on smaller scales and up to higher temperatures than previously possible. It is therefore timely to simulate the predicted molecular excitation and line profiles within the standard picture of a collapsing envelope. The aim is to identify diagnostic signatures of the different physical components and stages and to provide a reference for studies of more complex collapse dynamics.

A problem that is very closely connected to the collapse of protostellar envelopes is the formation of accretion disks. The presence of embedded disks was inferred from the excess of continuum emission at the smallest spatial scales through interferometric observations (eg. Keene & Masson 1990; Brown et al. 2000; Jørgensen et al. 2005a, 2009). Their physical structure can be determined by the combined modeling of the SED and the interferometric observations (Jørgensen et al. 2005a; Brinch et al. 2007b; Enoch et al. 2009). However, the excess continuum emission at small scales can also be due to other effects of a (magnetized) collapsing rotating envelope (pseudo-disk, Chiang et al. 2008). Therefore, resolved molecular line observations from interferometers such as ALMA are needed to clearly detect the presence or absence of a stable rotating embedded disk (Brinch et al. 2007b, 2008; Lommen et al. 2008; Jørgensen et al. 2009; Tobin et al. 2012).

A number of previous studies have modeled the line profiles based on the spherically symmetry inside-out collapse scenario described by Shu (1977) (eg., Zhou et al. 1993; Hogerheijde & Sandell 2000; Hogerheijde 2001; Lee et al. 2003, 2005; Evans et al. 2005). Also, numerical hydrodynamical collapse models have been coupled with chemistry and line radiative transfer to study the molecular line evolution in 1D (Aikawa et al. 2008) and 2D (Brinch et al. 2007b; van Weeren et al. 2009). Best-fit collapse parameters (e.g., sound speed and age) are obtained but depend on the temperature structure and abundance profile of the model. Visser et al. (2009) and Visser & Dullemond (2010) developed 2D semi-analytical models that describe the density and velocity structure as matter moves onto and through the forming disk. This model has been coupled with chemistry (Visser et al. 2009, 2011), but no line profiles have yet been simulated. The current paper presents the first study of the CO molecular line evolution within 2D disk formation models. CO and its isotopologs are chosen because it is a chemically stable molecule and readily observed.

Observationally, most early studies of low-mass embedded YSOs focused on the low$-J$ ($J_u \leq 6$) (sub-)millimeter CO lines in 20–30$''$ beams, thus probing scales of a few thousand AU in the nearest star-forming regions (e.g., Belloche et al. 2002; Jørgensen et al. 2002; Lee et al. 2003; Young et al. 2004; Crapsi et al. 2005). More recently, ground-based high-frequency observations of large samples up to $J_u=7$ are becoming routinely available (Hogerheijde et al. 1998; van Kempen et al. 2009b,a,d) and *Herschel*-HIFI (de Graauw et al. 2010) has opened up spectrally resolved observations of CO and its isotopologs up to $J_u = 16$ ($E_u = 660$ K) (Yıldız et al. 2010, 2012). In addition, the PACS (Poglitsch et al. 2010) and SPIRE (Griffin et al. 2010) instruments provide spectrally unresolved CO data from $J_u = 4$ to $J_u = 50$ ($E_u = 55 - 7300$ K), revealing multiple temperature components (e.g., van Kempen et al. 2010; Herczeg et al. 2012; Goicoechea et al. 2012; Manoj et al. 2013). Although the interpretation of the higher J_u lines requires additional physical processes than those considered here (Visser et al. 2012), our
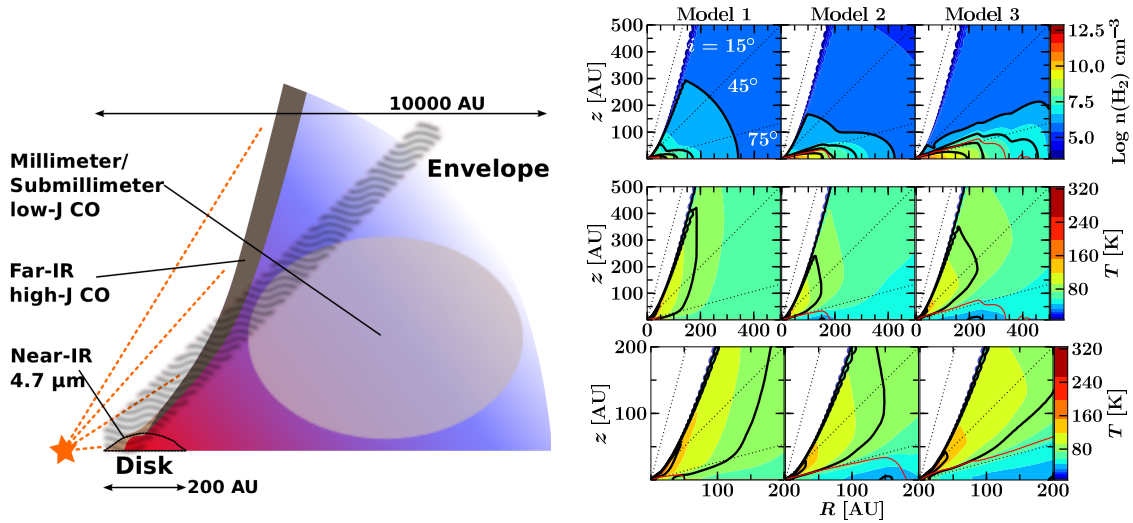
Figure 4.1 — *Left*: Sketch of one quadrant of an embedded protostellar system with a disk and envelope. The FIR/millimeter/submillimeter emission comes from the envelope and outflow cavity walls. On the other hand, the NIR absorption (gray shaded region) also probes the warm region close to the star through a pencil beam, illustrating the complementarity of the techniques. The dotted orange lines indicate the stellar light. *Right*: Final disk structure for the three models from Table 6.1 at $t = t_{acc}$. *Right top*: gas density in the inner 500 AU. The solid line contours mark densities of $10^{6,7,8,9}$ cm^{-3}. *Right middle*: temperature structure in the inner 500 AU. The temperature contours are logarithmically spaced from 10 to 320 K. The 20, 50 and 100 K isotherms are marked by the solid line contours. *Right bottom*: temperature structure in the inner 200 AU. In all panels, the dotted lines illustrate the lines of sight at inclinations of 15°, 45° and 75° and the red line indicates the final disk surface.

models provide a reference frame within which to analyze the lower-J lines.

Complementary information on the CO excitation is obtained from near-IR (NIR) observations of the 4.7 μm fundamental CO (v=1–0) band seen in absorption toward YSOs. Because the absorption probes a pencil beam line of sight toward the central source, the lines are more sensitive to the inner dense part of the envelope than the submillimeter emission line data, which are dominated by the outer envelope (see Fig. 4.1). The NIR data generally reveal a cold (< 30 K) and a warm (> 90 K) component (Mitchell et al. 1990; Boogert et al. 2002; Brittain et al. 2005; Smith et al. 2009; Herczeg et al. 2011). The cold component is seen toward all YSOs in all of the isotopolog absorptions. However, the warm temperature varies from source to source. The question is whether the standard picture of collapse and disk formation can also reproduce these multiple temperature components.

A description of the physical models and methods is given in Section 6.2. The evolution of the molecular excitation and the resulting far-infrared (FIR) to submm lines of the pure rotational transitions of CO is discussed in Section 4.3, whereas the NIR ro-vibrational transitions is presented in Section 4.4. The implication of the results and whether embedded disks can be observed during Stage 0 is discussed in Section 6.4. The results and conclusions are summarized in Section 6.5.

4.2   Method

4.2.1   Physical structure

The two-dimensional axisymmetric model of Visser et al. (2009), Visser & Dullemond (2010) and Visser et al. (2011) was used to simulate the collapse of a rotating isothermal spherical envelope into a pre-main sequence star with a circumstellar disk. The model is based on the ana-

Table 4.1 — Parameters used for the three different evolutionary models.

Model	Ω_0 [Hz]	c_s [km s^{-1}]	r_{env} [AU]	t_{acc} [10^5 yr]	M_d [$M_\odot$]	$R_{\mathrm{d,out}}$ [AU]
1	10^{-14}	0.26	6700	2.5	0.1	50
2	10^{-14}	0.19	12000	6.3	0.2	180
3	10^{-13}	0.26	6700	2.5	0.4	325

lytical collapse solutions of Shu (1977,hereafter S77), Cassen & Moosman (1981,hereafter CM81) and Terebey et al. (1984,hereafter TSC84). The formation and evolution of the disk follow according to the α_S viscosity prescription, which includes conservation of angular momentum (Shakura & Sunyaev 1973; Lynden-Bell & Pringle 1974). The dust temperature structure (T_{dust}) is a key quantity for the chemical evolution, so it is calculated through full 3D continuum radiative transfer with RADMC3D[1], considering the protostellar luminosity as the only heating source. The gas temperature is set equal to the dust temperature, which has been found to be a good assumption for submm molecular lines (Doty et al. 2002; Doty et al. 2004).

The model is modified slightly in order to be consistent with observational constraints. The density at $r = 1000$ AU (n_{1000}) should be at most 10^6 cm^{-3} for envelopes around low-mass YSOs (Jørgensen et al. 2002; Kristensen et al. 2012), but the interpolation scheme of Visser et al. (2009) violated that criterion. To correct this, the CM81 and TSC84 solutions are connected in terms of the dimension-less variable $\tau = \Omega_0 t$ by interpolating between $100\tau^2$ and $10\tau^2$ for $\Omega_0 = 10^{-13}$ Hz and between $100\tau^2$ and τ^2 for $\Omega_0 = 10^{-14}$ Hz, where Ω_0 is the envelope's initial solid body rotation rate. The overall collapse, the structure of the disk and the chemical evolution are unaffected by this modification. The models evolve until one accretion time, $t_{\mathrm{acc}} = M_0/\dot{M}$ where $\dot{M} \propto c_s^3/G$ with c_s the initial effective sound speed of the envelope, which is tabulated in Table 6.1.

Three different sets of initial conditions are used in this work (Table 6.1), which are a subset of the conditions explored by Visser et al. (2009) and Visser & Dullemond (2010). Each model begins with a 1 $M_\odot$ envelope. The two variables Ω_0 and c_s affect the final disk structure and mass. Model 1 ($c_s = 0.26$ km s^{-1}, $\Omega_0 = 10^{-14}$ Hz) produces a disk with a final mass ($t/t_{\mathrm{acc}} = 1$) of 0.1 $M_\odot$ and a final radius of 50 AU. Changing Ω_0 to 10^{-13} Hz (Model 3) yields the most massive and largest of the three disks (0.4 $M_\odot$, 325 AU). Starting with a lower sound speed of 0.19 km s^{-1} (Model 2) produces a disk of intermediate mass and size (0.2 $M_\odot$, 180 AU). The initial conditions also affect the flattened inner envelope structure. In Model 3, the flattening of the inner envelope extends to > 300 AU by $t/t_{\mathrm{acc}} = 0.5$ and extends up to ~ 1000 AU by the end of the accretion phase. In the other two models, the extent of the flattening is similar to the extent of the disk, with Model 2 showing more flattening in the inner envelope than Model 1. The different evolutionary stages are characterized by the relative masses in the different components (Robitaille et al. 2006): $M_{\mathrm{env}} >> M_\star$ (Stage 0, $t/t_{\mathrm{acc}} \leq 0.5$), $M_{\mathrm{env}} < M_\star$ but $M_{\mathrm{env}} > M_{\mathrm{disk}}$ (Stage 1, $t/t_{\mathrm{acc}} > 0.5$) and $M_{\mathrm{env}} < M_{\mathrm{disk}}$ (Stage 2) (see Appendix B).

Our main purpose is to investigate how the molecular lines evolve during different disk formation scenarios (Stage 0/I). Hence, the parameters were chosen to explore the formation of three different disk structures. Figure 4.1 zooms in on the final disk structures for the different models at the accretion time ($t = t_{\mathrm{acc}}$) where the red lines outline the disk surfaces. The angular velocities within these lines are assumed to be Keplerian while regions outside these lines are described by the analytical collapsing rotating envelope solutions (Visser et al. 2009).

---

[1]www.ita.uni-heidelberg.de/~dullemond/software/radmc-3d

The density structure is 2D axisymmetric with a 3D velocity field within the envelope and the disk.

4.2.2 CO abundance

The ^{12}CO abundance is obtained through the adsorption and thermal desorption chemistry as described in Section 2.7 of Visser et al. (2009). The main difference is that we have used both the forward and backward methods (Visser et al. 2011) to sample the trajectories through the disk and envelope. The chemistry is still solved in the forward direction.

CO completely freezes out at $T_d \leq 18$ K (Visser et al. 2009). For the majority of the time steps used for the molecular line simulations, the dust temperature is well above 18 K everywhere except for the outer envelope beyond $\sim$4000 AU. However, due to the low densities within this region, CO is still predominantly in the gas phase. Only at early time steps, early Stage 0, a large fraction of CO is frozen out within the inner envelope. Constant isotope ratios of ^{12}C/^{13}C = 70 and ^{16}O/^{18}O = 540 (Wilson & Rood 1994) are used throughout the model to compute the abundances of ^{13}CO and C^{18}O.

4.2.3 Line radiative transfer

A fast and accurate multi-dimensional molecular excitation and radiative transfer code is needed to obtain observables at a number of time steps. We use the escape probability method from Bruderer et al. (2012) (based on Takahashi et al. 1983 and Bruderer et al. 2010).

The most important aspect of simulating the rotational lines is the gridding of the physical structure. There are three components in the model that require proper gridding (Fig. 4.11): the outflow cavity, the envelope (> 6000 AU) and the disk (< 300 AU). To resolve the steep gradients between the different regions, $15\,000 - 25\,000$ cells are used. A detailed description of the grid can be found in Appendix 4.A. The line images are rendered at a number of time steps with a resolution of 0.1 km s^{-1} to resolve the dynamics of the collapsing envelope and the rotating disk.

In addition to pure rotational lines in the submm and FIR, this work also explores the evolution of the NIR fundamental v=1–0 rovibrational absorption of CO at 4.7 μm. RADLite is used to render the large number of NIR ro-vibrational spectra (Pontoppidan et al. 2009). This is done by assuming that all molecules are in the vibrational ground state given by the non-LTE calculation described above. The assumption is valid considering that the observed NIR emission lines by Herczeg et al. (2011) are blue-shifted by a few km s^{-1} and have broader line widths than that expected from $T_{gas} = T_{dust}$ that is being presented here. The observed emission toward the YSOs seem to originate from additional physics that are not present in our models. Thus, for the models presented here, it is valid to consider that the emission component from the inner region is negligible.

The main collisional partners are p-H$_2$ and o-H$_2$ with the collisional rate coefficients obtained from the LAMDA database (Schöier et al. 2005; Yang et al. 2010). The dust opacities used in our model are a distribution of silicates and graphite grains covered by ice mantles (Crapsi et al. 2008). Finally, the gas-to-dust mass ratio is set to 100.

4.2.4 Comparing to observations

The molecular lines are simulated considering a source at a distance of 140 pc. High spatial resolution in raytracing is needed for the $J_u \geq 5$ lines because of the small warm emitting region. A constant turbulent width of $b = 0.8$ km s^{-1} is used in addition to the temperature and

infall broadening to be consistent with the observed $C^{18}O$ turbulent widths toward quiescent gas surrounding low-mass YSOs with beams $> 9''$ (Jørgensen et al. 2002).

The simulated spectral cubes are convolved with Gaussian beams of $1''$, $9''$ and $20''$ with the *convol* routine in the *MIRIAD* data reduction package (Sault et al. 1995). The telescopes that observe the low-*J* rotational lines ($J_u \leq 5$) typically have $\geq 15''$ beams, as does *Herschel*-HIFI for the higher-*J* lines with $J_u \approx 10$. A $9''$ beam is appropriate for observations of $J_u > 5$ performed with, e.g., the ground-based APEX telescope at 650 GHz and with *Herschel*-PACS and HIFI for $J_u > 14$. A $1''$ beam simulates interferometric observations to be performed with ALMA. The submm lines are rendered nearly face-on ($i \sim 5°$) since this is the simplest geometry to quantify the disk contribution. For studies of the evolution of the velocity field, an inclination of $45°$ is taken. The NIR lines are analyzed for $45°$ and $75°$ inclination to study the different excitation conditions between lines of sight through the inner envelope and the disk (Fig. 4.1). A line of sight of $45°$ probes the inner envelope and does not go through the disk while a line of sight of $75°$ grazes the top layers of the disk. Both a pencil beam approximation toward the center is taken as well as the full RADLite simulation to study the radiative transfer effects on those lines.

4.2.5 Caveats

The synthetic CO spectra were simulated without the presence of fore- and background material, such as the diffuse gas of the large-scale cloud where these YSOs are forming. The overall emission of the large-scale cloud can affect the observed line profiles within a large beam ($> 15''$), in particular the $J_u \leq 4$ lines of ^{12}CO and ^{13}CO and the $J_u \leq 2$ lines of $C^{18}O$. Also not included in the simulations are energetic components such as jets, shocks, UV heating and winds. These energetics strongly affect the ^{12}CO lines, especially the intensity of the $J_u \geq 6$ rotational transitions (Spaans et al. 1995; van Kempen et al. 2009b; Visser et al. 2012). Luminosity flares associated with episodic accretion events can affect the CO abundance structure as discussed in Visser & Bergin (2012). Their effect on the evolution of the CO line profile and excitation is beyond the scope of this paper. In general, a higher CO flux is expected during an accretion burst.

4.3 FIR and submm CO evolution

The FIR and submm CO lines up to the $10 - 9$ transition (E_u = 290–304 K) have been simulated with i=5°. The geometrical effects on the line intensities (^{13}CO and $C^{18}O$) are less than 30% for different inclinations and the derived excitation temperatures differ by less than 5%, which is smaller than the *rms* error on the derived temperatures. On the other hand, inclination strongly affects the derived moment maps and interpretation of the velocity field, therefore an inclination of $45°$ is used in Section 4.3.4.

4.3.1 Line profiles

The first time step used for the molecular line simulation is at $t = 1000$ years ($t/t_{acc} \sim 10^{-3}$), where the central heating is not yet turned on. The evolution of the mass and the effective temperature is shown in the Appendix 4.B. The effective temperature during this time step is 10 K and the models are still spherically symmetric. The TSC84 velocity profile for this time step reaches a maximum radial component of 10 km s^{-1} at 0.1 AU. However, CO is frozen out in the inner envelope, so the FIR and submm lines (populated up to $J_u \leq 8$) show neither wing emission nor blue asymmetry as typical signposts of an infalling envelope. Instead, the CO
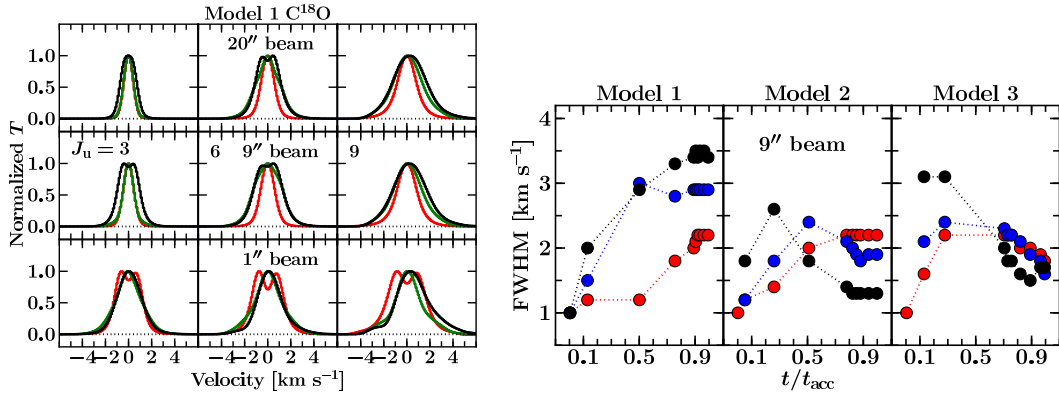
Figure 4.2 — *Left*: Normalized $C^{18}O$ line profiles as functions of evolution for $J_u = 3, 6$ and 9 at $t/t_{acc} = 0.13$ (red), 0.50 (green) and 0.96 (black) for $i = 5°$ orientation for Model 1. The lines are convolved to beams of 20″ (top), 9″ (middle) and 1″ (bottom). *Right*: ceo 3-2 (red), 6-5 (blue) and 9-8 (black) FWHM evolution within a 9″ beam for the 3 different models at $i = 5°$ orientation.

lines probe the static outer envelope at this point, where the low density has prevented CO from freezing out.

The line profiles change shape once the effective source temperature increases to above a few thousand K at $t > 10^4$ yr (see Fig. 4.2 and Appendix 4.B for the line profile evolution). The line profiles become more asymmetric (Fig. 4.12) toward higher excitation and smaller beams, because in both cases a larger contribution from warm, infalling gas in the inner envelope and optical depth affect the emission lines. The line widths are due to a combination of thermal broadening, turbulent width and velocity structure, but examination of models without a systematic velocity field confirm that the increase in broadening is mostly due to infall (see also Lee et al. 2003). Models 2 and 3 show narrower lines during Stage I ($t/t_{acc} \geq 0.5$) since they are relatively more rotationally dominated than in Model 1. As shown in Fig. 4.2, the higher-J ($J_u \geq 5$) lines are broadened significantly during Stage 0.
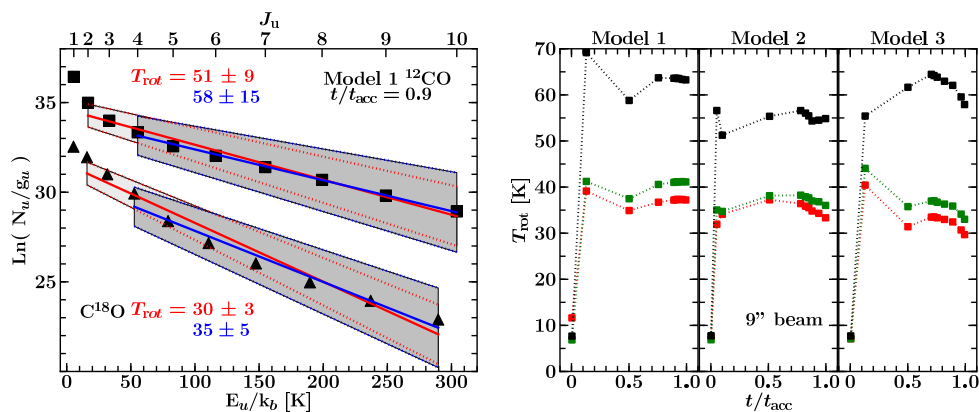

Figure 4.3 — *Left*: Examples of single-temperature fits through the ^{12}CO (squares) and $C^{18}O$ (triangles) lines obtained from Model 1 fluxes at $t/t_{acc} = 0.9$ in a 9″ beam. The red line shows the linear fit from $J_u = 2$ up to $J_u = 10$ while the blue line is the fit up starting from $J_u = 4$ up to $J_u = 10$. The gray shaded regions indicate one standard deviation from the best fit. *Right*: Evolution of the rotational temperature (T_{rot}) from a single-temperature fit through $J_u = 2 - 10$. The different colors are for different isotopologs: ^{12}CO (black), ^{13}CO (green) and $C^{18}O$ (blue). The typical errors are 15, 5 and 3 K for ^{12}CO, ^{13}CO and $C^{18}O$, respectively. The different panels show the results for different models as indicated.

The line profiles in a $1''$ beam depend strongly on the velocity field on small scales and show more structure than the line profiles in the larger beams (Figs. 4.2 and 4.14). The lines in a $1''$ beam are broader and show multiple velocity components (in particular for ^{12}CO and ^{13}CO) reflecting the complex dynamics due to infall and rotation plus the effects of optical depth and high angular resolution. A combination of CO isotopolog lines can provide a powerful diagnostic of the velocity and density structure on $10 - 1000$ AU scales (see also §3.4).

In summary, the infalling gas can significantly broaden the optically thin gas as shown in Fig. 4.2. The velocity profile in the inner envelope affects the broadening of the high-J ($J_{\rm u} > 6$) line. These lines can be a powerful diagnostic of the velocity and density structure in the inner 1000 AU ($\leq 9''$ beams).

4.3.2 CO rotational temperature

The observed integrated intensities (K km s^{-1}) are commonly analyzed by constructing a Boltzmann diagram and calculating the associated rotational temperature. Another useful representation is to plot the integrated flux ($\int F_\nu d\nu$ in W m^{-2}) as a function of upper level rotational quantum number (spectral line energy distribution or SLED) to determine the J level at which the peak of the molecular emission occurs. The conversion between integrated intensities and integrated flux is given by

$$\int F_\nu d\nu = \frac{2k}{\lambda^3} d\Omega \int T_v dv. \tag{4.1}$$

Examples of single-temperature fits through the modeled lines are shown in Fig. 4.3 for Model 1. Observationally, temperatures are generally measured from $J_{\rm u} = 2$ to 10 (Yıldız et al. 2012, 2013) and from 4 to 10 (Goicoechea et al. 2012). The evolution of the rotational temperatures within a $9''$ beam is shown in Fig. 4.3 for the three models. At very early times, $t/t_{\rm acc} < 0.1$, a single excitation temperature of ~ 8–12 K characterizes the CO Boltzmann diagrams. After the central source turns on, the excitation temperature is nearly constant with time. In a beam of $9''$, most of the flux up to $J_{\rm u} = 10$ comes from the > 100 AU region, which is not necessarily the > 100 K gas (Yıldız et al. 2010) even for face-on orientation. Therefore, within $\geq 9''$ beams, the observed emission is not sensitive to the warming up of material as the system evolves.

A value of 46 to 65 K characterizes the ^{12}CO distribution for all models. However, ^{12}CO is optically thick, which drives the temperature to higher values due to under-estimated low-J column densities. The C^{18}O and ^{13}CO distributions are fitted with similar excitation temperatures between 29 and 42 K within a $9''$ beam. Because Model 3 has a higher inner envelope density, the derived rotational temperature at the second time step is relatively high ($\gtrsim 40$ K) due to an optical depth effect.

The integrated fluxes can also be used to construct CO SLEDs. The ^{12}CO SLED peaks at $J_{\rm u} = 6 - 8$ with small dependence on the heating luminosity (Fig. 4.4). The peak of the SLED *does not* depend on the beam size for beams $\geq 9''$. The same applies to the ^{13}CO and C^{18}O SLEDs which peak at $J_{\rm u} = 4 - 5$. There is no significant observable evolution in the SLEDs once the star is turned on. A passively heated system is characterized by such SLEDs regardless of the evolutionary state as long as the heating luminosity is $\sim 1 - 10\ L_\odot$ ($T_\star \sim 1000$–4500 K).

The picture within a $1''$ beam is different since it resolves the inner envelope. The best-fit single temperature component depends on whether or not the disk fills a significant fraction of the beam. If it does (Models 2 and 3), the C^{18}O and ^{13}CO rotational temperatures are ~ 40–50 K. There is less spread than within the $9''$ beam due to the higher densities bringing the excitation closer to LTE. Without a significant disk contribution in a $1''$ beam (Model 1), the ^{13}CO excitation temperature is closer to 60 K while that of C^{18}O is similar to the other models
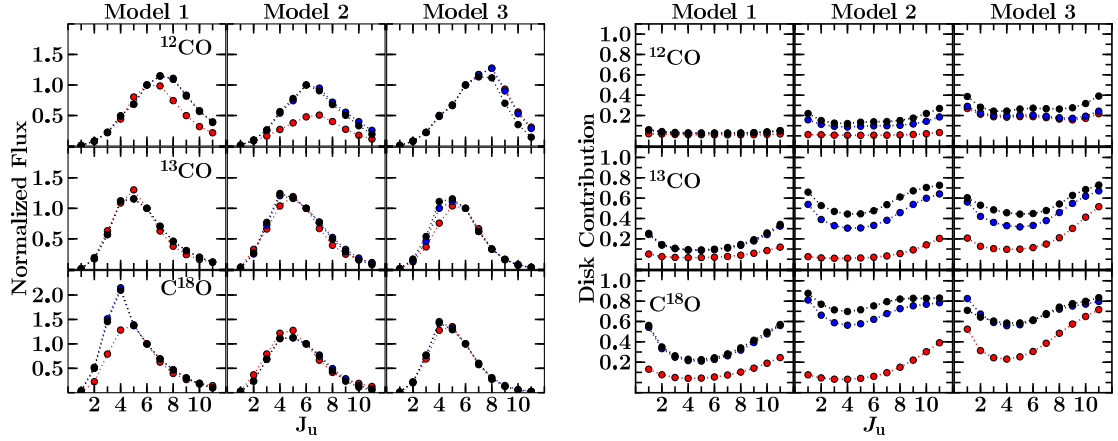
Figure 4.4 — *Left*: Evolution of normalized CO spectral line energy distribution (SLED) in a $9''$ beam. The CO integrated fluxes (W m^{-2}) are normalized to $J_{\mathrm{u}} = 6$. The different colors indicate different times: $t/t_{\mathrm{acc}} \sim 0.50$ (red), 0.75 (blue), 0.96 (black). *Right*: Disk contribution as a function of J_{u} within $1''$ (140 AU at 140 pc) for the three different models. The different colors correspond to different evolutionary stages: $t/t_{\mathrm{acc}} \sim 0.50$ (red, $M_{\mathrm{env}}/M_{\mathrm{disk}} \geq 3$), 0.75 (blue, $M_{\mathrm{env}}/M_{\mathrm{disk}} \sim 1$), 0.96 (black, $M_{\mathrm{env}}/M_{\mathrm{disk}} < 1$).

at ~ 40 K. The ^{12}CO rotational temperature is $T_{\mathrm{rot}} \simeq 70$ K in all of the models. Furthermore, the CO SLED within a $1''$ beam peaks at $J_{\mathrm{u}} = 6, 8$ and 10 for C^{18}O, ^{13}CO and ^{12}CO, respectively.

A comparison with the sample presented in Yıldız et al. (2013) indicates that the lack of T_{rot} evolution is consistent with observations, and our predicted values for T_{rot} match the data. On the other hand, the observed ^{13}CO T_{rot} and SLED are generally higher than predicted, which suggests an additional heating component is needed to excite the ^{13}CO lines. A more detailed comparison between model prediction and observation can be found in Yıldız et al. (2013).

In summary, both rotational temperatures derived from Boltzmann diagrams and CO SLEDs of passively heated systems do not evolve with time once the star is turned on. Optically thin ^{13}CO and C^{18}O lines are characterized by single excitation temperatures of the order 30–40 K within a wide range of beams ($\geq 9''$). The CO SLED peaks at $J_{\mathrm{u}} = 7 \pm 1$ and $J_{\mathrm{u}} = 4 - 5$ for ^{12}CO and other isotopologs, respectively. In $1''$ beam, the peak of the SLED shifts upward by $\sim 2\,J$ levels and a warmer rotational temperature by 10 K in the presence of a disk.

4.3.3 Disk contribution to line fluxes

After deriving a number of observables, an important question is, what the fraction of the flux contributed by the disk is? This contribution can be calculated from the averaged (over line profile and direction) escape probability of the line emission η_{ul}, which is the probability that a photon escapes both the dust and line absorption (Takahashi et al. 1983; Bruderer et al. 2012). The escape probabilities are used to calculate the cooling rate, $\Gamma_{\mathrm{cool},\nu}$, of each computational cell and each transition with the following formula

$$\Gamma_{\mathrm{cool},\nu} = \frac{V}{4\pi} h\nu_{\mathrm{ul}} A_{\mathrm{ul}} n x_{\mathrm{u}} \eta_{\mathrm{ul}}, \tag{4.2}$$

where ν_{ul} is the frequency of the line, A_{ul} is the Einstein A coefficient, x_{u} is the normalized population level and n is the density of the molecule. The disk contribution is then the ratio of the sum of cooling rates from the cells in the disk compared to the cells within a Gaussian beam. The cooling rates are weighted with a Gaussian beam of size $9''$ or $1''$ while the disk emitting region is defined as shown in Fig. 4.1. The flux is then given through an integration
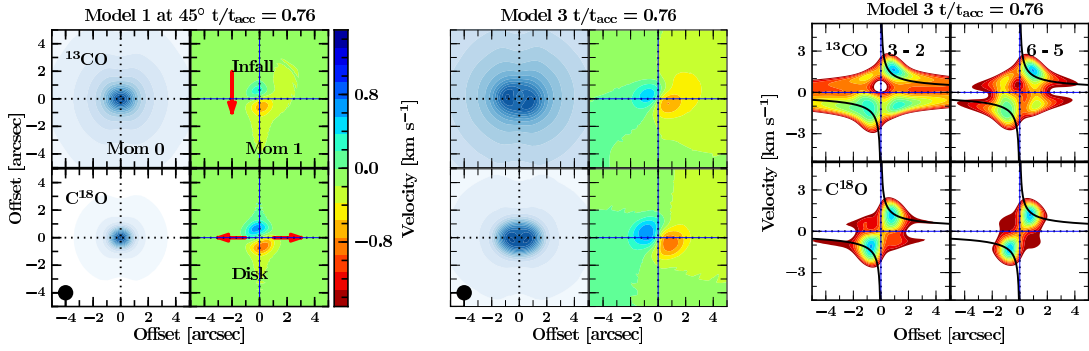
Figure 4.5 — *Left and middle*: ^{13}CO and $C^{18}O$ zeroth (left panels) and first (middle panels) moment maps for Model 1 and 3 at $45°$ inclination at a resolution of $1''$. The red arrows indicate the direction of infall and rotationally supported disk. The velocity scale is given on the right-hand side of the left figure. *Right*: Position-velocity slice for the ^{13}CO and $C^{18}O$ $J_u = 3$ and $J_u = 6$ transitions along the major axis of the zeroth moment map. The solid black lines are the Keplerian velocity structure calculated from the stellar mass.

of line of sight, $F_\nu = \int \Gamma_{cool,\nu} ds_{LOS}$, which translates into the same constant factor in both disk and total fluxes.

For a single-dish $9''$ beam, one needs to go to higher rotational transitions with $J_u > 6$ at later stages to obtain a $> 50\%$ disk contribution, if the disk can be detected at all (Fig. 4.13). The disk is difficult to observe directly in ^{12}CO and ^{13}CO emission since the lines quickly become optically thick unless lines with $J_u > 10$ are observed. A larger disk contribution is seen in the optically thin $C^{18}O$ lines, but here the low absolute flux may become prohibitive.

For example, the expected $C^{18}O$ disk fluxes for $J_u > 14$ within the PACS wavelength range are $\leq 10^{-20}$ W m^{-2} which will take > 100 hours to detect with PACS. *Herschel*-HIFI is able to spectrally resolved the $C^{18}O$ $J_u = 10$ and 9 lines but has a $\sim 20''$ beam, which lowers the disk fraction by a factor of 2 relative to a $9''$ beam. Peak temperatures of only 1–8 mK during Stage 0 and 2–12 mK in Stage I phase are expected, which are readily overwhelmed by the envelope emission. The spectrally resolved $C^{18}O$ spectra observed with HIFI indeed do not show any sign of disk emission, consistent with our predictions (San Jose-Garcia et al. 2013; Yıldız et al. 2012, 2013).

A more interesting result is the disk contribution to the CO lines within a $1''$ (140 AU) region as shown in Fig. 4.4. The simulations suggest a significant disk contribution ($> 50\%$) for the ^{13}CO and $C^{18}O$ lines within this scale, even for the $J = 1 - 0$ transition. For Model 3, the high disk contribution is expected to happen before the system enters Stage 1 ($M_{env} \leq M_\star$): a significant disk contribution is seen even at $t/t_{acc} = 0.3$. However, Model 2 shows a significant disk contribution only in the second half of the accretion phase. Model 2 shows a significant jump in the disk contribution between $t/t_{acc} = 0.5$ and 0.75 which is due to significant contribution from the flattened inner envelope within $1''$ at $t/t_{acc} = 0.5$. Thus, the relatively more optically thin CO isotopolog emission is dominated by the central rotating disk starting from the Stage 1 phase ($t/t_{acc} \geq 0.5$).

4.3.4   Disentangling the velocity field

How can the rotating and infalling flattened envelope be disentangled from the Keplerian motion of the disk? The evolution of the rotationally dominated region is consistent with that reported by Brinch et al. (2008) based on more detailed hydrodynamics simulations. All models become rotationally dominated within 500 AU at $t/t_{acc} > 0.3$.
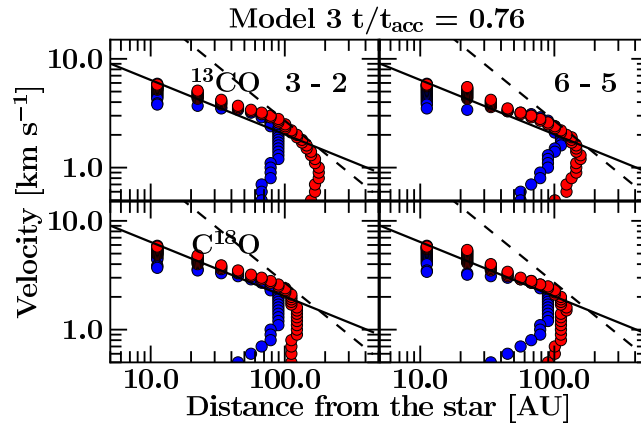
Figure 4.6 — Velocity as function of distance of the peak intensity position from the protostar, as measured in each channel map and for the same transitions as in Fig. 4.5. The red and blue colors represent the red- and blue-shifted components. The solid black line indicates the expected Keplerian structure from the stellar mass in the model, where as the dashed lines indicate the $v \propto R^{-1}$ relation as a comparison.

The presence of an embedded disk can be inferred from the presence of elongated ^{13}CO and C^{18}O integrated intensity maps (moment 0 of Fig. 4.5) coupled with the moment 1 map. In the presence of a stable disk, the zeroth moment map is elongated perpendicular to the outflow axis with a double peaked structure. This feature is not seen in Model 1 (Fig. 4.5 left) since the disk is much smaller than the 1″ beam. In the case of Model 3, the relatively massive disk exhibits a double peaked zeroth moment map which is perpendicular to the outflow direction.

A velocity gradient is seen in the moment 1 maps for both Models 1 and 3. With the high resolution of the modeled spectra, it is possible to differentiate between the disk and envelope (Hogerheijde 2001). The presence of a velocity gradient along the major axis of the elongation in the moment 1 map is a clear sign of a stable embedded disk in the case of Model 3. In addition, from the analysis in Sect. 4.3.3, we can also attribute the bulk of optically thin emission in Model 3 to the disk. Meanwhile, the infalling rotating envelope contribution can be detected through the fact that the moment 1 map is not perfectly aligned but skewed. On the other hand, a velocity gradient without the presence of elongation in the zeroth moment map such as in Model 1 (Fig. 4.5) indicates an infalling envelope.

Position-velocity (PV) diagrams provide another way to study the velocity structure. Figure 4.5 shows PV slices following the direction of the major axis of the disk (PA = 90°) in the integrated intensity map in the 3–2 and 6–5 lines. A simple way to analyze PV diagrams is to separate the diagram into four quadrants and examine which quadrants have considerable emission. An infall dominated PV diagram without rotation is symmetric about the velocity axis with all four quadrants filled (Ohashi et al. 1997b). The presence of rotation breaks the symmetry in the PV diagram and causes the peak positions to be off-centered. As found previously in hydrodynamical simulations by Brinch et al. (2008), infall dominates the PV diagrams at early times while rotation dominates the later times. These features have been observed toward low-mass YSOs which suggests that generally the infalling rotating envelope dominates the PV diagrams (eg. Sargent & Beckwith 1987; Hayashi et al. 1993; Saito et al. 1996; Ohashi et al. 1997b; Hogerheijde 2001).

Focusing on Model 3 at $t/t_{acc} = 0.76$ (near the end of Stage I) as shown in Fig. 4.5, the C^{18}O PV diagrams show a clearer pure rotation dominated structure than the ^{13}CO lines. They can thus be used to constrain the stellar mass as long as the inclination is known. Also, the higher-*J*

lines provide a better view into the rotating structure and should give tighter constraints on the stellar mass.

Another method is to plot the velocity as function of distance of the position of the peak intensity (Sargent & Beckwith 1987). This is done for the red-shifted and blue-shifted components, plotted in Fig. 4.6. The method is similar to the spectroastrometry technique employed in the optical and NIR observations (Takami et al. 2001; Baines et al. 2006; Pontoppidan et al. 2008). A Keplerian disk is characterized by a $v \propto r^{-0.5}$ with large contribution from the high velocity gas which is optically thin. As noted by Sargent & Beckwith (1987), as long as the line is spectrally resolved ($dV = 0.1$ km s^{-1}), the peak position corresponds to the maximum radius of a given velocity. On the other hand, the emission at low velocities ($dV \sim V$) is relatively more optically thick and is dominated by the infalling rotating envelope which peaks closer to the center (no offset). Such an analysis can be performed directly from the interferometric data and is a powerful tool in searching for embedded rotationally stable disks out of the rotating infalling envelope.

Why is there a difference between the red-shifted and blue-shifted components in Fig. 4.6? At high velocities, this is due to unresolved emission hence the different velocity components simply peak at the same position and the difference reflects the uncertainty in locating the emitting region. At low velocities, the optically thick infalling rotating envelope affects the peak positions. In an infalling envelope, the blue-shifted emission is relatively more optically thin than the red-shifted emission (Evans 1999). Such difference in the optical depth causes the red- and blue-shifted emissions to be asymmetric as found in the moment 1 map.

4.4 NIR CO absorption lines

A complementary probe of the molecular excitation conditions is provided by the NIR CO ro-vibrational absorption lines. In this work, we concentrate on the v $= 1 - 0$ band at 4.76 μm. This absorption takes place along the line of sight through the envelope and/or disk up to where the continuum is formed. The absorption lines are therefore computed for different inclinations of 45° and 75°. The inclinations were chosen such that they probe the envelope ($> 15°$) and the part of the disk that is not completely optically thick such that there is enough observable NIR continuum ($\leq 75°$), i.e., lines of sight that graze the disk atmosphere. Since our focus is on the excitation, the absorption lines have been calculated without any velocity field besides a turbulent width (Doppler b) of 0.8 km s^{-1}. More importantly, the formation of the 4.7μm continuum is strongly dependent on the inclination which affect the molecular absorption lines.

4.4.1 Evolution of NIR absorption spectra

4.4.1.1 *Radiative transfer and non-LTE effects*

The line center optical depth is one of the quantities derived from the model that can be compared to observations. This optical depth can either be determined by computing the line of sight integrated column densities and converting this to optical depth or by using a full RADLite calculation. For both approaches, the same level populations are used, i.e., the same model for the CO excitation is adopted as in Section 3. In the simplest method, the line center optical depth is obtained from

$$\tau_0 = \frac{c^3 g_{\mathrm{u}}}{8\pi\sqrt{\pi}b\nu^3 g_{\mathrm{l}}} A_{\mathrm{ul}} N_{\mathrm{l}}, \tag{4.3}$$
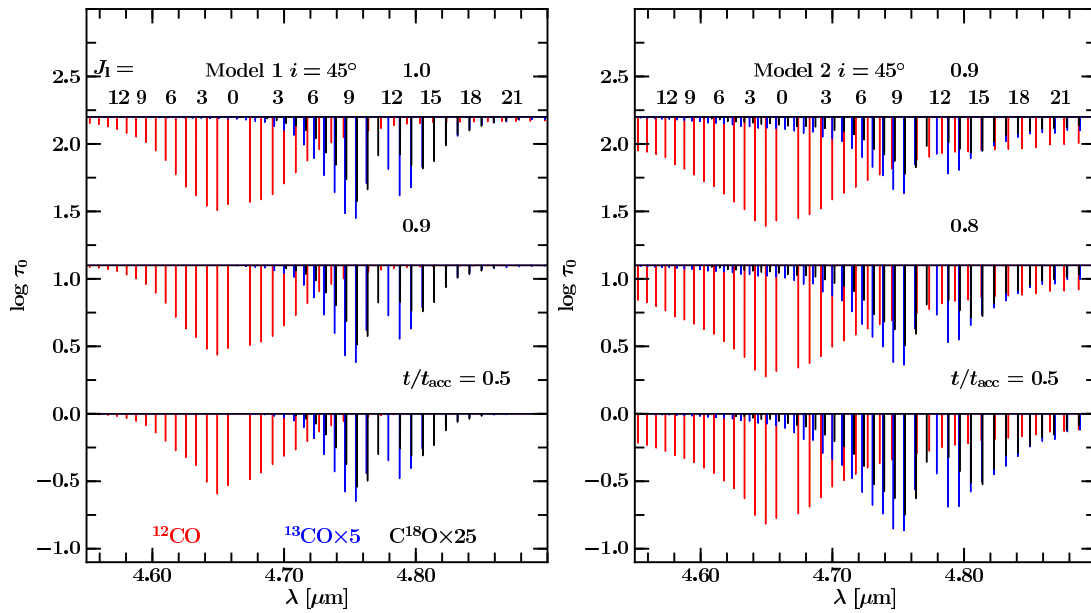
Figure 4.7 — Evolution of the ^{12}CO (red), ^{13}CO (blue) and C^{18}O (black) absorption lines for Model 1 at $i = 45°$. The evolution of the absorption lines for Model 2 is shown at the bottom panel. The lower rotational levels are indicated on top of the first spectrum. All of the ^{13}CO lines are multiplied by 5 and C^{18}O lines by 25.

where ν is the line frequency and N_1 is the lower level column density along the line of sight. The main difference between the methods is that RADLite solves the radiative transfer equation along the line of sight and thus accounts for continuum and line optical depth effects and scattered continuum photons, while such effects are not considered in the column density approach. In addition, RADLite accounts for the continuum formation, while a ray through the center does not. Thus, the two methods effectively compare the total mass present along a ray and the observed mass as probed by the line optical depth returned by RADLite. The optical depth is extracted from the RADLite spectra using the line-to-continuum ratio at the line center.

As discussed and illustrated extensively in Appendix 4.C.1, the two approaches can give very different results, especially for the higher J lines for which the line optical depths can differ by more than an order of magnitude. The main reason is illustrated in Fig. 4.16, which shows the region where the NIR continuum arises. For small inclinations, the continuum is essentially point-like, but for higher inclinations larger radii contribute significantly and the continuum is no longer a point source. Thus, for high inclinations, the high-J lines start absorbing off-center, away from warm gas in the inner few AU that are included in the column method. The location of the continuum is typically at >10 AU at $i = 75°$ which results in two to three orders of magnitude difference in total column density. For the case of $i \sim 45°$, the result depends on the physical structure in the inner few AU but the absorption can miss the warm high density region close to the midplane of the disk where most of the $J \geq 10$ is located (Fig. 4.15).

Figure 4.17 also compare LTE and non-LTE spectra. Consistent with Section 3, significant differences are found for the higher pure rotational levels which are subthermally excited. However, the radiative transfer effect is generally more important than the non-LTE effects for viewing angles through the disk/inner envelope surface.

4.4.1.2 NIR spectra

The NIR absorptions are rendered with RADLite for $t/t_{\rm acc} \geq 0.5$ which starts when $M_{\rm env} \sim M_\star$ (Stage 0/I boundary) in order to have a strong 4.7μm continuum. Figure 4.7 show the P and R branches of the CO isotopologs for Model 1 and 2 which show the greatest difference. In general, as shown in Fig. 4.7, the higher-J absorptions are stronger as the system evolves into Stage II due to the central luminosity. For Model 1, at $t/t_{\rm acc} = 0.5$, the ^{12}CO absorptions can be seen up to $J = 16$, and up to $J = 9$ for ^{13}CO and 7 for C^{18}O. The number of absorption lines that are above $\tau_\nu = 3 \times 10^{-3}$ (the 3σ observational limit with instruments such as VLT-CRIRES) doubles at the end of the accretion phase and the highest observable J shifts from 16 to > 30 for ^{12}CO and up to $\sim$ 15–20 for the isotopologs.

At early times, a similar number of lines are found for Model 3 but their optical depths are lower due to the difference in the inner envelope structure. On the other hand, the number of lines in Model 2 is much higher than in the other two models due to the lower continuum optical depth in the inner envelope. Thus, the absorbing column starts deeper than in the other two models, which results in stronger absorption features and an increased number of detectable high-J lines, up to $J > 40$ for ^{12}CO, $J \sim 25$ for ^{13}CO and $J \sim 15$ for C^{18}O (Fig. 4.7). Thus, in principle the appearance of the NIR spectrum could be a sensitive probe of the inner envelope structure. In practice, the ^{12}CO absorption will be affected by outflows and winds so the ^{13}CO and C^{18}O isotopologs are most useful for this purpose.

4.4.2 Rotational temperatures

A directly related observable is the rotational temperature derived from a Boltzmann diagram. Thus, the RADLite NIR spectra need to be converted into column densities. For this conversion, we use a standard curve-of-growth analysis (Spitzer 1989) with $b = 0.8$ km s^{-1} and oscillator strengths derived from the Einstein $A_{\rm ul}$ coefficients. By using the curve-of-growth method, it is assumed that the spectral lines are unresolved.

An example of a Boltzmann diagram is shown in Fig. 4.15 together with a two-temperature fit, as commonly done in observations (Mitchell et al. 1990; Smith et al. 2009; Herczeg et al. 2011). The rotational temperature of the cold component is obtained from fitting the P(1) to P(4) lines ($E_{\rm l} < 40$ K). Lines higher than P(5) ($E_{\rm l} > 40$ K) are used to obtain the temperature of the warm component. Model 2 at $t/t_{\rm acc} = 0.78$ is used since it clearly shows the break between the two temperatures.

How do the two temperatures evolve with time? As Table 4.2 shows, the cold component is between 20 and 35 K with no significant evolution, except in Model 2, as the disk is building up. The warm component, however, increases with inclination and time. The derived warm temperature component ranges from < 100 up to ~ 520 K and traces the warming up of material in the inner region as the envelope dissipates. From the simulations, a > 400 K warm component is a signature of an evolved system.

What is the origin of the two temperatures? This can be easily shown by plotting the cold ($<$50 K) and warm ($>$100 K) H$_2$ column along the line of sight at various inclinations (Fig. 4.8). The particular model and time were chosen as an example; the general picture is the same independent of evolutionary model, but the warm component shifts to lower viewing angle (left) for earlier times. The figure indicates that the warm material can be probed through $i > 25°$ viewing angles. The cold component probes the outer envelope where the gas temperature hardly changes as the system evolves. The warm component reflects the line of sight to the center through the warm inner envelope (the so-called 'hot core') or the disk surface where the gas is > 100 K in all of our models. The cumulative gas column density indicates that the cold

Table 4.2 — NIR rotational temperatures derived from $\tau_0 > 10^{-3}$ lines for $i = 45°$ and $75°$.

$t/t_{\rm acc}$	i [°]	^{12}CO $T_{\rm cold}$ [K]	$T_{\rm warm}$ [K]	^{13}CO $T_{\rm cold}$ [K]	$T_{\rm warm}$ [K]	C^{18}O $T_{\rm cold}$ [K]	$T_{\rm warm}$ [K]
				Model 1			
0.50	45	21 ± 9	80 ± 9	18 ± 11	49 ± 18	19 ± 13	...
	75	20 ± 9	66 ± 8	17 ± 10	44 ± 10	18 ± 10	...
0.76	45	26 ± 10	142 ± 21	19 ± 11	72 ± 20	19 ± 14	...
	75	25 ± 12	260 ± 67	25 ± 12	273 ± 69	19 ± 13	...
0.96	45	28 ± 10	201 ± 36	28 ± 13	207 ± 46	21 ± 16	...
	75	25 ± 10	271 ± 61	25 ± 13	301 ± 80	20 ± 13	...
				Model 2			
0.50	45	34 ± 20	245 ± 61	34 ± 25	253 ± 61	29 ± 23	183 ± 51
	75	31 ± 20	293 ± 85	31 ± 20	302 ± 86	27 ± 19	209 ± 67
0.78	45	31 ± 20	327 ± 100	31 ± 20	340 ± 110	28 ± 19	264 ± 89
	75	20 ± 11	489 ± 210	19 ± 11	481 ± 192	18 ± 11	423 ± 230
0.94	45	28 ± 18	402 ± 156	28 ± 18	410 ± 152	26 ± 17	333 ± 139
	75	18 ± 11	544 ± 255	17 ± 10	527 ± 223	17 ± 10	495 ± 308
				Model 3			
0.50	45	21 ± 6	193 ± 37	16 ± 8	42 ± 21	19 ± 9	...
	75	16 ± 7	37 ± 7	16 ± 10	...	16 ± 11	...
0.76	45	23 ± 9	287 ± 80	22 ± 9	304 ± 85	17 ± 11	...
	75	22 ± 8	289 ± 81	21 ± 8	302 ± 83	17 ± 10	...
0.96	45	22 ± 9	366 ± 128	21 ± 8	381 ± 129	17 ± 10	...
	75	18 ± 8	361 ± 121	18 ± 7	371 ± 119	16 ± 9	...

material is mostly absorbed at $R > 100$ AU while the warmer gas component is probing the inner few AU ($i > 60°$) up to ~ 20 AU ($i \sim 45°$). The excitation temperature of the warm component reflects the density structure in the inner few AU. With the lower densities and warmer temperatures in Model 2, which decreases the effective continuum optical depth, higher warm temperatures can be observed as the absorption probes deeper to smaller radii than the other two models.

4.5 Discussion

We have presented the evolution of CO molecular lines based on the standard picture of a prestellar core collapsing to form a star and 2D circumstellar disk. The main aim of this work is to study the evolution of observables that are derived from the spectra such as rotational temperatures, line profiles, and velocity fields. Specifically, signatures of disk formation during the embedded stage that can be obtained with the most commonly used molecule, CO, are investigated.

4.5.1 Detecting disk signatures in the embedded phase

How can one determine whether disks have formed in the earliest Stage 0? As discussed in Section 4.3.3, it is difficult to isolate an embedded disk component in single-dish observations. The disk contribution to the observed flux within $> 9''$ beams is only significant ($>60\%$) for
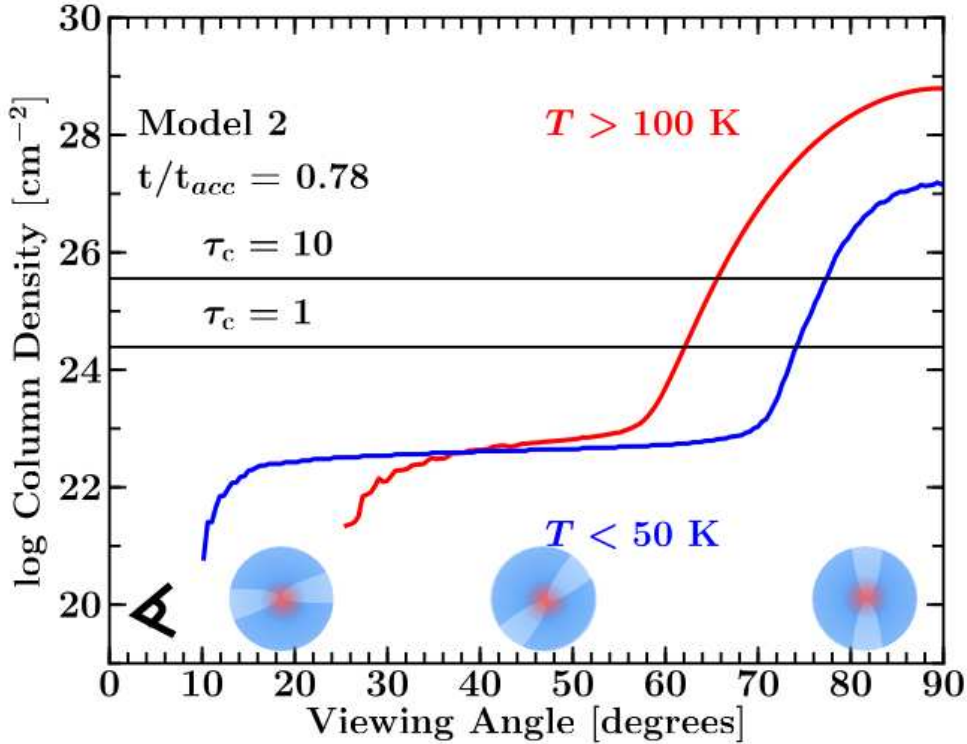
Figure 4.8 — Integrated gas column density along the different viewing angles for Model 2. The red and blues lines indicate the warm ($T > 100$ K) and cold gas ($T < 50$ K), respectively. The approximate continuum optical depths, $\tau_c = 1$ and 10, are also shown to indicate the amount material that is missed by properly solving the radiative transfer equation.

the ^{13}CO and C^{18}O $J_u > 9$ lines at $t/t_{acc} > 0.75$. However, the absolute fluxes are too low to be detected. Thus, spatially resolved observations at sub-arcsec scale are needed.

What are the signatures of an embedded rotationally supported disk on subarcsecond scales? We have analyzed some of the simulated images during the Stage 0 phase at a resolution of 0.1″ as can readily be observed with ALMA. Figure 4.9 shows the C^{18}O 3–2 moment-one map during the Stage 0 phase of Model 1 with a disk extending up to 20 AU at a resolution of 1, 0.3 and 0.1″. Velocity gradients are present in all of the moment-one maps although it is weaker within a 1″ beam. The right panel of the figure shows the spectroastrometry (Fig. 4.6) within the different resolutions. The velocity gradient within a 0.5–1″ beam exhibits a $v \propto R^{-1}$ relation since the inner envelope dominates the emission. Within the smaller beams, the velocity gradient is resolved into two components: $v \propto R^{-1}$ (blue dashed line) due to envelope and $v \propto R^{-0.5}$ (black dashed line) due to the stable disk. A $v \propto R^{-0.5}$ can be seen when the disk is marginally resolved, however, the derived stellar mass is far below the real stellar mass. It is very important that the disk is fully resolved in order to derive the stellar mass. With the C^{18}O lines, a resolved embedded disk in Stage 0 would have the following features:

- Elongated moment-zero map.
- A transition between an infalling envelope to a rotating disk: a skewed moment-one map.
- The Keplerian structure exhibits a clear $v \propto R^{-0.5}$ (Fig. 4.6 and bottom of Fig. 4.9) velocity gradient perpendicular to the outflow.
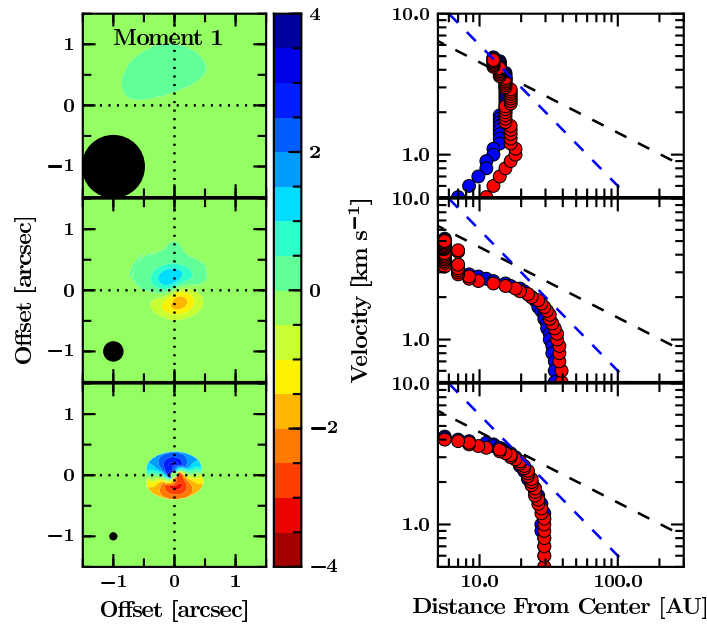
Figure 4.9 — $C^{18}O$ 3–2 moment-one (left) and spectroastrometry (right) for Model 1 at the end of Stage 0 convolved to a $1''$ (top), $0.3''$ (middle) and $0.1''$ (bottom) as shown by the solid circle. The Keplerian structure at this stage extends up to 20 AU (0.14$''$ radius). The black dashed line in the right panel shows the $v \propto R^{-0.5}$ and the blue dashed line indicates the $v \propto R^{-1}$ relation.

It is possible to search for rotationally supported disks in Stage 0 sources with characteristics of Model 1 with the full ALMA array in less than 30 minutes for the $C^{18}O$ 2–1 transition or up to 4 hours for the 6–5 transition. For Models 2 and 3, the disks have grown up to ~ 50 AU near the end of Stage 0 and up to twice more massive, thus it will take less than 2 hours to observe them with ALMA in the 6–5 transition and less than 30 minutes in the 2–1 and 3–2 transitions. Therefore, ALMA will allow us, for the first time, to test whether rotationally supported disks have grown beyond 10 AU by the end of the Stage 0 phase.

The question of when rotationally supported disks form is crucial to the physical and chemical evolution of accretion disks. In our evolutionary models, the disks have radii up to 50 AU at the end of Stage 0 phase and can be as small as 20 AU. Dapp & Basu (2010) and Dapp et al. (2012) numerically showed that disks do not grow beyond 10 AU during the Stage 0 phase in the presence of magnetic fields due to the magnetic breaking problem (see also Li et al. 2011; Joos et al. 2012). This is consistent with the lack of observed rotationally supported disks toward Stage 0 objects so far (Brinch et al. 2009; Maury et al. 2010). On the other hand, there is a growing body of observational evidence for rotating disks in Stage I YSOs (Brinch et al. 2007b; Lommen et al. 2008; Jørgensen et al. 2009; Takakuwa et al. 2012). The size of the rotationally supported disk depends on the initial parameters of the collapsing envelope. In our models, the sizes of Models 2 and 3 are consistent with the observed Keplerian velocity structure in Stage I sources (Jørgensen et al. 2009).

An additional caveat is that our models lead to a Keplerian disk with a flattened inner envelope on similar scales as the stable disk. Hydrodynamical simulations, on the other hand, show a stable disk embedded in a much larger rotating flattened structure and with more turbulent structure (Brinch et al. 2008; Kratter et al. 2010). Furthermore, the 3D simulations by Harsono et al. (2011) suggest that 50% of the embedded disk is sub-Keplerian due to interaction with the envelope. The predicted moment 1 maps and spectroastrometry with the current

models should be performed for these numerical simulations for comparison with ALMA observations.

4.5.2   Probing the temperature structure

The derived rotational temperatures from the submm and FIR lines (J_u = 1–10) within $> 9''$ beams do not evolve with time, in contrast with the continuum SED, and largely trace the outer envelope (Section 4.3.2). Even though the disk structure is hotter with time, the emission that comes from within that region is much smaller than the beam. The mass weighted temperature of the system which contributes to the overall emission is constant with time. The rotational temperatures also cannot differentiate between the three different evolutionary models. In addition, the peak of the CO SLED is constant throughout the evolution at $J_\mathrm{u} = 4$ for the ^{13}CO and C^{18}O. The higher observed excitation temperatures for ^{12}CO and ^{13}CO in a wide range of low-mass protostars from submm and FIR data point to other physical processes that are present in the system such as UV heating and C-shock components that affect the $J \geq 5$ lines (Visser et al. 2012; Yıldız et al. 2012).

The NIR absorption lines toward embedded YSOs are complementary to the submm/FIR rotational lines. Both techniques probe the bulk of the cold envelope, but the NIR lines also probe the warm component because the lines start absorbing at the $\tau \sim 1$ surface deep inside the inner envelope. Consequently, the cold component present in the NIR lines should be similar to the component observed in the submm. Indeed, the typical rotational temperatures of 20–30 K found in the NIR models for C^{18}O are comparable to the values of 30–40 K found from the submm simulations.

The warm up process is accessible through NIR molecular absorption lines. In Section 4.4.2, it is found that the warm component of the Boltzmann diagram evolves with time. The derived warm temperatures have a large spread depending on inclination and density structure in the inner few AU. A higher inner envelope and disk density correspond to a ~ 100 K warm component, whereas a more diffuse inner envelope has a warmer temperature that can be up to 500–600 K. Thus, as long as the inclination is known, the temperature of the warm component may give us a clue on the density structure of the inner few AU where the > 100 K gas resides.

The predicted cold and warm temperatures can be compared with those found in NIR data toward Stage I low-mass YSOs. For the cold component, a temperature of 15 K has been found for L1489 from ^{13}CO data (Boogert et al. 2002), and 10–20 K for Reipurth 50, Oph IRS43 and Oph IRS 63 from ^{13}CO and C^{18}O data (Smith et al. 2009; Smith et al. 2010), consistent with our envelope models. For the warm component, values ranging from 100 to 250 K are found for these sources from the isotopolog data. These warm rotational temperatures are on the low side of the model values in Table 4.2 for the later evolutionary stages, and may indicate either a compact envelope (high inner envelope densities) and/or high inclination (which effectively limits the absorption lines to probe the inner envelope component). Independent information on the inclination is needed to further test the physical structure of those sources.

4.6   Summary and conclusions

Two-dimensional self-consistent envelope collapse and disk formation models have been used to study the evolution of molecular lines during the embedded phase of star formation. The non-LTE molecular excitation has been computed with an escape probability method and spectral cubes have been simulated for both the FIR and NIR regimes. The gas temperature is taken to be well coupled to the dust temperature as obtained through a continuum full radiative transfer code. With the availability of spectrally resolved data from single dish submillime-

ter telescopes, the *Herschel* Space Observatory, VLT CRIRES and ALMA, it is now possible to compare the predicted collapse dynamics with observations. We have focused the analysis on the ^{13}CO and the C^{18}O lines since ^{12}CO lines are dominated by outflows and UV heating. The main conclusions are as follows:

- Spectrally resolved molecular lines are important in comparing theoretical models of star formation with observations and to distinguish the different physical components. The collapsing rotating envelope can readily be studied through the C^{18}O lines. Their FWHM probes the collapse dynamics, especially for the higher-J ($J_{\mathrm{u}} \geq 6$) lines where up to 50% of the line broadening can be due to infall.

- The derived rotational temperatures and SLED from submm and FIR pure rotational lines are found to be independent of evolution and do not probe the warm up process, in contrast to the continuum SED. The predicted rotational temperatures are consistent with observations for C^{18}O for a large sample of low-mass protostars.

- The predicted ^{12}CO and ^{13}CO rotational temperatures and high-J fluxes are lower than those found in observations of a wide variety of low-mass sources (Goicoechea et al. 2012; Yıldız et al. 2012, 2013). This indicates the presence of additional physical processes that heat the gas such as shocks and UV heating of the cavity walls (Visser et al. 2012).

- The NIR absorption lines are complementary to the FIR/submm lines since they probe both the cold outer envelope and the warm up process. Values obtained for the cold component are consistent with the observational data and models. For the warm component, the observed values are generally on the low side compared with the model results. The high-J NIR lines are strongly affected by radiative transfer effects, which depend on the physical structure of the inner few AU and thus form a unique probe of that region.

- The simulations indicate that an embedded disk in both Stage 0 ($M_{\mathrm{env}} > M_{\star}$) and I ($M_{\mathrm{env}} < M_{\star}$ but $M_{\mathrm{disk}} < M_{\mathrm{env}}$) does not contribute significantly ($< 50\%$) to the emergent $J_{\mathrm{u}} < 8$ lines within $> 9''$ beams. Higher-J isotopolog lines have a higher contribution but are generally too weak to observe. The disk contribution is significantly higher within $1''$ beam and the evolution within such a beam indicate rotationally supported disks should be detectable in Stage I phase consistent with observations (Jørgensen et al. 2009).

- Embedded disks during the Stage I phase are generally large enough to be detected with current interferometric instruments with $1''$ resolution, consistent with observations. On the other hand, high signal-to-noise ALMA data at $\sim 0.1''$ resolution are needed in order to find signatures of embedded disks during the Stage 0 phase. A careful analysis is needed to disentangle the disk from the envelope.

- We have shown that the rotationally dominated disk can be disentangled from the collapsing rotating envelope with high signal-to-noise and high spectral resolution interferometric observations (Section 4.3.4). The spectroastrometry with ALMA by plotting the velocity as function of peak positions can reveal the size of the Keplerian disk. The ^{13}CO lines within interferometric observations may still be contaminated by the infalling rotating envelope. Thus, more optically thin tracers are required.

The three different collapse models studied here differ mostly in their physical structure and velocity fields on 10–500 AU scales and illustrate the range of values that are likely to be encountered in observational studies of embedded YSOs. It is clear that the combination of spatially and spectrally resolved molecular line observations by ALMA and at NIR are crucial in determining the dynamical processes in the innermost regions during the early stages of star formation. A comparison between the standard picture presented here or hydrodynamical simulations and molecular line observations of Stage 0 YSOs will further test the theoretical picture of star and planet formation.
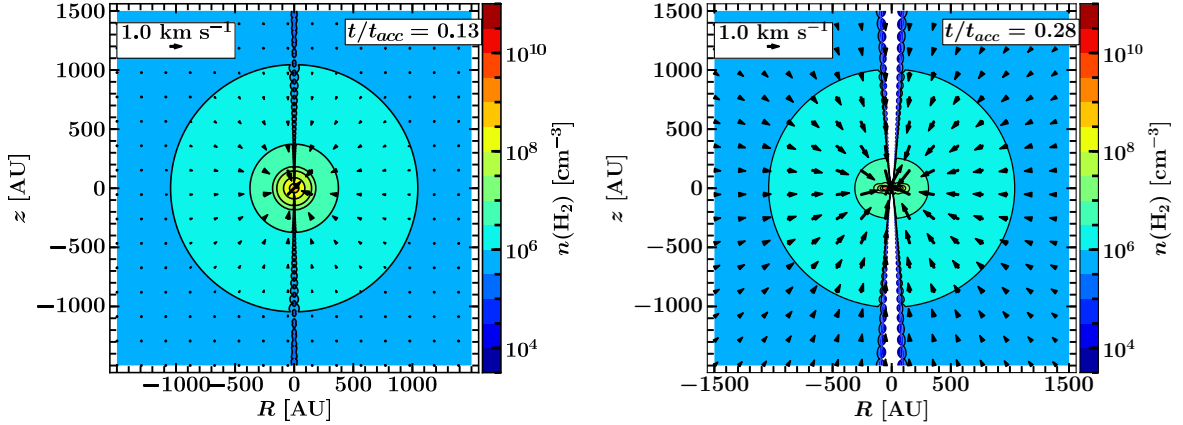
Figure 4.10 — Gas density and velocity field for Model 3 at $t/t_{\rm acc} = 0.13$ and 0.28 within 1500 AU. The density contours start from $\log(n/{\rm cm}^{-3}) = 5.5$ and increase by steps of 0.5 up to $\log(n/{\rm cm}^{-3}) = 9$. There are vertical and radial motions in the disk, which are not captured in this figure.

Acknowledgements

4.A   Two dimensional RT grid

The grid needs to resolve the steep density and velocity gradients at the boundaries between adjacent components as shown in Fig. 4.10. Improper gridding can lead to order-of-magnitude difference in the high-J ($J \geq 6$) line fluxes. The escape probability code begins with a set of regularly spaced cells on a logarithmic grid to resolve both small and large scales. Any cells where the abundance or density at the corners differs by more than a factor of 5, or where the temperature at the corners differs by more than a factor of 1.5, are split into smaller cells until the conditions across each cell are roughly constant. The full non-LTE excitation calculation takes about five minutes for a typical number of cells of 15 000 (Stage I) – 25 000 (Stage 0).

Figure 4.11 presents an example of the gridding in our models. Such gridding is most important for early time steps where the outflow cavity opening angle is small. The refining ensures that the non-LTE population calculation converges and high-J emission which comes from the inner region can escape.

4.B   FIR and submm lines

Figure 4.12 shows the mass evolution of the evolutionary models which indicates the times at which the models enter various evolutionary stages. Figure 4.12 presents the $C^{18}O$ 9–8 lines for the three different evolutionary models convolved to a 9″ beam. Most of the line is emitted

from the inner envelope region. The line is generally broader in later stages due to a combination of thermal, turbulent width and velocity structure. However, the width of the line depends on whether the emitting region is infall or rotation dominated. Figures 4.13 and 4.14 shows the $J_u = 3$, 6 and 9 line profiles for the different models and how they change within different beams. The disk contribution to the observed lines within a $9''$ beam is presented in Fig. 4.13 which is close to negligible for the low-J lines.

4.C NIR molecular lines

4.C.1 Inner disk

The formation of NIR continuum and the region where absorption happens depend on the physical structure in the inner few AU as will discussed extensively in the next section. Figure 4.15 shows the inner 5 AU structure of the three different models. In both Models 1 and 3, the $10^{4.5}$ cm^{-3} density contour extends up to the line of sight of $45°$ due to the presence of compact disk and massive disk, respectively. On the other hand, the density structure is flatter in Model 2. Thus, the NIR continuum emission is emitted through the high temperature region (mostly the red region in the temperature plot) and encounters more material along the line of sight to an observer in Models 1 and 3. Consequently, the emission from the region close to the midplane of the disk will not contribute to the NIR continuum. Figure 4.8 presents an example of the radial contribution to the column density along a line of sight from the star. At viewing angles $< 45°$, most of the warm material is located at 10–40 AU from the star along the line of sight while most of the cold material is located > 50 AU. The inner disk and high density region (< 1 AU) is only accessible through $i \geq 75°$ in our models.

4.C.2 Radiative transfer effects

Section 4.4 discusses the RADLite results with respect to the predicted observables. In this section, we present the comparison between RADLite and a simple calculation using the integrated column density (column method, equation 4.3) to examine the radiative transfer effects in particular where the 4.7 μm continuum is formed and its affect on the simulated absorption lines.
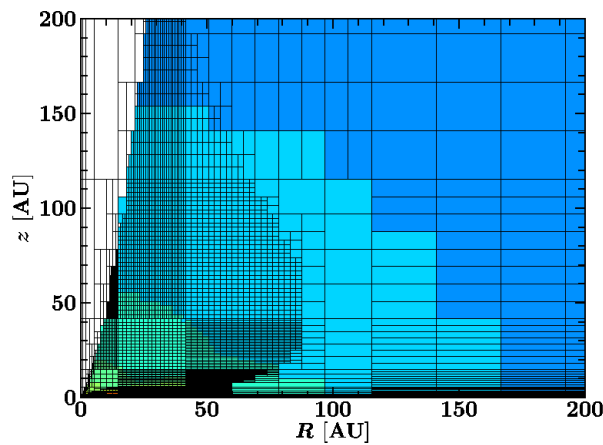

Figure 4.11 — Example of the gridding used in the Stage 0 phase to resolve the small extent of the outflow cavity and to resolve the density and velocity gradient from the disk midplane to the envelope. The color contours are the same as in Fig. 4.10. The structure shown is for Model 1 at $t/t_{\mathrm{acc}} = 0.13$.
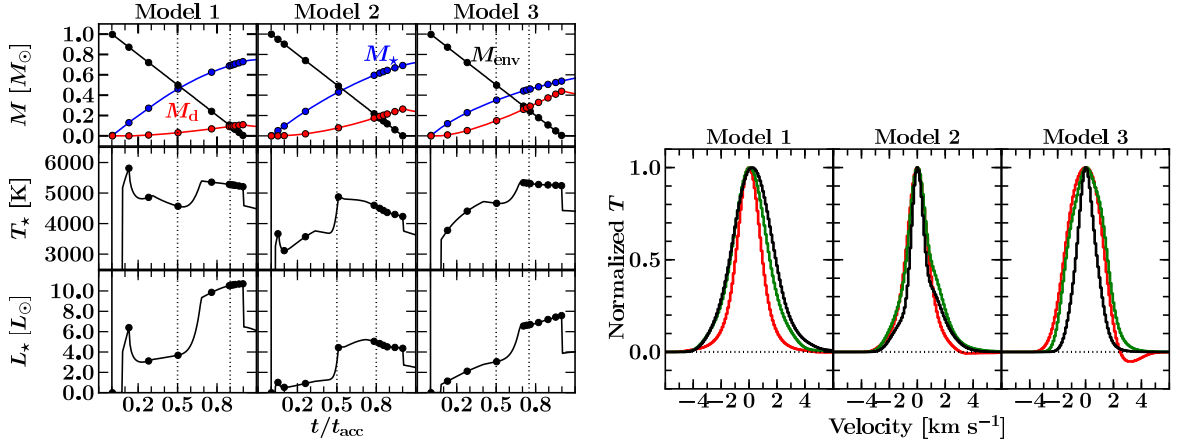
Figure 4.12 — *Left*: Evolution of the envelope, disk and stellar mass (top), effective stellar temperature (middle) and stellar luminosity (bottom) for the three different models as function of time (in units of $t_{\rm acc}$). The solid circles show the time steps (roughly around $t/t_{\rm acc} \sim 10^{-3}, 0.1, 0.5, 0.75, 0.89, 0.99$) used for rendering the molecular lines. The adopted time steps vary per model in order to cover properly the time when the model enters Stage 1 ($M_{\rm env} < M_\star$) and when the $M_{\rm d} = M_{\rm env}$ as indicated by the vertical dotted lines. *Right*: $C^{18}O$ $9-8$ line profiles convolved to a 9″ beam for the three models at $t/t_{\rm acc} = 0.13$ (red), 0.50 (green) and 0.96 (black).

Figure 4.17 illustrates the difference in line center optical depth between the formal solution of the radiative transfer equation and the column density approach at $i = 45°$ (Eq. 4.3). This particular model and time was chosen as an example that clearly shows the difference. The difference in τ_0 between the methods generally increases with $J_{\rm l}$ and are largest for $J_{\rm l} \sim 10$. Figure 4.16 shows the 4.7 μm continuum flux due to dust only (i.e., no stellar contribution) as function of radius at various viewing angles. The continuum is point-like for low inclinations but it is generally off-center for high inclinations. Thus, larger τ_0 differences between the two methods are expected for larger inclinations since the absorption does not take place directly along the line of sight to the star. The implication is that the column method overestimates τ_0
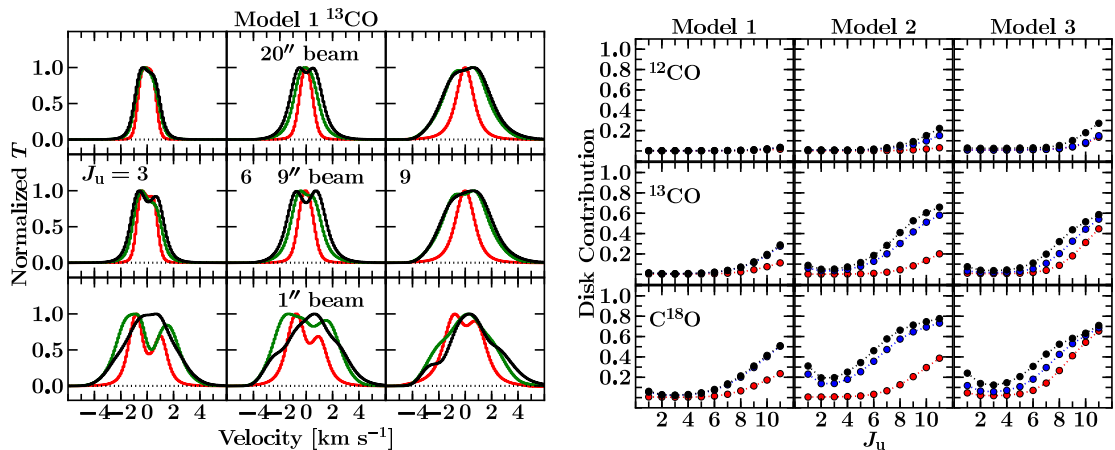
Figure 4.13 — *Left*: Normalized $C^{18}O$ and ^{13}CO line profiles as functions of evolution for $J_{\rm u} = 3$, 6 and 9 at $t/t_{\rm acc} = 0.13$ (red), 0.50 (green) and 0.96 (black) for $i = 5°$ orientation for Model 1. The lines are convolved to beams of 20″ (top), 9″ (middle) and 1″ (bottom). *Right*: Disk contribution to total emission as a function of $J_{\rm u}$ within a 9″ beam (1260 AU at 140 pc) for the three different models. The different colors correspond to different time steps: $t/t_{\rm acc} \sim 0.50$ (red), 0.75 (blue), 0.96 (black).

Figure 4.14 — As Figure4.2, but for Models 2 and 3.
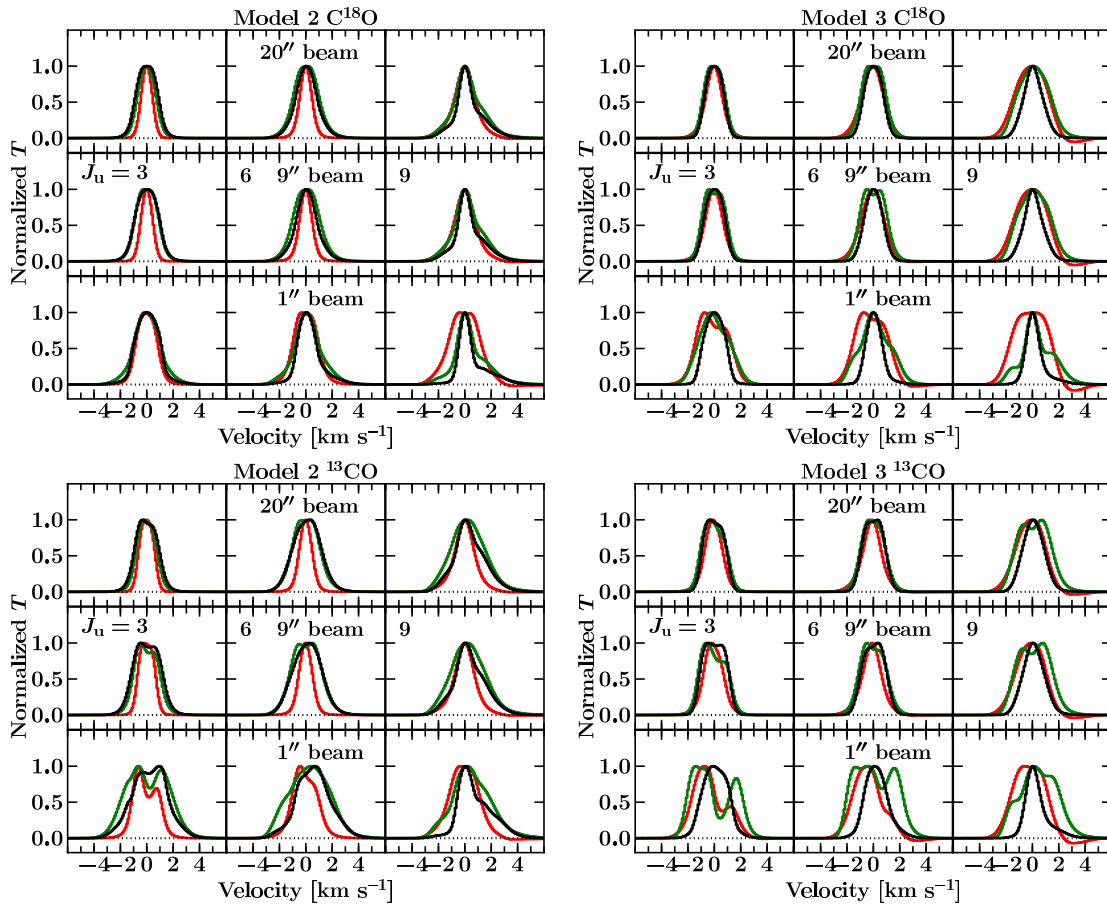
of the high-J absorptions as this method takes the full line of sight through the warm material into account.

What are the implications for translating observed optical depths to column densities and excitation temperatures? The differences are largest for $J \geq 5$ lines which result in lower derived warm temperature and column densities in the full treatment. Consequently, the direct transformation from the observed optical depth to column density requires additional information on where the absorption arises, i.e., the NIR continuum image. One way is to construct the physical structure and assess the NIR continuum image. Observationally, a comparison between interferometric submm and NIR continuum should result in different continuum position if the NIR continuum arises from scattered light. Observationally driven constraint is likely more useful in practice since modelling of the NIR continuum requires a sophisticated inner disk and envelope physical structure. For systems with an off-centered NIR continuum, the derived column densities and temperature of the warm component are lower limits.

4.C.3 Non-LTE effects

The effects of non-LTE excitation in the vibrational ground state are studied by either using the level populations calculated with the full non-LTE escape probability method (§3) or assuming LTE populations. The LTE level population is calculated using the partition functions provided by the HITRAN database (Rothman et al. 2009).
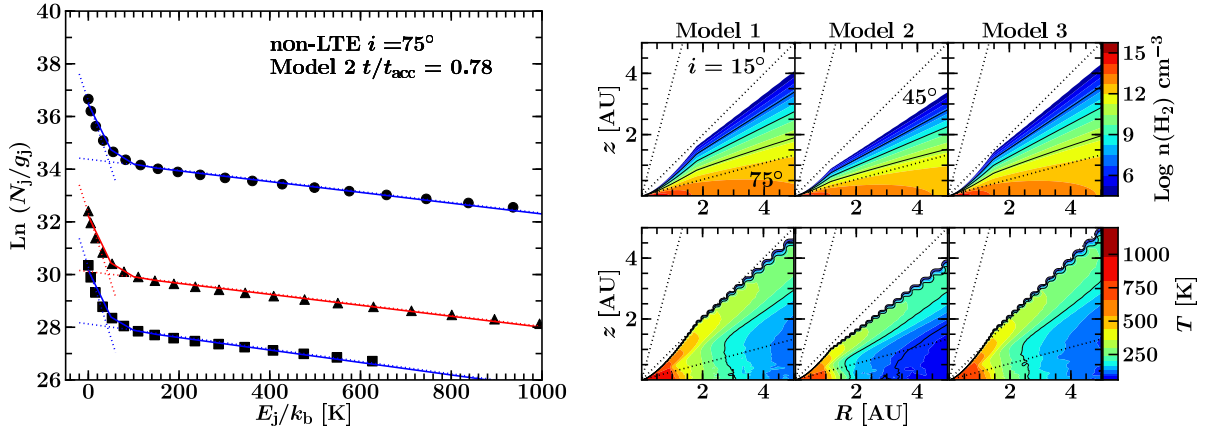
Figure 4.15 — *Left*: Example of the two-temperature fitting of the NIR lines. The column densities are derived from a curve-of-growth analysis performed on the simulated spectra using RADLite. The different symbols correspond to ^{12}CO (circle), ^{13}CO (triangles) and C^{18}O (squares). The solid lines are the combination of the cold and warm components. *Right*: Density structure in the inner 10 AU (starting from n(H$_2$) = $10^{4.5}$ cm^{-3}) and temperature structure (starting from 60 K) of the three models. The three viewing angles are shown by dotted lines.
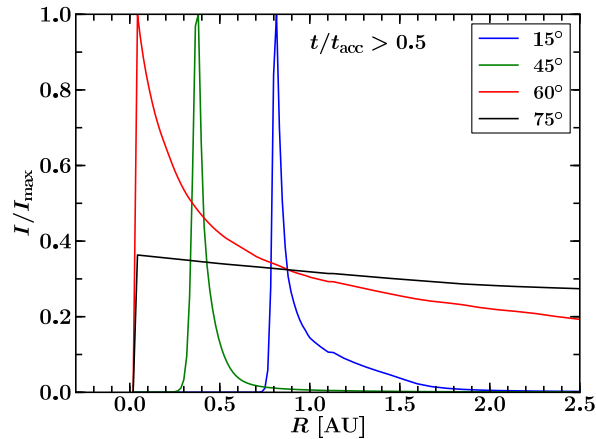

Figure 4.16 — Normalized continuum flux without the stellar photosphere as function of distance from the center along one direction. The figure is constructed from a NIR image of Model 1 at $t/t_{acc} = 0.7$ as an example. The general trend is similar for $t/t_{acc} > 0.5$ independent of evolutionary models. The normalized continuum is similar for the various evolutionary models for $t/t_{acc} > 0.5$. The continuum is shown to arise in the inner few AU region and to fall off very quickly for $i < 60°$. However, significant contributions from larger radii are expected for relatively high inclination.

Figure 4.17 compares LTE and non-LTE line center opacities of C^{18}O for Model 3 at an inclination of 45° (other isotopologs are shown in Figure 4.17). Model 3 was chosen as an example; in general, the non-LTE effects are most apparent for the higher levels independent of isotopologs and evolutionary models. This reflects the findings of §3: lower pure rotational levels are more easy to thermalize due to lower critical densities. The difference between LTE and non-LTE is independent of inclination while radiative transfer effects do. Thus, it is more important to treat the radiative transfer correctly in the NIR to derive observables.
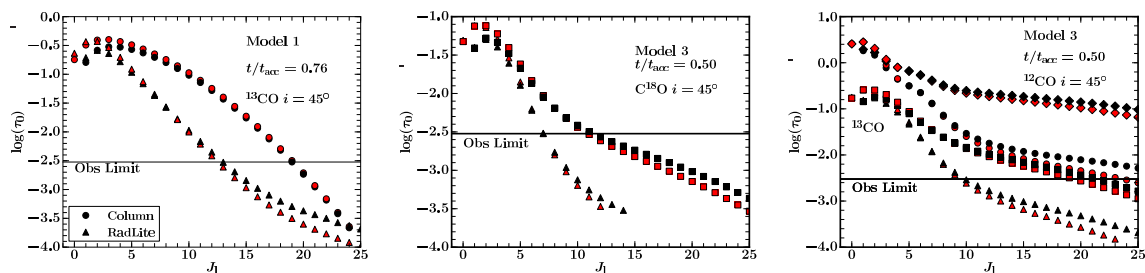
Figure 4.17 — *Left*: Comparison of the line center optical depth obtained from a simple integration of the column density along the line of sight (circles) and the radiative transfer calculation (triangles). The P and R branches are shown in black and red, respectively. The horizontal line indicates the current observation limit with CRIRES at $\tau \sim 3 \times 10^{-3}$. The ^{13}CO lines are shown for Model 1 at $t/t_{\rm acc} = 0.76$ for $i = 45°$. *Middle*: Comparison between LTE (squares) and non-LTE (triangles) line center optical depth obtained from RADLite for Model 3 at an inclination of $45°$. The different colors correspond to the P (black) and R (red) branches. *Right*: Similar to middle panel for ^{12}CO (diamonds and circles) and ^{13}CO (squares and triangles).

Chapter 5

Rotationally-supported disks around Class I sources in Taurus: disk formation constraints

Abstract. *Context*. Disks are observed around pre-main sequence stars, but how and when they form is still heavily debated. While disks around young stellar objects have been identified through thermal dust emission, spatially and spectrally resolved molecular line observations are needed to determine their nature. Only a handful of embedded rotationally supported disks have been identified to date.
Aims. We identify and characterize rotationally supported disks near the end of the main accretion phase of low-mass protostars by comparing their gas and dust structures.
Methods. Subarcsecond observations of dust and gas toward four Class I low-mass young stellar objects in Taurus are presented at significantly higher sensitivity than previous studies. The ^{13}CO and C^{18}O $J =$ 2–1 transitions at 220 GHz were observed with the Plateau de Bure Interferometer at a spatial resolution of $\leq 0.8''$ (56 AU radius at 140 pc) and analyzed using uv-space position velocity diagrams to determine the nature of their observed velocity gradient.
Results. Rotationally supported disks (RSDs) are detected around 3 of the 4 Class I sources studied. The derived masses identify them as Stage I objects; i.e., their stellar mass is higher than their envelope and disk masses. The outer radii of the Keplerian disks toward our sample of Class I sources are ≤ 100 AU. The lack of on-source C^{18}O emission for TMR1 puts an upper limit of 50 AU on its size. Flattened structures at radii > 100 AU around these sources are dominated by infalling motion ($v \propto r^{-1}$). A large-scale envelope model is required to estimate the basic parameters of the flattened structure from spatially resolved continuum data. Similarities and differences between the gas and dust disk are discussed. Combined with literature data, the sizes of the RSDs around Class I objects are best described with evolutionary models with an initial rotation of $\Omega = 10^{-14}$ Hz and slow sound speeds. Based on the comparison of gas and dust disk masses, little CO is frozen out within 100 AU in these disks.
Conclusions. Rotationally supported disks with radii up to 100 AU are present around Class I embedded objects. Larger surveys of both Class 0 and I objects are needed to determine whether most disks form late or early in the embedded phase.

D. Harsono, J. K. Jørgensen, E. F. van Dishoeck, M. R. Hogerheijde, S. Bruderer, M. V. Persson,
J. C. Mottram

5.1 Introduction

ROTATIONALLY supported accretion disks (RSDs) are thought to form very early during the star formation process (see, e.g., Bodenheimer 1995). The RSD transports a significant fraction of the mass from the envelope onto the young star and eventually evolves into a proto-planetary disk as the envelope dissipates. The presence of an RSD affects not only the physical structure of the system but also the chemical content and evolution as it promotes the production of more complex chemical species by providing a longer lifespan at mildly elevated temperature (Aikawa et al. 2008; Visser et al. 2011; Aikawa et al. 2011). Although the standard

picture of star formation predicts early formation and evolution of RSDs, theoretical studies suggest that the presence of magnetic fields prevents the formation of RSDs in the early stages of star formation (e.g., Galli & Shu 1993; Chiang et al. 2008; Li et al. 2011; Joos et al. 2012). Unstable flattened disk-like structures are formed in such simulations, and indeed, disks in the embedded phase have been inferred through continuum observations (e.g., Looney et al. 2003; Jørgensen et al. 2009; Enoch et al. 2011; Chiang et al. 2012). However, with only continuum data, it is difficult to distinguish between such a feature and an RSD. Thus, spatially and spectrally resolved observations of the gas are needed to unravel the nature of these embedded disks.

Only a handful of studies have explored the change in the velocity profiles from the envelope to the disk with spectrally resolved molecular lines (Lee 2010; Yen et al. 2013; Murillo et al. 2013). It is essential to differentiate between the disk and the infalling envelope through such analysis. This paper presents IRAM Plateau de Bure Interferometer (PdBI) observations of ^{13}CO and C^{18}O $J =$2–1 toward four Class I sources in Taurus ($d = 140$ pc) at higher angular resolution ($\sim 0.8''= 112$ AU diameter at 140 pc) and higher sensitivity than previously possible. We aim to study the velocity profile as revealed through these molecular lines and constrain the size of embedded RSDs toward these sources.

The embedded phase can be divided into the following stages (Robitaille et al. 2006): Stage 0 ($M_{\text{env}} > M_\star$), Stage I ($M_{\text{env}} < M_\star$ but $M_{\text{disk}} < M_{\text{env}}$) and Stage II ($M_{\text{env}} < M_{\text{disk}}$), where $M_\star$, M_{env} and M_{disk} are masses of the central protostar, envelop and RSD respectively. This is not to be confused with Classes, which are observationally derived evolutionary indicators (Lada & Wilking 1984; Andre et al. 1993) that do not necessarily trace evolutionary stage due to geometrical effects (Whitney et al. 2003b; Crapsi et al. 2008; Dunham et al. 2010). However, since all Class I sources discussed in this paper also turn out to be true Stage I sources, we use the Class notation throughout this paper for convenience.

RSDs are ubiquitous once most of the envelope has been dissipated away (Class II) with outer radius R_{out} up to approximately 200 AU (Williams & Cieza 2011,and references therein). On the other hand, the general kinematical structure of deeply embedded protostars on small scales is still not well understood. There is growing evidence of rotating flattened structures around Class I sources (Keene & Masson 1990; Hayashi et al. 1993; Ohashi et al. 1997a,b; Brinch et al. 2007b; Lommen et al. 2008; Jørgensen et al. 2009; Lee 2010, 2011; Takakuwa et al. 2012; Yen et al. 2013), but the question remains how and when RSDs form in the early stages of star formation and what their sizes are.

Class I young stellar objects (YSOs) are ideal targets to search for embedded RSDs. At this stage, the envelope mass has substantially decreased such that the embedded RSD dominates the spatially resolved CO emission (Harsono et al. 2013). CO is the second most abundant molecule and is chemically stable, thus the disk emission should be readily detected. Furthermore, Harsono et al. (2013) showed that the size of the RSD can be directly measured by analyzing the velocity profile observed through spatially and spectrally resolved CO observations. The sources targeted here are TMC1, TMR, L1536, and TMC1A. These Class I objects have been previously observed by the Submillimeter Array (SMA) and the Combined Array for Research in Millimeter-wave Astronomy (CARMA) at lower sensitivity and/or resolution (e.g., Jørgensen et al. 2009; Eisner 2012; Yen et al. 2013). Embedded rotating flattened structures have been proposed previously around TMC1 and TMC1A (Ohashi et al. 1997a; Hogerheijde et al. 1998; Brown & Chandler 1999; Yen et al. 2013). Thus, we target these sources to determine the presence of Keplerian disks, constrain their sizes near the end of the main accretion phase on scales down to 100 AU and compare this with the dust structure.

This paper is laid out as follows. Section 5.2 presents the observations and data reduc-

Table 5.1 — Noise levels and beam sizes.

Weighting	Beam	Continuum		Lines		
		RMS_{th}^a	RMS_{cl}^b	RMS_{th}	$^{13}CO\ RMS_{cl}$	$C^{18}O\ RMS_{cl}$
	size (PA)	[mJy beam^{-1}]		[mJy beam^{-1} channel^{-1}]		
		TMC1A (TMR1)				
Natural	$1.3'' \times 0.7''$ (16°)	0.12	3 (0.6)	24	30 (30)	20 (20)
Uniform	$0.8'' \times 0.7''$ (177°)	0.13	3 (0.6)	26	30 (29)	19 (20)
		L1536 (TMC1)				
Natural	$0.7'' \times 0.5''$ (36°)	0.14	1 (0.2)	26	20 (26)	18 (18)
Uniform	$0.6'' \times 0.5''$ (55°)	0.13	1 (0.2)	29	20 (24)	18 (18)

[a] Theoretical noise (RMS). [b] Peak of cleaned map noise for TMC1A or L1536. TMR1 or TMC1 cleaned noise is in parentheses. The cleaned noise toward TMR1 and TMC1 are significantly lower due to weaker total continuum flux.

tion. The continuum and line maps are presented in Section 5.3. In Section 5.4, disk masses and sizes are obtained through continuum visibility modelling. Position-velocity diagrams are then analyzed to determine the size of rotationally supported disks. Section 6.4 discusses the implications of the observed rotational supported disks toward Class 0 and I sources. Section 6.5 summarizes the conclusions of this paper.

5.2 Observations

5.2.1 IRAM PdBI Observations

The sources were observed with IRAM PdBI in the two different configurations tabulated in Table 5.8. Observations with *an on-source* time of ~ 3.5 hours per source with baselines from 15 to 445 m (11 kλ to 327 kλ) were obtained toward TMC1A and TMR1 in March 2012. Additional track-sharing observations of L1536 and TMC1 were obtained in March-April 2013 with an *on-source* time of ~ 3 hours per source and baselines between 20 to 450 m (15 kλ to 331 kλ). The receivers were tuned to 219.98 GHz (1.36 mm) in order to simultaneously observe the ^{13}CO (220.3987 GHz) and $C^{18}O$ (219.5603 GHz) $J =$2–1 lines. The narrow correlators (bandwidth of 40 MHz ~ 54 km s^{-1}) were centered on each line with a spectral resolution of 0.078 MHz (0.11 km s^{-1}). In addition, the WideX correlator was used, which covers a 3.6 GHz window at a resolution of 1.95 MHz (2.5–3 km s^{-1}) with 6 mJy beam^{-1} channel^{-1} RMS.

The calibration and imaging were performed using the CLIC and MAPPING packages of the IRAM GILDAS software[1]. The standard calibration was followed using the calibrators tabulated in Table 5.8. The data quality assessment tool flagged out any integrations with significantly deviating amplitude and/or phase and the continuum was subtracted from the line data before imaging. The continuum visibilities were constructed using the WideX correlator centered on 219.98 GHz (1.36 mm). The resulting beam sizes and noise levels for natural and uniform weightings can be found in Table 5.1. The uniform weighted images will be used for the analysis in the image space.

---

[1]http://www.iram.fr/IRAMFR/GILDAS

Table 5.2 — 1.36 mm continuum properties from elliptical Gaussian fits and derived disk and envelope masses (within 15″) from fluxes.

Source	RA	Dec	v_{lsr}	T_{bol}^a	L_{bol}^a	Size (PA)[b]	$F_{1.36mm}$	$S_{1.3mm}^{int,c}$	$S_{850\mu m}$ (15″)	M_{env}	M_{disk}
	(J2000)	(J2000)	[km s^{-1}]	[K]	$L_\odot$	[″] (°)	[mJy]	[mJy]	[mJy bm^{-1}]	[$M_\odot$]	[$M_\odot$]
TMC1A	04 39 35.20	+25 41 44.27	+6.6	118	2.7	0.45×0.25 (80)	164	450	780[e]	0.12	0.033
TMC1	04 41 12.70	+25 46 34.80	+5.2	101	0.9	0.8×0.3 (84)	22	300	380[d]	0.14	0.0039
TMR1	04 39 13.91	+25 53 20.57	+6.3	133	3.8	0.2	50	440	480[e]	0.10	0.011
L1536[f]	04 32 32.07	+22 57 26.25	+5.3	270	0.4	1.1×0.6 (69)	83	115	200[g]	...	0.021

[a] Values from Kristensen et al. (2012). [b] Gaussian fit is used for TMR1. [c] Integrated 1.3 mm flux from Motte & André (2001). [d] Peak flux of JCMT SCUBA maps from Di Francesco et al. (2008). [e] Peak flux from Jørgensen et al. (2009). [f] Position of L1536(W) is listed. [g] Peak flux from Young et al. (2003).
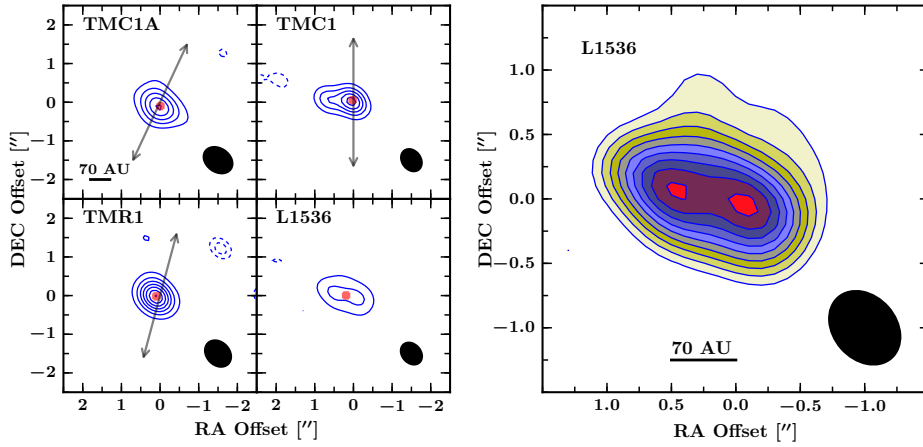

Figure 5.1 — *Left*: 1.36 mm uniform weighted continuum maps toward TMC1A (I4365+2535, top left), TMC1 (I4381+2540, top right), TMR1 (I4361+2547, bottom left), and L1536 (I4295+2251, bottom right). The contours start from 10σ up to 80σ by 10σ. The peak flux densities per beam are 11 mJy, 42 mJy, 23 mJy and 128 mJy for TMC1, TMR1, L1536 and TMC1A, respectively. The red circles indicate the best-fit source-position assuming elliptical Gaussian while the black ellipses show the synthesized beams. The arrows indicate the outflow direction. The RMS is given in Table 5.1. The dashed blue lines indicate the negative contours starting at 3σ. *Right*: Zoom of the continuum image toward L1536. Both of the line and color contours are drawn at 10% of the peak starting from 4σ up to the peak intensity of 23 mJy beam^{-1}, while the synthesized beam is indicated by the black ellipse in the bottom right corner.

5.2.2   WideX detections

The WideX correlators cover frequencies between 218.68 – 222.27 GHz. Strong molecular lines that are detected toward all of the sources within the WideX correlator include $C^{18}O$ 2–1 (219.5603541 GHz), SO 5_6–4_5 (219.9488184 GHz), and ^{13}CO 2–1 (220.3986841 GHz). The WideX spectra and integrated flux maps are presented in Appendix 5.C but not analyzed here.

5.3   Results

5.3.1   Continuum maps

Strong 1.36 mm continuum emission is detected toward all four sources up to $\sim$450 m baselines ($\sim$ 330 kλ, which corresponds to roughly 80 AU in diameter at the distance of Taurus). To estimate the continuum flux and the size of the emitting region, we performed elliptical Gaussian fits to the visibilities (> 25 kλ). The best fit parameters are listed in Table 5.2. Our derived PdBI

Table 5.3 — ^{13}CO and C^{18}O 2–1 integrated flux densities [Jy km s^{-1}] within a 5$''$ box around continuum position.

Line	Sources			
	TMC1A	TMC1	TMR1	L1536
^{13}CO 2–1[a]	12.2 ± 0.08	4.5 ± 0.07	10.5 ± 0.06	3.2 ± 0.08
C^{18}O 2–1[a]	5.3 ± 0.08	2.2 ± 0.09	3.0 ± 0.06	1.2 ± 0.08

[a] Integrated flux error is calculated through $1.2 \times \sigma_{\rm rms} \sqrt{FWZI \times \delta v}$. $FWZI$ is the full width zero intensity as calculated from the number of channels $> 5\sigma$.

1.36 mm fluxes are $< 30\%$ lower than the single-dish fluxes tabulated in Motte & André (2001). The only exception is L1536 for which 72% of the singe-dish flux is recovered, which indicates a lack of resolved out large-scale envelope around L1536. The deconvolved sizes indicate a large fraction of the emission is within < 100 AU diameter, consistent with compact flattened dust structures.

Figure 5.1 presents the uniform weighted continuum maps with red circles indicating the continuum positions (Table 5.2). The total flux of TMC1A is $\sim 30\%$ lower than in Yen et al. (2013) within a $4.0'' \times 3.5''$ beam, which indicates that some extended structure is resolved-out in our PdBI observations. The peak fluxes of our cleaned maps agree to within 15% with those reported by Eisner (2012) except toward L1536, which is a factor of two lower in our maps. However, our image toward L1536 (Fig. 5.1) shows that there are two peaks whose sum is within 15% of the peak flux reported in Eisner (2012). The position in Table 5.2 is centered on the Western peak and the two peaks are separated by ~ 70 AU. The analysis in the next section (Section 5.4) is with respect to the Western peak. The maps indicate the presence of elongated flattened structure perpendicular to the outflow direction found in the literature (TMC1: 0°; TMR1: 165°; TMC1A: 155°; L1536: None[2], Ohashi et al. 1997a; Hogerheijde et al. 1998; Brown & Chandler 1999). Such elongated dust emission is indicative of flattened disk-like structures.

5.3.2 Molecular lines: maps and morphologies

The ^{13}CO and C^{18}O 2–1 lines are detected toward all sources. Figure 5.2 presents the spectra integrated within a 1$''$ box around the continuum position. The integrated line flux densities within a 5$''$ box are tabulated in Table 5.3. The molecular line emission is strongest toward TMC1A and weakest toward L1536, while most of the emission around the systemic velocity is resolved out. This can be seen in the ^{13}CO channel map toward TMC1A (Figs. 5.2 and 5.3, see Appendix 5.A for channel maps toward other sources) where most of the emission is absent near $v_{\rm lsr} = 6.6$ km s^{-1}. In contrast to ^{13}CO, the C^{18}O line is detected around the systemic velocities (± 2 km s^{-1}) as shown in Fig. 5.2 except toward TMC1A, which shows emission within the velocity range comparable to that of ^{13}CO.

Single-dish observations of ^{13}CO $J =$3–2 (except for L1536, which is the $J =$2–1 transition) and C^{18}O $J =$2–1 are also shown in Fig. 5.2 (right). The comparison indicates that a large part of the emission at the systemic velocity originating from the large-scale envelope is filtered out in our PdBI observations. The PdBI spectra within a 1$''$ box around each source are also broader than the single-dish spectra. Thus, our PdBI observations are probing the kinematics within the inner few hundreds of AU.

The zeroth moment (i.e., velocity-integrated flux density) maps, are shown in Fig. 5.4 to-

---

[2]Recent ^{12}CO 3–2 observations with the JCMT do not show any indication of a bipolar outflow from this source, see Appendix 5.D.
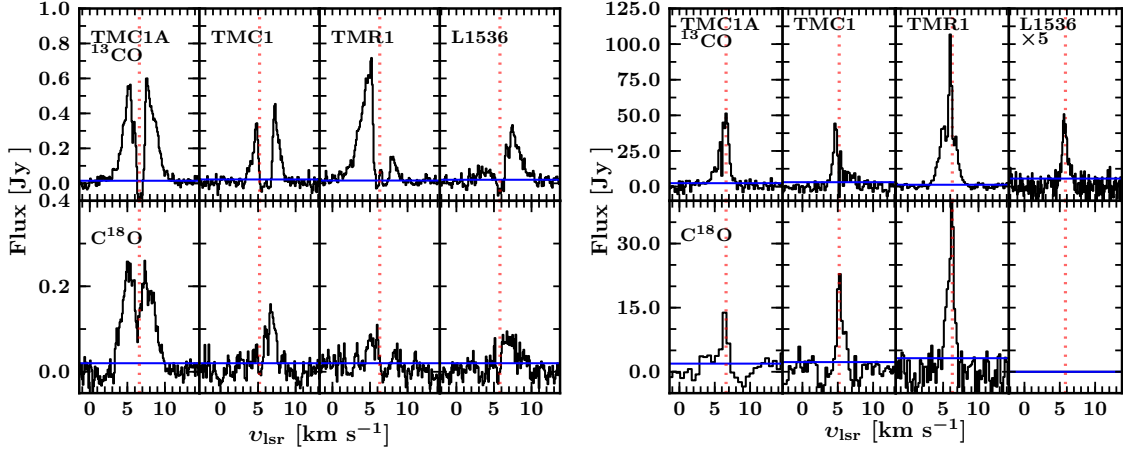
Figure 5.2 — *Left*: ^{13}CO (top) and C^{18}O 2–1 (bottom) spectra integrated within a 1″ box around the continuum position. Right: Single-dish spectra of ^{13}CO 3–2 (except for L1536, which is ^{13}CO 2–1) and C^{18}O 2–1. The vertical red dotted lines indicate the systemic velocities of each source derived from single dish C^{18}O and C^{17}O data (Yıldız et al. 2013). The horizontal blue lines indicate the spectral σ_{rms}.

ward all four sources. The morphologies of the ^{13}CO and C^{18}O maps are different toward 3 out of the 4 sources due to C^{18}O emission being weaker. Only toward TMC1A, which has the strongest C^{18}O emission, do the C^{18}O and ^{13}CO show a similar morphologies. In general, the zeroth moment maps indicate the presence of flattened gas structures that are perpendicular to the outflow direction except for TMR1. In most cases, the C^{18}O emission is weak and compact toward the continuum position as revealed by our higher S/N spectrally unresolved spectra taken with the WideX correlator (bottom panels of Fig. 5.4).

Moment one (i.e., intensity-weighted average velocity) maps are presented in Figure 5.5
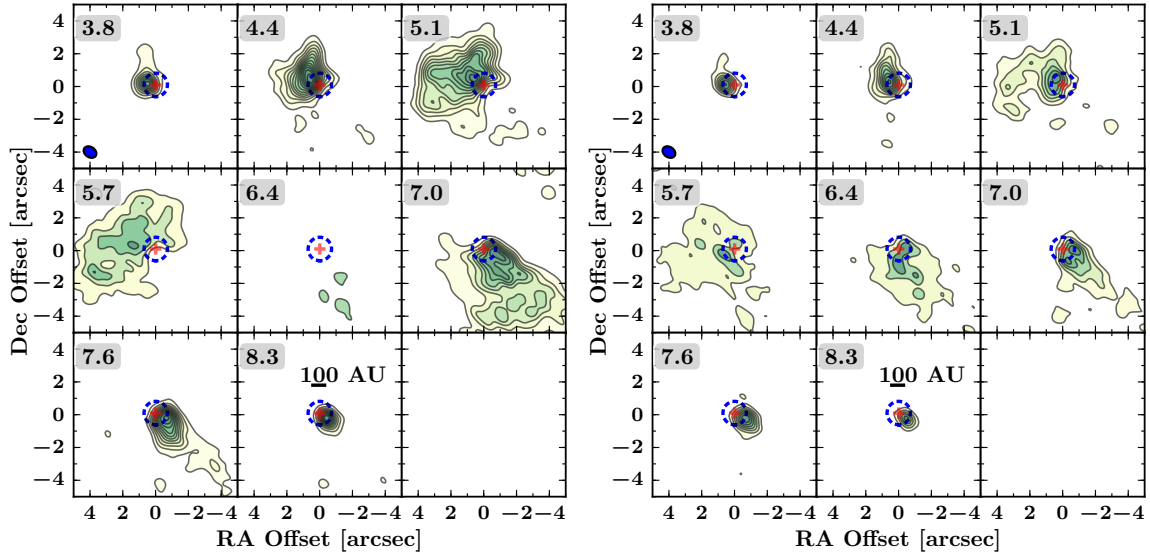

Figure 5.3 — ^{13}CO (left) and C^{18}O (right) 2–1 channel maps within the inner 10″ toward TMC1A. The velocities in km s^{-1} are indicated at the top left in each panel. The contours are drawn at every 3σ starting from 5σ where $\sigma = 12$ mJy km s^{-1} for ^{13}CO and 10 mJy km s^{-1} for C^{18}O.
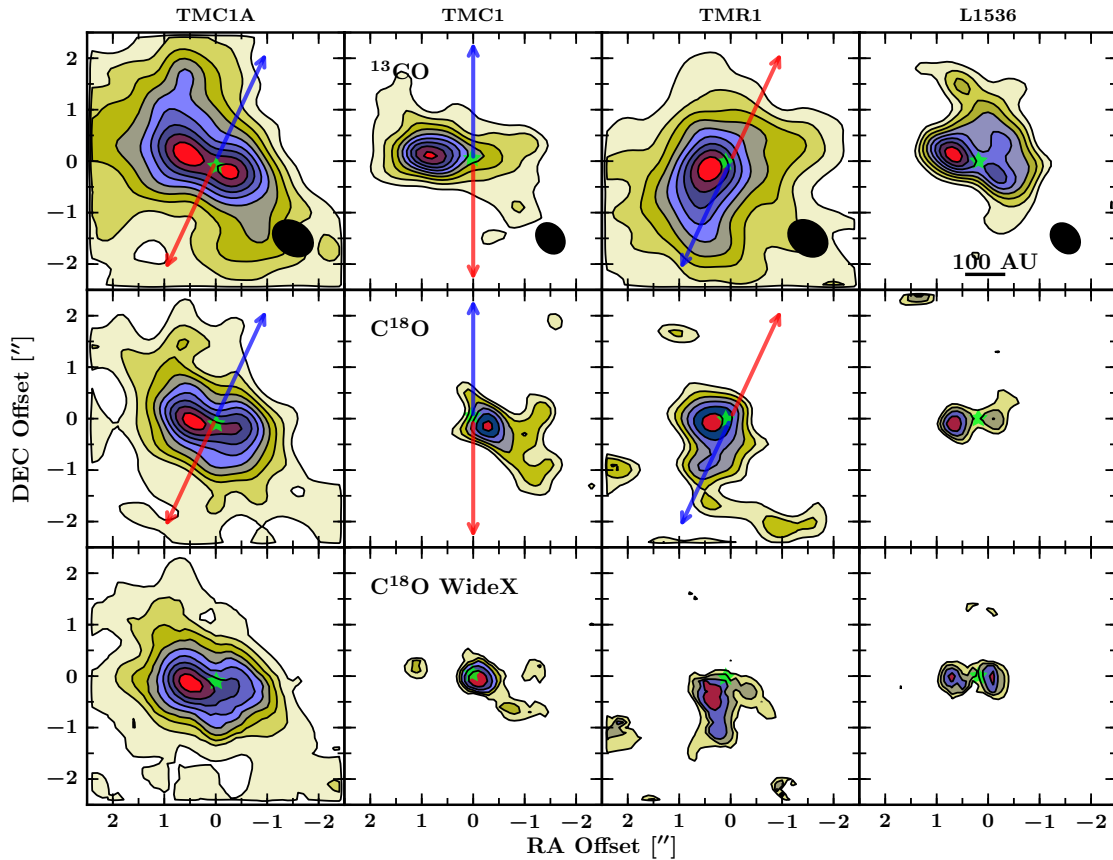
Figure 5.4 — ^{13}CO (top) and C^{18}O (bottom) moment zero maps. The contours are drawn at intervals of 10% of the peak starting from 5σ. The continuum position is indicated by the green stars and the arrows show the direction of the red and blue-shifted outflow components taken from the literature (TMC1: $0°$; TMR1: $165°$; TMC1A: $155°$; L1536: None Ohashi et al. 1997a; Hogerheijde et al. 1998; Brown & Chandler 1999). The bottom row show C^{18}O integrated flux maps from the velocity unresolved spectra (typically 1–2 channels) taken within the WideX with contours of 10% of the peak starting from 3σ ($\sim$30 mJy beam^{-1} km s^{-1}). The zero moment maps are obtained by integrating over the velocity ranges $[v_{min}, v_{max}]$ = [-3, 11], [-1, 11], [-2, 12], [-2, 12] for TMC1A, TMC1, TMR1, and L1536, respectively.

and show the presence of velocity gradients in the inner few hundreds of AU. These velocity gradients are perpendicular to the large-scale outflow. Large-scale rotation around TMC1A was reported previously by Ohashi et al. (1997a) extending up to 2000 AU. In addition, Hogerheijde et al. (1998) also detected rotation around TMC1. The high sensitivity and spatial resolution of our observations allow us to map the kinematics on much smaller scales and therefore unravel the nature of these gradients.

5.4 Analysis

5.4.1 Continuum: Dust disk versus envelope

The advantage of an interferometric observation is that one can disentangle the compact disk-like emission from the large-scale envelope. Thus, an estimate of the disk mass can be obtained using both the single-dish and the spatially resolved continuum observations (visibility amplitudes). Figure 5.6 shows the circularly averaged visibility amplitudes as a function of the projected baselines in kλ (assuming spherically symmetric emission). All sources show strong
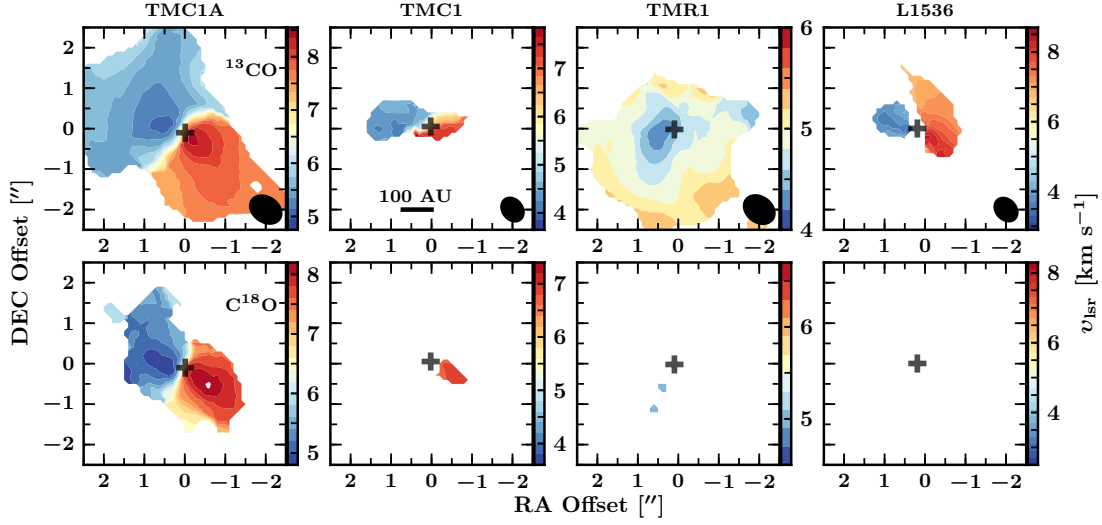
Figure 5.5 — ^{13}CO and C^{18}O moment 1 maps within the inner $5''$ (700 AU). The solid line indicate the 100 AU scale and the ellipses show the synthesized beams. The gray crosses show the continuum positions.

emission on long baselines that is near constant with increasing baseline. The continuum visibilities of TMR1 and TMC1A are consistent with the scaled ($F_\nu \propto \nu^\alpha$) 1.1 mm SMA observations (red circles, Jørgensen et al. 2009) with $\alpha = 2.5$. An excess of continuum emission at the longest baselines compared with the expected noise is seen toward all sources, which corresponds to unresolved continuum structure at scales smaller than 320 kλ (50 AU radius). Moreover, rapidly increasing amplitudes at short baselines are typically associated with the presence of a large-scale envelope. This combination of features in the visibilities is a typical signature of embedded disks (e.g., Looney et al. 2003; Jørgensen et al. 2005a; Enoch et al. 2009).

The first important step is quantifying the large-scale envelope contribution to the uv amplitudes. Using radiative transfer models, Jørgensen et al. (2009) estimated that a spherical envelope contributes at most 4% at 50 kλ at 1.1 mm, which translates to 2% at 1.36 mm. By using the single-dish 850 μm ($S_{15''}$) and the 50 kλ fluxes ($S_{50k\lambda}$), the envelope, S_{env}, and disk, S_{disk}, flux densities can be estimated by solving the following system of equations (Eqs. 2 and 3 in Jørgensen et al. 2009):

$$S_{50k\lambda} = S_{\text{disk}} + c \times S_{\text{env}} \tag{5.1}$$
$$S_{15''} = S_{\text{disk}}(1.36/0.85)^\alpha + S_{\text{env}}. \tag{5.2}$$

We have adopted $\alpha \simeq 2.5$ to translate the 850 μm disk flux to 1.36 mm (Jørgensen et al. 2007) and $c = 0.02$ as the fractional envelope contribution. The derived disk masses within 100 AU diameter are tabulated in Table 5.2 using the OH5 (Ossenkopf & Henning 1994) opacities at 1.36 mm and a dust temperature of 30 K. Our values for TMR1 and TMC1A are consistent with Jørgensen et al. (2009). The envelope masses listed in Table 5.2 were estimated using Equation (1) of Jørgensen et al. (2009). Three of the sources (TMC1, TMR1, TMC1A) have similar envelope masses of $\sim 0.1\ M_\odot$, which are higher than the disk masses. In contrast, at most a tenuous envelope seems to be present around L1536. Using the disk to envelope mass ratio as an evolutionary tracer, L1536 is the most evolved source in our sample, which is consistent with its high bolometric temperature. Thus, these sources are indeed near the end of the main accretion phase where a significant compact component is present in comparison to their large-scale envelope.

In interferometric observations toward YSOs, the lack of short baselines coverage may result in underestimation of the large-scale emission and, consequently, overestimating the compact structure. Kristensen et al. (2012) calculated 1D spherically symmetric models derived using the 1D continuum radiative transfer code DUSTY (Ivezic & Elitzur 1997) for a number of sources, including TMC1A, TMR1 and TMC1. The model is described by a power law density structure with an index p ($n = n_0(r/r_0)^{-p}$) where n is the number density and with an inner boundary r_0 at $T_{dust} = 250$ K. The parameters are determined through fitting the observed spectral energy distribution (SED) and the 450 and 850 μm dust emission profiles. These parameters are tabulated in Table 5.9. The models in Kristensen et al. (2012) do not take into account the possible contribution by the disk to the submillimeter fluxes and the envelope masses are consequently higher than ours by up to a factor of 2. Using these models, the missing flux can be estimated by modelling the large-scale continuum emission as it would be observed by the interferometer (blue line in Fig. 5.6). We can therefore place better constraints on the compact flattened structure.

5.4.2 Constraining the dust disk parameters

The goal of this section is to estimate the size and mass of the compact flattened dust structure or the disk using a number of more sophisticated methods than Eq. (1) and (2) to compare with the estimates from the gas in the next section. We define the disk component to be any compact flattened structure that deviates from the expected continuum emission due to the spher-
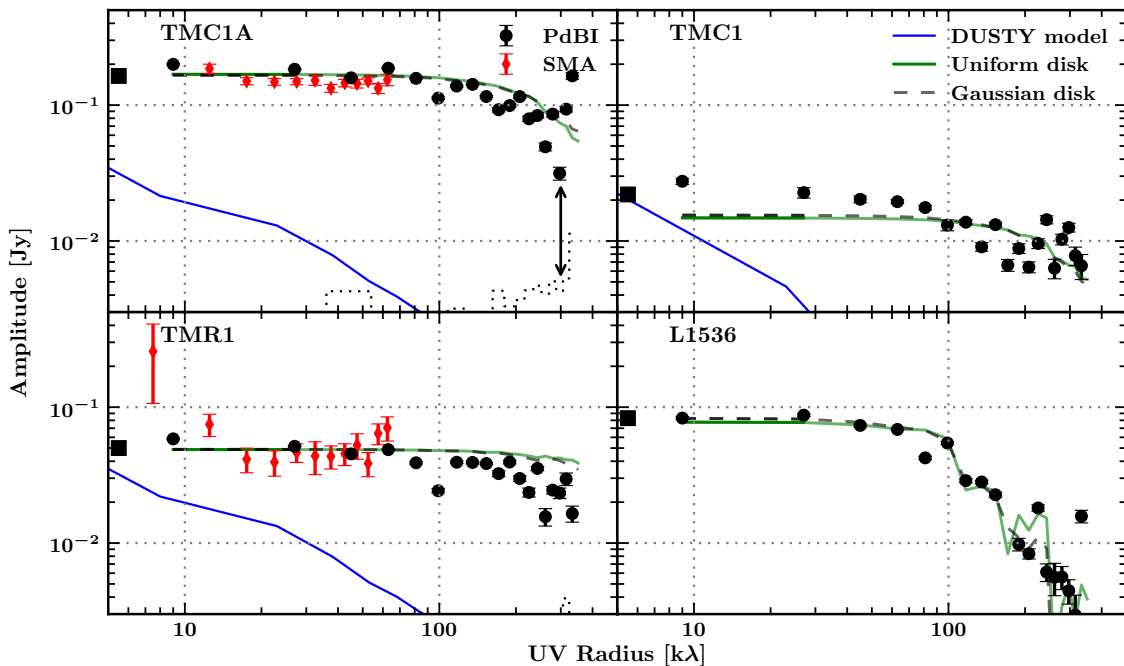
Figure 5.6 — Circularly averaged 1.36 mm visibility amplitudes as function of projected baselines in kλ. The black circles are from this work while the red circles are from previous SMA observations at 1.1 mm (Jørgensen et al. 2009) scaled to 1.36 mm with $\alpha = 2.5$. The error bars indicate the statistical errors of each bin. The blue line is the simulated continuum emission of the spherical envelope model from Kristensen et al. (2012) sampled using the observed uv points. An arrow in the first panel shows an example of the continuum excess toward TMC1A. Solid squares are the 1.36 mm single-dish flux. The zero-expectation level given in dotted line is the expected amplitude due to noise in the absence of source emission.

Table 5.4 — Disk sizes and masses derived from continuum visibilities modelling using uniform, Gaussian and power-law disk models.

Object	Parameters			
	R_{disk}	M_{disk}	i	PA
	[AU]	$[10^{-3}\,\mathrm{M}_\odot]$	[°]	[°]
Uniform disk				
TMC1A	$30-50$	48 ± 6	20–46	60–99
TMC1	$7-124$	4.7^{+4}_{-2}	30–70	65–105
TMR1	$7-40$	15 ± 2	5–30	-15–15
L1536	$100-171$	22 ± 5	30–73	60–100
Gaussian disk				
TMC1A	$17-32$	48 ± 6	24–56	62–96
TMC1	$7-80$	4.5^{+4}_{-2}	30–70	65–105
TMR1	$7-20$	15 ± 2	5–30	-15–15
L1536	$53-112$	24 ± 4	33–75	60–100
Power-law disk				
TMC1A	$80-220$	41 ± 8	24–76	60–99
TMC1	$41-300$	5.4^{+20}_{-0}	20–80	55–115
TMR1	$7-55$	10^{+100}_{-9}	2–45	-25–40
L1536	$135-300$	19^{+18}_{-4}	20–56	50–68

ical envelope model. In the following sections, the disk sizes will be estimated by fitting the continuum visibilities with the inclusion of emission from the large-scale structure described above. As the interferometric observation recovers a large fraction of the single-dish flux toward L1536, its large-scale envelope contribution is assumed to be insignificant, and therefore not included. The best-fit parameters are found through χ^2 minimization on the binned amplitudes. The range of values of R_{disk}, M_{disk}, i and PA shown in Table 5.4 correspond to models with χ^2 between χ^2_{min} and $\chi^2_{\mathrm{min}}+15$.

5.4.2.1 Uniform disk

The first estimate on the disk size and mass is obtained by fitting a uniform disk model assuming optically thin dust emission (see Fig. 5.7, Eisner 2012). Uniform disks are described by a constant intensity I within a diameter θ_{ud} whose flux is given by $F = \int I \cos\theta \, d\Omega = I\pi \left(\frac{\theta_{\mathrm{ud}}}{2}\right)^2$. The visibility amplitudes are given by:

$$V(u,v) = F \times 2\frac{J_1\left(\pi\theta r_{uv}\right)}{\pi\theta r_{\mathrm{uv}}}, \tag{5.3}$$
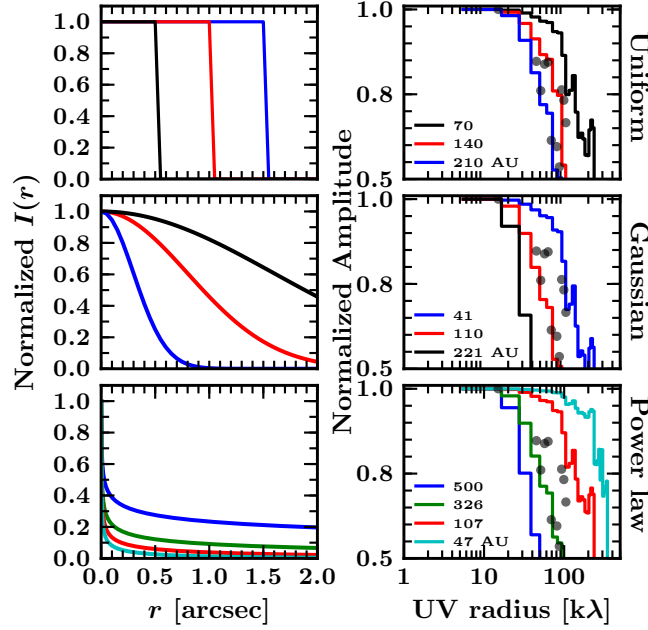
Figure 5.7 — Left: Normalized intensity profiles for the three different continuum models: Uniform disk (top), Gaussian Disk (middle), and power-law disk (bottom). Right: Normalized visibilities as function of uv radius. For comparison, the L1536 binned data are shown in gray circles.

where J_1 is the Bessel function of order 1 and r_{uv} is the projected baseline in terms of λ. Deprojection of the baselines follow the formula given in Berger & Segransan (2007):

$$u_{\mathrm{PA}} = u \cos PA + v \sin PA, \tag{5.4}$$

$$v_{\mathrm{PA}} = -u \sin PA + v \cos PA, \tag{5.5}$$

$$r_{uv,i} = \sqrt{(u_{\mathrm{PA}}^2 + v_{\mathrm{PA}}^2 \cos(i)^2)}, \tag{5.6}$$

where PA is the position angle (East of North) and i is the inclination.

The best fit parameters are tabulated in Table 5.4 with disk masses estimated using a dust temperature of 30 K and OH5 opacities (Table 5 of Ossenkopf & Henning 1994) within $\frac{\theta_{\mathrm{ud}}}{2}$ radius. The disk radii vary between 7 to 171 AU. The smallest disk size is found toward TMR1, which suggests that most of its continuum emission is due to the large-scale envelope. Moreover, disk sizes around TMR1 and TMC1A are 65%–90% lower than those reported by Eisner (2012, Table 3) since we have included the spherical envelope contribution. This illustrates the importance of including the large-scale contribution in analyzing the compact structure.

5.4.2.2 Gaussian disk

The next step is to use a Gaussian intensity distribution, which is a slightly more realistic intensity model that represents the mm emission due to an embedded disk. The visibility amplitudes are described by the following equation:

$$V(u,v) = F \times \exp\left(-\frac{\pi \theta_{\mathrm{G}} r_{uv}}{4 \log 2}\right), \tag{5.7}$$

where θ_{G} is the $FWHM$ of the Gaussian distribution and F is the total flux.

The difference between the Gaussian fit presented in Table 5.2 and this section is the inclusion of the large-scale emission. In Table 5.2, the Gaussian fit gives an estimate of the size of emission in the observed total image, while this section accounts for the simulated large-scale envelope emission in order to constrain the compact flattened structure. The free-parameters are similar to the uniform disk except that the size of the emitting region is defined by full-width half maximum ($FWHM$). For a Gaussian distribution, most of the radiation (95%) is emitted from within $2\sigma_G \sim 0.85 \times FWHM$, thus we define the disk radius to be $0.42 \times FWHM$. The best-fit parameters are tabulated in Table 5.4 and the corresponding emission is included in Fig. 5.6. The resulting disk sizes are slightly lower than those derived using a uniform disk.

The visibility amplitudes in Fig. 5.6 show the presence of an unresolved point source component at long baselines indicated by the arrow in the first panel. Jørgensen et al. (2005a) noted that a three components model (large-scale envelope + Gaussian disk + point-source) fits the continuum visibilities. By using such models, the disk sizes generally increase by 20–30 AU with the addition of an unresolved point flux, which is comparable to the uniform disk models. Such models were first introduced by Mundy et al. (1996) since the mm emission seems to be more centrally peaked than a single Gaussian. The unresolved point flux is more likely due to the unresolved disk structure since the free-free emission contribution is expected to be low toward Class I sources (Hogerheijde et al. 1998).

5.4.2.3 Power-law disk

The next step in sophistication is to fit the continuum visibilities with a power-law disk structure. The difference is that the first two disk models are based on the expected intensity profile of the disk, while the power-law disk models use a more realistic disk structure. Similar structures were previously used by Lay et al. (1997, see also Lay et al. 1994; Mundy et al. 1996; Dutrey et al. 2007; Malbet et al. 2005). We adopt a disk density structure described by $\Sigma_{\text{disk}} = \Sigma_{50\text{AU}} (R/50\text{AU})^{-p}$ where $\Sigma_{50\ \text{AU}}$ is the surface density at 50 AU with a temperature structure given as $T_{\text{disk}} = 1500 (R/0.1\text{AU})^{-q}$. The inner radius is fixed at 0.1 AU with a dust sublimation temperature of 1500 K, while the disk outer radius is defined at 15 K. The free parameters are p, q, $\Sigma_{50\text{AU}}$, i and PA where i is the inclination with respect of the plane of the sky in degrees ($0°$ is face-on) and PA is the position angle (East of North). The visibilities are constructed by considering the flux from a thin ring given by:

$$dS = \frac{2\pi \cos i}{d^2} B_\nu(T) \left(1 - \exp^{-\tau}\right) R \, dR, \tag{5.8}$$

where d is the distance, i is the inclination ($0°$ is face-on), $\tau = \frac{\Sigma(R)\kappa}{\cos i}$ is the optical depth and $B_\nu(T)$ is the Planck function. For the dust emissivity (κ), we adopt the OH5 values. Since the model is axisymmetric, the visibilities are given by a one-dimensional Hankel transform which is given by the analytical expression:

$$V(u,v) = dS \times J_0 \left(2\pi R r_{uv}\right), \tag{5.9}$$

where J_0 is the Bessel function of order 0. The total amplitude at a given r_{uv} is integrated over the whole disk.

The first advantage of such modelling is the treatment of the optical depth which gives better mass approximations. Secondly, the unresolved point-flux is already included in the model by simulating the emission from the unresolved disk component. Figure 5.7 shows the normalized visibilities for a fixed $p = 0.9$ and a number of R_{disk}. The best-fit parameters are tabulated in Table 5.4.

The derived disk masses obtained by integrating out to ~ 50 AU radius are similar to those from the 50 kλ point (Table 5.2). This is expected as the 1.3 mm continuum emission ($\kappa_{\text{OH5}} = 0.83$ cm^{2}g^{-1}) is on average nearly optically thin (Jørgensen et al. 2007). The optical depth can be up to 0.4 at radii < 10 AU for the best-fit power-law disk models with $i > 70°$. A wide range of 'best-fit' masses is found toward TMR1, which is mainly due to the uncertainties in the inclination.

More recently, Eisner (2012) presented embedded disk models derived from continuum data by fitting the *I* band image, SED and 1.3 mm visibilities. Our continuum disk radii toward TMC1A and TMR1 are consistent with their results. However, the high quality of our data allow us to rule out disks with $R_{\text{out}} > 100$ AU toward TMR1. On the other hand, our disk radius toward L1536 is a factor of 3 higher than that reported in Eisner (2012) due to the difference in the treatment of the large-scale envelope.

In summary, different methods have been used to constrain the disk parameters from thermal dust emission. The first two models, Gaussian and uniform disk models, are based on the intensity profile, while the power-law disk models use a simplified disk structure with given density and temperature profiles. The intensity based models find the smallest disk sizes, while the power-law disk models predict up to a factor of two larger disk sizes. On the other hand, the disk masses from these fitting methods are similar. The advantage of the power-law disk modeling is the determination of the density and temperature structures including the unresolved inner part of the disk. The continuum images provide no kinematic information, however, so the important question is whether these flattened structures are rotationally supported disks and if so, whether the continuum sizes agree with those of RSDs.

5.4.3 Line analysis: Keplerian or not?

The nature of the velocity gradient can already be inferred from the moment maps. First, the ^{13}CO integrated flux maps shown in Fig. 5.4 indicate the presence of flattened gas structures perpendicular to the outflow direction. Second, the velocity gradient is also oriented perpendicular to the outflow within hundreds of AU, which is a similar size scale to the compact dust structure measured in Section 5.4.2. On the other hand, the velocity gradient does not show a straight transition from the red to the blue shifted component as expected from a Keplerian disk. Taking TMC1A as an example, the blue-shifted emission starts at the North side and skews inward toward the continuum position. Such a skewed moment 1 map is expected for a Keplerian disk embedded in a rotating infalling envelope (Sargent & Beckwith 1987; Brinch et al. 2008). Thus, the moment maps indicate the presence of a rotating infalling envelope leading up to a rotationally dominated structure.

In image space, position velocity (PV) diagrams are generally used to determine the nature of the velocity gradient. Analysis of such diagrams starts by dividing it into four quadrants around the v_{lsr} and source position. A rotating structure occupies two of the four quadrants that are symmetric around the center, while an infalling structure will show emission in all quadrants (e.g., Ohashi et al. 1997a; Brinch et al. 2007b). In addition, one can infer the presence of outflow contamination by identifying a velocity gradient in PV space along the outflow direction (e.g., Cabrit et al. 1996).

Figure 5.8 presents PV diagrams at a direction perpendicular to the outflow direction; for L1536, the direction of elongation of the continuum was taken. In general, the PV diagrams are consistent with Keplerian profiles, except for TMR1. The PV diagram toward TMR1 seems to indicate that the ^{13}CO line is either dominated by infalling material or the source is oriented toward us, which is difficult to disentangle. However, recent ^{12}CO 3–2 and 6–5 maps presented in Yıldız et al. (in prep.) suggest that the disk is more likely oriented face-on ($i < 15°$). Further-
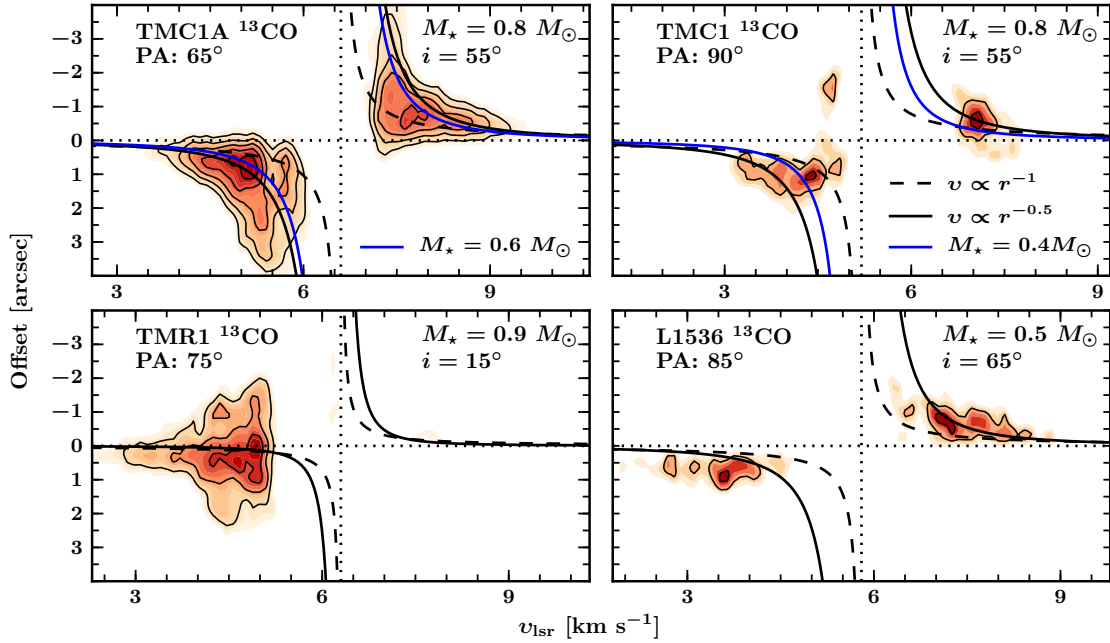
Figure 5.8 — ^{13}CO position velocity diagrams along the direction perpendicular to the outflow: TMC1A (top left), TMC1 (top right), TMR1 (bottom left), and L1536 (bottom right). The color contours start from 3σ and increase by 1σ while the black line contours are drawn at 5σ, 8σ, 11σ, and so on up to the peak intensity. The black solid curves show the best-fit Keplerian curves, while the dashed lines indicate the r^{-1} curves. For TMC1A and TMC1 (top row), the blue solid line presents a $0.4\ M_\odot$ Keplerian curve.

more, a velocity gradient is present in the ^{13}CO PV analysis both along and perpendicular to the outflow direction indicating minor outflow contamination for this source.

The focus of this paper is to differentiate between the infalling gas and the rotationally supported disk. Such analysis in image space is not sensitive to the point where the infalling rotating material ($v \propto r^{-1}$) enters the disk and becomes Keplerian ($v \propto r^{-0.5}$). Thus, additional analysis is needed to differentiate between the two cases.

As pointed out by Lin et al. (1994), infalling gas that conserves its angular momentum exhibits a steeper velocity profile ($v \propto r^{-1}$) than free-falling gas ($v \propto r^{-0.5}$). In the case of spectrally resolved optically thin lines, the peak position of the emission corresponds to the maximum possible position of the emitting gas (Sargent & Beckwith 1987; Harsono et al. 2013). On the other hand, molecular emission closer to the systemic velocity is optically thick and, consequently, the inferred positions are only lower limits. Thus, with such a method, one can differentiate between the Keplerian disk and the infalling rotating gas. Moreover, Harsono et al. (2013) suggested that the point where the two velocity profiles meet corresponds to the size of the Keplerian disk, $R_{\rm k}$. In the following sections, we will attempt to constrain the size of the Keplerian disk using this method, which we will term the uv-space PV diagram.

The peak positions are determined by fitting the velocity resolved visibilities with Gaussian functions (Lommen et al. 2008; Jørgensen et al. 2009). It can be seen from the channel maps (Fig. 5.3 and Appendix A) that a Gaussian brightness distribution is a good approximation in determining the peak positions of the high velocity channels.

To characterize the profile of the velocity gradient, the peak positions are projected along
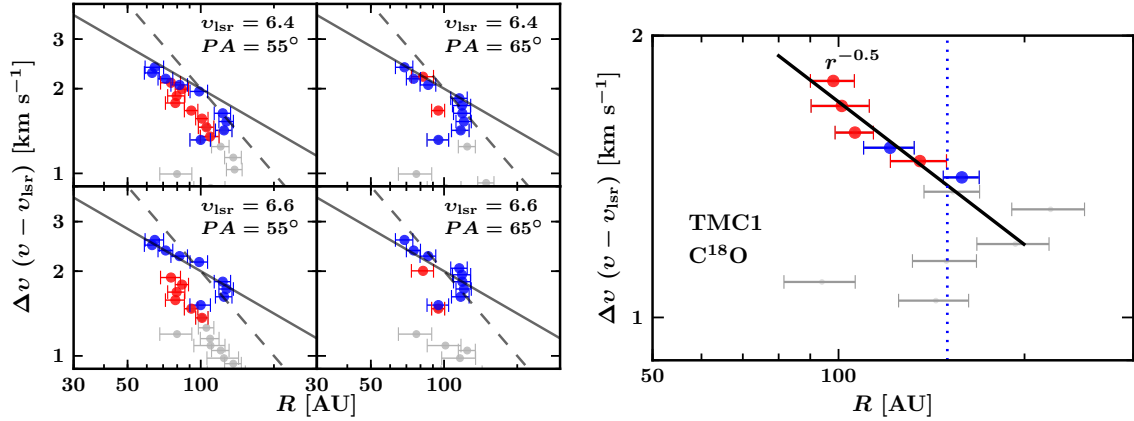
Figure 5.9 — *Left*: $C^{18}O$ *uv*-space PV diagrams toward TMC1A with $PA = 55°, 65°$ and $v_{lsr} = 6.6, 6.4 \, \mathrm{km \, s^{-1}}$. The solid lines are the $r^{-0.5}$ curves and dashed lines are the r^{-1} curves. The red and blue colors indicate the red- and blue-shifted components, respectively. Gray points show the rest of the peaks that were not included in the fitting. *Right*: $C^{18}O$ *uv*-space PV diagrams toward TMC1 derived from the emission peaks. The solid line indicates the best-fit power-law slope to the peaks between 1.3–1.9 $\mathrm{km \, s^{-1}}$. The vertical blue dotted lines indicate the 150 AU radius. The red and blue colors indicate the red- and blue-shifted components, respectively.

the velocity gradient. This is done by using the following transformation

$$x_{PA} = x \cos(PA) + y \sin(PA), \tag{5.10}$$
$$y_{PA} = -x \sin(PA) + y \cos(PA), \tag{5.11}$$

where x, y are the peak positions and x_θ, y_θ are the rotated positions. A velocity profile ($v \propto r^{-\eta}$) is then fitted to a subset of the red- and blue-shifted peaks to determine the best velocity profile.

5.4.3.1 TMC1A

TMC1A shows the greatest promise so far for an embedded Keplerian disk around a Class I protostar . The moment 1 maps (Fig. 5.5) indicate a gradual change from blue- to red-shifted gas in the inner few hundreds of AU, which is consistent with a Keplerian disk. Figure 5.9 presents the $C^{18}O$ velocity profiles using the nominal v_{lsr} and PA perpendicular to the outflow direction along with small deviations from those values, which correspond to the uncertainty in outflow direction. In the absence of foreground clouds, one expects that the blue and red-shifted peaks overlap for a rotating system, which is the case if one adopts $v_{lsr} = +6.4 \, \mathrm{km \, s^{-1}}$. The $C^{18}O$ and $C^{17}O$ observations presented in Jørgensen et al. (2002) indicate a $v_{lsr} = +6.6 \, \mathrm{km \, s^{-1}}$, however $v_{lsr} = +6.4 \, \mathrm{km \, s^{-1}}$ is consistent with the N_2H^+ observations toward the nearby L1534 core (Caselli et al. 2002). For comparison, the ^{13}CO velocity profile with $v_{lsr} = +6.4 \, \mathrm{km \, s^{-1}}$ and PA perpendicular to the outflow direction is shown in Fig 5.10. Both of the ^{13}CO and $C^{18}O$ lines show a velocity profile close to $v \propto r^{-0.5}$, which indicates that the gas lines trace similar rotationally supported structures. The typical uncertainty in the power-law slope is ± 0.2. In the region where the red- and blue-shifted peaks overlap, a clear break from $r^{\sim -0.5}$ to a steeper slope of r^{-1} can be seen at ~ 100 AU. This break may shift inward at other PAs and v_{lsr} to 80 AU. However, it is clear that the flattened structure outside of 100 AU flattened structure is dominated by infalling rotating motions. Thus, the embedded RSD toward TMC1A has a radius between 80–100 AU.

To derive the stellar mass associated with the rotationally dominated region, simultaneous fitting to the PV diagrams in both image and *uv* space has been performed. The best-fit stellar

mass associated with the observed rotation toward TMC1A is $0.53^{+0.2}_{-0.1}\,M_\odot$ at $i = 55° \pm 10°$.

Additional analysis is performed for TMC1A with a simple radiative transfer model to confirm the extent of the Keplerian disk following a method similar to that used by Murillo et al. (2013) for the VLA 1623 Class 0 source. Such fitting is only performed for this source to investigate whether they give similar results. A flat disk model given by:

$$ T = T_0 \, (r/r_0)^{-q}, \tag{5.12} $$
$$ N = N_0 \, (r/r_0)^{-p}, \tag{5.13} $$

where N is the gas column density with T_0 and N_0 as the reference gas temperature and column densities, respectively, at the reference radius, r_0. Similar to the power-law disk models in Section 5.4.2.3, we have used $T_0 = 1500$ K at r_0 of 0.1 AU. The images are then convolved with the clean beams in Table 5.1. We have assumed $i = 55°$ and $PA = 65°$. For such orientation, we find that a Keplerian structure within the inner 100 AU is needed, surrounded by a rotating infalling envelope. The radius of the Keplerian structure is similar to the radius derived from previous methods ($\sim$ 100 AU), however, a stellar mass of $0.8 \pm 0.3\,M_\odot$ is needed to reproduce the observed molecular lines. This is consistent with Yen et al. (2013) calculated at $i = 30°$, but a factor of 1.5 higher than the value obtained earlier (although the two values agree within their respective uncertainties).

5.4.3.2 TMC1

The velocity profile for TMC1 projected along $PA = 90°$ is shown in Figure 5.10 for ^{13}CO. The moment maps toward this source indicate the presence of a compact flattened structure around
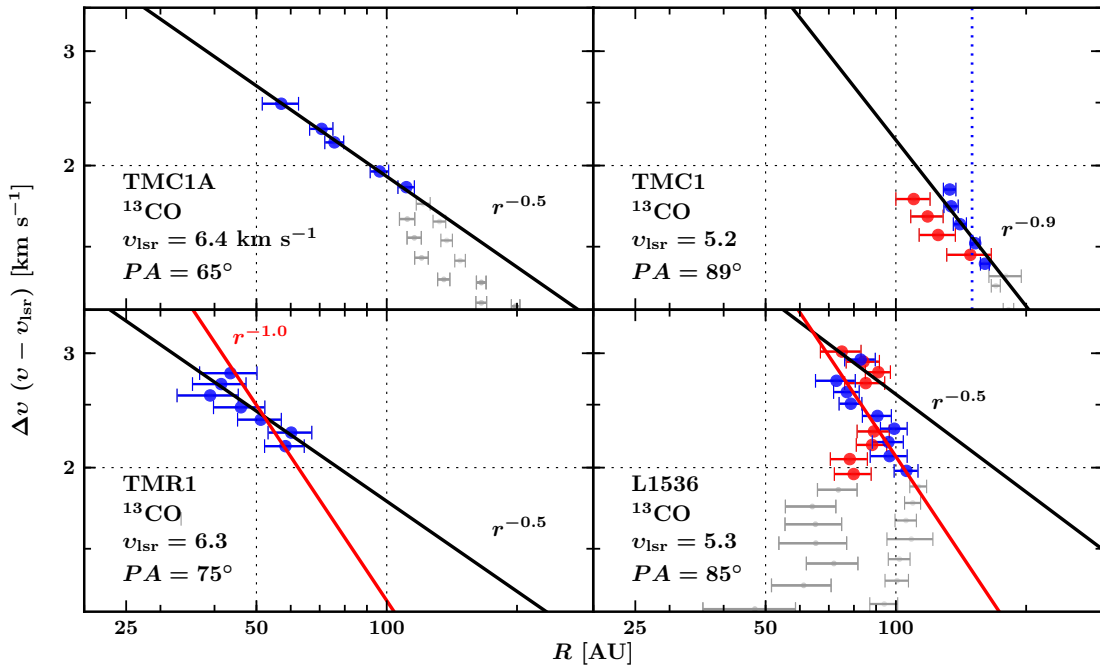

Figure 5.10 — ^{13}CO uv-space PV diagrams toward all sources with the best fit profiles superposed in black lines (except for L1536). The red lines indicate a $v \propto r^{-1}$ as comparison. Gray points show the peaks that were not included in the fitting.

the continuum position. Similar to TMC1A, the PV diagram also indicates a rotationally dominated structure. However, in contrast to TMC1A, the ^{13}CO line is best described by an r^{-1} profile indicating that it traces infalling rotating gas, while the C^{18}O line is fitted well with a $r^{-0.5}$ slope as shown in Fig. 5.9 indicative of an RSD. Such discrepancy can occur if the two lines are tracing different regions. The moment zero maps in Fig. 5.4 already gave some indication that the ^{13}CO and C^{18}O emissions do not arise from similar structure. Furthermore, the disk mass toward TMC1 as inferred through the continuum is the lowest in our sample, hence it is also possible that the embedded RSD is not massive enough to significantly contribute to both the ^{13}CO and C^{18}O emission. The relatively more optically thick ^{13}CO traces the inner envelope and thus is dominated by its kinematics, while the rotationally supported structure significantly contributes to the C^{18}O line. A smooth extrapolation of the envelope down to 100–150 AU scales predicts C^{18}O emission $< 18\%$ of the observe emission at > 1.5 km s^{-1}, suggesting that the majority of the emission at these velocities originates in a disk (see also models by Harsono et al. 2013, figure 8). Hence, using the C^{18}O line, the fit indicates the presence of an RSD extending between 100–150 AU in radius. The best-fit stellar mass is $0.54^{+0.2}_{-0.1}$ $M_{\odot}$ at $i = 55°$ with typical error of ± 0.2 km s^{-1} on the determination of v_{lsr}. The stellar mass is a factor of 1.5 lower than that previously derived by Hogerheijde et al. (1998) as indicated by the black lines in Fig. 5.8. However, a stellar mass of 0.4 $M_{\odot}$ also reasonably fits the ^{13}CO PV diagram. In addition, the discrepancy between the ^{13}CO and C^{18}O velocity profiles may suggest that the most stable RSD is less than the C^{18}O break point. Thus, we will use 100 AU as the size of the RSD toward TMC1.

5.4.3.3   TMR1

The determination of the velocity profile toward TMR1 is difficult. Adopting $v_{\mathrm{lsr}} = +6.3$ km s^{-1} (Kristensen et al. 2012; Yıldız et al. 2013), the red-shifted peaks do not coincide with the blue-shifted peaks as expected from a symmetric rotating infalling structure in the absence of foreground clouds. The ^{13}CO velocity profile is uncertain with a slope between 0.5 to 1 (Fig. 5.10). However, a velocity gradient is present in the PV analysis along and perpendicular to the outflow direction, which suggest outflow contamination toward TMR1. With the 5σ threshold used for this analysis, only 3 peaks are available in the C^{18}O line, which are located along the blue outflow lobe as inferred from the ^{12}CO $J =$3–2 and $J =$6–5 maps in Yıldız et al, in prep. The on-source C^{18}O line is detected within the WideX correlator, which is double peaked within 100 AU diameter (Fig. 5.4). Thus, the non-detection of the turn-over from r^{-1} to $r^{-0.5}$ indicates that the disk is much smaller than the synthesized beam ($< 0.7'' = 98$ AU diameter). Also, the RSD has to be less massive than TMC1 and TMC1A due to the lack of on-source C^{18}O emission and rotational motion. Thus, the compact flattened dust structure at > 50 kλ toward this source cannot be fully associated with an RSD. The molecular emission from TMR1 must be mostly due to the infalling rotating envelope and the entrained outflow gas similar to the conclusion of Jørgensen et al. (2009).

5.4.3.4   L1536

Figure 5.10 shows the uv-space PV diagram with systemic velocity of $v_{\mathrm{lsr}} = +5.3$ km s^{-1}. The peak positions were shifted to the center of the two peaks seen in the continuum (Fig. 5.1) and the C^{18}O integrated map (Fig. 5.4). The dominant motion at low velocity offsets ($\Delta v = \pm 2$ km s^{-1}) is infall, while a flatter slope with a power-law close to $r^{-0.5}$ best describes the high velocity components. If the peak positions were not shifted, only the blue-shifted peaks follow the $r^{-0.5}$ profile starting from 70–80 AU. The flat velocity profile is based on 4 points and it

Table 5.5 — Derived disk sizes and stellar masses from the break radius in the uv-space PV diagrams corrected for inclination.

	TMC1A	TMC1	TMR1	L1536
R_K [AU]	80–100	100	< 50	80
$M_\star$ [$M_\odot$]	$0.53^{+0.2}_{-0.1}$	$0.54^{+0.2}_{-0.1}$	...	0.7–0.8
i [°]	55	55	15	65

Table 5.6 — $C^{18}O$ $J =$2–1 integrated intensities within R_K box as defined in table 5.5. Disk masses [10^{-3} $M_\odot$] inferred from the gas lines and continuum.

	TMC1A	TMC1	TMR1	L1536
$\int S_\nu dv$[a] [Jy km s^{-1}]	1.93	0.63	0.26	0.17
$M_{\rm disk}$ gas	75	24	10	6.8
$M_{\rm disk}$ dust[b]	41–49	4.6–5.4	10–15	19–24

[a] Typical errors are 0.03–0.04 Jy km s^{-1}. [b] Disk masses from the range of dust masses obtained with the different methods in Sections 5.4.1 and 5.4.2 with a gas-to-dust ratio of 100.

does not show a very clear Keplerian disk profile such as seen toward TMC1A. From the high velocity peaks, the velocity profile seems to indicate a break at $\sim$80 AU.

5.4.4 Summary and stellar masses

Three out of the four Class I sources show clear indications of embedded RSDs. From the turn-over radius (from r^{-1} to $r^{-0.5}$), the radii of the Keplerian disks must be between 100–150 AU in TMC1, 80 AU toward L1536 and 100 AU toward TMC1A. Considering that the turnover radius is the outer radius of the embedded Keplerian disk, the stellar masses are derived from that radius and tabulated in Table 5.5. In the case of L1536, we chose the red-shifted peak (~ 3 km s^{-1}) at 70 AU as the turnover radius to determine the combined stellar masses. Thus, by obtaining the masses of the different components (envelope, disk, and star), it is now possible to place the sources in an evolutionary stage for comparison with theoretical models. The three sources are indeed in Stage I of the embedded phase, where the star has accreted most of its final mass.

The uv-space PV diagram assumes that the disk rotation is perpendicular to the outflow direction as inferred from large ^{12}CO maps, foreground clouds do not contaminate the molecular lines, and the source systemic velocity is well determined. Small systemic velocity shifts can indeed shift both the red-shifted and blue-shifted velocity profiles from $r^{-0.5}$ to a steeper slope. However, for the firm detection of an embedded RSD toward TMC1A, this does not significantly affect the break radius. Further observations at higher resolution and sensitivity are certainly needed to confirm the extent of the Keplerian disks toward all of these sources. However, we argue that even with the current data it is possible to differentiate the RSD from the infalling rotating envelope with spatially and spectrally resolved molecular line observations.

5.4.5 Disk gas masses

After determining the extent of the embedded Keplerian disks, their gas masses can be estimated from the $C^{18}O$ integrated intensities. The $J=$2–1 line is expected to be thermalized at the typical densities ($n_{H_2} > 10^7$ cm^{-3}) of the inner envelope due to the low critical density. The gas

mass assuming no significant freeze-out is then given by the following equation (Scoville et al. 1986; Hogerheijde et al. 1998; Momose et al. 1998):

$$M_{\text{gas}} = 5.45 \times 10^{-4} \frac{T_{\text{ex}} + 0.93}{\exp\left(-E_{\text{u}}/kT_{\text{ex}}\right)} \frac{\tau}{1 - \exp^{-\tau}} \int S_{\upsilon} d\upsilon \ M_{\odot}, \tag{5.14}$$

where h and k are natural constants, T_{ex} is the excitation temperature, τ is the line optical depth, E_{u} is the upper energy level in K and $\int S_{\nu} d\upsilon$ is the integrated flux densities in Jy km s^{-1} using a distance of 140 pc. The gas mass estimates of the disks inferred by integrating over a region similar to the extent of R_{K} in Table 5.5 are listed in Table 5.6 with $\tau = 0.5$ and $T_{\text{ex}} = 40$ K. The adopted excitation temperature comes from the expected C^{18}O rotational temperature within a $1''$ beam if a disk dominates such emission (Harsono et al. 2013). From the observed $\frac{^{13}\text{CO}}{\text{C}^{18}\text{O}}$ flux ratios, the $\tau_{^{13}\text{CO}}$ is estimated to be ≤ 4.0 with isotopic ratios of ^{12}C/^{13}C = 70 and ^{16}O/^{18}O = 550 (Wilson & Rood 1994). This implies that the C^{18}O is almost optically thin ($\tau_{\text{C}^{18}\text{O}} \leq 0.5$) and only a small correction is needed under the assumption that ^{13}CO and C^{18}O trace the same structure. Uncertainties due to the combined T_{ex} and τ result in a factor of ≤ 2 uncertainty in the derived disk masses. The gas disk masses toward TMC1A, TMC1 and TMR1 are at least a factor of 2 higher than the mass derived from the continuum data (assuming gas to dust ratio of 100). Since the velocity gradient is prominent in the moment one maps, there must be enough C^{18}O in the gas phase within the RSD in order to significantly contribute to the lines. This is consistent with the evolutionary models of Visser et al. (2009) and Harsono et al. (2013) where only a low fraction of CO is frozen out within the embedded disks unless $R_{\text{K}} > 100$ AU due to the higher luminosities. Only toward L1536, which is the most evolved source in our sample, is the gas mass a factor of 5 lower than the mass derived from the continuum. This would be consistent with CO starting to freeze-out within the disk near the end of the main accretion phase (Visser et al. 2009). Thus, the small differences between gas and dust masses indicate relatively low CO freeze-out in embedded disks.

5.5 Discussion

5.5.1 Disk structure comparison: dust versus gas

In this paper, we have determined the sizes of the disk-like structures around Class I embedded YSOs using both the continuum and the gas lines. The continuum analysis focuses on the extent of continuum emission excluding the large-scale emission, while the gas line analysis focuses on placing constraint on the size of the RSD. The continuum analysis utilizes both intensity based disk models and a simple disk structure (power-law disk model). The intensity based disk models give a large spread of disk radii toward all sources. On the other other hand, the best-fit radii of power-law disks are larger than the Keplerian disk toward TMR1 and L1536, while the values are comparable toward TMC1A and TMC1. Not all of the disk structure derived from continuum observations may be associated to an RSD.

The main caveat in deriving the flattened disk structure from continuum visibilities is the estimate of the large-scale envelope emission. It has been previously shown that the large-scale envelope can deviate from spherical symmetry (e.g., Looney et al. 2007; Tobin et al. 2010). Disk structures may change if one adopts a 2D flattened envelope structure due to the mass distribution at 50–300 AU scale. However, in this paper, we focused on the size of the flattened structure where any deviation from the spherically symmetry model gives an estimate of its size. For the purpose of this paper, a spherical envelope model is used to estimate the large-scale envelope contribution since it is simple, fits the observed visibilities at short baselines, and does not require additional parameters.

5.5.1.1   Comparison to disk sizes and masses from SED modelling

A number of 2D envelope and disk models have been published previously constrained solely using continuum data. More recently, Eisner (2012) used the combination of high resolution near-IR images, the SED and millimeter continuum visibilities to constrain the structures around TMR1, TMC1A and L1536. The size of his disk is defined by the centrifugal radius, which is the radius at which the material distribution becomes more flattened (Ulrich 1976). His inferred sizes are consistent with the extent of RSDs in our sample (TMR1: 30–450 AU; L1536: 30–100 AU; TMC1A: 100 AU), but our higher resolution data narrow this range. For the case of TMR1, we can definitely rule out any disk sizes > 100 AU.

Others have used a similar definition of the centrifugal radius using the envelope structure given by Ulrich (1976) with and without disk component (e.g., Eisner et al. 2005; Gramajo et al. 2007; Furlan et al. 2008). Thus, the value of R_c gives an approximate outer radius of the RSD. These models are then fitted to the SED and high resolution near-IR images without interferometric data. In general, the values of R_c derived from such models are lower (at least by factor of 2) than the extent of the RSDs as indicated by our molecular line observations. By trying to fit the models to the near-IR images which are dominated by the hot dust within the disk, they put more weight to the inner region. Thus, we argue that spatially resolved millimeter data are necessary in order to place better constraints on the compact flattened structure.

The disk masses derived in our work from both 50 kλ flux and uv modelling are consistent with each other. These values are typically higher by a factor of 2 and a factor of 8 for TMC1A[3] than the disk masses reported by Eisner (2012) and Gramajo et al. (2010,only toward TMR1). The discrepancy may be due to the difference in the combination of the assumed inclination, the adopted envelope structure, and definition of the flattened structure.

5.5.2   Constraints on disk formation

A number of RSDs toward other embedded YSOs have been reported in the literature, which are summarized in Table 5.7. The values are obtained from analysis that included interferometric molecular line observations. Keplerian radii, R_K, between 80 and 300 AU are found toward these sources with disk masses in the range 0.004–0.055 $M_\odot$ around 0.2–2.5 $M_\odot$ stars. Most of the observed RSDs are found toward Stage I sources ($M_\star > M_{env}$), while RSDs are claimed toward three Stage 0/I sources. From the sample, large (≥ 100 AU) RSDs are generally found toward sources where $M_\star/M_{tot} > 0.65$ with $M_{tot} = M_\star + M_{env} + M_{disk}$.

How do these disks compare to disk formation models? Semi-analytical disk formation models by Visser et al. (2009), which are based on Terebey et al. (1984) and Cassen & Moosman (1981), predict that > 100 AU RSDs are expected by the end of the accretion phase ($M_{env} < M_{disk}$, see also Young & Evans 2005). The disk sizes depend on the initial envelope temperature or sound speed and the rotation rate. The evolution of R_K within these models is shown in Fig. 5.11 for the same initial conditions as Harsono et al. (2013) with comparable initial rotation rates to those measured by Goodman et al. (1993). Remarkably, the observed RSDs in Stage I fall within the expected sizes from these semi-analytical models. On the other hand, most of the Class 0 disks fall outside of these models. From this comparison, the observed RSDs in Stage I can be well represented by models with $\Omega = 10^{-14}$ Hz and $c_s = 0.19$–0.26 km s^{-1}.

In semi-analytical models, the disk forms as a consequence of angular momentum conservation. However, recent numerical simulations of collapse and disk formation with the presence of magnetic fields do not always form a large RSD (> 100 AU). Galli et al. (2006) showed

---

[3]We note that our observed visibilities (Fig. 5.6) are a factor of 3 higher than that reported by Eisner (2012) for TMC1A at 50 kλ.

Table 5.7 — Properties of observed embedded RSDs.

Source	$M_\star$ [$M_\odot$]	$M_{\rm disk}$ [$M_\odot$]	$R_{\rm K}^{\rm a}$ [AU]	$M_\star/M_{\rm tot}^{\rm b}$	$M_{\rm disk}/M_\star$	$\Theta_{\rm disk}^{\rm c}$ [deg]	$\Theta_{\rm rotation}^{\rm d}$ [deg]	$\lambda_{\rm eff}^{\rm e}$	References
				Class 0					
NGC1333 IRAS4A2	0.08	0.25	310	0.02	3.1	108.9	...	...	1,2,3
L1527	0.19	0.029–0.075	90	0.2	0.13–0.34	0	-177	...	1,2,4,5
VLA1623	0.20	0.02	150	0.4–0.6	...	-145	...	...	6,7
				Class I					
R CrA IRS7B	1.7	0.024	50	0.43	0.01	-65	...	...	8
L1551 NE	0.8	0.026	300	0.65	0.032	167	...	...	9
L1489-IRS	1.3	0.004	200	0.83–0.93	0.0030	-120	110	...	1,2,10
IRS43	1.9	0.004	190	0.89	0.002	107	...	...	1, 12
IRS63	0.8	0.099	165	0.83	0.12	-10	...	...	11, 12
Elias29	2.5	0.011	200	0.98	< 0.003	...	...	...	11
TMC1A	0.53	0.045–0.075	100	0.75–0.78	0.08–0.14	-115	25	> 10	13
TMC1	0.54	0.005–0.024	100	0.76–0.79	0.01–0.06	-90	35	4	13
TMR1	0.7	0.01–0.015	< 50	0.72$^{\rm f}$	0.02–0.03	...	...	...	13
L1536$^{\rm g}$	0.4	0.007–0.024	80	0.95–0.97	0.02–0.06	-95	-7	...	13

[a] Outer radius of the Keplerian disk. [b] $M_{\rm tot} = M_\star + M_{\rm disk} + M_{\rm env}$. [c] Direction of the disk rotation from blue to red. [d] Direction of the envelope rotation associated to or near the sources from Caselli et al. (2002) except for L1527 whose value is from Goodman et al. (1993). [e] Effective mass-to-flux ratio scaled from the average value in Troland & Crutcher (2008) with magnetic field strengths from Crutcher et al. (2010). [f] Stellar mass adopted from Hogerheijde et al. (1998), which assumes that all of the luminosity is due the star. [g] The stellar mass is sum of the two stars in the binary.

(1) Jørgensen et al. 2009; (2) Kristensen et al. 2012; (3) Choi et al. 2010; (4) Tobin et al. 2012; (5) Tobin et al. 2013; (6) Murillo & Lai 2013; (7) Murillo et al. 2013; (8) Lindberg et al. 2014; (9) Takakuwa et al. 2012; (10) Brinch et al. 2007b; (11) Lommen et al. 2008; (12) Brinch & Jørgensen 2013; (13) This work

that an RSD does not form in the ideal magnetohydrodynamics (MHD) case due to efficient magnetic breaking (e.g., Galli & Shu 1993; Mellon & Li 2008). The problem can be alleviated if the magnetic field is weak or with the inclusion of non-ideal MHD, although the results with non-ideal MHD are not entirely clear (Mellon & Li 2008, 2009; Dapp & Basu 2010; Krasnopolsky et al. 2011; Li et al. 2011; Braiding & Wardle 2012). Once the RSD forms, it can easily evolve to > 400 AU (Dapp et al. 2012; Vorobyov 2010; Joos et al. 2012). The question centers on whether RSDs are already present in the Class 0 phase. This depends on the strength and orientation of the magnetic field, as well as the initial rotation rate of the envelope.

5.5.2.1 On the magnetic field

The dynamical importance of the magnetic field can be numerically determined through the value of the effective mass-to-flux ratio, $\lambda_{\rm eff}$, which is the ratio of the gravitational and magnetic energies within the cloud. A value of 1 means that the cloud is strongly magnetized while value of > 10 characterizes weakly magnetized clouds. Troland & Crutcher (2008) presented a recent survey of magnetic field strengths toward molecular cloud cores. They find an average $\lambda_{\rm eff} \sim 2 - 3$ or an average magnetic field strength of 16 μG, which argues for the importance of magnetic field during the dynamical evolution of pre- and protostellar cores (see also Crutcher 2012).
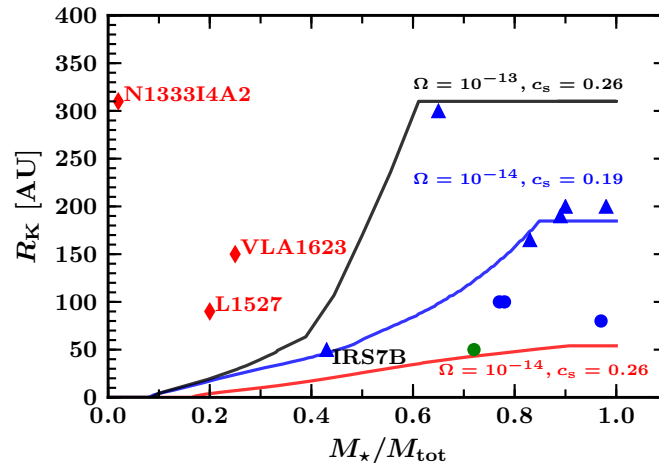
Figure 5.11 — Comparison of the observed RSDs (symbols) and semi-analytical models (lines) from Harsono et al. (2013). The red diamonds indicate the Class 0 sources, blue circles show the Class I sources we have analyzed, and blue triangles show the Class I sources whose parameters were taken from the literatures. TMR1 is indicated by the green circle since the stellar mass is derived from the bolometric luminosity. Different lines show the evolution of RSDs with different initial conditions ($c_s = 0.26$ km s^{-1} (black and red) and 0.19 km s^{-1} (blue); $\Omega = 10^{-13}$ Hz (black) and 10^{-14} Hz (red and blue)), keeping the initial core mass fixed at 1 M$_\odot$.

The magnetic field strength within Taurus is found to vary toward different cores. For example, TMC1A is within the L1534 core whose line of sight magnetic field is weak ($< 1.2\ \mu$G, Crutcher et al. 2010), while the TMC1 dark cloud has considerable magnetic field strength of the order of $9.1 \pm 2.2\ \mu$G. Since λ is inversely proportional to the magnetic field strength, the $\lambda_{\rm eff}$ toward these two sources are > 10 and ~ 4 around TMC1A and TMC1, respectively. It is interesting to note that a large and massive RSD ($R = 100$ AU and $M_{\rm disk}/M_\star \sim 0.1$) is found toward TMC1A, while the RSDs toward both TMC1 and TMR1, which are located closer to the TMC1 dark cloud, are small and less massive. Considering that $M_{\rm disk}/M_{\rm env}$ is lower toward TMC1 and TMR1 than toward TMC1A, this also illustrates that the magnetic field may play an important role in determining the disk properties.

How likely are these disks formed out of weakly magnetized cores? Molecular cloud cores are found to have lower than average magnetic field strength ($\lambda_{\rm eff} > 3$, Crutcher et al. 2010), than found on cloud scales. On the other hand, the fraction of cores with $\lambda_{\rm eff} > 5$ is low. Consequently, it is unlikely that TMC1A and other observed RSDs in Stage I all formed out of weakly magnetized cores. Thus, simulations need to be able to form RSDs out of a moderately magnetized core that evolve up to sizes of 100–200 AU by Stage I. In addition, we can argue that the magnetic breaking efficiency drops as the envelope dissipates, which allows the rapid growth of RSDs near the end of the main accretion phase as shown in Fig 5.11. On the other hand, there may be a low fraction of cores which are weakly magnetized, which facilitate formation of large disks as early as Stage 0 phase (Krumholz et al. 2013; Murillo et al. 2013).

5.5.2.2   On the large-scale rotation

Another important parameter is the large-scale rotation around these sources, which is a parameter used in both simulations and semi-analytical models. Generally, a cloud rotation rate between 10^{-14} Hz to a few 10^{-13} Hz is used in numerical simulations (e.g., Yorke & Bodenheimer 1999; Li et al. 2011). The average rotation rate measured by Goodman et al. (1993) is $\sim 10^{-14}$ Hz, which is consistent with the initial rotation rate of the semi-analytical model that

best describes a large fraction of the observed RSDs. The time at which Stage I starts within that model is 3×10^5 years. For comparison, around the same computational time, Yorke & Bodenheimer (1999) form a > 500 AU RSD for their low-mass case (J). Similarly, Vorobyov (2010) also found > 200 AU RSDs close to the start of the Class II phase. We find no evidence of such large RSDs at similar evolutionary stages in our observations.

Another aspect of the large-scale rotation that is worth investigating is its direction with respect to that of the disk rotation. Models assume that the disk rotation direction is the same as the rotation of its core. To compare the directions, we have used the velocity gradients reported by Caselli et al. (2002) and Goodman et al. (1993) toward the dark cores in Taurus. Velocity gradients are detected toward L1534 (TMC1A), L1536 and TMC-1C, which is located to the North East of TMR1 and TMC1. Table 5.7 lists the velocity gradients of the RSDs toward the embedded objects and their envelope/core rotation[4]. It is interesting to note that the large-scale rotation detected around or nearby the RSDs have a different velocity gradient direction. Similar misalignments in rotation have been pointed out by Takakuwa et al. (2012) toward L1551 NE and by Tobin et al. (2013) for L1527. Although the positions of the detected molecular emission in Caselli et al. (2002) do not necessarily coincide with the embedded objects due to chemical effects, the systematic velocities of the cores are similar. Misalignment at 1000 AU scales was also concluded by Brinch et al. (2007b) toward L1489 where they found that the Keplerian disk and the rotating envelope are at an angle of $30°$ with respect to each other. If these objects formed out of these cores in the distant past, then either the collapse process changed the angular momentum of the envelope and, consequently, the disk rotation direction or it affects the angular momentum distribution of nearby cores through feedback. Interestingly, the former may suggest the importance of the non-ideal MHD effect called the Hall effect during disk formation, which can produce counter-rotating disks (Li et al. 2011; Braiding & Wardle 2012).

Finally, the simulations and models above require the initial core to be rotating in order to form RSDs. However, by analyzing the angular momentum distribution of magnetized cores, Dzib et al. (2010) suggested that the NH_3 and N_2H^+ measurements may overestimate the angular momentum by a factor of $\sim 8 - 10$. This poses further problems to disk formation in previous numerical studies of collapse and disk formation. On the other hand, the inclusion of the Hall effect does not require a rotating envelope core to form arotating structure (e.g., Krasnopolsky et al. 2011; Li et al. 2011). Further studies are required to compare the expected observables from rotating and non-rotating models.

5.5.3 Disk stability

Self gravitating disks can be important during the early stages of star formation in regulating the accretion process onto the protostar, which can be variable (e.g., Vorobyov 2010). Dunham & Vorobyov (2012) show that such episodic accretion events can reproduce the observed population of YSOs. A self-gravitating disk is expected when $M_{disk}/M_{star} \geq 0.1$ (e.g., Lodato & Rice 2004; Boley et al. 2006; Cossins et al. 2009). However, most of the observed embedded RSDs around Class I sources have disk masses such that $M_{disk}/M_{star} \leq 0.1$. It is unlikely for such disks to become self-gravitating, but they may have been in the past. Interestingly, a few embedded disk seem to be self-gravitating since their $M_{disk}/M_{star} \geq 0.1$ such as toward TMC1A, IRS63, L1527 and NGC1333 IRAS4A2 (See Table 5.7).

The low fraction of large and massive disks during the embedded phase suggests that disk

---

[4]The direction is in degrees East of North and increasing v_{lsr} (blue to red) to be consistent with Caselli et al. (2002) and Goodman et al. (1993).

instabilities may have taken place in the past and limited their current observed numbers (i.e. low fluxes at long baselines). In this scenario, the embedded disks will have a faster evolution and, thus, spend most of their lifetime with small radii. Alternatively, disks experiencing high infall rates from envelope to the disk as expected during the embedded phase may also have higher accretion rates (Harsono et al. 2011). Such a scenario argues for disk instabilities to be present even for $M_{\mathrm{disk}}/M_\star < 0.1$. In both cases, the dominant motion of the compact flattened structure during the embedded phase is infall rather than rotation. There are indeed sources where higher sensitivity and spatial resolution observations such as with Atacama Large Millimeter/submillimeter Array (ALMA) can detect features associated with disk instabilities (e.g., Cossins et al. 2010; Forgan et al. 2012; Douglas et al. 2013).

5.6 Conclusions

We present spatially and spectrally resolved observations down to a radius of 56 AU around four Class I YSOs in Taurus. The C^{18}O and ^{13}CO 2–1 lines are used to differentiate the infalling rotating envelope from the rotationally supported disk. Analysis of the dust and gas lines were performed directly in uv space to avoid any artefacts introduced during the inversion process. The main results of this paper are:

- Dust disk sizes and masses can be derived from the continuum by using a power-law spherical envelope model to account for the large-scale envelope emission. Intensity based disk models (Uniform and Gaussian) give similar disk sizes to each other which are lower by typically 25%-90% than realistic disk models (power-law disk). On the other hand, they give similar disk masses to more realistic models, which are consistent with the disk mass derived from the 50 kλ flux point. Inclusion of the envelope in the analysis is important to obtain reliable disk masses. The observationally derived masses indicate that there is still a significant envelope present toward three of the four sources: TM1A, TMC1, and TMR1.

- Three of the four sources (TMC1, L1536, TMC1A) host embedded rotationally supported disks (RSDs) derived from line data. By fitting velocity profiles ($v \propto r^{-0.5}$ or $\propto r^{-1.0}$) to the red- and blue-shifted peaks, the RSDs are found to have outer radii of ~ 80–100 AU. In addition, the large-scale structure (> 100 AU) is dominated by the infalling rotating envelope ($v \propto r^{-1}$). The derived stellar masses of these sources are of order 0.4–0.8 $M_\odot$, consistent with previous values. Consequently, these objects are indeed Stage I young stellar objects with $M_\star/(M_{\mathrm{env}} + M_{\mathrm{disk}} + M_\star) > 0.7$.

- Disk radii derived from the power-law dust disk models toward TMC1 and TMC1A are consistent with sizes of their RSDs. However, the dust disk radii toward TMR1 and L1536 are not the same as the extent of their RSDs. Thus, we emphasize that spatially and spectrally resolved gas lines observations are required to study the nature of flattened structures toward embedded YSOs.

- Semi-analytical models with $\Omega = 10^{-14}$ Hz and $c_s = 0.19 - 0.26$ km s^{-1}describe most of the observed RSDs in Stage I. The observed RSDs argue for inefficient magnetic breaking near the end of the main accretion phase ($M_\star/M_{\mathrm{tot}} > 0.65$). More theoretical studies are needed to understand how and when RSDs form under such conditions.

- Comparison between disk masses derived from the continuum and C^{18}O integrated line intensities (Table 5.6) suggests that relatively little of CO is frozen out within the embedded disk.

The current constraints on disk formation rely on a small number of observed RSDs around Class I sources. Certainly one needs to constrain the size of RSDs near the end of the main

Table 5.8 — Observational log

Date	Configuration	No. Antenna	Bandpass calibrators (flux)	Gain calibrators (flux)
			Track sharing of TMR1 and TMC1A	
2012 Mar 3	B	6	0234+285 (3.07 Jy)	0400+258 (0.37 Jy), 0507+179 (2.71 Jy)
Mar 7	B	6	3C84 (9.93 Jy)	0400+258 (0.35 Jy), 0507+179 (2.54 Jy)
Mar 10	B	6	3C84 (9.44 Jy)	0400+258 (0.33 Jy), 0507+179 (2.35 Jy)
Mar 12	B	5	3C84 (8.68 Jy)	0400+258 (0.29 Jy), 0507+179 (1.88 Jy)
Mar 12	B	6	3C84 (9.95 Jy)	0400+258 (0.47 Jy), 0507+179 (3.12 Jy)
Mar 31	C	6	2200+420 (7.05 Jy)	0400+258 (0.28 Jy), 0507+179 (1.79 Jy)
			Track sharing of TMC1 and L1536	
2013 Mar 2	B	6	3C84 (11.86 Jy)	0400+258 (0.29 Jy), 0459+252 (0.35 Jy)
Mar 3	B	6	3C84 (14.29 Jy)	0400+258 (0.34 Jy), 0459+252 (0.40 Jy)
Mar 16	B	6	3C84 (12.40 Jy)	0400+258 (0.25 Jy), 0459+252 (0.21 Jy)
Mar 19	B	6	3C84 (10.74 Jy)	0400+258 (0.26 Jy), 0459+252 (0.29 Jy)
Mar 22	B	6	2200+420 (12.18 Jy)	0400+258 (0.29 Jy), 0459+252 (0.28 Jy)
Mar 27	B	6	3C84 (12.88 Jy)	0400+258 (0.28 Jy), 0459+252 (0.34 Jy)
Apr 7	C	6	3C84 (10.32 Jy)	0400+258 (0.25 Jy),0459+252 (0.32 Jy)

accretion phase to understand how late Class II disks form. On the other hand, the observed RSDs in the Class I phase do not answer the question when and how RSDs form. Such constraints require the detection and characterization of RSDs during Class 0 phase, which are currently lacking. From the sample of sources in Yen et al. (2013) and our results, it is clear that the infalling rotating flattened structure is present at >100 AU. Thus, extending molecular line observations down to < 50 AU radius with ALMA toward Class 0 YSOs will be crucial for differentiating between the different scenarios for disk formation.

Acknowledgements

5.A   Observational data

The observational log can be found in Table 5.8 and the channel maps of all the observed lines toward the four sources are shown in Figure 5.12.
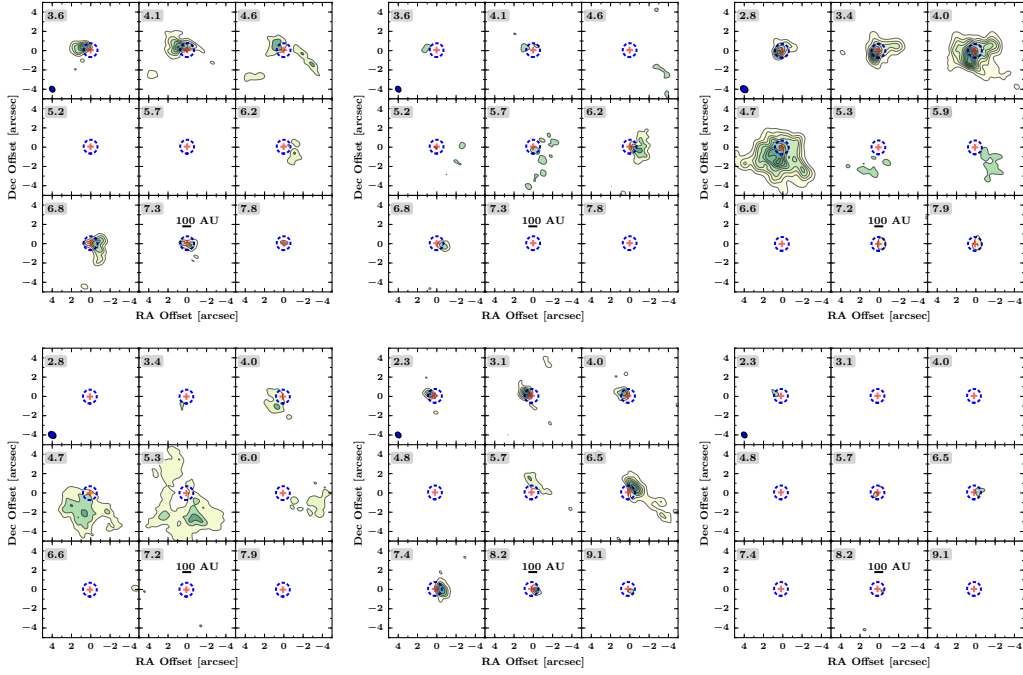
Figure 5.12 — *Top left*: ^{13}CO 2–1 channel maps similar to Fig. 5.3 toward TMC1. *Top middle*: C^{18}O 2–1 channel maps toward TMC1. *Top right*: ^{13}CO 2–1 channel maps toward TMR1. *Bottom left*: C^{18}O 2–1 channel maps toward TMR1. *Bottom middle*: ^{13}CO 2–1 channel maps toward L1536. *Bottom right*: C^{18}O 2–1 channel maps toward L1536.

Table 5.9 — 1D spherical envelope parameters as published by Kristensen et al. (2012).

Source	p	Y[a]	$r_{\rm in}$	$n_{\rm in}$	$n(1000{\rm AU})$
			[AU]	[cm^{-3}]	[cm^{-3}]
TMC1	1.1	1800	3.7	8.5×10^7	1.8×10^5
TMR1	1.6	900	8.8	4.1×10^8	2.1×10^5
TMC1A	1.6	900	7.7	5.2×10^8	2.2×10^5

$^{\rm a}$ $Y = r_{\rm out}/r_{\rm in}$.

5.B Large-scale structure

The parameters of the large-scale envelope structure used to estimate the continuum emission at short baselines are in Table 5.9.

5.C WideX data

Spectra toward all sources integrated within a $3''$ box around their continuum positions are shown in Fig. 5.13. The integrated flux density maps toward C^{18}O, SO $5_6 - 4_5$ and SO$_2$ $11_{1_1} - 10_{0_{10}}$ (221.96521 GHz) are shown in Fig. 5.15. The SO emission toward all sources is much more extended compared to the C^{18}O emission, while the SO$_2$ emission is compact.

5.D L1536

Figure 5.16 shows the ^{12}CO $J =$3–2 spectral map obtained with JCMT, where there is no indication of classical bipolar outflows are present.
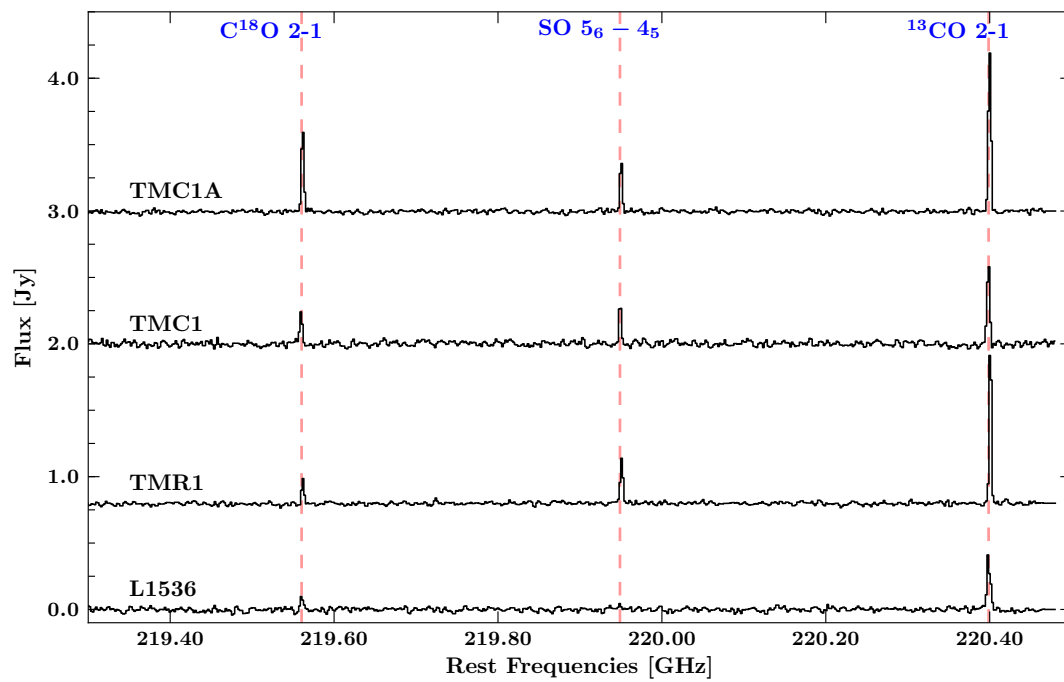
Figure 5.13 — Integrated flux of $C^{18}O$ J =2–1, SO $5_6 - 4_5$ and ^{13}CO J =2–1 within a 3ʺ box around each source in the WideX spectra.
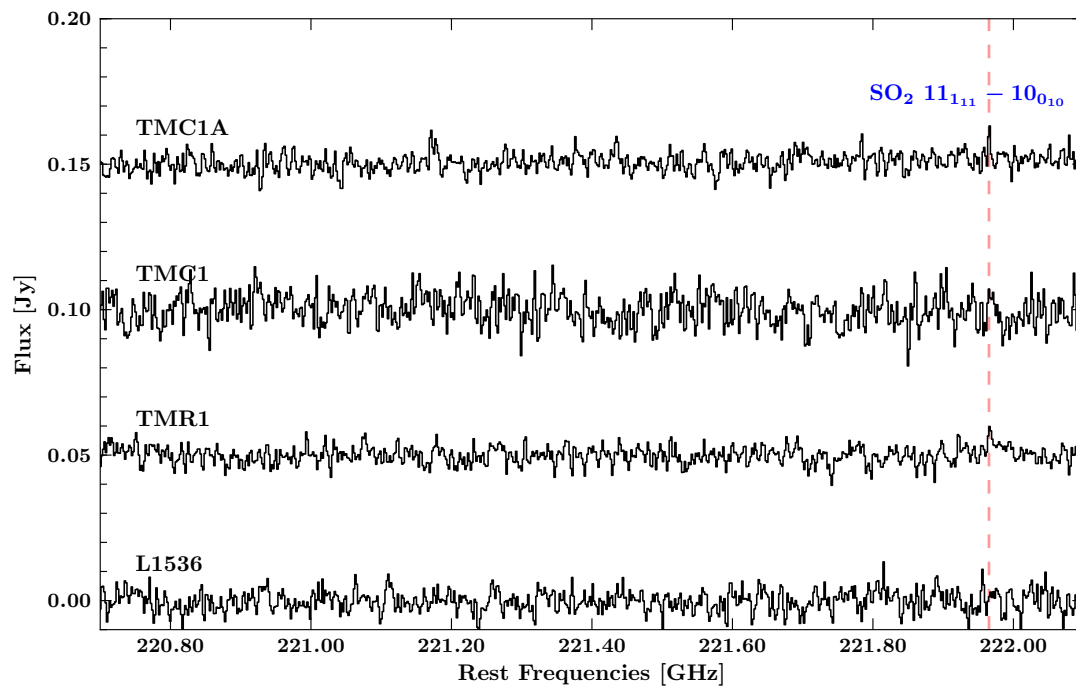

Figure 5.14 — Integrated flux within a 1ʺ box around each source in the WideX spectra between 220.7–222.1 GHz.
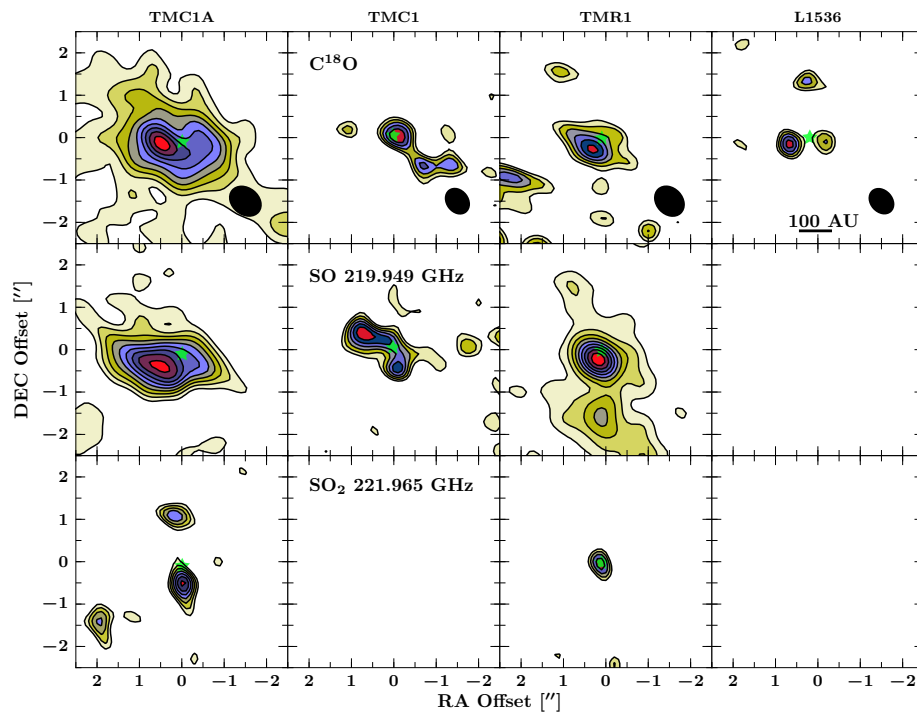
Figure 5.15 — Moment 0 maps of $C^{18}O$ J =2–1, SO $5_6 - 4_5$ and SO$_2$ $11_{1_11} - 10_{0_{10}}$ toward all sources from the WideX data. The contours are drawn at 10% of the peak starting at 3σ. Green star indicates the continuum position and black ellipses show the synthesized beams.
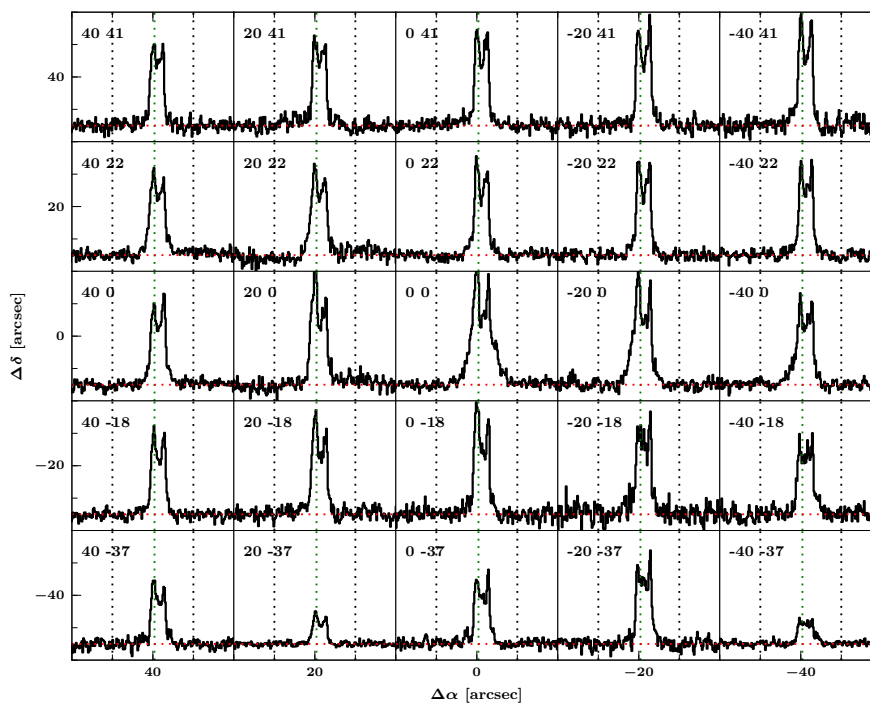

Figure 5.16 — ^{12}CO J =3–2 spectral map obtained with the JCMT from -5 km s^{-1} to 15 km s^{-1} and intensities from -0.5 K to 3.5 K. The vertical dotted lines show 0, 5.2, and 10 km s^{-1} for guidance.

Chapter 6

Volatile snowlines in embedded disks around low-mass protostars

Abstract. *Context.* Models of the young solar nebula assume that the disk is hot initially such that most volatiles are in the gas phase. Water emission arising from within 50 AU radius has been detected around low-mass embedded young stellar objects. The question remains whether an actively accreting disk can be warm enough to have gas-phase water up to 50 AU radius. No detailed studies have yet been performed on the extent of snowlines in an accreting disk embedded in a dense envelope (Stage 0). *Aims.* Quantify the location of gas-phase volatiles in the inner envelope and disk system for an actively accreting embedded disk.
Methods. Two-dimensional physical and radiative transfer models have been used to calculate the temperature structure of embedded protostellar systems. The heating due to viscous accretion is added through the diffusion approximation. Gas and ice abundances of H_2O, CO_2, and CO are calculated using the density dependent thermal desorption formulation.
Results. The midplane water snowline increases from 5 to ~ 30 AU for accretion rates between 10^{-9}–10^{-4} $M_\odot$ yr^{-1}. CO_2 can remain in the solid phase within the disk for $\dot{M} \leq 10^{-5}$ $M_\odot$ yr^{-1} down to ~ 40 AU. CO is always in the gas phase for an actively accreting disk independent of disk properties and accretion rate. The predicted optically thin water emission is consistent with the detected water emission toward the Stage 0 embedded young stellar objects. An accreting embedded disk can only account for water emission arising from $R < 50$ AU, however, and drops rapidly for $\dot{M} \leq 10^{-5}$ $M_\odot$yr^{-1}. Thus, this extent can be tested with future ALMA observations.
Conclusion. Volatiles such as H_2O, CH_3OH, and CO_2 sublimate out to 30 AU in the midplane in young disks and, thus, can reset the chemical content inherited from the envelope. A hot young solar nebula out to 30 AU can only have occurred during the deeply embedded Stage 0, not during the T Tauri phase of our early solar system.

D. Harsono, S. Bruderer, E. F. van Dishoeck
in prep.

6.1 Introduction

The snowlines of various volatiles play a major role for planet formation. Beyond the snowline, the high abundances of solids allow for efficient sticking to form larger bodies. Thus, the amount of larger bodies is increased by the presence of ices (e.g. Stevenson & Lunine 1988; Ros & Johansen 2013). Extensive studies have investigated the snowline in protoplanetary disks around pre-main-sequence stars during which supposedly the solar system was formed (e.g. Lissauer 1987; Pollack et al. 1996). It is thought the early pre-solar nebula was (> 1500 K) such that both volatiles and refractories are in the gas phase (Cassen 2001; Scott 2007). This pushes the water snowline up to beyond a few AU radius. The evidences of such a hot solar nebula come from the history of the refractories, however the volatile content of comets seems to indicate that a part of the disk remains cold (see Pontoppidan et al. 2014). The evolution of the

snowline due to disk and star evolution and its accretion rate affect the chemical composition in the region relevant to planet formation (e.g., Lodders 2004; Davis 2005; Öberg et al. 2011b). The most relevant volatiles are the known major ice species, H_2O, CO_2, and CO. Observations and theoretical models of protoplanetary disks around pre-main sequence T-Tauri stars are not warm enough to have gas-phase volatiles in the midplane beyond 30 AU and for the case of H_2O, only a few AU (e.g., D'Alessio et al. 1998; Dullemond et al. 2007). Such high temperature at large radii could potentially only be achieved during the deeply embedded phase of star formation when the accretion rate is high. The question remains how hot can an embedded accreting disk become due to its high accretion rate ($\geq 10^{-6}$ $M_\odot$ yr^{-1}, Dunham et al. 2014).

Spatially resolved warm water emission ($T_{ex} \sim 120$ K, Persson et al. 2014) has been recently detected from within the inner 50 AU radius of several deeply embedded (Class 0) low-mass protostars (e.g., Jørgensen & van Dishoeck 2010b; Persson et al. 2012). These are very young objects whose envelope mass is substantially larger than the mass at smaller scales (also denoted as Stage 0, Robitaille et al. 2006). The emission is expected to arise from $T_{dust} > 100$ K regions where the gas-phase water abundance is at its maximum (Fraser et al. 2001; Aikawa et al. 2008; Mottram et al. 2013). This inner region is, however, also where the disk forms (Larson 2003; Williams & Cieza 2011; Li et al. 2014a). Rotationally supported disks (RSDs) have been detected recently around low-mass protostars (e.g., Tobin et al. 2012; Murillo et al. 2013). This paper studies the volatiles content in such embedded disks to investigate the location of their snowlines when the accretional heating is included.

Direct observational evidence of snowlines of the major ice species toward protoplanetary disks around pre-main sequence stars rely on the chemical changes that occur when a molecule is absent from the gas phase. The commonly observed snowline is that of CO through the detection of DCO^+ and N_2H^+ lines, which are both destroyed in reactions with CO (e.g. van Dishoeck et al. 2003; Guilloteau et al. 2006; Qi et al. 2008; Mathews et al. 2013; Qi et al. 2013). The CO snowline location with respect to water and CO_2 snowlines have direct impact on the amount of water present in giant planets atmospheres (Madhusudhan et al. 2011; Moses et al. 2013). The water snowline has been inferred to be within a few AU from direct observation of mid-infrared water lines (Pontoppidan et al. 2010; Zhang et al. 2013). Thus, significant progress has been made in identifying snowlines in protoplanetary disks in the later stages and their location with respect to gas giant formation (e.g., Kennedy & Kenyon 2008; Pontoppidan et al. 2014). Yet, the accretion process through the disk begins in the early stages of star formation at the time that the disk itself is forming. The amount of gaseous volatiles within embedded disks is, therefore, affected by their formation process which results in different chemical structures of the emerging protoplanetary disks (Visser et al. 2011). A related question centers whether these volatiles are 'inherited' or 'reset' during the planet formation process (Pontoppidan et al. 2014). The 'reset' scenario refers to the chemical processing of ices as the gas and dust are exposed to elevated temperatures (> 40 K) during their voyage from the envelope to the disk.

Water is the key volatile in star and planet formation; it is also the major constituent of ices on the grains that facilitate planet formation (Gibb et al. 2004; Öberg et al. 2011a) and a major coolant (Karska et al. 2013). Most of the water is formed during the pre-stellar stage, and then transported through the envelope into the disk and planets. Tracing the water history from early stages of star formation to planet forming regions hints at the origin of water in planets (van Dishoeck et al. 2014). The crucial step that is yet relatively unexplored is the processing of water during the disk formation process.

The water vapor content around protostars is investigated by the 'Water In Star-forming regions with Herschel' key program (WISH, van Dishoeck et al. 2011). Due to the large beam of *Herschel*, a significant fraction of the detected water emission is from the large-scale envelope

and the bipolar outflow (Kristensen et al. 2012; Herczeg et al. 2012; Mottram et al. 2014). More importantly, most of the detected water emission comes from water in the outflow that will escape the system and will not be retained by the disk. In order to determine the amount of water vapor associated with the inner envelope or disk, an isotopolog of warm water ($H_2^{18}O$) was observed toward a few low-mass embedded protostars. Visser et al. (2013) reported a detection of the $H_2^{18}O$ line (1096 GHz) with HIFI (de Graauw et al. 2010) toward the embedded protostar NGC 1333 IRAS2A. However, they found that the line is still optically thick with an emitting region of ~ 100 AU. Thus, it remains difficult to constrain the amount of water vapor in embedded disks with single-dish observations.

Although $H_2^{16}O$ line emission cannot be observed from the ground, except for masers, a few of the rotational transitions of its isotopologs are observable such as $H_2^{18}O$ and deuterated water (HDO). Furthermore, interferometric facilities such as the Plateau de Bure Interferometry (PdBI) and the Submillimeter Array (SMA) can spatially and spectrally resolve these lines. With those facilities, Jørgensen & van Dishoeck (2010a,b) detected $H_2^{18}O$ and HDO emission originating from within the inner 25 AU radius of a Class 0 low-mass protostar. More recently, spatially and spectrally resolved warm water emission has been detected toward four low-mass embedded protostars with the PdBI (Persson et al. 2012, 2013) and toward one high mass disk (van der Tak et al. 2006; Wang et al. 2012). From the kinematical information, both Jørgensen & van Dishoeck (2010b) and Persson et al. (2012) found that the water emission does not show Keplerian motion and concluded that it must be emitted from a flattened disk-like structure that is still dominated by the radial infalling motions.

This paper investigates snowlines of volatiles within an accreting disk embedded in a massive envelope. The spatial extent and the water vapor emission are compared with the observed values toward three deeply embedded protostars. The thermal structure of an actively accreting disk is computed including the additional heating due to the energy released from the viscous dissipation. Most previous studies of the thermal structure of an accreting disk focused on the later evolutionary stage of disk evolution where the envelope has largely dissipated away. Furthermore, they focused on the midplane temperature structure (e.g., Sasselov & Lecar 2000; Lecar et al. 2006; Kennedy & Kenyon 2008). This additional heating shifts the snowlines of volatiles outward to larger radii than in disks around pre-main sequence stars (Davis 2005; Garaud & Lin 2007; Min et al. 2011). The details of the physical and chemical structure of the embedded disk are presented in Section 6.2. Section 6.3 presents the snowlines location as function of disk and stellar properties. The results are compared with observations and discussed in Section 6.4. Section 6.5 summarizes the main results and conclusions.

6.2 Physical and chemical structures

6.2.1 Physical structure

A simple parametrized embedded disk (disk + flattened envelope) model is used to construct the density structure following Crapsi et al. (2008). The main parameters are disk mass (M_{disk}) and disk radius (R_{disk}). A number of parameters defining the envelope and the disk are fixed and summarized in Table 6.1. Through the combined continuum spectral energy distribution and submm continuum images modelling, the envelope masses toward the observed embedded sources (NGC1333 IRAS2A, IRAS4A, and IRAS4B) are found to be between $3 - 5\ M_\odot$ (Kristensen et al. 2012). For this purpose, the envelope mass is fixed at $1\ M_\odot$, which is appropriate for the objects from which the water emission has been detected (Jørgensen et al. 2009; Kristensen et al. 2012).

For the large-scale envelope, a flattened envelope due to rotation as described by Ulrich

Table 6.1 — Parameters for the embedded disk + envelope models. The varied parameters are indicated in boldface.

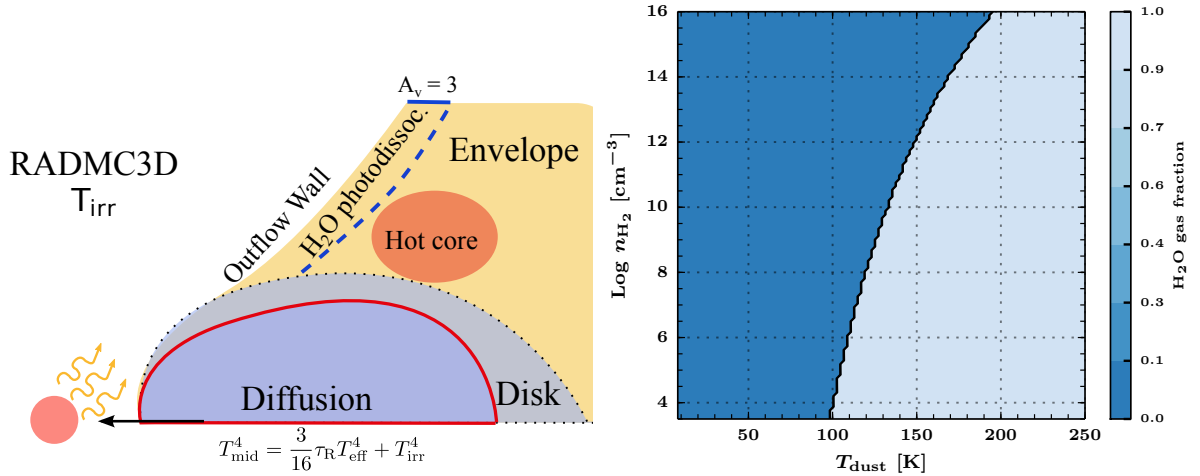| Variable [unit]	Description	Value(s)
$r_{\rm out}$ [AU]	Outer radius	10^4
$r_{\rm in}$ [AU]	Inner radius	0.1
$R_{\rm cen}$ [AU]	Centrifugal radius	200
$M_{\rm env}$ [$M_\odot$]	Envelope mass	1.0
$M_{\rm disk}$ [$M_\odot$]	**Disk mass**	0.05, 0.1, 0.2, 0.5
$R_{\rm disk}$ [AU]	**Disk radii**	50, 100, 200
H_0 [AU]	Scale height at 1 AU	0.2
$T_\star$ [K]	Stellar temperature	4000
$M_\star$ [$M_\odot$]	Stellar mass	0.5
$L_\star$ [$L_\odot$]	**Stellar luminosity**	1, 5, 8
$\dot{M}$ [$M_\odot$ yr^{-1}]	**Accretion rate**	$10^{-4,-5,-6,-7,-8,-9}$

Figure 6.1 — *Left*: Schematic showing the calculation of the thermal structure of the disk by combining both the RADMC3D Monte Carlo simulation and the diffusion equation. The Monte Carlo simulation calculates the temperature structure due to the irradiation ($T_{\rm irr}$) from a central star while the diffusion equation is used to solve the temperature structure at high optical depths ($\tau_R > 1$) as indicated by the red line. This high optical depth region starts typically below the disk surface. The outflow wall, classical hot core ($T_{\rm dust} > 100$ K) and photodissociation region are indicated. *Right*: Gas fraction ($n_{\rm gas}/n_{\rm gas} + n_{\rm ice}$) for H$_2^{16}$O as a function of density and temperature.

(1976) is adopted whose densities are given by the following equation:

$$\rho_{\mathrm{env}}(r, \mu) \propto \left(\frac{R_{\mathrm{cen}}}{r}\right)^{1.5} \left(1 + \frac{\mu}{\mu_0}\right)^{-1/2} \left(\frac{\mu}{2\mu_0} + \frac{R_{\mathrm{cen}}}{r}\mu_0^2\right)^{-1}, \tag{6.1}$$

where $\mu \equiv \cos\theta$, R_{cen} is the centrifugal radius, and r is the spherical radius. The centrifugal radius defines the region in which the material no longer flows radially and enters the disk. It is fixed at 200 AU, which corresponds to the maximum disk radius (~ 180 AU) observed toward a Class 0 embedded low-mass YSO (Murillo et al. 2013). For a given centrifugal radius, a particle follows a parabolic motion given by

$$\frac{r}{R_{\mathrm{cen}}}\frac{1 - \mu/\mu_0}{1 - \mu_0^2} = 1, \tag{6.2}$$

where μ_0 satisfies the condition above at every r and μ. The outer radius of the envelope is fixed at $r_{\mathrm{out}} = 10^4$ AU with an inner radius of 0.1 AU where the dust typically sublimates.

An outflow cavity is then carved out from the envelope density structure at $\mu_0 > 0.95$. Following Crapsi et al. (2008), the density inside the cavity is equal to that of the densities at r_{out}. This creates a conical outflow with an aperture of 30° at large radii (semi-aperture of 15°). For a 1 $M_\odot$ envelope, gas densities $\sim 10^4$ cm^{-3} fill the envelope cavity, which is consistent with those observed toward YSOs (e. g, Bachiller & Tafalla 1999; Whitney et al. 2003b)

A flared accretion disk is added to the envelope density structure. The density within the disk follows the power law dependence radially and has a Gaussian distribution vertically in z as expected from a hydrostatic disk. The flared disk densities (Shakura & Sunyaev 1973; Pringle 1981; Hartmann et al. 1998; Williams & Cieza 2011) are described by

$$\rho_{\mathrm{disk}}(R, z) = \frac{\Sigma(R/R_{\mathrm{disk}})^{-1}}{\sqrt{2\pi}H(R)} \exp\left[-\frac{1}{2}\left(\frac{z}{H(R)}\right)^2\right], \tag{6.3}$$

where H is the scale height fixed to 0.2 AU (H_0) at 1 AU (R_0), R_{disk} is the disk radius and R is the cylindrical radius. The radial dependence of the scale height is $H(R) = R\, H_0/R_0\, (R/R_0)^{2/7}$ (Chiang & Goldreich 1997). The densities are scaled with a constant factor such that the total disk mass is equal to the values in Table 6.1, distributed within the R_{disk}. The total gas density in the model is $\rho = \rho_{\mathrm{disk}} + \rho_{\mathrm{env}}$ with a gas-to-dust mass ratio of 100.

6.2.2 Temperature structure and heating terms

The three-dimensional dust continuum radiative transfer code, RADMC-3D[1] is used to calculate the dust temperature structure. A 4000 K star characterized by 1, 5 and 15 $L_\odot$ is adopted (White & Hillenbrand 2004; Nisini et al. 2005). An accurate dust temperature structure of the disk is crucial in determining the location where various volatiles thermally desorb from the grain. This is difficult computationally for a massive optically thick disk being modelled here (see Min et al. 2009). Thus, we have separated the dust temperature calculations due to the central star irradiation (passive) from the viscous heating treatment (see Fig. 6.1 L). The former is determined by RADMC3D considering a black body central star as given in Table 6.1. The dust properties of Crapsi et al. (2008) are adopted and are composed of a distribution of ice coated silicates and graphite grains. The removal of ices from the grain at $T_{\mathrm{dust}} > 100$ K does not strongly alter the dust temperature structure.

---

[1]http://www.ita.uni-heidelberg.de/~dullemond/software/radmc-3d

An actively accreting disk provides additional heating from the loss of mechanical energy as the gas flows inward. The steady state accretion rate is typically between $10^{-5} - 10^{-7}$ $M_\odot$ yr^{-1} (Hueso & Guillot 2005). However, episodic accretion events such as those simulated by Vorobyov (2009) can have transient spikes with an accretion rate up to 10^{-4} $M_\odot$ yr^{-1}. Thus, disk accretion rates between 10^{-9}–10^{-4} $M_\odot$ yr^{-1} are adopted following the α disk formalism (Shakura & Sunyaev 1973; Williams & Cieza 2011). The viscous heating rate per volume is given by

$$Q_{\text{visc}} = \frac{9}{4}\rho_{\text{disk}}v\Omega^2, \tag{6.4}$$

where $v = \alpha c_{\text{s}}H$ is the α dependent turbulent viscosity parameter, c_{s} is the sound speed of the gas, and Ω is the Keplerian angular velocity. At steady state, the viscosity is related to the disk mass and the accretion rate through (Lodato 2008):

$$\dot{M} = 3\pi v\Sigma. \tag{6.5}$$

To explore the amount of heating, the viscosity term v is varied for the explored accretion rates at a fixed disk mass. The effective temperature (T_{visc}) associated with the total energy released at the inner radius assuming a hydrostatic disk is

$$\sigma_{\text{SB}}T_{\text{visc}}^4(R) = \int Q_{\text{visc}}(R)\,dz = \frac{3}{8\pi}\frac{GM_\star}{R^3}\dot{M}\left(1 - \sqrt{\frac{R_\star}{R}}\right). \tag{6.6}$$

This is obtained by integrating over the viscous heating terms vertically for each radius. Furthermore, T_{visc} is the effective temperature of the disk at the optically thin photosphere without the addition of stellar irradiation. However, the real temperature at the midplane of an active disk is proportional to the optical depth (Hubeny 1990): $T_{\text{mid}}^4 \sim \kappa_{\text{R}}\Sigma_{\text{gas}}T_{\text{visc}}^4$ with κ_R the Rosseland mean opacity which results in higher midplane temperatures. Such a method is similar to that of Kennedy & Kenyon (2008) and Hueso & Guillot (2005) in the optically thick regime. Note that the heating from the accreting disk is caused by dissipation of energy of both gas and dust. To account for the irradiation from the accreting disk, $L_{\text{visc}} = \int \pi\sigma T_{\text{visc}}(R)^4 R\,dR$ is added to the central luminosity $L_\star$ by determining its blackbody spectrum at T_{visc} at all radii.

The following steps are taken to calculate the dust temperature of an accreting embedded disk.

- Monte Carlo dust continuum radiative transfer is used to simulate the photon propagation to determine the passively heated dust temperature structure (T_{irr}) due to the stellar luminosity ($L_\star + L_{\text{visc}}$).

- Viscous heating is added to the region of the disk where $\tau_{\text{R}} > 1$. This is done by fixing the midplane temperatures to $T_{\text{mid}} = \left(\frac{3}{16}\kappa_{\text{R}}\Sigma_{\text{gas}}T_{\text{visc}}^4 + T_{\text{irr}}^4\right)^{1/4}$. The vertical dust temperature structure is calculated using the diffusion approximation $\nabla D\nabla T^4 = 0$ bounded by T_{irr} at the surface and T_{mid} at the midplane where $D = (3\rho_{\text{dust}}\kappa_{\text{R}})^{-1}$. The diffusion is performed within the $\tau_{\text{R}} > 1$ regions.

The addition of the viscous heating can increase the dust temperatures to > 2000 K. The typical dust vaporization temperature is ~ 1500 K, therefore, we have limited the dust temperature to 1500 K. Gas opacities in the inner disk is not taken into account, which will affect the exact temperature in that region. This does not change the location of the snowlines since they are defined by dust temperatures $T_{\text{dust}} \leq 160$ K.

The snowlines of protoplanetary disks without an envelope were obtained (see Fig. 6.8) and compared with Min et al. (2011) to verify our approach. Using this formulation, the differences in predicted water snowlines are typically within 2 AU at high accretion rates.

6.2.3 Molecular abundances

The aim of this paper is to calculate the 2D snowlines or snow 'surfaces' for CO, CO_2, and $H_2^{16}O$ in embedded disks. The region in which these volatiles freeze-out onto grains depends on the temperature and density structure. At steady state, the rate at which the molecule is adsorbed on the grain, $\mathcal{R}_{ads}$, is balanced by the thermal desorption rate, $\mathcal{R}_{des}$. The adsorption rate is given by

$$\mathcal{R}_{ads} = n_X n_{dust} \pi a_{dust}^2 \sqrt{3k_B T_{gas}/m_X}, \tag{6.7}$$

where m_X is the molecular mass, n_X is the number density of the molecule, T_{gas} is the gas temperature, $n_{dust} = 10^{-12} n_H$ is the dust number density (Visser et al. 2009) with $a_{dust} = 0.1 \, \mu$m as the effective grain size, and k_B is the Boltzmann constant. The thermal desorption rate is

$$\mathcal{R}_{thdes} = 4\pi a_{dust}^2 n_{dust} \nu_1 \exp(-E_b/k_B T_{dust})\xi, \tag{6.8}$$

where ν_1 is the first-order pre-exponential factor as calculated from the binding energy, E_b (Hasegawa et al. 1992; Walsh et al. 2010)

$$\nu_1 = \sqrt{\frac{2N_{ss}E_b}{\pi^2 m_X}} \; \text{s}^{-1} \tag{6.9}$$

with the number of binding sites, N_{ss} taken to be 8×10^{14} cm^{-2} for a 0.1 μm grain following Visser et al. (2011), and T_{dust} the dust temperature. A dimensionless factor ξ is used to switch between zeroth order to first order desorption when the ice thickness is less than a monolayer:

$$\xi = \frac{n_{ice}}{\max(n_{ice}, N_b n_{dust})} \tag{6.10}$$

with $N_b = 10^6$ the number of binding sites per dust grain. The properties for each molecule are given in Table 6.2 along with the calculated pre-exponential factor ν_1. These binding energies assume pure ices. Figure 6.1 (R) shows an example of the gas fraction for water at different densities and temperatures. At steady state, the number density of solids of species X is simply given by

$$\frac{n_{ice}}{n_{gas}} = \frac{n_{dust}\pi a_{dust}^2 \left(3k_B T_{gas}/m_X\right)^{1/2}}{\nu_1 \exp\left(-E_b/T_{dust}\right)\xi}. \tag{6.11}$$

The typical timescales for adsorption are $4 - 6 \times 10^3$ year at temperature of 50 K and number densities of 10^6 cm^{-3}. This implies that the steady state assumption is not valid at lower densities present in the large-scale envelope ($r > 1000$ AU) where the freeze-out timescales becomes longer than the lifetime of the core (e.g., Jørgensen et al. 2005b). On the other hand, this paper focuses on the gas phase abundances at small-scales $r \leq 100$ AU where the number densities are $n_H > 10^6$ cm^{-3}. Photodesorption can be ignored at such high densities and within the disk, but it may be important at the disk's surface and along the outflow cavity wall. Since the water vapor will also be rapidly photodissociated in those locations, these regions are not major water reservoirs (see Fig. 6.1 L). To approximate this region, water is assumed not to be present within a region that is characterized by $A_V \leq 3$ or $N_H \leq 6 \times 10^{21}$ cm^{-2}. A more detailed gas phase abundance structure through a chemical network will be explored in the future.

Table 6.2 — Molecular parameters to calculate $\mathcal{R}_{des}$.

Molecule	ν_1^a	E_b	Refs.
	$[s^{-1}]$	$[K]$	
CO	6.4×10^{11}	855	Bisschop et al. 2006
CO_2	8.2×10^{11}	2400	Burke & Brown 2010
$H_2^{16}O$	2.1×10^{12}	5773	Fraser et al. 2001

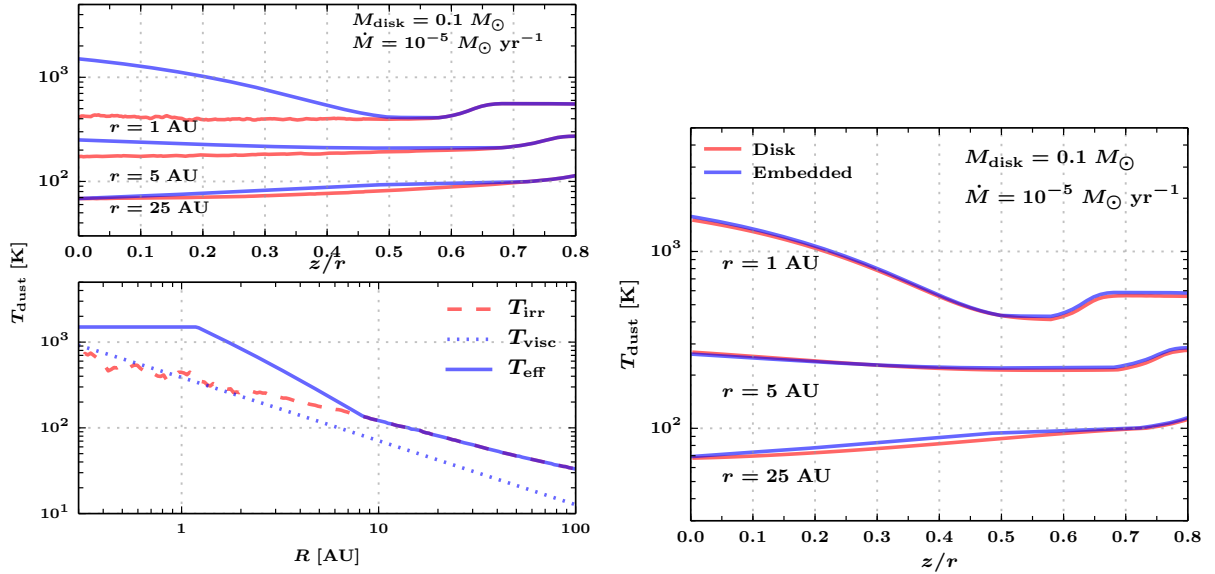[a] First order desorption pre-exponential factor calculated from the binding energies.

Figure 6.2 — *Left*: Midplane radial (*bottom*) and vertical temperatures (*top*) at 1, 5, and 25 AU for a $0.1\ M_\odot$ disk and an accretion rate of $10^{-5}\ M_\odot\ yr^{-1}$. The red dashed (*bottom*) and solid (*top*) lines indicate the thermal structure of a passively irradiated disk (T_{irr}) calculated by the Monte Carlo simulation. The blue solid lines indicate the temperatures including the viscous heating ($T_{eff} = \left(\frac{3}{16}\kappa_R \Sigma_{gas} T_{visc}^4 + T_{irr}^4\right)^{1/4}$). The viscous temperature as calculated from Eq. 6.6 is indicated by the dotted blue lines. *Right*: Comparison of the vertical temperature structure at 1, 5 and 25 AU between a protoplanetary disk (*red*) and an embedded disk (*blue*). The envelope mass is $1\ M_\odot$ for the embedded disk model. *Right*: Comparison of the vertical temperature structure at 1, 5 and 25 AU between a protoplanetary disk (*red*) and an embedded disk (*blue*). The envelope mass is $1\ M_\odot$ for the embedded disk model.

6.3 Results

6.3.1 Thermal structure of an actively accreting embedded disk

The locations at which various molecules can thermally desorb from the dust grain depend on the temperature structure of the disk. Irradiated disks have a warm upper layer with a cooler midplane. Figure 6.2 (red dashed lines) shows the midplane (*bottom*) and vertical (*top*) temperature at a number of radii for an embedded disk passively irradiated by a $1\ L_\odot$ central source. Here, we present the results for a $0.1\ M_\odot$ disk embedded in a $1\ M_\odot$ envelope (Fig. 6.2 left top). This result is also compared with a disk without any envelope in Fig. 6.2 (R). The difference is small in the inner disk, and lies primarily at large radii where the midplane temperature structure ($T_{mid} \propto \Sigma$) is weakly affected by the adopted envelope model. Even at $r > 25$ AU, the difference is small since the centrifugal radius of the envelope is defined at 200 AU. This results
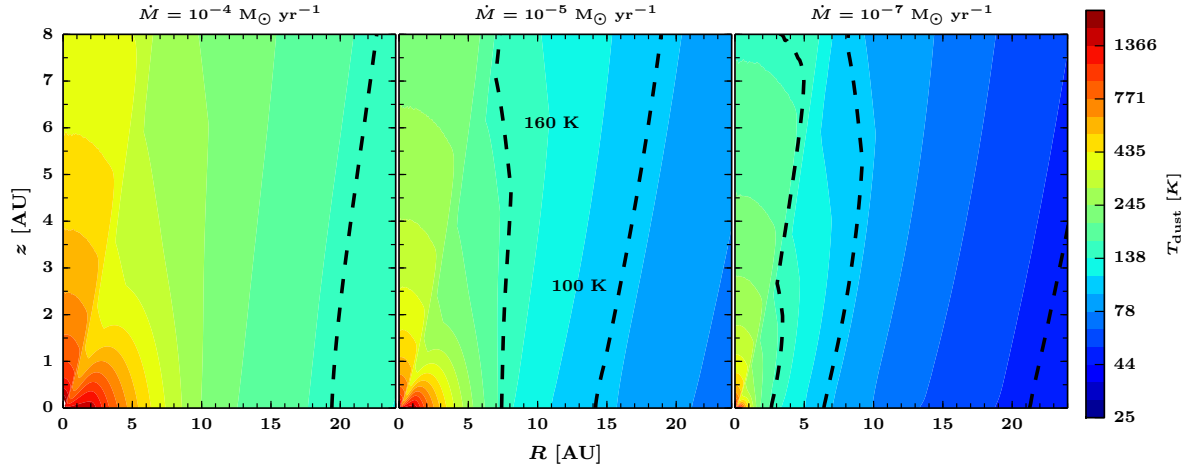
Figure 6.3 — Dust temperature structure in the inner 24 AU for three different accretion rates for a 0.1 $M_\odot$ disk embedded in a 1 $M_\odot$ envelope. A 1 $L_\odot$ central heating source is adopted for these models. The two dashed lines indicate the 160 K and 100 K contours, which are important for the water snowlines.

in density pile-up, which is responsible for the increase of temperature, at 200 AU. A more flattened envelope model ($R_c \sim 50$ AU) will result in a larger difference in the temperature. The inner few AU are highly optically thick at the peak wavelength of the central source such that few photons reach these regions. This does not affect the exact location of the snowline since $T \gg T_{\text{desorb}}$ as indicated in Fig. 6.1 (R) for water.

The temperatures of an actively accreting disk are indicated by the blue lines in Fig. 6.2. The dotted line shows the viscous temperature (T_{visc}) as expected at the photosphere (optically thin) while the solid blue lines show the effective dust temperature corrected for optical depth and passive irradiation. As previously found, the addition of viscous heating can raise the temperatures in the inner few AU to > 1000 K (e.g., Calvet et al. 1991; D'Alessio et al. 1997; Davis 2005). The 2D dust temperature structure in the inner 20 AU is shown in Fig. 6.3 for three different accretion rates. The disk temperature is above 100 K up to ≥ 10 AU for an accretion rate of 10^{-5} $M_\odot$ yr^{-1}. As noted in Eq. 6.6, the viscous temperature depends on stellar mass (0.5 $M_\odot$) and the accretion rate through the disk (see Kennedy & Kenyon 2008). In addition, the effective temperature within the disk depends on the disk mass through Σ and the central luminosity ($L_\star$). Due to the R^{-3} dependence, the viscous heating is dominant in the inner few AU as indicated in Fig. 6.2 (*left bottom*). Consequently, the passive irradiation due to the central luminosity dominates the temperatures along the disk's photosphere and the outflow cavity wall while the viscous dissipation dominates the heating deep within the disk.

6.3.2 Water snowline

Using the obtained dust temperatures, the gas and ice number densities are calculated at each cell. To determine the snowline, the total available water mass is calculated adopting a water abundance of 10^{-4} with respect to H_2. The total available mass is then multiplied by the gas fraction to determine the total gas mass. The snowline is defined as the radius at which 50% of the total available water has frozen onto the grains ($M_{\text{gas}}/M_{\text{ice}} = 0.5$) (e.g., Min et al. 2011). This typically occurs at $\sim$160 K at high density regions ($n_H \sim 10^{14}$ cm^{-3}, see dashed line in Fig. 6.3).

Figure 6.4 (L) presents the midplane snowline radius as a function of accretion rate. In the absence of accretion heating, the water snowline is located at ~ 5 AU. This does not strongly

depend on the accretion rate until a value of $\dot{M} > 10^{-7}\ M_\odot\ \mathrm{yr}^{-1}$ is reached. The maximum water snowline is ~ 30 AU at an accretion rate of $10^{-4}\ M_\odot\ \mathrm{yr}^{-1}$. The water snowline does not depend strongly on disk mass: it is located at only slightly smaller radius for a less massive disk as indicated in Fig. 6.4 (L).

The steep increase of the water snowline at high accretion rates can be understood by comparing the stellar luminosity with the accretion luminosity. The irradiating central luminosity is $1\ L_\odot$. The accretion luminosity is estimated by integrating Eq. 6.6 radially over the active disk between 0.1 and 200 AU in this case and is approximately $L_{\mathrm{acc}} \sim 0.5 \times GM_{\mathrm{star}}\dot{M}/R_{\mathrm{in}}$. Thus, the accretion luminosity is equal to that of the central star for $\dot{M} \sim 3 \times 10^{-6}\ M_\odot\ \mathrm{yr}^{-1}$. For a central luminosity of $1\ L_\odot$, the accretion luminosity starts to contribute to the heating at $\dot{M} > 10^{-7}\ M_\odot\ \mathrm{yr}^{-1}$.

The observable water emission depends on the water vapor column density. The water vapor column extends somewhat further than the snowline due to the vertical gradient in water vapor abundance. The available water is rapidly frozen out onto dust grains beyond the snowline. To determine whether the location of the snowline is within the disk or not, the hydrostatic disk surface is calculated through $H = c_{\mathrm{s}}/\Omega_{\mathrm{K}}$ where $c_{\mathrm{s}} = \sqrt{k_{\mathrm{B}}T_{\mathrm{mid}}/\mu m_{\mathrm{H}}}$ is the sound speed and Ω_{K} is the Keplerian angular frequency. This is the approximated regime where the gas should be in Keplerian motion. For a $1\ L_\odot$ central star, most of the water emission arises from the classical hot core region above the hydrostatic disk surface as shown by the yellow line in Fig. 6.4 (R) if a constant water abundance of 10^{-4} with respect to H_2 is adopted.
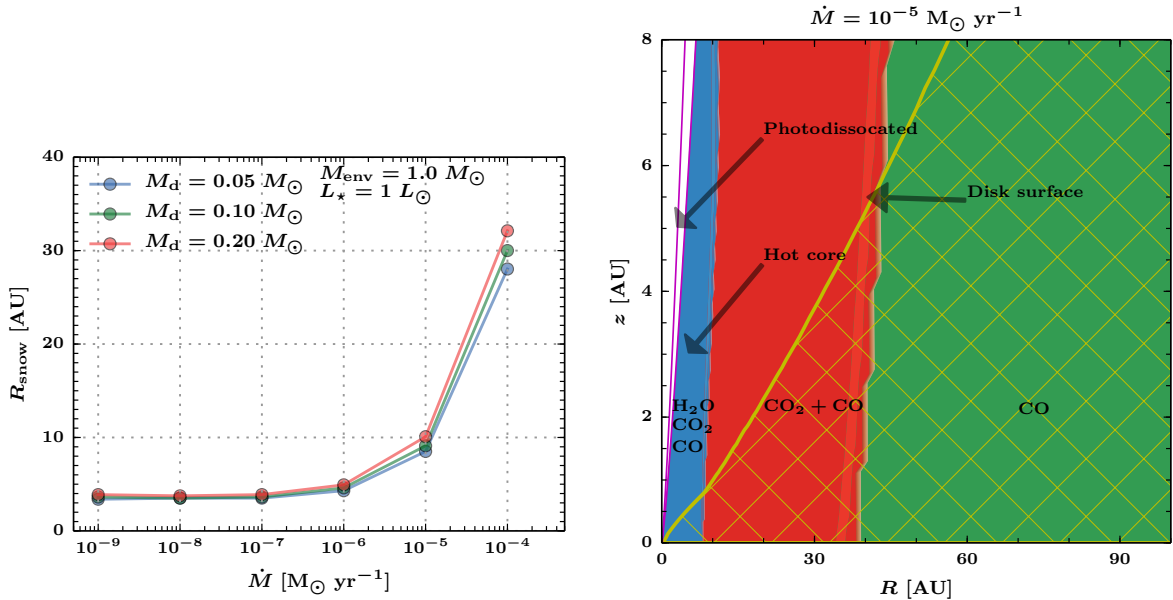

Figure 6.4 — *Left*: Midplane water snowlines as function of accretion rates and disk mass for a 200 AU disk. The different colors indicate the snowlines dependence on disk mass at a fixed stellar luminosity and envelope mass. *Right*: Locations of gas phase volatiles in the 0.1 $M_\odot$ disk embedded in a 1 $M_\odot$ envelope. The different colors indicate the different volatiles: water ($H_2^{16}O$, blue), CO_2 (red), and CO (green). The species that are in the gas phase within each region are all indicated. The accretion rate is indicated at the top. Three different regions are highlighted: photo-dissociation region defined by $A_{\mathrm{V}} = 3$, hot core, and the disk surface (yellow line assuming $T_{\mathrm{gas}} = T_{\mathrm{dust}}$).
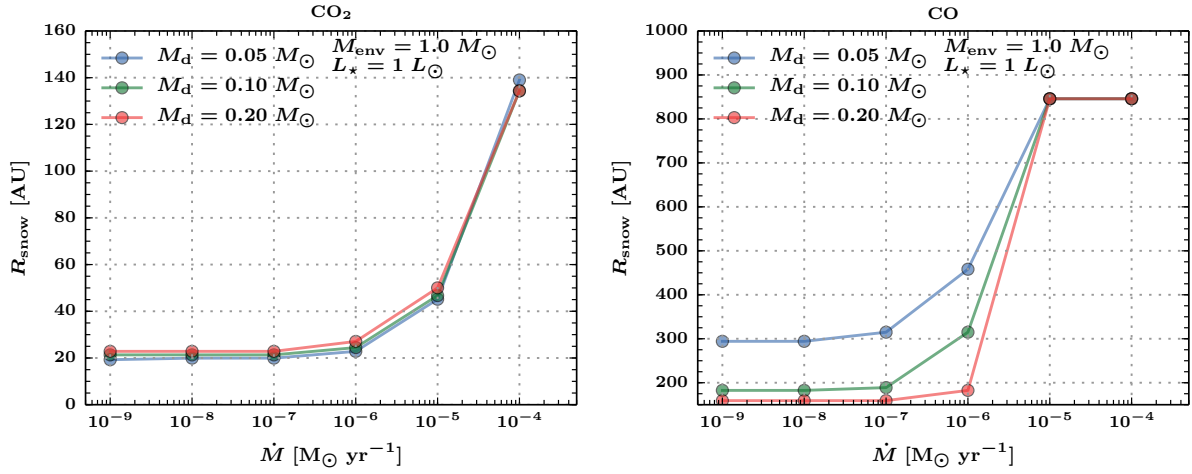
Figure 6.5 — *Left*: Midplane CO_2 snowlines as a function of accretion rates and disk mass for a 200 AU disk. *Right*: Midplane CO snowlines as a function of accretion rates for the same disk. The different colors indicate the snowlines dependence on disk mass at a fixed stellar luminosity (1 $L_\odot$) and envelope mass (1 $M_\odot$).
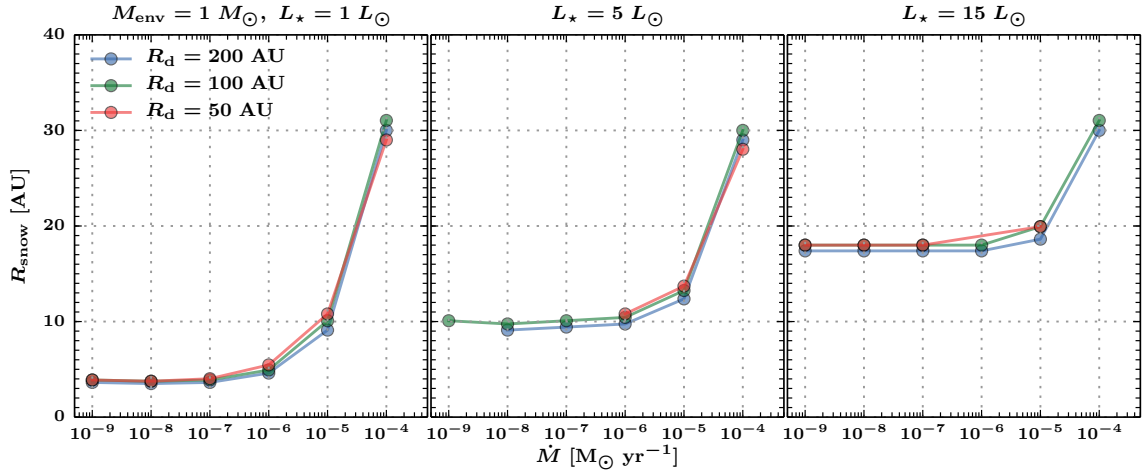

Figure 6.6 — Midplane water snowline as a function of stellar luminosity, accretion rate, and disk radius. The envelope mass is fixed at 1 $M_\odot$ with a disk mass of 0.1 $M_\odot$. The different panels show the water snowline as a function of stellar luminosity: 1 $L_\odot$ (*left*), 5 $L_\odot$ (*center*), and 15 $L_\odot$ (*right*). The different colors indicate the disk radius: 200 AU (*blue*), 100 AU (*green*), and 50 AU (*red*).

6.3.3 CO and CO_2 snow lines

Pure CO_2 and CO ice thermally desorb from the dust grain over a narrow range of dust temperatures between 40–80 K and 15–30 K, respectively depending on the pressure (see Fig. 6.9 in the appendix). Due to their lower binding energies relative to water, CO and CO_2 are in the gas phase within a large part of the embedded disk. The CO_2 snowline is between 15–120 AU for 10^{-9}–10^{-4} $M_\odot$ yr^{-1} accretion rates. Thus, the entire disk including the midplane lacks of CO_2 ice for high accretion rates ($\dot{M} \sim 10^{-4}$ $M_\odot$ yr^{-1}). The snowline is located at $\sim$20 AU for a more massive disk with lower accretion rates. The steep rise of the CO_2 snowline at high accretion rates is similar to that of water as shown in Fig. 6.5.

Since the adopted binding energy of CO is significantly lower than that of the other two

molecules, CO largely remains in the gas phase within the disk for $L_\star \geq 1\ L_\odot$ independent of the accretion rate (see Fig. 6.5 right). At low accretion rates, the snowline is located at ~ 150 AU at the midplane indicating the presence of CO ice between 150 to 200 AU within the disk. However, the bulk of CO within the disk remains in the gas phase as shown in Fig. 6.4 (R). A smaller disk during the embedded phase would lead to stronger envelope irradiation (e.g. D'Alessio et al. 1997), and, consequently, CO is not frozen out within the disk. A sufficiently large and massive disk ($M_{\mathrm{disk}} > 0.2\ M_\odot$ irradiated by a $1\ L_\odot$ star) could contain a larger fraction of CO ice at large radii. This is simply due to the increase of optical depth and, thus, lower dust temperatures at large radii.

6.3.4   Dependence on stellar and disk properties

Previous sections presented the vapor content for a $0.1\ M_\odot$ embedded disk surrounded by a 1 $M_\odot$ envelope irradiated by a $1\ L_\odot$ central star. As noted in Section 6.2.2, the effective midplane temperature (T_{eff}) depends on the disk mass but an increasing disk mass leads to only a small change to the water snowline as shown in Fig. 6.4 (L). Figure 6.4 (R) shows that the water vapor can be either within the disk or within the hot core. The temperature along the outflow cavity wall is controlled by the central luminosity while the effective temperature deep inside the disk is proportional to its mass at a fixed accretion rate. This section investigates how the vapor content depends on disk radius and central luminosity at a fixed envelope and disk mass.

Figure 6.6 presents the locations of water snowline as a function of accretion rate, luminosity and disk radius. For a given disk structure, a factor of 5 increase in luminosity increases the midplane water snowline by a factor of 2 from 5 AU to ~ 10 AU at low accretion rates ($\dot{M} < 10^{-7}\ M_\odot\ \mathrm{yr}^{-1}$). A factor of 15 increase in luminosity yields a factor of ~ 4 increase at the location of the water snowline. A decreasing disk radius does not affect the midplane water snowline until the accretion luminosity starts to significantly contribute to the total luminosity. Thus, an increasing stellar luminosity ($L_\star$) has a greater effect on the midplane water snowline. This leads to a greater amounts of water vapor in the hot core (see Fig. 6.4 R) at low accretion rates. However, there is no change in terms of the water snowline location at high accretion rates ($\dot{M} > 10^{-5}\ M_\odot\ \mathrm{yr}^{-1}$) since the total luminosity is dominated by the accretion luminosity for these scenarios.

The CO_2 midplane snowline shows similar behavior as the water snowline (Fig. 6.10). It is in the gas phase at $R > 40$ AU for $L \geq 5\ L_\odot$. However, the CO_2 snowline shows a stronger dependence on the disk radius than that of water. For the high luminosity case $L_\star = 15\ L_\odot$, the CO_2 snowline increases from 40 AU to 80 AU as the disk radius increases from 50 AU to 200 AU. The CO midplane snowline depends on the disk radius for the $1\ L_\odot$ case (Fig. 6.11). Its location (> 500 AU) no longer depends on accretion rate for $L \geq 5L_\odot$ for the adopted disk and envelope parameters. Thus, CO remains in the gas phase within the disk for $L \geq 5L_\odot$.

6.4   Discussion

6.4.1   Comparison with previous results

In the absence of an envelope, similar stellar parameters and an accretion rate of $10^{-8}\ M_\odot\ \mathrm{yr}^{-1}$ lead to the midplane water snowline located at ~ 1 AU (e.g., Sasselov & Lecar 2000) while our water snowline is located at ~ 3 AU (see Fig. 6.8). Lecar et al. (2006) suggest that the snowline can move out by increasing the accretion rate, disk mass and the dust opacities. The differences between the derived snowlines are unlikely to be due to the differences in radiative transfer treatment. Garaud & Lin (2007) also derived similar water snowlines to that of Min et al. (2011) (1 AU vs 2 AU) using different methods in deriving the dust temperatures and different

opacities for similar accretion rates. The later takes into account the 2D vertical structure of the disk in detail. As Min et al. (2011) shows, most of the differences are due to the adopted dust opacities. Our value is 1 AU larger than the values tabulated in Min et al. (2011) adopting different dust opacity table. Furthermore, most of the previous studies adopt the minimum mass solar nebula (MMSN) model where $\Sigma \propto R^{-1.5}$ instead of the R^{-1} 2D parametric model used in this paper (see e.g., Andrews et al. 2009). At the same accretion rate, the water snowline is at ~ 5 AU with the adopted disk embedded in a massive envelope models.

6.4.2 Caveats

The effect of convection in vertical direction is not included in this study. It is typically found to be important in the case of high accretion rates ($\dot{M} > 10^{-6}$ $M_\odot$ yr^{-1}, D'Alessio et al. 1998, Min et al. 2011). Convection is found to cool the midplane temperatures at $T_{\mathrm{dust}} > 500$ K. Thus, this should not affect the water (100–160 K), CO_2 (~ 50 K) and CO (~ 20 K) snowlines.

Under the assumption of the steady state accretion disk model, the typical values of $\alpha > 1$ is obtained for the case of an accretion rate of $\dot{M} = 10^{-4}$ $M_\odot$ yr^{-1}. This is significantly higher than that expected from magnetorotational instability (MRI) driven accretion in a MHD disk ($\alpha = 0.01$, Balbus & Hawley 1998). King et al. (2007) indicated that α could be ~ 0.4 for disks around compact systems. Such a high value of α in our models are obtained since we have fixed the density distribution for a high accretion rate. In reality, such a disk is unphysical. However, this is only encountered for the highest accretion rate of 10^{-4} $M_\odot$ yr^{-1}. Such a high accretion rate is expected to occur for a very short time. Furthermore, this paper explores the effect of the adopted accretion rates and disk masses for a given fixed parameters. Self-consistent models should be explored in details in the future.

An additional heating term that is not included is the magnetospheric shock (Calvet & Gullbring 1998). For the case of high accretion rates, it is expected that the accretion proceeds straight onto the star instead of stopping at R_{in}. The luminosity that it generates is given by

$$L_{\mathrm{acc}} = \frac{GM_\star \dot{M}}{2R_\star}. \tag{6.12}$$

An accretion rate of 3×10^{-7} $M_\odot$ yr^{-1} will produce a shock luminosity equal to that of 1 $L_\odot$. Thus, the magnetospheric shock luminosity is expected to be one order of magnitude higher than that of the accretion luminosity from the disk at a fixed accretion rate irradiated by a 1 $L_\odot$ central star. Currently, this is not included in the total luminosity as emitted by the central star. On the other hand, this is similar to the results with a higher central luminosity of 15 $L_\odot$. The qualitative effect on the water snowline with the inclusion of magnetospheric shock can be explored by comparing the results at two different luminosities at a fixed accretion rate (see Sect 6.3.4).

6.4.3 Comparison with observations

The extent of the observed spatially resolved water emission toward low-mass embedded YSOs is between 25–90 AU (Jørgensen & van Dishoeck 2010b; Persson et al. 2012, 2014). The water snowline is weakly affected by the envelope properties investigated here. The maximum midplane water snowline in our models is ~ 30 AU with a disk mass of 0.1 $M_\odot$ with $R_{\mathrm{disk}} = 200$ AU and an accretion rate of 10^{-4} $M_\odot$ yr^{-1}. Thus, our results indicate that most of the water emission at $R < 50$ AU would originate from the combine disk and hot core if accretion rates can indeed be this high (see Fig. 6.4 R).
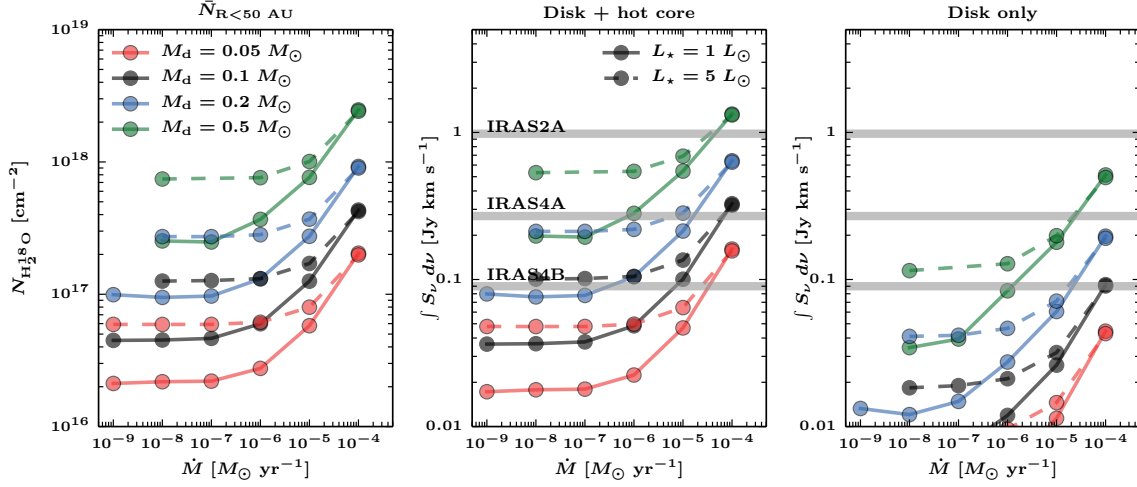
Figure 6.7 — *Left:* Beam averaged water ($H_2^{18}O$) column densities within 50 AU radius as a function of accretion rates. The different colors indicate the disk mass dependence: $M_d = 0.05\,M_\odot$ (red), 0.1 (black), 0.2 (blue) and 0.5 (green). The different lines show the luminosity dependence: $L_\star = 1\,L_\odot$ (solid) and 5 $L_\odot$ (dashed). *Center:* Integrated line flux densities assuming a Gaussian linewidth of 1 km s^{-1} which is appropriate for NGC1333-IRAS4B. The observed integrated $H_2^{18}O$ line is indicated by the gray lines for the three different embedded YSOs in Persson et al. (2014). *Right:* Integrated line flux densities arising from the disk only as defined by the yellow line in Fig. 6.4 (R).

The amount of water vapor in the embedded disk models can be compared to the observed optically thin millimeter water emission toward deeply embedded YSOs. Thermalized $H_2^{18}O$ emission at 203.4 GHz ($3_{1,3} - 2_{2,0}$) is calculated using the following equation

$$I_\nu \approx B_\nu\,(T_{ex})\,(1 - e^{-\tau}),\tag{6.13}$$

$$\tau = \frac{\bar{N}}{\mathcal{Q}\,(T_{ex})\,\Delta V}\frac{A_{ul}c^3}{8\pi\nu^3}e^{h\nu/k_B T_{ex}},\tag{6.14}$$

where A_{ul} is the Einstein A coefficient of the 203 GHz transition is 4.5×10^{-7} s^{-1}, T_{ex} is taken to be 150 K, $E_u = 204$ K is the upper energy level, $g_u = 7$ is the weight of the upper level, and $\mathcal{Q}$ is the temperature dependent partition function adopted form the HITRAN database (Rothman et al. 2009). The beam averaged column density ($\bar{N}$) is taken from within 50 AU radius with $^{16}O{:}^{18}O$ isotopic ratio of 540 (Wilson & Rood 1994). The line profile is assumed to be Gaussian with a $FWHM$ (Δv) = 1–4 km s^{-1} as observed toward the three embedded sources reported by Persson et al. (2014).

Figure 6.7 (*left*) presents the mean $H_2^{18}O$ column density as a function of accretion rate for different disk masses and stellar luminosities. The mean column density rises sharply for $\dot{M} > 10^{-7}\,M_\odot$ as expected for a 1 $L_\odot$ stellar luminosity while it is shifted to $\dot{M} > 10^{-6}\,M_\odot$ for a 5 $L_\odot$ irradiating source. The typical line optical depth at the line center ($v = 0$ km s^{-1}) can be up to $\tau \geq 1$. The typical average column densities of water between 50 AU to 1000 AU are > 4 orders of magnitude lower than the values in Fig. 6.7. Thus, the water present within 50 AU dominates the total water mass for the adopted models.

The expected integrated $H_2^{18}O$ $3_{1,3}$–$2_{2,0}$ (203.4 GHz) line flux densities for the embedded disk models are also shown in Fig. 6.7 (*right*). The plotted integrated line flux densities are calculated with a Gaussian line profile with $\Delta v = 1$ km s^{-1} ($1.06S_{v=0} \times \Delta V$ where $S_{v=0}$ is the peak flux density at line center) as observed toward NGC1333-IRAS4B (Persson et al. 2014). The

observed line widths toward IRAS2A and IRAS4A are 4 and 3 $km\,s^{-1}$, respectively. Increasing Δv slightly increases the model integrated line flux densities.

The predicted integrated line flux densities from actively accreting embedded disk models are consistent with that observed toward NGC1333 IRAS4B if $M_{\rm d} \leq 0.2\ M_\odot$ with $\dot{M} \sim 3 \times 10^{-7}\ M_\odot\ yr^{-1}$ for $L = 1\ L_\odot$. Jørgensen et al. (2009) estimated from the continuum that the disk mass is $\sim 0.2\ M_\odot$, which is consistent with our results. Decreasing the disk mass implies a higher accretion rate is required to reproduce the observed water emission. A higher accretion rate ($\sim 5 \times 10^{-5}\ M_\odot\ yr^{-1}$) with lower disk mass is also consistent with the observed extent of water emission at ~ 20 AU. A similar conclusion is reached for the case of IRAS4A whose disk is estimated to be $\sim 0.5\ M_\odot$ (Jørgensen et al. 2009). At these accretion rates, the accretion luminosity is of the order of the adopted central luminosity (1 $L_\odot$). Since the bolometric luminosity toward NGC1333 IRAS4A and IRAS4B are a factor of 4–9 higher than the adopted central luminosity, a model with a factor of 2 lower mass disk can also reproduce the observed flux density. With such a lower mass disk, the hot core is the dominant source of emission instead of the Keplerian disk.

IRAS2A shows stronger integrated line emission (~ 1 Jy $km\,s^{-1}$) relative to the other 2 sources extending up to 90 AU radius. As pointed out above, a disk cannot be responsible for any warm water emission at $R > 50$ AU. Furthermore, Brinch et al. (2009) and Jørgensen et al. (2009) estimated that the disk is at most $\sim 0.05\ M_\odot$, which lowers the expected disk's contribution to the observed water emission. There are two possible scenarios that can explain such a high water emission: a more luminous star ($L_\star > 10\ L_\odot$) or an extremely high accretion rate ($> 10^{-4}\ M_\odot\ yr^{-1}$). The former is consistent with the high bolometric luminosity of IRAS2A ($L_{\rm bol} = 35.7\ L_\odot$, Kristensen et al. 2012). In this case, most of the water emission arises from the hot core.

To quantify whether the water emission arises from the disk or the hot core, the integrated flux densities as expected to arise from the disk are shown in Fig. 6.7 (far right). For the adopted physical models, disks with masses $M_{\rm d} \geq 0.2\ M_\odot$ with accretion rates of a few times $10^{-5}\ M_\odot\ yr^{-1}$ can also reproduce the water emission without the hot core. However, as shown in Fig. 6.7, most of the emission arises from the hot core assuming a constant water abundance of 10^{-4} with respect to H_2.

The best cases for an actively accreting embedded disk scenario are IRAS4A and IRAS4B. More detailed modelling of their physical structure at < 100 AU radius is required to further constrain the relation between disk accretion (envelope to disk) and stellar accretion rate (disk to star). Mottram et al. (2013) suggests that the infall rate from the large-scale envelope toward IRAS4A at 1000 AU to be $\sim 10^{-4}\ M_\odot\ yr^{-1}$. For the cases of disk masses between 0.2–0.5 $M_\odot$, the disk must also process the material at similar rate (within a factor of 10), which is consistent with the models presented here.

6.4.4 Connecting to the young solar nebula

It is thought that the disk out of which the solar system formed (the solar nebula) was initially hot enough to vaporize all material inherited from the collapsing cloud into atoms, then into solids according to a condensation sequence as the nebula cools (Lewis 1974; Grossman & Larimer 1974). Evidence for energetic processing and subsequent condensation comes from meteoritic data collected in the inner solar system (see Kerridge & Matthews 1988; Scott 2007; Apai & Lauretta 2010,for reviews). After the refractory phases have formed, more volatile species such as ices can also condense at larger distances from the young Sun, with the ice composition depending on the temperature and pressure as well as the elemental abundance ratios (e.g., Lunine et al. 1991; Owen & Bar-Nun 1993; Mousis et al. 2009; Pontoppidan et al.

2014). Using cooling curves appropriate for the solar nebula, models show that various ices including H_2O, CH_3OH, NH_3 and CO_2 ice form by condensation out of warm gas out to at least 20 AU (Mousis et al. 2012; Marboeuf et al. 2014). This condensation process is important to explain the composition of volatiles in the atmospheres of solar-system giant planets and comets.

Where and when does this heating and condensation in the disk actually occur? The above processes are usually discussed in the context of protoplanetary disks where the envelope has dissipated and where the water snowline is eventually at a few AU once the disk has cooled. However, neither observations nor models of disks around solar-mass T-Tauri stars show any evidence that disks are as warm as required above to have condensation happening out to 20 AU (Beckwith et al. 1990; D'Alessio et al. 1998; Dullemond et al. 2007). The results from this paper indicate that instead such a hot disk may be more common in the early stages of disk formation during the *embedded* phase. The disk is then expected to have the high accretion rates which provide the necessary additional heating. Furthermore, the high accretion rates necessary to push the midplane snowlines to 20 AU and beyond tend to occur for only a short time (e.g., Vorobyov 2009). Most volatiles including H_2O, CH_3OH, CO_2 and CO presented here will then be in the gas-phase within this 20–30 AU radius through sublimation of ices. Shortly after, the volatiles re-condense as the accretion rate decreases, with the process controlled by the freeze-out timescale. The inclusion of the gas motions (radially and vertically) and kinetics does not allow for instantaneous re-condensation, thus some gas-phase volatiles should remain near the snowline (Lewis & Prinn 1980; Ciesla & Cuzzi 2006).

A related question is whether the volatiles that are incorporated into planetesimals and eventually planets and icy bodies in the critical 5–30 AU zone are then *inherited* or *reset* during the disk formation process. Evolutionary models by Visser et al. (2009) and Visser et al. (2011) suggest that strongly bound ices such as H_2O are largely pristine interstellar ices in the outer disk, whereas more volatile species can have sublimated, recondensed and reprocessed several times on their way to the inner disk. However, these models have not included internal viscous dissipation as an additional heating source. A warmer early disk can facilitate ice evolution and formation of complex organic molecules in the temperature regime between 20–40 K (Garrod et al. 2008; Nomura et al. 2009; Walsh et al. 2014; Drozdovskaya et al. 2014). Our results including the accretion heating indicate that significant ice re-processing may occur out to larger radii than thought before, well in the comet formation zone. Such a *reset* scenario is supported by the meteoritic data from the inner few AU, but the fraction of material that is reset at larger (e.g. Pontoppidan et al. 2014).

6.5 Summary and conclusions

Two-dimensional embedded disk models have been presented to investigate the location of the snowlines of H_2O, CO_2 and CO. The dust temperature structure is calculated using the 3D dust radiative transfer code RADMC3D with a central heating source ($L_\star + L_{\mathrm{visc}}$). An additional heating term from an actively accreting disk has been added through a diffusion approximation. The main parameters that are explored in this paper are $L_\star$, envelope mass, disk radius, disk mass, and disk accretion rate. In addition, the extent of the snowline and optically thin water emission are compared with observations toward three deeply embedded low-mass YSOs. The following lists the main results of this paper.

- The midplane water snowline can extend up to ~ 30 AU for a disk accreting at 10^{-4} $M_\odot$ yr^{-1}. The CO_2 snowline is located at 100 AU for the same accretion rate. Both H_2O and CO_2 can remain in the solid phase at large radii ($R > 100$ AU) in the midplane

within the boundaries of an embedded hydrostatic disk.

- CO is largely found to be in the gas phase within the embedded disk independent of accretion rate and disk properties. Some CO could be frozen out at large radii in the midplane for a relatively massive disk ($M_d \geq 0.1\ M_\odot$).

- The predicted water snowlines in our actively accreting embedded disk models can explain the water emission within $R < 50$ AU emitted from the combined hot core and the disk (see Fig. 6.4 R).

- The predicted optically thin water emission is consistent with that observed toward NGC1333 IRAS4A and IRAS4B for $\dot{M} > 10^{-6}\ M_\odot\ \mathrm{yr}^{-1}$ for the adopted disk masses of 0.5 $M_\odot$ and 0.2 $M_\odot$, respectively. The observed size of water emission can also be explained with a slightly higher accretion rate model with a lower disk mass. The comparison with the observed water emission toward IRAS2A suggests less disk's contribution relative to IRAS4A and IRAS4B. More detailed physical structure models of NGC1333 IRAS4A and IRAS4B are needed to further quantify the disk's contribution to the observed water emission.

- Significant chemical processing is expected to occur in the inner 100 AU region during the disk formation process in Stage 0. Midplane temperatures between 20–40 K are expected to be prevalent up to 100 AU radius, and 100 K out to 30 AU, for typical accretion rates found in the early phases of star formation. During these warm phases, the chemistry inherited from the collapsing cloud could be reset and more complex molecules could form.

In connection to the solar system formation, the young disk is found to be warm enough such that the water vapor can up to the 30 AU radius within the disk. It is important to realize, however, that a hot young solar nebula out to 30 AU can only occur during the deeply embedded phase, not the T Tauri phase of our solar system. Our models predict that most of the optically thin water emission arises within the inner 50 AU radius. Future Atacama Large Millimeter Array (ALMA) observations spatially resolving the inner 50 AU will test the embedded accreting disk models coupled with better physical models for individual sources. This will lead to better understanding of the physical and chemical structure and evolution of disks in the early stages of star formation.

Acknowledgements

6.A Snowline test

Water snowlines were inferred and compared with results from Min et al. (2011) in Fig. 6.8 using the minimum mass solar nebula (MMSN) model ($\Sigma \propto r^{-1.5}$). The comparison shows that our adopted method reproduces the water snowlines at high accretion rates. For low accretion rates $\dot{M} \leq 10^{-9}\ M_\odot\ \mathrm{yr}^{-1}$, our values are slightly smaller yet consistent with those reported in literature.
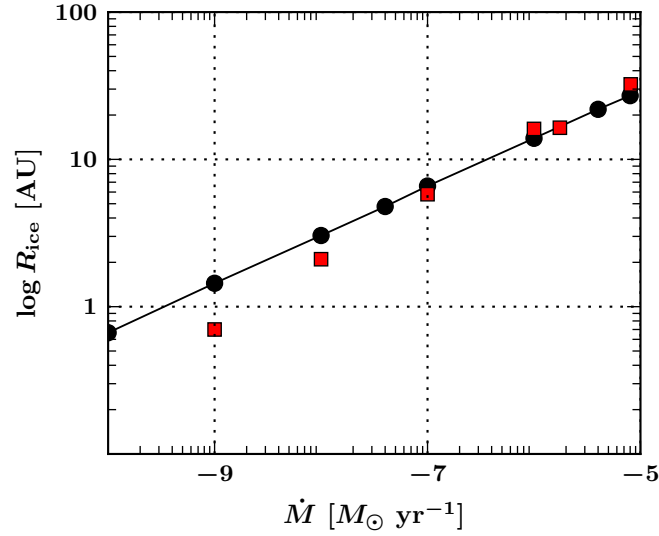
Figure 6.8 — Snowlines for the MMSN disk without an envelope: black circles show the radii calculated with our method and red squares are tabulated values from Min et al. (2011).
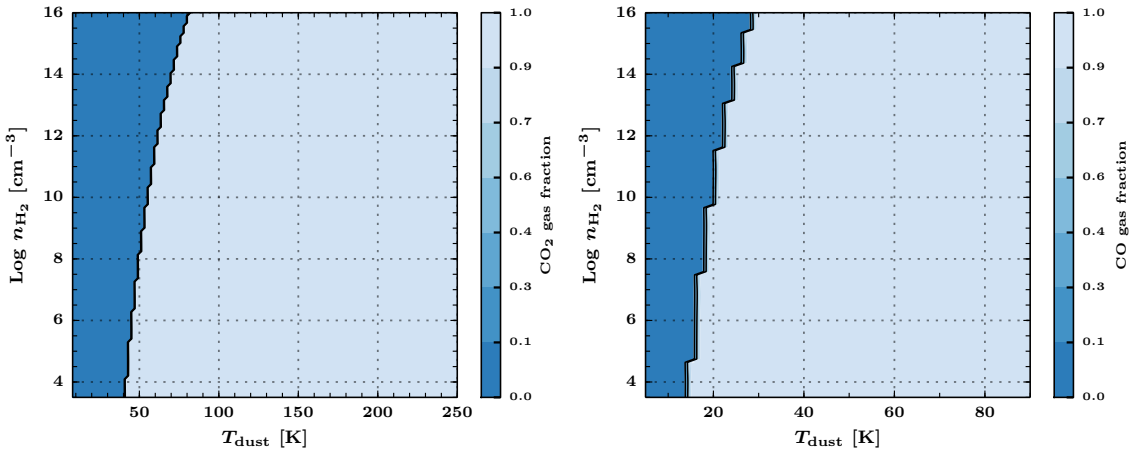

Figure 6.9 — Gas fraction ($n_{gas}/n_{gas} + n_{ice}$) for CO_2 (*Top*) and CO (*Bottom*) as a function of density and temperatures.

6.B CO_2 and CO gas fraction

The CO_2 and CO gas pressure dependent gas fraction abundance are shown in Fig. 6.9. The range of density and temperature is the same as Fig. 6.1 (R) except for CO. Figures 6.10 and 6.11 show the midplane CO_2 and CO snowlines as a function of luminosity and R_d similar to that of Fig. 6.6 for H_2O.

Figure 6.10 — Midplane CO_2 snowline as a function of stellar luminosity, accretion rate, and disk radius. The parameters are similar to that of Fig. 6.6.
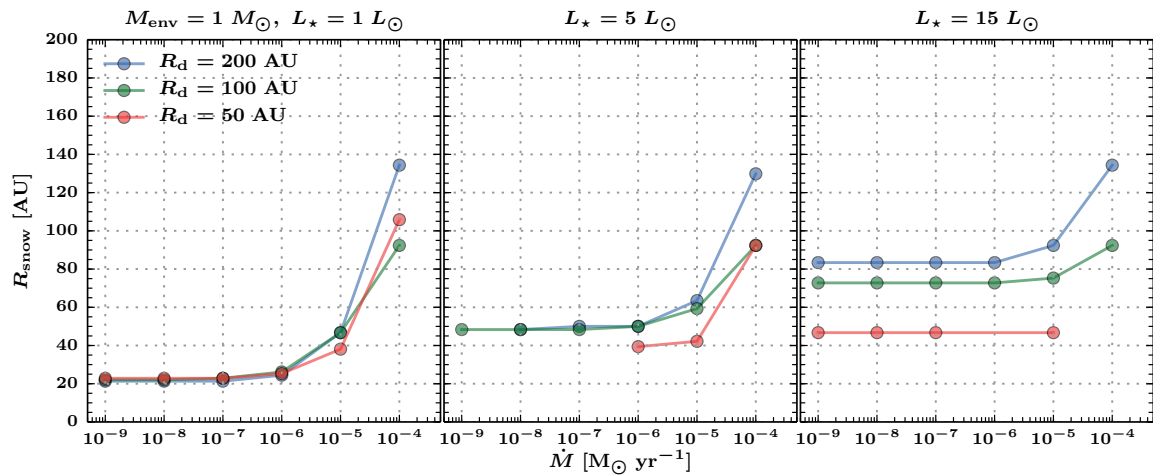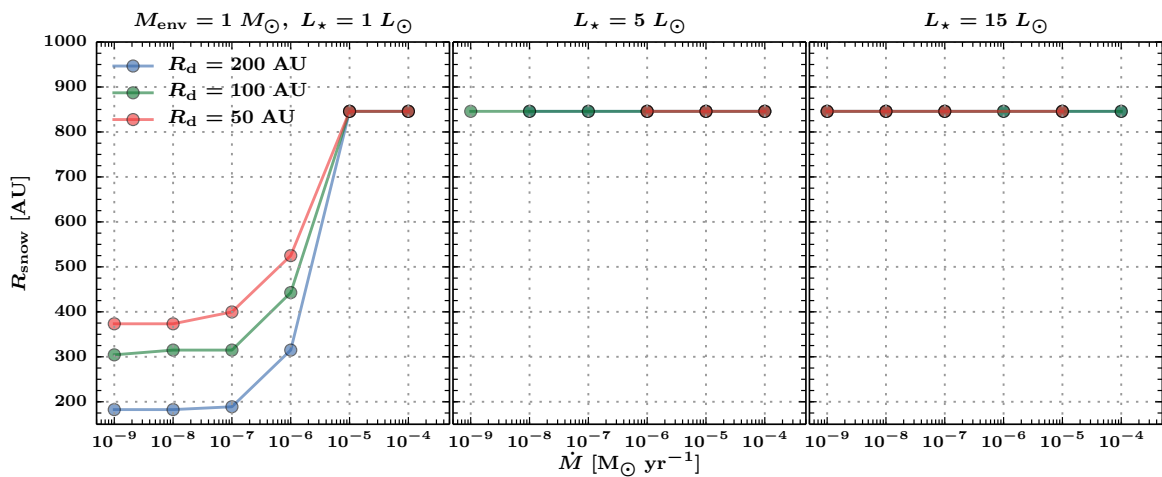

Figure 6.11 — Midplane CO snowline as a function of stellar luminosity, accretion rate, and disk radius. The parameters are similar to that of Fig. 6.6.

Bibliography

Adams, F. C., Ruden, S. P., & Shu, F. H. 1989, ApJ, 347, 959

Agertz, O., Moore, B., Stadel, J., et al. 2007, MNRAS, 380, 963

Aikawa, Y., Furuya, K., Wakelam, V., et al. 2011, in The Molecular Universe, IAU Symposium 280, ed. J. Cernicharo & R. Bachiller (Cambridge Univ. Press, Cambridge), 33–42

Aikawa, Y., Wakelam, V., Garrod, R. T., & Herbst, E. 2008, ApJ, 674, 984

Alexander, R. D., Armitage, P. J., Cuadra, J., & Begelman, M. C. 2008, ApJ, 674, 927

André, P., Di Francesco, J., Ward-Thompson, D., et al. 2014, in Protostars and Planets VI, ed. H. Beuther, C. Dullemond, & T. Henning (Univ. of Arizona Press, Tucson), in press

André, P., Men'shchikov, A., Bontemps, S., et al. 2010, A&A, 518, L102

Andre, P., Ward-Thompson, D., & Barsony, M. 1993, ApJ, 406, 122

Andrews, S. M., Wilner, D. J., Hughes, A. M., Qi, C., & Dullemond, C. P. 2009, ApJ, 700, 1502

Apai, D. A. & Lauretta, D. S. 2010, Protoplanetary Dust: Astrophysical and Cosmochemical Perspectives (Cambridge Univ. Press, Cambridge)

Arce, H. G., Shepherd, D., Gueth, F., et al. 2007, in Protostars and Planets V, ed. B. Reipurth, D. Jewitt, & K. Keil (Univ. of Arizona Press, Tucson), 245–260

Armitage, P. J., Livio, M., & Pringle, J. E. 2001, MNRAS, 324, 705

Bachiller, R. & Tafalla, M. 1999, in NATO ASIC Proc. 540: The Origin of Stars and Planetary Systems, ed. C. J. Lada & N. D. Kylafis, 227

Baines, D., Oudmaijer, R. D., Porter, J. M., & Pozzo, M. 2006, MNRAS, 367, 737

Balbus, S. A. & Hawley, J. F. 1991, ApJ, 376, 214

Balbus, S. A. & Hawley, J. F. 1998, Rev. Mod. Phys., 70, 1

Balbus, S. A. & Papaloizou, J. C. B. 1999, ApJ, 521, 650

Balsara, D. S. 1995, Journal of Computational Physics, 121, 357

Batalha, N. M., Rowe, J. F., Bryson, S. T., et al. 2013, ApJ, 204, 24

Beckwith, S., Skrutskie, M. F., Zuckerman, B., & Dyck, H. M. 1984, ApJ, 287, 793

Beckwith, S. V. W., Sargent, A. I., Chini, R. S., & Guesten, R. 1990, AJ, 99, 924

Bell, K. R., Cassen, P. M., Klahr, H. H., & Henning, T. 1997, ApJ, 486, 372

Bell, K. R. & Lin, D. N. C. 1994, ApJ, 427, 987

Belloche, A. 2013, in EAS Publications Series 62, 25–66

Belloche, A., André, P., Despois, D., & Blinder, S. 2002, A&A, 393, 927

Berger, J. P. & Segransan, D. 2007, New Astron. Rev., 51, 576

Bergin, E. A. & Tafalla, M. 2007, ARA&A, 45, 339

Bisschop, S. E., Fraser, H. J., Öberg, K. I., van Dishoeck, E. F., & Schlemmer, S. 2006, A&A, 449, 1297

Bjorkman, J. E. & Wood, K. 2001, ApJ, 554, 615

Bodenheimer, P. 1995, ARA&A, 33, 199

Boley, A. C. 2009, ApJ, 695, L53

Boley, A. C., Mejía, A. C., Durisen, R. H., et al. 2006, ApJ, 651, 517

Bonnell, I. A. & Rice, W. K. M. 2008, Science, 321, 1060

Boogert, A. C. A., Hogerheijde, M. R., & Blake, G. A. 2002, ApJ, 568, 761

Braiding, C. R. & Wardle, M. 2012, MNRAS, 422, 261

Brinch, C., Crapsi, A., Hogerheijde, M. R., & Jørgensen, J. K. 2007a, A&A, 461, 1037

Brinch, C., Crapsi, A., Jørgensen, J. K., Hogerheijde, M. R., & Hill, T. 2007b, A&A, 475, 915

Brinch, C. & Hogerheijde, M. R. 2010, A&A, 523, 25

Brinch, C., Hogerheijde, M. R., & Richling, S. 2008, A&A, 489, 607

Brinch, C. & Jørgensen, J. K. 2013, A&A, 559, A82

Brinch, C., Jørgensen, J. K., & Hogerheijde, M. R. 2009, A&A, 502, 199

Brittain, S. D., Rettig, T. W., Simon, T., & Kulesa, C. 2005, ApJ, 626, 283

Brown, D. W. & Chandler, C. J. 1999, MNRAS, 303, 855

Brown, D. W., Chandler, C. J., Carlstrom, J. E., et al. 2000, MNRAS, 319, 154

Bruderer, S. 2010, PhD thesis, ETH Zurich

Bruderer, S., Benz, A. O., Stäuber, P., & Doty, S. D. 2010, ApJ, 720, 1432

Bruderer, S., van Dishoeck, E. F., Doty, S. D., & Herczeg, G. J. 2012, A&A, 541, A91

Burke, D. J. & Brown, W. A. 2010, Phys. Chem. Chem. Phys., 12, 5947

Burkert, A. & Bodenheimer, P. 2000, ApJ, 543, 822

Cabrit, S., Guilloteau, S., Andre, P., et al. 1996, A&A, 305, 527

Calvet, N. & Gullbring, E. 1998, ApJ, 509, 802

Calvet, N., Hartmann, L., & Strom, S. E. 2000, in Protostars and Planets IV, ed. V. Mannings, A. P. Boss, & S. S. Russel (Univ. of Arizona Press, Tucson), 377

Calvet, N., Patino, A., Magris, G. C., & D'Alessio, P. 1991, ApJ, 380, 617

Caselli, P., Benson, P. J., Myers, P. C., & Tafalla, M. 2002, ApJ, 572, 238

Cassen, P. 2001, Meteoritics and Planetary Science, 36, 671

Cassen, P. & Moosman, A. 1981, Icarus, 48, 353

Cesaroni, R., Galli, D., Lodato, G., Walmsley, C. M., & Zhang, Q. 2007, in Protostars and Planets V, ed. B. Reipurth, D. Jewitt, & K. Keil (Univ. of Arizona Press, Tucson), 197–212

Cesaroni, R., Galli, D., Lodato, G., Walmsley, M., & Zhang, Q. 2006, Nature, 444, 703

Chandra, S. & Sharma, A. K. 2001, A&A, 376, 356

Chiang, E. I. & Goldreich, P. 1997, ApJ, 490, 368

Chiang, E. I., Joung, M. K., Creech-Eakman, M. J., et al. 2001, ApJ, 547, 1077

Chiang, H.-F., Looney, L. W., Tassis, K., Mundy, L. G., & Mouschovias, T. C. 2008, ApJ, 680, 474

Chiang, H.-F., Looney, L. W., & Tobin, J. J. 2012, ApJ, 756, 168

Choi, M., Tatematsu, K., & Kang, M. 2010, ApJ, 723, L34

Ciesla, F. J. & Cuzzi, J. N. 2006, Icarus, 181, 178

Clarke, C. J. 2009, MNRAS, 396, 1066

Commerçon, B., Launhardt, R., Dullemond, C., & Henning, T. 2012a, A&A, 545, A98

Commerçon, B., Levrier, F., Maury, A. J., Henning, T., & Launhardt, R. 2012b, A&A, 548, A39

Cossins, P., Lodato, G., & Clarke, C. J. 2009, MNRAS, 393, 1157

Cossins, P., Lodato, G., & Testi, L. 2010, MNRAS, 407, 181

Crapsi, A., Devries, C. H., Huard, T. L., et al. 2005, A&A, 439,

1023

Crapsi, A., van Dishoeck, E. F., Hogerheijde, M. R., Pontoppidan, K. M., & Dullemond, C. P. 2008, A&A, 486, 245

Crutcher, R. M. 2012, ARA&A, 50, 29

Crutcher, R. M., Hakobian, N., & Troland, T. H. 2010, MNRAS, 402, L64

Cuadra, J., Nayakshin, S., Springel, V., & Di Matteo, T. 2006, MNRAS, 366, 358

D'Alessio, P., Calvet, N., & Hartmann, L. 1997, ApJ, 474, 397

D'Alessio, P., Cantö, J., Calvet, N., & Lizano, S. 1998, ApJ, 500, 411

Dapp, W. B. & Basu, S. 2010, A&A, 521, L56

Dapp, W. B., Basu, S., & Kunz, M. W. 2012, A&A, 541, A35

Davis, S. S. 2005, ApJ, 620, 994

de Graauw, T., Helmich, F. P., Phillips, T. G., et al. 2010, A&A, 518, L6

Di Francesco, J., Johnstone, D., Kirk, H., MacKenzie, T., & Ledwosinska, E. 2008, ApJ, 175, 277

Dib, S., Hennebelle, P., Pineda, J. E., et al. 2010, ApJ, 723, 425

Doty, S. D., Schöier, F. L., & van Dishoeck, E. F. 2004, A&A, 418, 1021

Doty, S. D., van Dishoeck, E. F., van der Tak, F. F. S., & Boonman, A. M. S. 2002, A&A, 389, 446

Douglas, T. A., Caselli, P., Ilee, J. D., et al. 2013, MNRAS, 433, 2064

Drozdovskaya, M. N., C., W., R., V., D., H., & van Dishoeck, E. F. 2014, MNRAS, subm.

Dullemond, C. P. & Dominik, C. 2004, A&A, 421, 1075

Dullemond, C. P., Hollenbach, D., Kamp, I., & D'Alessio, P. 2007, in Protostars and Planets V, ed. B. Reipurth, D. Jewitt, & K. Keil (Univ. of Arizona Press, Tucson), 555–572

Dullemond, C. P. & Monnier, J. D. 2010, ARA&A, 48, 205

Dunham, M. M., Evans, II, N. J., Terebey, S., Dullemond, C. P., & Young, C. H. 2010, ApJ, 710, 470

Dunham, M. M., Stutz, A. M., Allen, L. E., et al. 2014, in Protostars and Planets VI, ed. H. Beuther, C. Dullemond, & T. Henning (Univ. of Arizona Press, Tucson), in press

Dunham, M. M. & Vorobyov, E. I. 2012, ApJ, 747, 52

Durisen, R. H., Boss, A. P., Mayer, L., et al. 2007, in Protostars and Planets V, ed. B. Reipurth, D. Jewitt, & K. Keil (Univ. of Arizona Press, Tucson), 607–622

Dutrey, A., Guilloteau, S., & Ho, P. 2007, in Protostars and Planets V, ed. B. Reipurth, D. Jewitt, & K. Keil (Univ. of Arizona Press, Tucson), 495–506

Dzib, S., Loinard, L., Mioduszewski, A. J., et al. 2010, ApJ, 718, 610

Eddington, A. S. 1937, The Observatory, 60, 99

Eisner, J. A. 2012, ApJ, 755, 23

Eisner, J. A., Hillenbrand, L. A., Carpenter, J. M., & Wolf, S. 2005, ApJ, 635, 396

Enoch, M. L., Corder, S., Duchêne, G., et al. 2011, ApJ, 195, 21

Enoch, M. L., Corder, S., Dunham, M. M., & Duchêne, G. 2009, ApJ, 707, 103

Evans, N., Calvet, N., Cieza, L., et al. 2009a, ArXiv e-prints

Evans, II, N. J. 1999, ARA&A, 37, 311

Evans, II, N. J., Dunham, M. M., Jørgensen, J. K., et al. 2009b, ApJ, 181, 321

Evans, II, N. J., Lee, J.-E., Rawlings, J. M. C., & Choi, M. 2005, ApJ, 626, 919

Fayolle, E. C., Bertin, M., Romanzin, C., et al. 2011, ApJ, 739, L36

Fedele, D., Bruderer, S., van Dishoeck, E. F., et al. 2013, ApJ, 776, L3

Fleming, T. P., Stone, J. M., & Hawley, J. F. 2000, ApJ, 530, 464

Forgan, D., Armitage, P. J., & Simon, J. B. 2012, MNRAS, 426, 2419

Fraser, H. J., Collings, M. P., McCoustra, M. R. S., & Williams, D. A. 2001, MNRAS, 327, 1165

Furlan, E., McClure, M., Calvet, N., et al. 2008, ApJ, 176, 184

Galli, D., Lizano, S., Shu, F. H., & Allen, A. 2006, ApJ, 647, 374

Galli, D. & Palla, F. 2013, ARA&A, 51, 163

Galli, D. & Shu, F. H. 1993, ApJ, 417, 220

Gammie, C. F. 1996, ApJ, 457, 355

Gammie, C. F. 2001, ApJ, 553, 174

Garaud, P. & Lin, D. N. C. 2007, ApJ, 654, 606

Garrod, R. T., Weaver, S. L. W., & Herbst, E. 2008, ApJ, 682, 283

Genzel, R., Schödel, R., Ott, T., et al. 2003, ApJ, 594, 812

Ghez, A. M., Salim, S., Hornstein, S. D., et al. 2005, ApJ, 620, 744

Gibb, E. L., Whittet, D. C. B., Boogert, A. C. A., & Tielens, A. G. G. M. 2004, ApJ, 151, 35

Gillett, F. C. & Forrest, W. J. 1973, ApJ, 179, 483

Gingold, R. A. & Monaghan, J. J. 1977, MNRAS, 181, 375

Goicoechea, J. R., Cernicharo, J., Karska, A., et al. 2012, A&A, 548, A77

Goldflam, R., Kouri, D. J., & Green, S. 1977, J. Chem. Phys., 67, 4149

Goodman, A. A., Benson, P. J., Fuller, G. A., & Myers, P. C. 1993, ApJ, 406, 528

Gramajo, L. V., Whitney, B. A., Gómez, M., & Robitaille, T. P. 2010, AJ, 139, 2504

Gramajo, L. V., Whitney, B. A., Kenyon, S. J., Gómez, M., & Merrill, K. M. 2007, AJ, 133, 1911

Greaves, J. S., Richards, A. M. S., Rice, W. K. M., & Muxlow, T. W. B. 2008, MNRAS, 391, L74

Griffin, M. J., Abergel, A., Abreu, A., et al. 2010, A&A, 518, L3

Grossman, L. & Larimer, J. W. 1974, Reviews of Geophysics and Space Physics, 12, 71

Guilloteau, S., Piétu, V., Dutrey, A., & Guélin, M. 2006, A&A, 448, L5

Haisch, Jr., K. E., Lada, E. A., & Lada, C. J. 2001, ApJ, 553, L153

Harsono, D., Alexander, R. D., & Levin, Y. 2011, MNRAS, 413, 423

Harsono, D., Jørgensen, J. K., van Dishoeck, E. F., et al. 2014, A&A, 562, A77

Harsono, D., Visser, R., Bruderer, S., van Dishoeck, E. F., & Kristensen, L. E. 2013, A&A, 555, A45

Hartmann, L., Calvet, N., Gullbring, E., & D'Alessio, P. 1998, ApJ, 495, 385

Hartmann, L. & Kenyon, S. J. 1985, ApJ, 299, 462

Hartmann, L. & Kenyon, S. J. 1987, ApJ, 312, 243

Hasegawa, T. I., Herbst, E., & Leung, C. M. 1992, ApJ, 82, 167

Hayashi, C. 1981, in Fundamental Problems in the Theory of Stellar Evolution, IAU Symposium 93, ed. D. Sugimoto, D. Q. Lamb, & D. N. Schramm (D. Reidel Publishing Co., Dordrecht), 113–126

Hayashi, M., Ohashi, N., & Miyama, S. M. 1993, ApJ, 418, L71

Hennebelle, P. & Ciardi, A. 2009, A&A, 506, L29

Hennebelle, P. & Falgarone, E. 2012, A&A Rev., 20, 55

Herczeg, G. J., Brown, J. M., van Dishoeck, E. F., & Pontoppidan, K. M. 2011, A&A, 533, A112

Herczeg, G. J., Karska, A., Bruderer, S., et al. 2012, A&A, 540, A84

Hogerheijde, M. R. 2001, ApJ, 553, 618

Hogerheijde, M. R. & Sandell, G. 2000, ApJ, 534, 880

Hogerheijde, M. R. & van der Tak, F. F. S. 2000, A&A, 362, 697

Hogerheijde, M. R., van Dishoeck, E. F., Blake, G. A., & van

Langevelde, H. J. 1998, ApJ, 502, 315

Hubeny, I. 1990, ApJ, 351, 632

Hueso, R. & Guillot, T. 2005, A&A, 442, 703

Hughes, A. M., Wilner, D. J., Andrews, S. M., Qi, C., & Hogerheijde, M. R. 2011, ApJ, 727, 85

Ivezic, Z. & Elitzur, M. 1997, MNRAS, 287, 799

Joos, M., Hennebelle, P., & Ciardi, A. 2012, A&A, 543, A128

Joos, M., Hennebelle, P., Ciardi, A., & Fromang, S. 2013, A&A, 554, A17

Jørgensen, J. K., Bourke, T. L., Myers, P. C., et al. 2007, ApJ, 659, 479

Jørgensen, J. K., Bourke, T. L., Myers, P. C., et al. 2005a, ApJ, 632, 973

Jørgensen, J. K., Schöier, F. L., & van Dishoeck, E. F. 2002, A&A, 389, 908

Jørgensen, J. K., Schöier, F. L., & van Dishoeck, E. F. 2005b, A&A, 435, 177

Jørgensen, J. K. & van Dishoeck, E. F. 2010a, ApJ, 725, L172

Jørgensen, J. K. & van Dishoeck, E. F. 2010b, ApJ, 710, L72

Jørgensen, J. K., van Dishoeck, E. F., Visser, R., et al. 2009, A&A, 507, 861

Jørgensen, J. K., Visser, R., Sakai, N., et al. 2013, ApJ, 779, L22

Karska, A., Herczeg, G. J., van Dishoeck, E. F., et al. 2013, A&A, 552, A141

Keene, J. & Masson, C. R. 1990, ApJ, 355, 635

Kennedy, G. M. & Kenyon, S. J. 2008, ApJ, 673, 502

Kennicutt, R. C. & Evans, N. J. 2012, ARA&A, 50, 531

Kenyon, S. J., Calvet, N., & Hartmann, L. 1993, ApJ, 414, 676

Kenyon, S. J. & Hartmann, L. 1987, ApJ, 323, 714

Kenyon, S. J. & Hartmann, L. W. 1990, ApJ, 349, 197

Kerridge, J. F. & Matthews, M. S. 1988, Meteorites and the early solar system (Univ. of Arizona Press, Tucson)

King, A. R., Pringle, J. E., & Livio, M. 2007, MNRAS, 376, 1740

Krasnopolsky, R., Li, Z.-Y., & Shang, H. 2011, ApJ, 733, 54

Kratter, K. M. & Matzner, C. D. 2006, MNRAS, 373, 1563

Kratter, K. M., Matzner, C. D., Krumholz, M. R., & Klein, R. I. 2010, ApJ, 708, 1585

Kristensen, L. E., van Dishoeck, E. F., Benz, A. O., et al. 2013, A&A, 557, A23

Kristensen, L. E., van Dishoeck, E. F., Bergin, E. A., et al. 2012, A&A, 542, A8

Krumholz, M. R., Crutcher, R. M., & Hull, C. L. H. 2013, ApJ, 767, L11

Krumholz, M. R., Klein, R. I., & McKee, C. F. 2007, ApJ, 656, 959

Lada, C. J. & Wilking, B. A. 1984, ApJ, 287, 610

Larson, R. B. 1969, MNRAS, 145, 271

Larson, R. B. 1972, MNRAS, 156, 437

Larson, R. B. 2003, Reports on Progress in Physics, 66, 1651

Laughlin, G. & Bodenheimer, P. 1994, ApJ, 436, 335

Laughlin, G., Korchagin, V., & Adams, F. C. 1998, ApJ, 504, 945

Lay, O. P., Carlstrom, J. E., & Hills, R. E. 1997, ApJ, 489, 917

Lay, O. P., Carlstrom, J. E., Hills, R. E., & Phillips, T. G. 1994, ApJ, 434, L75

Lecar, M., Podolak, M., Sasselov, D., & Chiang, E. 2006, ApJ, 640, 1115

Lee, C.-F. 2010, ApJ, 725, 712

Lee, C.-F. 2011, ApJ, 741, 62

Lee, J.-E., Evans, II, N. J., & Bergin, E. A. 2005, ApJ, 631, 351

Lee, J.-E., Evans, II, N. J., Shirley, Y. L., & Tatematsu, K. 2003, ApJ, 583, 789

Levin, Y. 2003, ArXiv Astrophysics e-prints

Levin, Y. 2007, MNRAS, 377, 159

Levin, Y. & Beloborodov, A. M. 2003, ApJ, 590, L33

Lewis, J. S. 1974, Science, 186, 440

Lewis, J. S. & Prinn, R. G. 1980, ApJ, 238, 357

Li, Z.-Y., Banerjee, R., Pudritz, R. E., et al. 2014a, in Protostars and Planets VI, ed. H. Beuther, C. Dullemond, & T. Henning (Univ. of Arizona Press, Tucson), in press

Li, Z.-Y., Krasnopolsky, R., & Shang, H. 2011, ApJ, 738, 180

Li, Z.-Y., Krasnopolsky, R., & Shang, H. 2013, ApJ, 774, 82

Li, Z.-Y., Krasnopolsky, R., Shang, H., & Zhao, B. 2014b, ApJ, in press

Lin, D. N. C., Hayashi, M., Bell, K. R., & Ohashi, N. 1994, ApJ, 435, 821

Lin, D. N. C. & Pringle, J. E. 1990, ApJ, 358, 515

Lindberg, J. E., Jørgensen, J. K., Brinch, C., et al. 2014, A&A, 566, A74

Lissauer, J. J. 1987, Icarus, 69, 249

Lodato, G. 2008, New Astron. Rev., 52, 21

Lodato, G. & Rice, W. K. M. 2004, MNRAS, 351, 630

Lodato, G. & Rice, W. K. M. 2005, MNRAS, 358, 1489

Lodders, K. 2004, ApJ, 611, 587

Lommen, D., Jørgensen, J. K., van Dishoeck, E. F., & Crapsi, A. 2008, A&A, 481, 141

Looney, L. W., Mundy, L. G., & Welch, W. J. 2003, ApJ, 592, 255

Looney, L. W., Tobin, J. J., & Kwon, W. 2007, ApJ, 670, L131

Lucy, L. B. 1977, AJ, 82, 1013

Luhman, K. L. 2012, ARA&A, 50, 65

Lunine, J. I., Engel, S., Rizk, B., & Horanyi, M. 1991, Icarus, 94, 333

Lynden-Bell, D. & Kalnajs, A. J. 1972, MNRAS, 157, 1

Lynden-Bell, D. & Pringle, J. E. 1974, MNRAS, 168, 603

Mac Low, M.-M. & Klessen, R. S. 2004, Reviews of Modern Physics, 76, 125

Machida, M. N. & Matsumoto, T. 2011, MNRAS, 413, 2767

Madhusudhan, N., Harrington, J., Stevenson, K. B., et al. 2011, Nature, 469, 64

Malbet, F., Lachaume, R., Berger, J.-P., et al. 2005, A&A, 437, 627

Manoj, P., Watson, D. M., Neufeld, D. A., et al. 2013, ApJ, 763, 83

Marboeuf, U., Thiabaud, A., Alibert, Y., Cabral, N., & Benz, W. 2014, ArXiv e-prints

Mathews, G. S., Klaassen, P. D., Juhász, A., et al. 2013, A&A, 557, A132

Matsumoto, R. & Tajima, T. 1995, ApJ, 445, 767

Matthews, B. C., Krivov, A. V., Wyatt, M. C., Bryden, G., & Eiroa, C. 2014, in Protostars and planets VI, ed. H. Beuther, C. Dullemond, & T. Henning (Univ. of Arizona Press, Tucson), in press

Matzner, C. D. & Levin, Y. 2005, ApJ, 628, 817

Maury, A. J., André, P., Hennebelle, P., et al. 2010, A&A, 512, A40

McKee, C. F. & Ostriker, E. C. 2007, ARA&A, 45, 565

McKee, C. F., Zweibel, E. G., Goodman, A. A., & Heiles, C. 1993, in Protostars and Planets III, ed. E. H. Levy & J. I. Lunine (Univ. of Arizona Press, Tucson), 327

Mejía, A. C., Durisen, R. H., Pickett, M. K., & Cai, K. 2005, ApJ, 619, 1098

Mellon, R. R. & Li, Z.-Y. 2008, ApJ, 681, 1356

Mellon, R. R. & Li, Z.-Y. 2009, ApJ, 698, 922

Mestel, L. & Spitzer, Jr., L. 1956, MNRAS, 116, 503

Milosavljević, M. & Loeb, A. 2004, ApJ, 604, L45

Min, M., Dullemond, C. P., Dominik, C., de Koter, A., & Hov-

enier, J. W. 2009, A&A, 497, 155

Min, M., Dullemond, C. P., Kama, M., & Dominik, C. 2011, Icarus, 212, 416

Mitchell, G. F., Maillard, J.-P., Allen, M., Beer, R., & Belcourt, K. 1990, ApJ, 363, 554

Momose, M., Ohashi, N., Kawabe, R., Nakano, T., & Hayashi, M. 1998, ApJ, 504, 314

Monaghan, J. & Gingold, R. 1983, Journal of Computational Physics, 52, 374

Monaghan, J. J. 1992, ARA&A, 30, 543

Moses, J. I., Line, M. R., Visscher, C., et al. 2013, ApJ, 777, 34

Motte, F. & André, P. 2001, A&A, 365, 440

Mottram, J. C., Kristensen, L. E., van Dishoeck, E. F., et al. 2014, A&A, subm.

Mottram, J. C., van Dishoeck, E. F., Schmalzl, M., et al. 2013, A&A, 558, A126

Mousis, O., Lunine, J. I., Madhusudhan, N., & Johnson, T. V. 2012, ApJ, 751, L7

Mousis, O., Lunine, J. I., Thomas, C., et al. 2009, ApJ, 691, 1780

Mundy, L. G., Looney, L. W., Erickson, W., et al. 1996, ApJ, 464, L169

Murillo, N. M. & Lai, S.-P. 2013, ApJ, 764, L15

Murillo, N. M., Lai, S.-P., Bruderer, S., Harsono, D., & van Dishoeck, E. F. 2013, A&A, 560, A103

Murray, J. R. 1996, MNRAS, 279, 402

Myers, A. T., McKee, C. F., Cunningham, A. J., Klein, R. I., & Krumholz, M. R. 2013, ApJ, 766, 97

Nakano, T. & Nakamura, T. 1978, PASJ, 30, 671

Nayakshin, S. 2006, MNRAS, 372, 143

Nelson, A. F. 2006, MNRAS, 373, 1039

Neufeld, D. A. 2012, ApJ, 749, 125

Nisini, B., Antoniucci, S., Giannini, T., & Lorenzetti, D. 2005, A&A, 429, 543

Nomura, H., Aikawa, Y., Nakagawa, Y., & Millar, T. J. 2009, A&A, 495, 183

Öberg, K. I., Boogert, A. C. A., Pontoppidan, K. M., et al. 2011a, ApJ, 740, 109

Öberg, K. I., Murray-Clay, R., & Bergin, E. A. 2011b, ApJ, 743, L16

Öberg, K. I., van Dishoeck, E. F., & Linnartz, H. 2009, A&A, 496, 281

O'Dell, C. R. & Wen, Z. 1994, ApJ, 436, 194

Ogino, S., Tomisaka, K., & Nakamura, F. 1999, PASJ, 51, 637

Ohashi, N., Hayashi, M., Ho, P. T. P., & Momose, M. 1997a, ApJ, 475, 211

Ohashi, N., Hayashi, M., Ho, P. T. P., et al. 1997b, ApJ, 488, 317

Oliveira, I., Olofsson, J., Pontoppidan, K. M., et al. 2011, ApJ, 734, 51

Oliveira, I., Pontoppidan, K. M., Merín, B., et al. 2010, ApJ, 714, 778

Ossenkopf, V. & Henning, T. 1994, A&A, 291, 943

Owen, T. & Bar-Nun, A. 1993, Nature, 361, 693

Persson, M. V., Jørgensen, J. K., & van Dishoeck, E. F. 2012, A&A, 541, A39

Persson, M. V., Jørgensen, J. K., & van Dishoeck, E. F. 2013, A&A, 549, L3

Persson, M. V., Jørgensen, J. K., van Dishoeck, E. F., & Harsono, D. 2014, A&A, 563, A74

Pinto, R. F., Brun, A. S., Jouve, L., & Grappin, R. 2011, ApJ, 737, 72

Poglitsch, A., Waelkens, C., Geis, N., et al. 2010, A&A, 518, L2

Pollack, J. B., Hubickyj, O., Bodenheimer, P., et al. 1996, Icarus, 124, 62

Pontoppidan, K. M., Blake, G. A., van Dishoeck, E. F., et al.

2008, ApJ, 684, 1323

Pontoppidan, K. M., Meijerink, R., Dullemond, C. P., & Blake, G. a. 2009, ApJ, 704, 1482

Pontoppidan, K. M., Salyk, C., Bergin, E. A., et al. 2014, in Protostars and Planets VI, ed. H. Beuther, C. Dullemond, & T. Henning (Univ. of Arizona Press, Tucson), in press

Pontoppidan, K. M., Salyk, C., Blake, G. A., & Käufl, H. U. 2010, ApJ, 722, L173

Price, D. J. 2007, PASA, 24, 159

Pringle, J. E. 1981, ARA&A, 19, 137

Qi, C., Öberg, K. I., Wilner, D. J., et al. 2013, Science, 341, 630

Qi, C., Wilner, D. J., Aikawa, Y., Blake, G. A., & Hogerheijde, M. R. 2008, ApJ, 681, 1396

Rafikov, R. R. 2007, ApJ, 662, 642

Rafikov, R. R. 2009, ApJ, 704, 281

Rice, W. K. M., Armitage, P. J., Bate, M. R., & Bonnell, I. A. 2003, MNRAS, 339, 1025

Rice, W. K. M., Lodato, G., & Armitage, P. J. 2005, MNRAS, 364, L56

Robitaille, T. P. 2011, A&A, 536, A79

Robitaille, T. P., Whitney, B. A., Indebetouw, R., & Wood, K. 2007, ApJ, 169, 328

Robitaille, T. P., Whitney, B. A., Indebetouw, R., Wood, K., & Denzmore, P. 2006, ApJ, 167, 256

Ros, K. & Johansen, A. 2013, A&A, 552, A137

Rothman, L., Gordon, I., Barbe, A., et al. 2009, Journal of Quantitative Spectroscopy and Radiative Transfer, 110, 533

Roueff, E. & Lique, F. 2013, Chemical Reviews, 113, 8906

Safronov, V. S. 1969, Evoliutsiia doplanetnogo oblaka.

Saito, M., Kawabe, R., Kitamura, Y., & Sunada, K. 1996, ApJ, 473, 464

San Jose-Garcia, I., Mottram, J. C., Kristensen, L. E.and van Dishoeck, E. F., et al. 2013, A&A, 553, A125

Santos-Lima, R., de Gouveia Dal Pino, E. M., & Lazarian, A. 2012, ApJ, 747, 21

Sargent, A. I. & Beckwith, S. 1987, ApJ, 323, 294

Sasselov, D. D. & Lecar, M. 2000, ApJ, 528, 995

Sault, R. J., Teuben, P. J., & Wright, M. C. 1995, Astronomical Data Analysis Software and Systems IV, 77, 433

Schneider, N., Csengeri, T., Hennemann, M., et al. 2012, A&A, 540, L11

Schöier, F. L., van der Tak, F. F. S., van Dishoeck, E. F., & Black, J. H. 2005, A&A, 432, 369

Scott, E. R. D. 2007, Annual Review of Earth and Planetary Sciences, 35, 577

Scoville, N. Z., Sargent, A. I., Sanders, D. B., et al. 1986, ApJ, 303, 416

Seifried, D., Banerjee, R., Pudritz, R. E., & Klessen, R. S. 2012, MNRAS, 423, L40

Shakura, N. I. & Sunyaev, R. A. 1973, A&A, 24, 337

Shu, F. H. 1977, ApJ, 214, 488

Shu, F. H., Tremaine, S., Adams, F. C., & Ruden, S. P. 1990, ApJ, 358, 495

Smith, R. J., Shetty, R., Stutz, A. M., & Klessen, R. S. 2012, ApJ, 750, 64

Smith, R. L., Pontoppidan, K. M., Young, E. D., & Morris, M. R. 2010, Meteoritics and Planetary Science Supplement, 73, 5381

Smith, R. L., Pontoppidan, K. M., Young, E. D., Morris, M. R., & van Dishoeck, E. F. 2009, ApJ, 701, 163

Spaans, M., Hogerheijde, M. R., Mundy, L. G., & van Dishoeck, E. F. 1995, ApJL, 455, 167

Spitzer, Jr., L. 1989, ARA&A, 27, 1

Springel, V. 2005, MNRAS, 364, 1105

Springel, V. 2010, ARA&A, 48, 391

Stamatellos, D., Whitworth, A. P., Bisbas, T., & Goodwin, S. 2007, A&A, 475, 37

Steinacker, J., Baes, M., & Gordon, K. D. 2013, ARA&A, 51, 63

Stevenson, D. J. & Lunine, J. I. 1988, Icarus, 75, 146

Stone, J. M. & Norman, M. L. 1992, ApJ, 80, 753

Strom, K. M., Strom, S. E., Edwards, S., Cabrit, S., & Skrutskie, M. F. 1989, AJ, 97, 1451

Takahashi, T., Silk, T., & Holenbach, D. J. 1983, ApJ, 275, 145

Takakuwa, S., Saito, M., Lim, J., et al. 2012, ApJ, 754, 52

Takami, M., Bailey, J., Gledhill, T. M., Chrysostomou, A., & Hough, J. H. 2001, MNRAS, 323, 177

Tasker, E. J., Brunino, R., Mitchell, N. L., et al. 2008, MNRAS, 390, 1267

Terebey, S., Chandler, C. J., & Andre, P. 1993, ApJ, 414, 759

Terebey, S., Shu, F. H., & Cassen, P. 1984, ApJ, 286, 529

Tielens, A. G. G. M. 2005, The Physics and Chemistry of the Interstellar Medium (Cambridge Univ. Press, Cambridge)

Tielens, A. G. G. M. 2013, Reviews of Modern Physics, 85, 1021

Tobin, J. J., Hartmann, L., Chiang, H.-F., et al. 2011, ApJ, 740, 45

Tobin, J. J., Hartmann, L., Chiang, H.-F., et al. 2012, Nature, 492, 83

Tobin, J. J., Hartmann, L., Chiang, H.-F., et al. 2013, ApJ, 771, 48

Tobin, J. J., Hartmann, L., Looney, L. W., & Chiang, H.-F. 2010, ApJ, 712, 1010

Toomre, A. 1964, ApJ, 139, 1217

Troland, T. H. & Crutcher, R. M. 2008, ApJ, 680, 457

Ulrich, R. K. 1976, ApJ, 210, 377

van der Tak, F. 2011, in IAU Symposium 280, ed. J. Cernicharo & R. Bachiller (Cambridge Univ. Press, Cambridge), 449–460

van der Tak, F. F. S., Black, J. H., Schöier, F. L., Jansen, D. J., & van Dishoeck, E. F. 2007, A&A, 468, 627

van der Tak, F. F. S., Walmsley, C. M., Herpin, F., & Ceccarelli, C. 2006, A&A, 447, 1011

van Dishoeck, E. F., Bergin, E. A., Lis, D. C., & Lunine, J. I. 2014, in Protostars and Planets VI, ed. H. Beuther, C. Dullemond, & T. Henning (Univ. of Arizona Press, Tucson), in press

van Dishoeck, E. F., Jonkheid, B., & van Hemert, M. C. 2006, Faraday Discussions, 133, 231

van Dishoeck, E. F., Kristensen, L. E., Benz, A. O., et al. 2011, PASP, 123, 138

van Dishoeck, E. F., Thi, W.-F., & van Zadelhoff, G.-J. 2003, A&A, 400, L1

van Kempen, T. A., Green, J. D., Evans, N. J., et al. 2010, A&A, 518, L128

van Kempen, T. A., van Dishoeck, E. F., Güsten, R., et al. 2009a, A&A, 507, 1425

van Kempen, T. A., van Dishoeck, E. F., Güsten, R., et al. 2009b, A&A, 501, 633

van Kempen, T. A., van Dishoeck, E. F., Hogerheijde, M. R., & Güsten, R. 2009c, A&A, 508, 259

van Kempen, T. A., van Dishoeck, E. F., Salter, D. M., et al. 2009d, A&A, 498, 167

van Leer, B. 1979, Journal of Computational Physics, 32, 101

van Weeren, R. J., Brinch, C., & Hogerheijde, M. R. 2009, A&A, 497, 773

Visser, R. & Bergin, E. A. 2012, ApJ, 754, L18

Visser, R., Doty, S. D., & van Dishoeck, E. F. 2011, A&A, 534, A132

Visser, R. & Dullemond, C. P. 2010, A&A, 519, A28

Visser, R., Jørgensen, J. K., Kristensen, L. E., van Dishoeck, E. F., & Bergin, E. A. 2013, ApJ, 769, 19

Visser, R., Kristensen, L. E., Bruderer, S., et al. 2012, A&A, 537, 55

Visser, R., van Dishoeck, E. F., Doty, S. D., & Dullemond, C. P. 2009, A&A, 495, 881

Vorobyov, E. I. 2009, ApJ, 704, 715

Vorobyov, E. I. 2010, ApJ, 723, 1294

Vorobyov, E. I. & Basu, S. 2006, ApJ, 650, 956

Vorobyov, E. I. & Basu, S. 2007, MNRAS, 381, 1009

Vorobyov, E. I. & Basu, S. 2009, MNRAS, 393, 822

Vorobyov, E. I. & Basu, S. 2010, ApJ, 719, 1896

Vorobyov, E. I., Zakhozhay, O. V., & Dunham, M. M. 2013, MNRAS, 433, 3256

Walsh, C., Millar, T. J., & Nomura, H. 2010, ApJ, 722, 1607

Walsh, C., Millar, T. J., Nomura, H., et al. 2014, A&A, 563, A33

Wang, K.-S., van der Tak, F. F. S., & Hogerheijde, M. R. 2012, A&A, 543, A22

White, R. J. & Hillenbrand, L. A. 2004, ApJ, 616, 998

Whitney, B. A. & Hartmann, L. 1993, ApJ, 402, 605

Whitney, B. A., Wood, K., Bjorkman, J. E., & Cohen, M. 2003a, ApJ, 598, 1079

Whitney, B. A., Wood, K., Bjorkman, J. E., & Wolff, M. J. 2003b, ApJ, 591, 1049

Williams, J. P. & Cieza, L. A. 2011, ARA&A, 49, 67

Wilson, T. L. & Rood, R. 1994, ARA&A, 32, 191

Woodward, P. & Colella, P. 1984, Journal of Computational Physics, 54, 115

Woodward, P. R. 1978, ARA&A, 16, 555

Wyatt, M. C. 2008, ARA&A, 46, 339

Yang, B., Stancil, P. C., Balakrishnan, N., & Forrey, R. C. 2010, ApJ, 718, 1062

Yen, H.-W., Takakuwa, S., Ohashi, N., & Ho, P. T. P. 2013, ApJ, 772, 22

Yıldız, U. A., Kristensen, L. E., van Dishoeck, E. F., et al. 2012, A&A, 542, A86

Yıldız, U. A., Kristensen, L. E., van Dishoeck, E. F., et al. 2013, A&A, 556, A89

Yıldız, U. A., van Dishoeck, E. F., Kristensen, L. E., et al. 2010, A&A, 521, L40

Yorke, H. W. & Bodenheimer, P. 1999, ApJ, 525, 330

Young, C. H. & Evans, II, N. J. 2005, ApJ, 627, 293

Young, C. H., Jørgensen, J. K., Shirley, Y. L., et al. 2004, ApJ, 154, 396

Young, C. H., Shirley, Y. L., Evans, II, N. J., & Rawlings, J. M. C. 2003, ApJ, 145, 111

Zhang, K., Pontoppidan, K. M., Salyk, C., & Blake, G. A. 2013, ApJ, 766, 82

Zhou, S., Evans, N. J., Kömpe, C., & Walmsley, C. M. 1993, ApJ, 404, 232

Zhu, Z., Hartmann, L., Gammie, C., & McKinney, J. C. 2009, ApJ, 701, 620

Zhu, Z., Hartmann, L., Gammie, C. F., et al. 2010, ApJ, 713, 1134

Zweibel, E. G. 1988, ApJ, 329, 384

Nederlandse samenvatting

Dᴇᴛᴇᴄᴛɪᴇs van exoplaneten tonen aan dat er ten minste één planeet om elke ster draait. Planeten worden gevormd in de accretieschijf die de nieuw gevormde ster voedt. Het onderwerp van dit proefschrift is het begrijpen van de processen die plaats vinden in de vroegste stadia van ster- en planeetvorming. De vorming en evolutie van deze schijven, die uiteindelijk de bouwstenen worden van planeten en leven, zijn nog niet goed begrepen.

Het overgrote deel van de chemische elementen die nodig zijn voor leven zoals wij het kennen (SPONCH) worden geproduceerd in sterren. In de vroege stadia van het universum werden alleen de chemische elementen tot lithium gevormd. Tijdens de levensloop van een ster worden in zijn kern via kernfusie elementen tot ijzer (Fe) aangemaakt dat later, bij het einde van de levensloop van de ster, in het universum terecht komen. Na verloop van tijd worden meer van deze zwaardere elementen geproduceerd en opgenomen in de volgende generatie(s) van sterren en planeten. De elementen worden op hun beurt opgenomen in simpele en complexe moleculen die ruimschoots aanwezig zijn in dichte wolken.

Ster en planeetvorming zijn nauw aan elkaar verbonden door de accretie schijf. Het concept van accretieschijven werd al voorgesteld door Kant en Laplace in de 18$^{\text{de}}$ eeuw. Het duurde echter nog twee eeuwen voordat waarnemingen het direct bewijs leverden. De vorming en evolutie van accretieschijven hebben een fundamentele invloed op de hoeveelheid materiaal dat in de ster terecht komt en hoeveel er overblijft om planeten te vormen.

De vorming van sterren en planeten

Sterren worden gevormd door het langzaam ineenkrimpen van een koude, geconcentreerde kern (10 K = - 263$\deg$ C) bestaande uit gas en stof. Recente waarnemingen met de *Herschel ruimtetelescoop* tonen aan dat deze kernen voorkomen in moleculaire wolken die bestaan uit draadvormige structuren of filamenten (Fig. S.1). In deze structuren bestaat een verscheidenheid aan grootte en massa van kernen. De kleinere kernen in het filament zullen later sterren van lage massa worden, zoals onze zon. Uit het materiaal van de kern wordt de ster en het planeten stelsel gevormd. Recent is grote vooruitgang geboekt in het begrijpen van de vorming van deze filamenten en de moleculaire wolken waarin ze zich bevinden. Supersonische turbulentie in het interstellaire medium (ISM, de ruimte tussen de sterren) zorgt voor de samendrukking van gas in platte structuren en filamenten. Terwijl de kern materie van de moleculaire wolk opneemt, zal deze beginnen te krimpen onder zijn eigen zwaartekracht en uiteindelijk een protoster vormen. Dit proces wordt beheerst door een aantal bijkomende processen zoals thermische druk, magnetische velden en turbulentie.

Een (proto)ster is een hete lichtgevende bol van gas die aangedreven wordt door de energie die vrijkomt bij de nucleaire reacties in zijn kern. De verschillende stadia van de vorming van sterren met lage massa ($M \leq 2M_{\odot}$, de massa van de zon is $M_{\odot}$) zijn redelijk goed begrepen in vergelijking met sterren met een hogere massa, maar verschillende details blijven onduidelijk. Hoewel massievere sterren helderder en makkelijk waar te nemen zijn, zijn sterren met lagere massa talrijker. Het bestuderen van de fysische processen die plaatsvinden gedurende stervorming geeft inzicht in de vorming van ons eigen zonnestelsel en in het ontstaan van leven op aarde.

Bij de krimp als gevolg van behoud van energie en impuls wordt een accretieschijf ge-
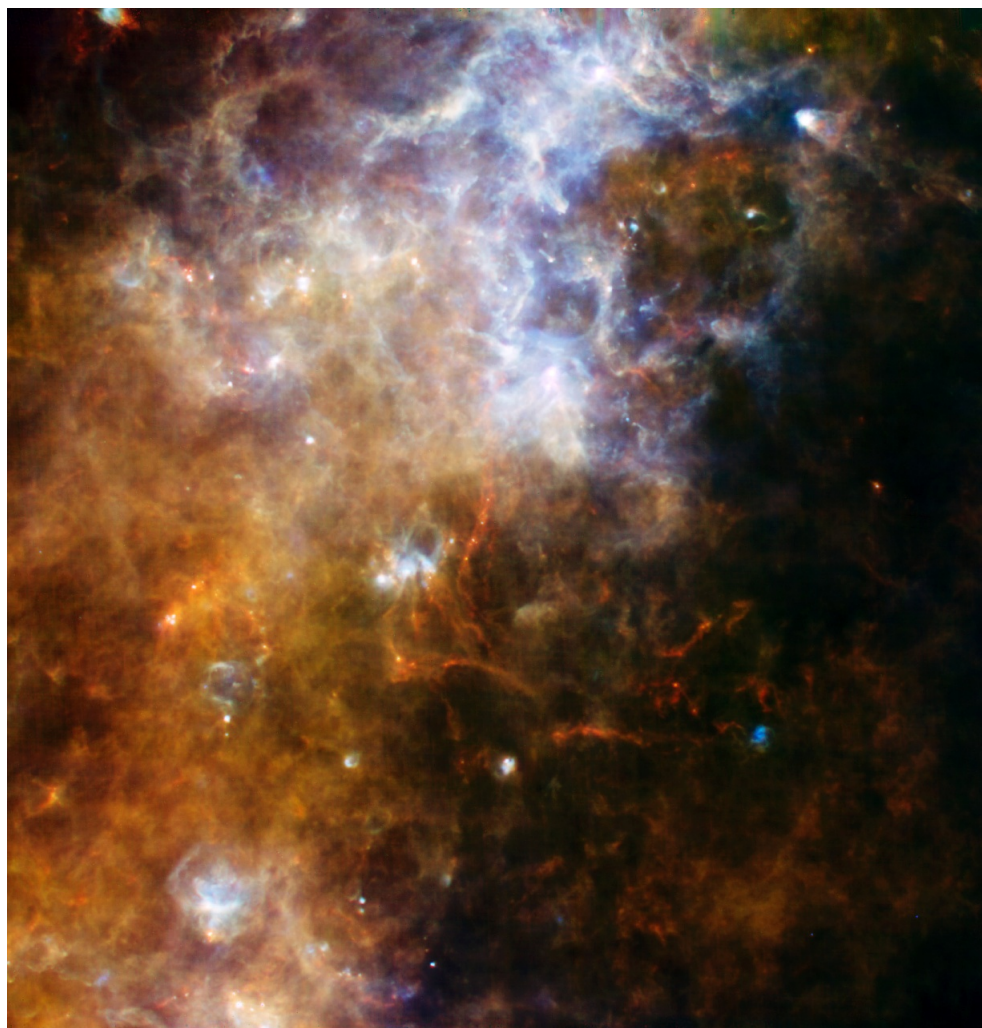
Figuur S.1 — Samengestelde kleurenafbeelding van vijf verschillende golflengtes in het Zuiderkruis, genomen met de Photodetector Array Camera and Spectrometer (PACS) en de Spectral and Photometric Imaging Receiver (SPIRE) van de Herschel ruimtetelescoop. De meeste golflengtes vallen buiten het optisch bereik, maar zijn zichtbaar in het infrarood door straling van het gas en stof dat zich rond de nieuwe ster bevindt. Deze materie is niet uniform verdeeld: de meest heldere straling komt uit de actieve stervormingsgebieden die verbonden zijn met de filamenten. Blauw geeft straling van het warme stof aan, en rood van koud stof. Credits: ESA en de SPIRE & PACS consortium.

vormd. De eerste theoretische studies van accretieschijven komen uit de jaren 70 door Shakura en Sunyaev. Op dat moment was er reeds indirect bewijs voor het bestaan van accretieschijven rond jonge sterren, op basis van polarimetrische waarnemingen van atomaire optische lijnen. Het duurde tot 1989 voordat Strom en medewerkers de eerste statistische studies van accretieschijven uitvoerden, met behulp van de *Infrared Astronomical Satellite (IRAS)*. Zij verrichtten waarnemingen van accretieschijven door middel van de straling van het warme stof in de schijf. Hierna werd het belangrijkste bewijs voor het bestaan van schijven geleverd door de directe waarnemingen met *Hubble* in 1994 door ODell en medewerkers (Fig. S.2). Tegenwoordig weet men dat er zich rond elke jonge ster een accretischijf bevindt en dat deze een cruciale rol speelt bij de planeet- en stervorming.

Op het moment van schrijven zijn er meer dan 1000 exoplaneten bekend en meer dan 3000 kandidaten. Het meest aanvaarde scenario van planeetvorming is via het samenklonteren van

Figuur S.2 — Een afbeelding van de zijkant van een protoplanetaire schijf, genomen met Hubble ruimtetelescoop in zichtbaar licht. Het stof in de schijf blokkeert de straling van het gas en stof in de Orion nevel in de achtergrond. Dit is een vergelijkbare afbeelding zoals genomen in 1993 door O'Dell, die het cruciale bewijs vormde voor accretieschijven rond jonge sterren. Credits: J. Bally (Universiteit van Colorado) en H. Throop (SWRI).

kleine stofdeeltjes die op deze manier grotere lichamen vormen. Echter, van grotere deeltjes (radius > 1 cm) is het bekend dat deze zich gemiddeld sneller voort bewegen dan kleinere deeltjes. De hoogste snelheden van het stof ten opzichte van het gas in het binnenste deel van de schijf worden gevonden voor deeltjes van ongeveer 1 m groot. Bij een botsing tussen twee grote projectielen met hoge snelheid kunnen deze in stukken breken waarbij delen in de ster terecht kunnen komen. Dit mechanisme beperkt de grootte van de brokstukken tot 1 m en staat dus de vorming van planeten in de weg. Het wordt de meter-grootte barrière genoemd. Een oplossing voor dit probleem werd voorgesteld door Eddington in 1937 en bestaat erin dat via ijs grotere brokstukken gevormd kunnen worden. Deze stelling werd bevestigd via waarnemingen door Gillett en Forrest in 1973. Dankzij vele waarnemingen van ijs rond kleine stofdeeltjes, is het gedurende de afgelopen jaren duidelijk geworden dat water het hoofdbestanddeel van dit ijs vormt. Het ijs zorgt ervoer dat stofdeeltjes gemakkelijker aan elkaar plakken bij een botsing en het op deze manier mogelijk maken om grote brokken in de accretieschijf te vormen. Tijdens de vroege stadia bevinden zich naast stof ook grote hoeveelheden gas in de accretieschijf. Dit is noodzakelijk voor de vorming van gasreuzen zoals Jupiter.

Dit proefschrift bestudeert de kritische fysische processen tijdens de vroegste stadia van stervorming, $\sim 10^4$–10^5 jaar na de ineenstorting van de wolk. Het is algemeen aanvaard dat planeten in accretieschijven vormen en dat accretieschijven een belangrijk onderdeel zijn in de vorming en levensloop van sterren. De vorming van een accretieschijf en vroege stadia in hun levensloop zijn tot op heden nog helemaal niet goed begrepen. De voornamelijkste vragen van dit proefschrift zijn als volgt:

- Bestaan er accretieschijven, zoals deze gevonden worden rond pre-hoofdreeks sterren, ook al rond nieuw geboren sterren?
- Kunnen accretieschijven waargenomen worden en hoe kunnen ze onderscheiden worden van hun geboorteomgeving?
- Is de fysische en chemische structuur consistent met de huidige modellen van accretie-

schijfvorming?
- Hoe stabiel zijn accretieschijven in deze vroege fase, als materiaal uit het omhulsel nog invalt op de schijf?
- Hoeveel dragen accretieschijven bij aan de waagenomen moleculaire lijnen?

Stralingsprocessen: continuüm en spectraallijnen

De eigenschappen van jonge sterren worden typisch afgeleid door middel van breedbandige infrarode straling van het stof. Door de UV straling van de jonge ster wordt het stof opgewarmd, vervolgens zal het stof deze warmte uitstralen bij langere golflengte in het (ver)infrarood. Het evenwicht tussen beiden bepaalt de temperatuur van het stof. Dus, hoe meer de (proto)ster straalt, hoe warmer het stof. Tegelijkertijd neemt de (proto)ster nog materiaal op uit zijn omgeving. In de vroege stadia van stervorming bevindt zich in de accretieschijf veel koud materiaal omdat alle UV straling snel door het stof is geabsorbeerd. Hierdoor is het moeijk om de groeiende ster en accretieschijf te bestuderen. Theoretische modellen worden daarom gebruikt om de waargenomen straling te begrijpen.

Hoewel de warmtestraling van het stof de energie van het groeiende stelsel traceert, kunnen alleen atomaire en moleculaire lijnen gebruikt worden om de structuur van de buitenste gaslagen van jonge schijven te bepalen. Een enorme rijkdom aan moleculen wordt in de verschillende fysische stadia gevonden. Door middel van waarnemingen van verschillende moleculaire overgangen kunnen de verschillende fysische condities, zoals temperatuur, dichtheid en snelheidsstructuren onderzocht worden. Belangrijk is dat deze overgangen zich op vaste frequenties bevinden. Koolstofmonoxide (CO) wordt hierin het meest gebruikt. Elke beweging van het gas veroorzaakt een Doppler verschuiving van de waargenomen frequentie. Wanneer de lijnen spectraal opgelost kunnen worden kan op deze manier de beweging van het gas bepaald worden.

Observationeel gereedschap

Om een jonge accretieschijf in zijn omhulsel te bestuderen zijn interferometrische waarnemingen op millimeter golflengte nodig. Op deze manier wordt warmtestraling van de accretieschijf onderscheiden van de omgeving. Interferometrie is een techniek waarbij signalen van meerdere telescopen gecombineerd worden om op deze manier genoeg ruimtelijke resolutie te verkrijgen en zo de schijf op te kunnen lossen. Bijvoorbeeld, een 12 meter telescoop kan CO straling oplossen uit een gebied ter grote van 7000 AE (7000 astronomische eenheden, d.w.z. 7000 keer de afstand van de aarde tot de zon). Twee van deze telescopen op een afstand van 1 km van elkaar hebben een oplossend vermogen van 80 AE in hetzelfde gebied.

Interferometrische waarnemingen van stof en gas in het millimeter gebied zijn cruciaal geweest om de processen binnenin stervormingsgebieden aan te tonen. De afstand tussen de interferometrische telescopen is variabel om zo, afhankelijk van de nood, verschillende resoluties (0.5″–20″) te verkrijgen. Een paar telescopen op korte afstand wordt vooral gebruikt voor het waarnemen van grootschalige structuren, zoals het omhulsel, terwijl een paar telescopen op grote afstand, en dus een hogere resolutie, gebruikt wordt om in te zoomen op de accretieschijf. Door meer dan twee telescopen met verschillende afstanden te combineren in verschillende configuraties kunnen alle schalen tegelijkertijd waargenomen worden. Een afbeelding wordt verkregen door de Fourier transformatie van een verzameling van deze gecorreleerde gegevens. Een stationaire groep telescopen maakt gebruik van de aardrotatie om gecorreleerde waarnemingen te verrichten. Vele gecorreleerde waarnemingen zijn nodig om een volledige afbeelding te verkrijgen. Een typische waarneming in dit proefschrift heeft meer

dan 5.000 gecorreleerde waarnemingen. De nieuwste telescoop is de Atacama Large Millimeter Array (ALMA, 66 telescopen) in Chili. Met een dergelijke grote hoeveelheid telescopen zal het makkelijker zijn om de zwakke structuren in een stervormingsgebied waar te nemen.

Dit proefschrift

Dit proefschrift behandelt zowel de theoretische en obervationele aspecten van accretieschijf-vorming gedurende de vroege stadia van stervorming. Semi-analytische en numerieke hydro-dynamische modellen zijn samengevoegd met breedbandige stralingsoverdracht berekeningen van het stof. De voorspelde moleculaire lijn emissies zijn vergeleken met de waarnemingen. Deze simulaties en voorspellingen worden gecombineerd met ruimtelijk en spectraal opgeloste waarnemingen van CO lijnen in iets verder gevolueerde schijven. De waarnemingen zijn uit-gevoerd met de Plateau de Bure Interferometer (PdBI) in Frankrijk. De volgende lijst geeft een overzicht van de resultaten van dit proefschrift.

- De breedbandige straling en de moleculaire lijnen worden gesimuleerd door drie dimen-sionale hydrodynamische simulaties inclusief magnetische velden in **Hoofdstuk 2**. Het is een bekend probleem in de astrofysica dat de aanwezigheid van magnetische velden de vorming van accretieschijven kan belemmeren. Twee van deze simulaties worden ge-bruikt om de overeenkomsten en verschillen te onderzoeken tussen een simulatie waarin de schijf wel vormt, en één waarin dit niet gebeurt. De voorspellingen van 3D simula-ties worden vergeleken met 2D semi-analitische modellen van ster- en accretieschijfvor-ming. De vergelijking toont aan dat interferometrische waarnemingen, zoals geleverd door ALMA, nodig zijn om de vormingsprocessen van accretieschijven te onderzoeken. Het zal daardoor mogelijk zijn om deze theoretische modellen in de nabije toekomst te testen.
- Tijdens de vroegste stadia van stervorming kan de accretieschijf koud en dik zijn. Dit lijdt tot gravitationele samentrekking hierin, en zorgt op deze wijze voor instabiliteiten. Hier-bij komt dat deze instabiliteiten plaats vinden terwijl het omhullende materiaal verder op schijf valt. Dit soort instabiliteiten zijn voorgesteld als een mechanisme voor planeet vorming omdat ze een deel van de accretieschijf fragmenteren door de afkoeling. **Hoofd-stuk 3** onderzoekt door middel van 3D simulaties of de schijf kan fragmenteren als er een grote hoeveelheid materiaal ophoopt. Het resultaat suggereert dat de schijf niet breekt, maar gewelddadige verschuivingen ondergaat waardoor een grote hoeveelheid materie in n keer op in de ster terecht komt.
- **Hoofdstuk** 4 presenteert de voorspelde evolutie van moleculaire lijnen en hun eigen-schappen door middel van 2D modellen. De moleculaire emissielijnen van koolstofmo-noxide worden gesimuleerd en vergeleken met waarnemingen van de *Herschel ruimtete-lescoop*. De voorspellingen bij kortere golflengte worden vergeleken met die in het infra-rood. Veranderingen in de vibrationele en rotationele energie zorgt voor infrarode stra-ling, terwijl veranderingen in rotatie de oorzaak zijn van straling op langere golflengte. De verandering van energie is groter in het infrarode spectrum en is dus een betere maat voor het warme gas.
- Hoofdstukken 2 en 4 suggereren dat de jonge accretieschijf diep in het omhulsel alleen in kaart kan worden gebracht door ruimtelijk en spectraal opgeloste waarnemingen van mo-leculaire lijnen. Deze emissie van de schijf is makkelijker te detecteren als een substantieel gedeelte van het omhulsel al is weggevallen, zoals verwacht voor verder geëvolueerde systemen. **Hoofdstuk 5** presenteert interferometrische waarnemingen van ^{13}CO en C^{18}O 21 lijnen voor vier jonge protosterren. Drie van deze vier objecten tonen de aanwezigheid

van roterende schijven aan. De grootte van de schijven is consistent met de 2D modellen van schijfvorming.

- Deze schijven kunnen niet alleen verwarmd worden door de jonge (proto)ster. Extra warmte komt vrij als materie door de schijf naar binnen wordt getransporteerd richting de ster, omdat het zijn impulsmoment en energie moet behouden. Dit energetische proces verwarmt de schijf vanuit het centrum zodat ijs alleen ver weg van de centrale ster aanwezig kan zijn. **Hoofdstuk 6** presenteert een theoretische studie van de belangrijkste ijs soorten (H_2O, CO, CO_2) van actieve schijven rond de jongste protosterren. Deze hete schijf wordt gedacht representatief te zijn voor de vroege stadia van de vorming van ons zonnestelsel. Dit hoofdstuk presenteert het verband tussen de vroege stadia van stervorming tot de vorming van planeten. De voorspellingen worden vervolgens vergeleken met de waargenomen emissie van water rond protosterren.

Toekomstperspectieven Huidige waarnemingen hebben de aanwezigheid van roterende schijven aangetoond in de binnenste paar 100 AU rond een aantal uiterst jonge protosterren. Dit proefschrift vergelijkt ook de omvang van het gebied waarover het gas volgens de wetten van Kepler beweegt met de schijfvormingsmodellen. Om de details van schijfvorming en evolutie in de vroege stadia van stervorming echter verder te kunnen bestuderen is de resolutie en gevoeligheid die ALMA zal leveren nodig. Waarnemingen met hogere ruimtelijke en spectrale resolutie van moleculaire lijnen kunnen de Kepleriaanse schijf van het ineenstortende omhulsel onderscheiden. De temperatuursverdeling over de schijf, die cruciaal is voor het onderzoek naar het verwarmingsproces, vereist twee verschillende overgangen van een molecuul om hun excitatie te kunnen onderzoeken en daaruit informatie over de temperatuur en dichtheid te halen. Verder is een hoog-gevoelige waarneming nodig om de snelheidsstructuren van de schijf te kunnen onderzoeken aangezien de moleculaire lijnen bij hoge snelheden veel zwakker zijn vergeleken met de centrale snelheid. Dit kan in de toekomst veel makkelijker worden gedaan om zo de kinematiek op de kleine schaal bloot te leggen. De chemische structuur van de jonge schijf is ook een essentiéel onderdeel voor ons begrip van de vorming van planetaire stelsels.

Ringkasan

J UMLAH terbaru eksoplanet yang telah dideteksi menunjukkan bahwa paling tidak ada satu planet mengorbit setiap bintang. Planet terbentuk di dalam cakram akresi yang menyediakan bahan bagi bintang yang baru lahir. Tema disertasi ini adalah pemahaman proses-proses fisis yang terjadi pada tahapan paling dini dari pembentukan bintang dan planet. Pembentukan dan evolusi dini cakram—yang akan menyediakan bangun dasar bagi planet-planet dan kehidupan—tidaklah begitu dipahami dengan baik.

Sebagian besar unsur-unsur kimia yang penting bagi kehidupan (Belerang, Fosfor, Oksigen, Nitrogen, Karbon, dan Hidrogen, biasa disingkat SPONCH) sebagaimana kita ketahui, dibentuk di dalam bintang. Di alam semesta dini, hanya unsur-unsur ringan dari Hidrogen hingga Litium yang terbentuk. Siklus hidup bintang memperkaya medium antar bintang melalui reaksi nuklir pada inti bintang-bintang. Dalam reaksi ini terjadi fusi unsur-unsur ringan untuk menghasilkan unsur-unsur yang lebih berat hingga terbentuknya besi (Fe). Dengon berjalannya waktu, semakin banyak unsur-unsur berat ini terbentuk dan kemudian menjadi bagian dari proses pembentukan bintang dan planet generasi-generasi selanjutnya. Unsur-unsur ini akan membentuk molekul-molekul sepanjang proses pembentukan bintang dan planet.

Pembentukan bintang dan planet terkait sangat erat melalui cakram akresi. Teori cakram telah diusulkan oleh Kant dan Laplace pada abad ke-18, namun dibutuhkan waktu 2 abad untuk menemukan bukti pengamatan akan adanya cakram. Pembentukan dan evolusi cakram menentukan jumlah material yang disalurkan kepada bintang dan yang tersisa untuk pembentukan planet-planet.

Pembentukan bintang dan planet

Bintang terbentuk dari kontraksi gumpalan gas dan debu yang dingin dan padat (10 K = $-263°$ C. Pengamatan-pengamatan terbaru dengan menggunakan Teleskop Antariksa *Herschel* menunjukkan bahwa gumpalan-gumpalan ini terletak di dalam suatu struktur berwujud filamen (lihat Gambar S.1). Di dalam filamen-filamen ini terdapat gumpalan-gumpalan dan gas molekul padat dengan berbagai ukuran dan massa. Sepanjang untaian filamen ini terdapat inti-inti kecil yang akan membentuk bintang-bintang bermassa rendah seperti Matahari kita. Inti-inti padat ini menjadi tempat penyimpanan massa untuk pembentukan bintang dan sistem tata surya. Baru-baru ini telah terjadi kemajuan penting dalam memahami pembentukan filamen-filamen ini dan awan-awan molekul di dalamnya. Pergolakan supersonik di dalam materi antar bintang akan membuat gas termampatkan menjadi lembaran-lembaran dan filamen-filamen. Selagi inti menarik massa dari awan yang melingkupinya, ia mulai memampat akibat gaya gravitasinya sendiri. Rincian tepat bagaimana inti ini berkontraksi bergantung pada proses-proses fisis tambahan seperti tekanan termal, medan magnetik, dan pergolakan gas.

Bayi bintang adalah sebuah bola gas panas yang bersinar karena ditenagai oleh energi yang dilepaskan dari akresi pada tahapan dini pembentukan bintang dan dari reaksi nuklir pada tahapan lanjut. Tahapan-tahapan pembentukan bintang bermassa rendah ($M \leq 2 \ M_\odot$, massa Matahari adalah 1 $M_\odot$) relatif sudah dipahami dengan baik apabila dibandingkan dengan pembentukan bintang bermassa tinggi, akan tetapi beberapa aspek masih belum jelas. Bintang-bintang masif ($M \geq 8 \ M_\odot$) sangat terang dan lebih mudah untuk diamati, namun bintang-
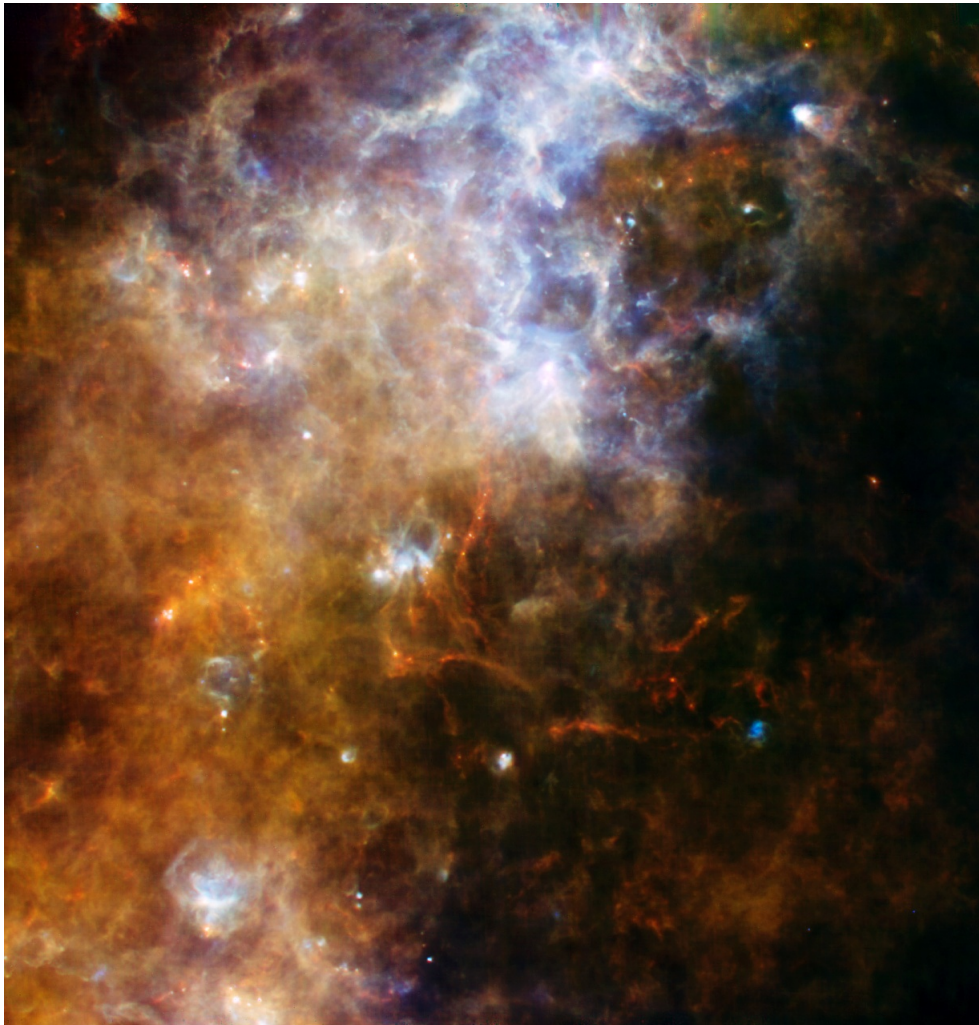
Gambar S.1 — Citra gabungan berwarna pada lima panjang gelombang berbeda dari Salib Selatan yang diambil oleh instrumen *Photodetector Array Camera and Spectrometer (PACS)* dan *Spectral and Photometric Imaging Receiver (SPIRE)* pada Teleskop Antariksa *Herschel*. Sebagian dari objek-objek dalam citra ini tidak teramati dalam panjang gelombang optik, namun bersinar terang dalam inframerah karena radiasi gas dan debu yang membentuk bintang-bintang baru. Materi-materi ini terdistribusi secara merata namun pancaran yang paling terang datang dari daerah-daerah pembentukan bintang yang saling terhubung satu sama lain melalui filamen-filamen. Warna buru menunjukkan pancaran radiasi dari debu hangat, sementara warna merah menunjukkan radiasi dari debu dingin. Sumber: ESA dan konsorsium SPIRE dan PACS.

bintang bermassa lebih lazim ditemui. Studi tentang proses-proses fisis yang terjadi selama pembentukan bintang bermassa rendah dapat memberikan pemahaman tentang bagaimana sistem tata surya kita terbentuk dan kehidupan di Bumi muncul.

Sementara keruntuhan gravitasi berlanjut, beberapa material akan membentuk cakram sebagai akibat dari konservasi energi dan momentum. Studi-studi teoritis tentang sifat-sifat cakram tidak dimulai hingga tahun 1970an oleh Shakura dan Sunyaev. Bukti awal tak langsung mengenai keberadaan cakram akresi ditemukan melalui citra polarisasi optik dan garis-garis spektrum molekul. Akan tetapi baru pada tahun 1989 dilakukan studi pertama tentang statistik cakram oleh Strom dan sejawat berkat data yang diambil oleh satelit IRAS (*Infrared Astronomical Satellite*, Satelit Astronomi Inframerah). Mereka mengamati cakram melalui pancaran radiasi

Gambar S.2 — Sebuah citra optik sebuah cakram protoplanet, diambil oleh Teleskop *Hubble*. Debu di dalam cakram menghalangi pancaran radiasi latar gas dan debu. Citra serupa juga diambil pada tahun 1993 oleh O'Dell yang menjadi bukti kunci keberadaan piringan di sekitar bintang-bintang muda. Sumber: J. Bally (Universitas Kolorado) dan H. Throop (SWRI)

dari debu hangat pada cakram. Bukti kunci keberadaan cakram adalah citra optik langsung cakram pada tahun 1994 yang diamati dengan menggunakan Teleskop Antariksa *Hubble* oleh O'Dell dan sejawat (lihat Gambar S.2). Kini telah diketahui bahwa piringan cakram selalu melingkupi setiap bintang muda dan merupakan bagian penting dalam pembentukan bintang dan planet.

Di dalam cakram ini planet pada akhirnya akan terbentuk. Pada saat ini ada sekitar 1000 planet yang sudah dikonfirmasi mengorbit bintang lain, dan lebih dari 3000 kandidat planet luat surya [1]. Skenario yang paling digemari pada saat ini adalah bahwa planet-planet ini terbentuk melalui bulir-bulir kecil debu yang menggumpal membentuk bulir yang berukuran lebih besar. Akan tetapi bulir-bulir yang lebih besar (radius > cm) cenderung bergerak dengan kecepatan yang lebih tinggi walaupun tidak lebih cepat dari kecepatan maksimal sebuah bulir berukuran 1 meter. Bulir yang bergerak cepat ini dapat menumbuk bulir lain dan akan pecah menjadi pecahan-pecahan kecil, atau bergerak masuk menuju bintang. Masalah ini menyulitkan pembentukan batuan yang ukurannya lebih besar dari 1 meter yang menjadi syarat pembentukan planet bebatuan seperti Bumi. Permasalahan dalam pembentukan bintang ini disebut rintangan ukuran meter. Satu solusi yang memungkinkan adalah keberadaan bulir-bulir es dan debu yang diusulkan oleh Eddington pada tahun 1937 dan akhirnya dideteksi oleh Gillet dan Forrest pada tahun 1973. Pada tahun-tahun terakhir setelah banyaknya survey dengan menggunakan teleskop-teleskop landas Bumi maupun observatorium antariksa, nampak jelas bahwa air adalah salah satu penyusun utama es-es ini saat molekul-molekul membeku menjadi bulir debu dingin. Es ini diduga membantu partikel-partikel debu saling menempel dan membentuk bebatuan di dalam cakram. Pada tahapan dini evoluti cakram, mereka mengandung sejumlah besar gas yang akan menjadi faktor penting bagi pembentukan planet-planet raksasa yang kaya akan gas seperti Jupiter.

Disertasi ini difokuskan pada proses-proses fisika yang terjadi pada tahapan paling dini

---

[1]Lihat http://exoplanets.org untuk jumlah yang lebih baru.

pembentukan bintang, $\sim 10^{4-5}$ tahun setelah kontraksi gravitasi sebuah inti padat. Telah banyak disepakati bahwa planet terbentuk di dalam cakram dan bahwa cakram memegang peran penting dalam pembentukan dan evolusi bintang. Pembentukan dan evolusi dini bintang tidak sepenuhnya dipahami. Pertanyaan-pertanyaan utama disertasi ini adalah sebagai berikut:

- Apakah cakram seperti yang mengitari bintang-bintang pra-deret utama sudah ada ketika bintang baru saja lahir?
- Apakah cakram tersebut dapat diamati dan bagaimana mereka dapat dibedakan dari selubung yang menjadi tempat kelahiran bintang?
- Apakah struktur fisis dan kimiawi cakram ini konsisten dengan model mutakhir pembentukan cakram?
- Sestabil apakah cakram yang terbenam di dalam selubung dan dapatkah mereka menahan laju keruntuhan tinggi dari selubung?
- Seberapa besar cakram yang terbenam berkontribusi pada garis-garis molekul yang diamati?

Proses radiatif: Kontinum debu dan garis-garis molekul

Karakteristik bintang muda secara umum dipelajari dari radiasi kontinum yang dipancarkan oleh debu. Debu menghangat dengan cara memproses ulang pancaran radiasi bintang pada energi tinggi (gelombang pendek) menjadi foton energi rendah (gelombang panjang). Struktur temperatur debu ini dikendalikan oleh energi yang dipancarkan oleh bayi bintang seiring dengan pengumpulan material-material dari ruang lingkupnya. Debu tersebut kemudian menangkap cahaya dengan cara penyerapan atau hamburan. Debu hangat pada cakram memancarkan cahaya inframerah. Akan tetapi, pada tahapan dini pembentukan bintang, selubung yang dingin dan masif akan menghalangi radiasi yang dipancarkan cakram. Dengan demikian, sulit untuk mempelajari secara langsung pertumbuhan bintang dan cakram yang baru lahir tersebut. Model-model teoritis kemudian digunakan untuk memahami radiasi yang diamati.

Apabila emisi termal debu digunakan untuk mengamati jejak energi keseluruhan sistem yang sedang tumbuh, maka garis-garis emisi atom dan molekul digunakan untuk mengamati massa dominan dari sekitar bintang-bintang muda. Alam semesta diisi oleh berbagai molekul yang berada pada berbagai kondisi fisis yang berbeda. Melalui pengamatan berbagai transisi molekuler kita dapat menyelidiki berbagai kondisi fisis yang menghasilkan transisi molekul tersebut, antara lain temperatur, kepadatan, dan struktur kecepatan. Yang paling penting, transisi-transisi ini diskret sedemikian rupa sehingga mereka dipancarkan hanya pada frekuensi tertentu. Transisi molekuler yang paling lumrah ditemui adalah yang berasal dari karbon monoksida (CO). Jejak pergerakan gas dapat diamati dari pergeseran Doppler yang terjadi pada frekuensi yang diamati. Dengan demikian, dengan mengamati frekuensi dari garis-garis yang diamati, kita dapat mempelajari kinematika dari gas-gas ini.

Perkakas pengamatan

Untuk mempelajari cakram yang terbenam di dalam selubungnya dibutuhkan pengamatan interferometri pada panjang gelombang milimeter. Pengamatan inin dibutuhkan agar kita dapat mengamati emisi debu termal dari selubung bagian dalam dimana cakram tersebut berada. Interferometri adalah sebuah teknik yang menggabungkan dan mengkorelasikan sinyal dari berbagai teleskop, untuk dapat mencapai resolusi spasial yang tinggi, yang dibutuhkan untuk mengamati cakram. Sebagai contoh, sebuah teleskop 12 m dapat mengamati radiasi CO dari suatu wilayah sebesar 7000 AU (7000 kali jarak Bumi ke Matahari). Dua buah teleskop seperti

ini yang terpisahkan sejauh 1 km dapat mengamati radiasi yang sama dari wilayah sebesar 80 AU. Pengamatan-pengamatan gas dan debu dengan menggunakan interferometri pada panjang gelombang milimeter dan submilimeter telah menjadi kunci dalam menyibakkan cara kerja wilayah wilayah pembentukan bintang. Teleskop-teleskop ini terpisahkan sejauh jarak tertentu sehingga dapat mencakup berbagai resolusi sudut (0.5"–20"). Jarak antara kedua teleskop ini disebut dengan garis dasar (baseline). Sepasang teleskop yang terpisahkan sejauh garis dasar pendek akan mengamati radiasi yang dipancarkan selubung, sementara sepasang teleskop yang terpisahkan sejauh garis dasar sangat panjang akan dapat mengamati radiasi dari cakram. Dengan menggabungkan berbagai konfigurasi kita dapat mengamati seluruh skala fisis secara serempak. Berbeda dengan pengamatan teleskop konvensional citra dari sebuah pengamatan interferometri dibangun melalui transformasi Fourier dari koleksi fluks yang sudah dikorelasikan. Pasangan teleskop yang diam memanfaatkan rotasi Bumi untuk mengamati dan memperoleh fluks yang terkorelasi. Kita membutuhkan banyak fluks yang terkorelasi untuk dapat membangun citra yang terpercaya. Pengamatan yang digunakan dalam disertasi ini lazimnya memiliki lebih dari 5000 titik fluks yang terkorelasi. Fasilitas terbaru dalam interferometri milimeter adalah Rangakaian Milimeter Besar Atacama (*Atacama Large Milimeter Array* atau ALMA, terdiri atas 66 teleskop) di Cile. Dengan jumlah teleskop yang begitu besar akan lebih mudah mengamati struktur-struktur redup suatu pembentukan bintang yang sedang berjalan.

Disertasi ini dan pandangan ke depan

Disertasi ini menjelajahi baik aspek teoritis maupun observasional dari pembentukan cakram pada tahapan dini pembentukan bintang. Model semi analitis dan model hidrodinamika numerik telah digabungkan dengan berbagai perkakas hantaran radiasi kontinum debu. Garis-garis emisi molekuler yang diprediksikan kemudian dibandingkan dengan pengamatan. Simulasi dan prediksi ini juga didampingi dengan pengamatan spasial dan spektral resolusi tinggi garis-garis emisi CO dengan ketebalan optik yang rendah dari objek-objek bintang muda yang tidak terlalu tertanam (i.e. lebih lanjut dalam tahapan evolusinya) dalam selubung. Pengamatan-pengamatan ini dilakukan dengan menggunakan Interferometer Plateau de Bure (PDBI) di Perancis. Berikut ini adalah garis-garis besar hasil disertasi ini:

- Dalam **Bab 2** garis-garis kontinum dan molekuler disimulasikan dengan menggunakan simulasi hidrodinamika tiga dimensi yang mengikutkan medan magnetik. Keberadaan medan magnetik dapat mencegah terbentuknya cakram. Ini merupakan sebuah permasalahan yang sudah diketahui dalam astrofisika. Dua dari simulasi-simulasi ini digunakan untuk meneliti persamaan dan kesamaan antara simulasi yang membentuk cakram dan yang tidak. Prediksi-prediksi simulasi tiga dimensi kemudian dibandingkan dengan model-model semi-analitis dua dimensi pembentukan bintang dan cakram. Perbandingan antara keduanya menunjukkan bahwa dibutuhkan pengamatan-pengamatan interferometris seperti yang akan dihantarkan oleh ALMA untuk dapat mempelajari proses pembentukan cakram. Dengan demikian di masa depan akan dimungkinkan untuk menguji model-model teoritis ini.
- Pada tahapan terdini pembentukan bintang cakram dalam keadaan dingin dan masif. Ini akan mengarah pada kontraksi gravitasi ke dalam dirinya sendiri dan dengan demikian menciptakan ketidakstabilan. Sebagai tambahan, ketidakstabilan terjadi saat material-material di sekitar jatuh di atas cakram tersebut. Ketidakstabilan seperti ini telah diusulkan sebagai mekanisme pembentukan planet dengan adanya pecahan-pecahan cakram. **Bab 3** menyelidiki, dengan simulasi tiga dimensi, apakah cakram dapat pecah apabila

sejumlah besar materi jatuh menumpuk di atasnya. Hasilnya menunjukkan bahwa cakram tidak terpecah tetapi mengalami penyaluran materi yang pesat menuju bintang.

- **Bab 4** menghadirkan prediksi evolusi karakteristik garis-garis molekuler dengan menggunakan model dua dimensi. Emisi garis-garis molekuler karbon monoksida disimulasikan dengan mengikutkan garis-garis molekular yang dimati oleh *Herschel* baru-baru ini. Prediksi-prediksi pada daerah gelombang panjang (milimeter) dibandingkan dengan garis-garis pada daerah inframerah. Dua himpunan garis-garis ini berasal dari daerah yang berbeda. Pancaran pada daerah inframerah disebabkan oleh energi yang dilepaskan karena pergantian rotasi dan getaran molekul sementara pada gelombang panjang disebabkan oleh pergantian rotasi. Terjadi pergantian energi yang lebih besar pada daerah inframerah sehingga dengan demikian kita dapat menyelidiki komponen gas yang lebih hangat.

- Bab 2 dan 4 menunjukkan bahwa cakram yang terbenam dalam-dalam dapat dengan mudah dikuak oleh pengamatan spasial dan spektral resolusi tinggi garis-garis molekuler. Pancaran ini seharusnya dipancarkan oleh cakram jika sejumlah besar selubung telah terlempar menjauh sebagaimana diharapkan dalam sistem-sistem yang telah berevolusi lebih lanjut. **Bab 5** menghadirkan pengamatan interferometris garis-garis ^{13}CO dan C^{18}O pada transisi rotasi $J = 2 - 1$ dari empat protobintang yang telah dikenal dengan baik. Tiga dari empat benda ini mengisyaratkan keberadaan cakram yang berotasi. Ukuran cakram-cakram ini selaras dengan model dua dimensi pembentukan cakram.

- Keberadaan cakram-cakram ini dapat menjadi sumber pemanasan tambahan. Cakram melepaskan energi saat ia menghantarkan material ke arah dalam menuju bintang, karena cakram harus mempertahankan konservasi momentum sudut dan energi. Proses enerjik ini memanaskan cakram sedemikian rupa sehingga es hanya dapat ditemukan jauh dari bintang pusat. **Bab 6** menghadirkan studi teoritis spesies-spesies utama es (H$_2$O, CO, CO$_2$) pada sebuah cakram aktif di sekitar protobintang yang terbenam. Cakram panas ini diduga diperlukan untuk pembentukan Tata Surya kita. Dengan demikian bab ini menghadirkan hubungan antara tahapan-tahapan dini pembentukan bintang dan pembentukan sistem keplanetan. Prediksi-prediksi yang dibuat kemudian dibandingkan dengan emisi air yang teramati di sekitar protobintang.

Pandangan ke masa depan. Pengamatan-pengamatan pada saat ini telah menguak keberadaan cakram berotasi pada jarak beberapa ratus AU dari protobintang terselubung. Disertasi ini juga membandingkan cakupan cakram terbenam yang disangga rotasi dengan model pembentukan cakram. Akan tetapi dibutuhkan resolusi spasial dan kpekaan yang akan dimiliki ALMA untuk lebih lanjut mempelajari detil-detil pembentukan cakram dan proses evolusi pada tahapan-tahapan terdini pembentukan bintang. Pengamatan garis-garis molekul dengan resolusi spasial dan spektral yang lebih tinggi akan dapat membedakan antara cakram Keplerian dengan selubung yang runtuh. Untuk menyelidiki struktur temperatur suatu cakram (yang penting untuk menyelidiki proses pemanasan) dibutuhkan pengamatan dua transisi berbeda dari suatu molekul agar kondisi eksitasinya dapat diselidiki. Lebih lanjut suatu pengamatan dengan kepekaan tinggi dibutuhkan untuk menyelidiki struktur kecepatan suatu cakram. Hal ini disebabkan karena emisi molekuler pada kecepatan tinggi lebih lemah dari pada pusat garis. Akan lebih mudah pada masa depan untuk menguak kinematika pada skala kecil. Struktur kimiawi cakram-cakram muda juga akan menjadi penting dalam memahami pembentukan sistem keplanetan.

Curriculum vitae

I was born in Sumenep, Indonesia, which is located on the island of Madura. It is located about 40 minutes from a few nice, serene white sand beaches. I attended a Catholic primary school 'Sang Timur' built by the Dutch missionaries. After 11 years living in Indonesia, my brother and I migrated to United States (apparently, I was persistent in wanting to leave). I finished my last year of primary school (6th year) in the greater Los Angeles area, a few minutes away from the Santa Monica beach.

After finishing high school at Chaminade College Preparatory (West Hills, California) in 2003, I started my B.Sc. in astrophysics at the University of California, Los Angeles with a minor in mathematics. During this time, I worked with Dr. Michael Muno on compiling X-ray fluxes from O and B stars in young stellar clusters using data taken by the *Chandra X-ray Observatory*. In the middle of my third year, I participated in the Research Experience for Undergraduate (REU) program in La Serena, Chile, which is located on ocean terraces. The program is hosted by Cerro-Tololo Inter-American Observatory (CTIO). I worked with Dr. Roberto de Propris on the luminosity function of cluster galaxies using images taken by the *Hubble Space Telescope*. During my stay, I gained some experience in observation utilizing the 1 meter and the 4 meter Victor M. Blanco telescope.

I moved to Leiden, a few minutes from the beach, after obtaining my B.Sc. degree to continue my studies in astronomy supported by Oort and Huygens scholarships. For my minor project, I worked with Dr. Richard Alexander on characterizing the transport properties of self-gravitating disks. For my major project, continuing my trend in shifting to the lower energy part of the spectrum, I worked with Dr. Lars Kristensen and Dr. Ruud Visser on submillimeter and near-IR molecular emission from young stellar objects in the Serpens molecular cloud. Thus, I have completely moved from looking for keV photons to meV radiation (6 orders of magnitude in energy) in roughly 4 years.

After my M.Sc., I started my Ph.D. in Leiden. I organized the astrochem seminars in my first 2 years. I was also a teaching assistant for the 'Star and Planet Formation' course by Prof. Ewine van Dishoeck, and the 'Radiation Processes in Astrophysics' course by Dr. Elena Rossi. During the past 4 wonderful years, I have presented the results of my thesis in international conferences in Europe and in the USA. I also had the opportunity to visit the James Clerk Maxwell Telescope in Hawaii. After finishing, I will be a postdoctoral researcher at Institute for Theoretical astrophysics (ITA) in Heidelberg, Germany. For the first time, I will be living inland away from the beaches.

Refereed publications

16. **D. Harsono** et al., *Discriminating protostellar disk formation models with continuum and spectral line observations*, 2014, A&A, subm.

15. M. N. Drozdovskaya et al., *Methanol along the path from envelope to protoplanetary disk*, 2014, MNRAS, subm.

14. C. Walsh et al., *ALMA hints at the presence of two companions in the disk around HD100546*, 2014, ApJL, 791, L6

13. J. E. Lindberg et al., *ALMA observations of the kinematics and chemistry of disc formation*, 2014, A&A, 566, A74

12. M. V. Persson et al., *The deuterium fractionation of water on solar-system scales in deeply-embedded low-mass protostars*, 2014, A&A, 563, A74

11. **D. Harsono** et al., *Rotationally-supported disks around Class I sources in Taurus: disk formation constraints* 2014, A&A, 562, A77

10. N. Murillo et al., *A Keplerian disk around a Class 0 source: ALMA observations of VLA1623A*, 2013, A&A, 560, A103

9. J. K. Jørgensen et al., *A recent accretion burst in the low-mass protostar IRAS 15398-3359: ALMA imaging of its related chemistry*, 2013, ApJL, 779, 22

8. G. S. Mathews et al., *ALMA imaging of the CO snowline of the HD 163296 disk with DCO^+*, 2013, A&A, 557, 132

7. U. A. Yıldız et al., *Water in low-mass star-forming regions with Herschel (WISH-LM) High-J CO survey observed with HIFI*, 2013, A&A, 556, 89

6. **D. Harsono** et al., *Evolution of CO lines in time-dependent models of protostellar disk formation*, 2013, A&A, 555, 45

5. L. E. Kristensen et al., *Water in star-forming regions with Herschel (WISH): II. Evolution of 557 GHz 110-101 emission in low-mass protostars*, 2012, A&A, 542, 8

4. R. Visser et al., *Modelling Herschel observations of hot molecular gas emission from embedded low-mass protostars*, 2012, A&A, 537, 55

3. **D. Harsono**, R. D. Alexander and Y. Levin, *Global gravitational instabilities in embedded discs*, 2011, MNRAS, 413, 423

2. **D. Harsono**, and R. De Propris. *The luminosity function of galaxies to $M_{BgVriz} \sim -14$ in z ~ 0.3 clusters*, 2009, Astronomical Journal, 137, 3091

1. **D. Harsono** , and R. De Propris. *The cluster galaxy luminosity function at z = 0.3: a recent origin for a faint-end upturn?*, 2007, MNRAS, 380, 1036

Acknowledgements

THese past few years could not be ever more enjoyable and entertaining without certain groups of people that accompanied me. I certainly cannot name them all. Also, my deepest gratitudes go beyond these simple words below.

Simon, without your patience and constant guidance through the details of radiative transfer, a large part of this thesis would not be in the state that it is now. I enjoyed our skype conversations during some un-Godly hours. Dear Lars, I have you to thank for introducing me to the world of astrochemistry and shocks. Without your guidance and advices, things would had turned out differently or possibly more 'confused'. Ruud, it was a pleasure having you as my office mate for a brief moment and introducing me to 'simple' chemical models. Greg, your straightforward comments on both scientific and non-scientific aspects gave me a refreshing look in this whole craziness called 'life'. Richard Alexander, I have enjoyed learning about disks and simulations from you. Roberto de Propris, I have you to thank for my first scientific publication. More importantly, you were the one that sent me the link to Leiden and told me to apply even though the deadline has passed. Things in Leiden would not have run smoothly without the excellent support from the computer group and the secretaries.

Linda and Carl, I truly appreciated the countless times the two of you dragged me out of my office to enjoy movies, drinks, and dinners. I finally got to ski because of the two of you. Fike and Cindy, I enjoyed so many conversations and complaints that we shared. Oxalis and Maarten, many thanks for bringing colors and arts into our lives. Finally, the past years would not be the same without your company and occasional gossips at Annie's in the late evenings.

To the board games/beach/park group: Giorgia, Bernadetta, Thibaut, Emilie, Stefania, Rasmus, Daniel Risquez, Carmen Blasco, Steven Rieder, Jeroen Bédorf, Tri, Markus, Eva, Nikta, Yuri Cavechi, Atakan Gürkan, I have enjoyed all of our entertaining nights and days. It was my pleasure being the 'Game Master' for the Huygens-Oort Diplomacy game, and I hope it will never happen again. To Giorgia, your tiramisu is truly the original one. To Michiko and Bernadetta, those Japanese snacks, sushi dinners, and afternoon teas were greatly missed after you left. To Emilie, watching Thibaut dance was one of the highlights of my summer. Belgian beers trip, swimming in the evenings, Essen trips, and centreparc trips were all legen-wait for it...dary. Let's have our own Tuxedo night.

Dear Ted and Hailey, I have enjoyed your company every time I am in the Los Angeles area. The hospitality and friendliness of your family members both in US and China are much appreciated. To James Wigglesworth, Emin Menachekanian, and others, we need more Korean BBQ times. Dearest Indara, it was wonderful meeting up in Munich after all these years and our skype chats are entertaining.

Irene, having you as my office mate made my working hours enjoyable. I have to appreciate the fact that you did not use that ruler extensively. Dearest Edith, all of the conversations, laughs, margaritas, cakes, and the coffees during the past few months are much appreciated: they were 'almost as good' as legendary. To my Brazillian buddy Isa, my weekends in the office and coffee breaks would not be the same without you. You made me laugh every weekend in the office.

Adwin Boogert, our drinks and conversations in Pasadena certainly pushed me toward going to Leiden. I enjoyed our random skype chats and sight-seeing in Utrecht during your short visit in the Netherlands. Dear Stella Kafka, your enthusiasm is truly inspirational and thanks

for the all of the advices, letters, and a short Washington D. C. tour to a Mexican restaurant. I hope to see you soon in Athens.

Dear Joe and Kirsty, you taught me how to properly enjoy Eurovision (with British humours). Pam, the coffee breaks and Friday borrels would not be the same without your presence and keeping me confused at times. Geoff and Star, I miss our board game nights. Catherine, your Irish craziness certainly came in at the right moment. Magnus and Mihaela, your hospitality in Malmö, Bucharest, and Leiden is never forgotten, so... where to next. Niels, just remember that I am always wrong and the cake is a lie. Thanks for making the 5th floor corridor in Leiden as loud as possible: Jeanette, Kalle, Umut, Christian B., Kuo-Song, Silvia V., Thanja, Xiaohu, Koju, Paola, Mihkel, Maria, Alan, Anton, Atilla, and Nienke. My experience in Garching and biergartens would not be the same without: Davide, Stephanie R, Nadia, and Anna. Dear Agata, we actually managed to graduate on the same day!

My weekends and afternoons would not have been as fun without the various people I met through Leiden social football club, badminton (Nuriltje), basketball, rowing for 'Asopos de Vliet' (Remco van der Burg and Willem de Pous, the coaches), and futsal.

To my family members: Ko Elyon, Ci Jeanne, Mommy Fei-Fei, Om Tony, Ko Erwin, and Ci Fenny, thank you for all of the support both from US and Indonesia and for sending me pictures of food that I have never tasted for the past years, I have put them in good use. To my parents, my dad, grandparents, and Om Ritwan, your constant support and teachings over the years have made me the person that I am today.